EXPLORING SUPRAMOLECULAR FEATURES OF SOME INORGANIC AND ORGANIC COMPOUNDS IN THE CONTEXT OF CRYSTAL ENGINEERING

THESIS SUBMITTED FOR THE DEGREE OF
DOCTOR OF PHILOSOPHY (SCIENCE)
JADAVPUR UNIVERSITY
2023

BY

SUPARNA TRIPATHI, M. Sc.

DEPARTMENT OF PHYSICS

JADAVPUR UNIVERSITY

KOLKATA–700032

INDIA

যাদবপুর বিশ্ববিদ্যালয়
কলকাতা-৭০০ ০৩২, ভারত

*JADAVPUR UNIVERSITY
KOLKATA-700032, INDIA

FACULTY OF SCIENCE : DEPARTMENT OF CHEMISTRY : INORGANIC SECTION

CERTIFICATE FROM THE SUPERVISOR

This is to certify that the thesis entitled "**EXPLORING SUPRAMOLECULAR FEATURES OF SOME INORGANIC AND ORGANIC COMPOUNDS IN THE CONTEXT OF CRYSTAL ENGINEERING**" submitted by Suparna Tripathi who got her name registered (Index No: 104/16/Phys./24; Registration Number: SOPHY1110416) on 10/05/2016 in the Department of Physics for the award of Ph. D. (Science) degree of Jadavpur University, is absolutely based upon her own work under the supervision of Dr. Subrata Mukhopadhyay, Professor, Department of Chemistry, Jadavpur University, Kolkata 700032. It is also mentioning that neither this thesis nor any part of it has been submitted for any degree / diploma or any other academic award anywhere before.

Subrata Mukhopadhyay 20/1/2023

Subrata Mukhopadhyay
Professor of Chemistry
Jadavpur University

Dr. Subrata Mukhopadhyay
Professor of Chemistry
Jadavpur University
Kolkata – 700032

Signature of the Supervisor & Date with official seal

*Established on and from 24th December, 1955 vide Notification No. 10986-Edn/IU-42/55 dated 6th December, 1955 under Jadavpur University Act, 1955 (West Bengal Act XXXIII of 1955) followed by Jadavpur University Act, 1981 (West Bengal Act XXIV of 1981)

দূরভাষ : ২৪১৪-৬৬৬৬/৬১৯৪/৬৬৪৩/৬৪৯৫/৬৪৪৩ প্রসারণ : ২৪৬৯ Website : www.jadavpur.edu Phone : 2414-6666/6194/6643/6495/6443 Extn. 2469
দূরবার্তা : (৯১)-০৩৩-২৪১৪-৬৪১৪/২৪১৩-৭১২১/২৪১৪-৬২১০ E-mail : registrar@admin.jdvu.ac.in Fax : (91)-033-2414-6414/2413-7121/2414-6210

Dedicated to
My Beloved Parents
&
Parents in Law

Acknowledgements

It is said that an author never finishes a book, he/she rather desolates it. While such a truth might not be as strongly founded for a thesis, it gains greater strength when it comes to writing its acknowledgement…! I wish to express my profound gratitude to Prof. Subrata Mukhopadhyay under whose expert guidance; I had the privilege of conducting my research. His knowledgeable supervision, academic insights, wise counsel, and immense support and encouragement were invaluable. He not only provided excellent mentoring and learning opportunities, but also offered immeasurable liberty for creativity and self-innovation, which has inevitably opened up new avenues to move forward in coming days. Apart from his invaluable guidance, helpful suggestions, illuminating discussions, his endless tolerance in organizing and representing scientific results with ultimate precision deserves special mention. For that, once again, I would like to express my heartiest thanks and endless gratitude to him, who has added a new dimension in my academic career.

In addition, I am greatly thankful to other faculty members of the Department of Physics, who have provided me not only with inspiration and encouragement but also with the rich academic environment, intellectual stimulation and academic resources essential to the pursuit of my research. I would also like to thank the central instrument facilities of Department of Physics, Jadavpur University and Library staffs for providing me different facilities. The Department of Physics and Chemistry of Jadavpur University provides a rich academic environment and an outstanding heritage, which is something to be cherished forever.

My unfailing thanks go to my labmates Dr. Manojit Mitra, Dr. Anowar Hossain, Dr. Tripti Mondal, Mr. Samit Pramanik, Mr. Samiul Islam, Ms. Prantika Das, Mr. Pratik Dey for their earnest cooperation and support, both academic and non-academic, who contributed in making my time at Jadavpur University even more cordial and enjoyable.

To my parents, parents in law, elder sisters and brother, whose boundless warmth and affection, limitless encouragement, and unflinching motivation and support have been inexhaustible source of strength for me. I convey my deepest respect, love and affection for the encouragement and constant mental back up provided by my beloved husband Dr. Saikat Kumar Seth. I would like to thank our daughter Silvia for showing me the beauty and opposite site of life and making my mind relax during the hard times of my thesis.

I would like to thank our family friends Dr. Dipankar Pradhan, Mrs. Runu Pradhan, Mr. Sayan Pradhan, Mr. Tanmoy Pradhan, Dr. Anindya Sasmal, Mrs. Arpita Das for their affection and patient encouragement towards my academic activities.

My gratefulness in its sincerest terms also goes to Mr. Nabadwip Kuiry (H.M. Swami Shraddhananda Vidyapith, Purulia) and Mrs. Bulu Laha Das (Ex-H.M. Tamralipta Balika Vidyapith, Tamluk, Purba Medinipur), without their support in regard to my research work, it wouldn't have been possible. I would like to thank all of my colleagues of Tamralipta Balika Vidyapith, for their encouragement and kind cooperation.

The blessing, inspiration and good wishes of my family members enabled me to achieve this cumbersome goal. I would like to dedicate this dissertation to them.

Dated: 20/01/2023
Department of Physics
Jadavpur University
Jadavpur, Kolkata-700032, India.

Suparna Tripathi
(SUPARNA TRIPATHI)

ABSTRACT

Title of the thesis: EXPLORING SUPRAMOLECULAR FEATURES OF SOME INORGANIC AND ORGANIC COMPOUNDS IN THE CONTEXT OF CRYSTAL ENGINEERING

Submitted by: Suparna Tripathi **[Index No: 104/16/Phys./24]**

Department: Physics

This thesis includes synthesis and X-ray structural characterization of some inorganic and organic compounds by exploring supramolecular self-assemblies in the solid state. Supramolecular chemistry is the study of noncovalent interactions between molecules. Many new functional materials have been synthesized and structurally characterized by mimicking nature and utilizing the synthesis approaches toward supramolecular chemistry. Although crystal engineering deals with the individual potentiality of weak forces, an exciting aspect is still in a state of infancy, that is, the associative interactions of noncovalent forces to form extended networks and their supramolecular consequences in the solid state.

In this dissertation, X-ray crystallographic and theoretical studies have been critically analyzed various supramolecular architectures of the metal complex and organic compounds. Attempts have been made to understand the grown solids' precise structure and explore intermolecular interactions involved within the structures. Attempts have been made to explore the robust feature of the cooperativity of noncovalent interactions in the context of crystal engineering. Several supramolecular structural diversities have been explored for the first time in the solid-state, where weak interactions play a decisive role in building self-assembled structures. The noncovalent interactions have been quantified by Hirshfeld surface analysis.

The supramolecular interactions have also been successfully rationalized by density functional theory (DFT), Molecular electrostatic potential (MEP), Bader's theory of Atoms in Molecules (AIM), and noncovalent interaction plot index (NCI) to characterize the noncovalent interactions.

Subrata Mukhopadhyay
20/1/2023

Signature of the supervisor

Suparna Tripathi

Signature of the candidate

Dr. Subrata Mukhopadhyay
Professor of Chemistry
Jadavpur University
Kolkata - 700032

CONTENTS

PREFACE

*The title of the present thesis is "**EXPLORING SUPRAMOLECULAR FEATURES OF SOME INORGANIC AND ORGANIC COMPOUNDS IN THE CONTEXT OF CRYSTAL ENGINEERING**". The analysis of the crystalline and molecular structures of organic, inorganic, and other molecules of intrinsic interest can be effectively done using single crystal X-ray diffraction techniques. The primary obstacle to using the single crystal X-ray diffraction technique to determine structure is getting the sample to crystallize in the right size and shape. The proposed research project focuses on spectroscopic and single crystal X-ray diffraction studies of the crystal and molecular structures of organic molecules and metal organic complexes. The investigation would include determining crystal and molecular structure from X-ray intensity data. The conformation of the molecules has been revealed by crystallographic research, and the significance of intermolecular interactions in molecular packing has also been examined, with an emphasis on the formation of self-assembly.*

To get a thorough understanding of the subject matter, various supramolecular features of all compounds and complexes are thoroughly studied while studying the most recent advancements in crystal engineering and crystallography. Crystal engineering is relatively a new field of study that addresses issues with intermolecular interactions. Weak interactions-based self-assembly has proven to be a helpful and effective approach for the creation of predesigned and well-defined architectures. Even though hydrogen bonds are the most reliable and widely used in molecular recognition of crystalline materials, other weaker contacts have been examined and their fascinating roles in the development of supramolecular self-assembly are studied.

Tools based on the Hirshfeld surface give a distinctive method for predicting crystal structure, and this approach makes it simple to learn about patterns in crystal packing. By identifying the packing motifs, the derivation of the Hirshfeld surface and breakdown of the corresponding 2D fingerprint-plot offer a practical method for quantifying the interactions within crystal structures, revealing notable similarities and differences between related structures, and holding significant promise for crystal engineering. The

energetic and geometric features of salt-bridge interaction are studied and its impact on the resultant supramolecular organization is analyzed using theoretical DFT-D3 calculations.
The theoretical study combines the energetic features of the noncovalent forces that participate in the extended network and the characterization of the diverse interactions by means of Bader's theory of 'atoms in molecules'(AIM) and 'noncovalent interaction' plot index (NCI).

The study of noncovalent weak interactions between molecules or similar entities is known as crystal engineering. It is a multidisciplinary branch of research that examines the physical, chemical, and biological properties of various chemical compounds with a higher level of complexity. Numerous new functional and technologically advanced materials have been created by mimicking nature and applying synthetic techniques to supramolecular chemistry. By using X-ray crystallographic and other physico-chemical techniques, numerous supramolecular structures of both organic molecules and inorganic complexes are critically examined in the current dissertation. There are four chapters in the current thesis. The contents of respective chapters are summarized below.

In ***Chapter 1****, the fundamental ideas guiding single-crystal X-ray diffraction techniques for crystal structure determination of small molecules are briefly discussed. The phase problem in crystallography, structure determination from single crystal X-ray data, structure solution methods, structure refinement, various methods for characterization of the grown solids are included in detail in this chapter. This chapter illustrates the background for the work presented in this thesis. Molecular recognition, self-assembly, crystal engineering, supramolecular synthon and other intermolecular interactions (including non-covalent interactions) have all been covered in detail. The general characteristics of distinct packing forces that account for the diverse topologies observed thus far have been outlined. This chapter also covers the Hirshfeld surface concepts and related Fingerprint plots, which have been utilized to illustrate the authenticity of the thesis's provided structures.*

*In **Chapter 2**, a new octahedral Co(III) complex namely 5-ethyl-2-methylpyridinium trans-bis(iminodiacetato-k$_3$O,N,O′)cobaltate(III), has been synthesized and structurally characterized by single crystal X-ray diffraction analysis. In the solid state, the structure is stabilized through various hydrogen bonds, C–H···π and π–π stacking interactions that leads the molecules to generate diverse supramolecular architectures. The solid-state supramolecular structure has been corroborated with theoretical calculations. The intermolecular interactions are quantified via Hirshfeld surface analysis and corresponding total energy framework has been calculated. The intricate combination of C–H···π and π–π stacking interactions are fully analyzed by computational studies. The noncovalent interactions have been characterized by Bader's theory of "atoms-in-molecules" (AIM) and "noncovalent interaction" (NCI) plot index.*

*In **Chapter 3**, a series of pyridinium-carboxylate salts (**1–3**) were designed, synthesized and structurally characterized to explore the importance of salt-bridge (SB) interactions in building self-assembled structures. We present a comprehensive analysis of the SB interaction in crystal structures of 4,4′-oxybis(benzoic acid) with substituted aminopyridines where the SBs displays extremely well defined geometric preferences. In the solid-state, compound (**1**) exhibit lone-pair(l.p)···(SB)/(SB)···π^+ assemblies while compound (**2**) shows C–H···(SB)/(SB)···π network. Interestingly, compound (**3**) exhibits two distinct networks π^+···(SB)/(SB)···(SB)/(SB)···π^+ and C–H···(SB)/(SB)···H–C. These unexplored extended supramolecular networks are evident and explored for the first time in crystal structures. The duality of the SBs in stabilizing the π-facial interactions with electron rich and/or electron poor moieties are also described. The energetic and geometric features of salt-bridge interaction are studied and its impact on the resultant supramolecular organization are analyzed using theoretical DFT-D3 calculations. The theoretical study combines the energetic features of the noncovalent forces that participate in the extended network and the characterization of the diverse interactions by means of Bader's theory of 'atoms in molecules'(AIM)..*

*In **Chapter 4**, three versatile 4′-substituted 2,2′:6′,2″-terpyridine compounds (**1–3**) having different substitutions (4-ethoxyphenyl, 4-methoxyphenyl and pyridyl) at 4′-position of the central pyridine ring have been synthesized and structurally characterized. Three representative crystal structures have been determined through single crystal X-ray diffraction analysis. X-ray crystallography revels that the structures are stabilized through C–H···π and π–π stacking interactions. In the solid-state, the supramolecular assemblies of the title compounds have been explored in detail. Compounds (**1**) and (**3**) exhibits both C–H···π and π–π interactions in building supramolecular assemblies whereas compound (**2**) exhibit π–π interaction only. All the intermolecular interactions that are involved within the structures are quantified through Hirshfeld surface analyses. The weak noncovalent interactions that played significant role in building supramolecular assemblies are further characterized by Bader's theory of 'atoms-in-molecules' (AIM). Finally, the supramolecular networks are characterized by theoretical 'Noncovalent Interaction' (NCI) plot index.*

Chapter 1

X-ray structure solution and crystal engineering: Theory and methodologies

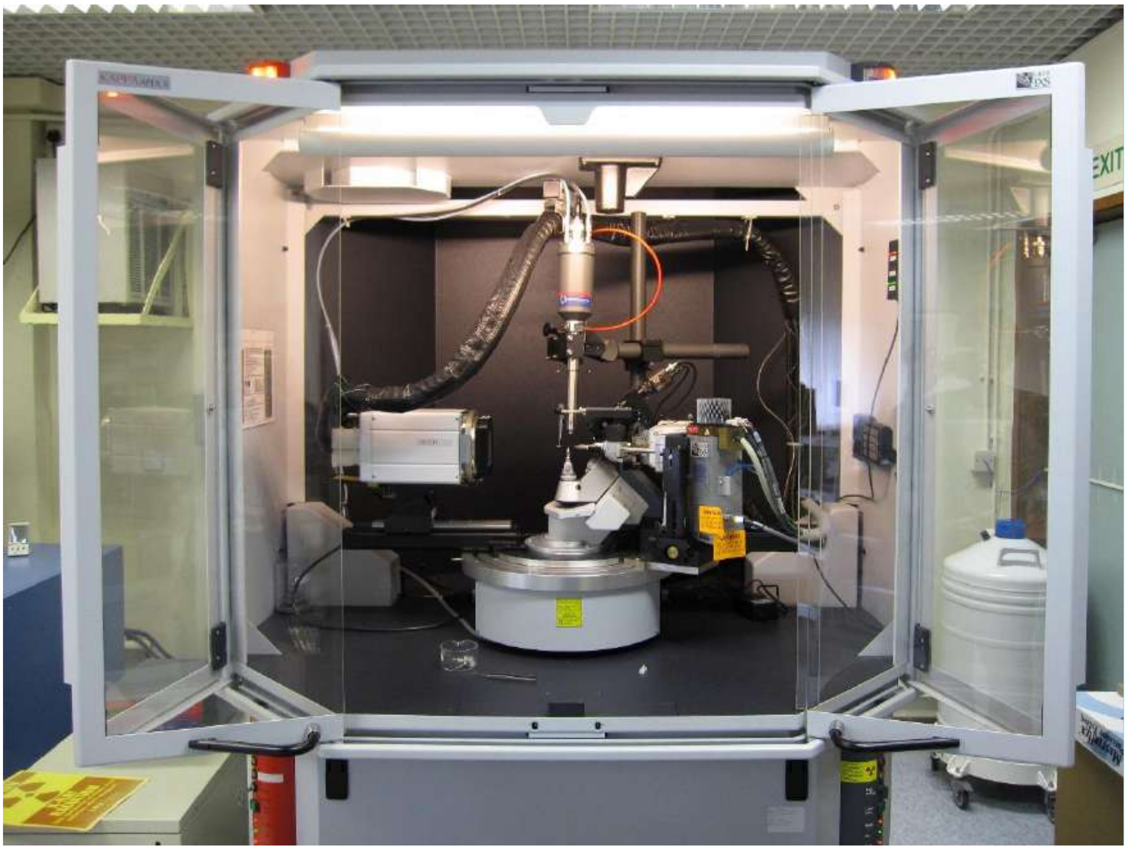

X-ray diffraction and crystallography is absolutely the most powerful analytical approach for characterizing crystalline solids' structural properties. A crystal can appear as a periodic arrangement of an array of atoms. One imagines three families of planes, the planes in every family being parallel to and equidistant from one another. Accordingly, one obtains a tiling of the crystal space via congruent parallelepipeds, which is said to be a fundamental parallelepiped, or unit cell, of the crystal. If every unit cell includes a molecule, a collection of atoms in its interior, and if the atoms are arranged in precisely the same way in all the unit cells, then each unit cell and its contents are indistinguishable from every other unit cell and its contents. The relation between physical, chemical, biological properties and structural order reflects crystallography's role in basic sciences and is an interdisciplinary subject. The subsequent sections have provided a brief summary of the study's methods and the principles underlying such methods.

1.1. X-ray diffraction and the phase problem in crystallography

There corresponds to each atom an electron density function; as a result, with the aid of superposition of the atomic electron density functions, one obtains an overall electron density function $\varrho(r)$, a non-negative function of the position vector $\mathbf{r}(x,y,x)$ which gives the number of electrons per unit volume at the position $\mathbf{r}(x,y,z)$. It is clear from the geometric construction that the electron density function in any unit cell is the same as that in every other unit cell. Consequently, $\varrho(\mathbf{r})$ is a triply periodic function of position, and the electron density distribution in a crystal may be represented by way of three-dimensional Fourier series

$$\rho(x,y,z) = \tfrac{1}{V}\sum_{h}\sum_{k}^{\infty}_{-\infty}\sum_{l} \; F_{hkl}\exp[-2\pi i\,(hx+ky+lz)] \qquad (1.1)$$

where the coefficient of the Fourier summations are the F_{hkl}'s of the diverse diffraction spectra, V is the volume of the unit cell, and F_{hkl} is the crystal structure factors. $\varrho(r)$ is the electron density function that is a non-negative function of position vector **r**(x,y,x) and offers the number of electrons per unit volume at the position **r**(x,y,x).

As soon as the summation on the right-hand side is performed, locating atoms on the electron density peaks is trivial.

The structure factor F_{hkl} can be conveyed as

$$F_{hkl} = |F_{hkl}| \exp(i\,\varphi_{hkl}) \qquad (1.2)$$

where $|F_{hkl}|$ is the magnitude of the structure factor and φ_{hkl} is the phase of the structure factor. Once the electron density at every point in the unit cell is known, finding the atom at the electron density maxima is insignificant. The magnitude of F's may be received from experimentally observed intensity; however, there are no experimental methods to record the phases, φ_{hkl}. Accordingly, the data from the diffraction experiment are insufficient for carrying out the Fourier synthesis. The experiments offer only half the required data. In a situation like this, it seems that the summation of the terms of (1.1) and, therefore, the finding of atoms in the unit cell, i.e., crystal structures, are independent due to a lack of phase data that establishes the phase problem of crystallography. If there had been a few ways of learning these phases, it would be habitual to discover the arrangement of atoms in any crystal, but it is probably complicated.

In the absence of direct phase information, crystal structures are solved by indirectly finding the phases. Two general methods may result in a solution-

- A Fourier summation can be organized wherein the coefficients only use magnitudes. This effects a map of a function defined in crystal space that relates to the image of the crystal structure this is sincerely sought.
- The second sort of effort to overcome conquer the phase problem can be made in Fourier space by means of trying to assign phases to the F_{hkl}'s so that the mathematical summation of R.H.S of eq(1.1) may be done.

1.2. Structure determination from single crystal X-ray diffraction

The various steps concerned all through crystal structure determination starting from crystal selection to refinement, are depicted below:

- Selection of suitable single crystal
- Obtain unit cell geometry and preliminary symmetry information
- Collection of intensity data
- Data reduction
- Structure solution
- Refinement of the model structure

1.2.1. Collection of X-ray intensity data

The intensity data collection using a single crystal diffractometer could be easily executed in the following manner.

- Selection of an excellent quality single crystal and mounting it at the goniometer head
- Location of few diffraction maxima and their indexing for determination of unit cell parameters
- Collection of the intensity data accompanied by data reduction (Lorentz, polarization and absorption corrections).

1.2.2. Space group determination

This is one of the most significant steps for determining crystal structure from single crystal X-ray diffraction data. The theory of space groups, one of the triumphs of mathematical crystallography, relates crystal symmetry, on the atomic scale, to the viable atomic arrangements which possess that symmetry. For instance, if a given substance is known to be orthorhombic symmetry and has ‘n’ atoms in the unit cell, then space-group theory lists all feasible arrangements of ‘n’ atoms with orthorhombic symmetry. A further reduction in the number of possibilities can be made by noting the reflection indices absent from the diffraction pattern. By such means alone, group theory can often exclude all but two or three possible atomic arrangements.

Few space groups can be determined uniquely from the systematic absence criteria of the diffraction pattern. When systematic absences of the diffraction data fail to determine the space group uniquely, numerous alternative space groups must be considered, and only a successful structure solution is accepted.

1.2.3. Crystal structure solution

The most usually used approaches for overcoming the phase problem and for solving crystal structures of small molecules are (i) the Patterson method, which treats the subject in crystal space, and (ii) the direct method, which treats diffraction (reciprocal) space.

1.2.3a. Patterson method

It is impossible to discover the electron density of a crystal by using the experimental data in a Fourier synthesis because only the magnitudes of the amplitudes are measurable. A. L. Patterson, however, confirmed that the square of these magnitudes yields precious information about the crystal structure.

A. L. Patterson [1] showed the first systematic approach to structure determination from the experimentally measured intensity in 1934. The inability to synthesize an electron density straightforwardly from the measured intensities is because the Fourier coefficients F_{hkl}'s are not fully available. Using the famous 'Convolution' function of Fourier theory to the specific problem of crystal structure analysis, a function in the form of a Fourier series depending on the $|F_{hkl}|^2$ alone, known as the Patterson function, can be obtained. This kind of function is primarily based on Fourier coefficients, $|F_{hkl}|^2$ can be derived by forming products of each Fourier coefficient F_{hkl} with its complex conjugate. Products like this can be devised from products of the electron-density function. For simplicity, the derivation is achieved for a one-dimensional case that could be extended to two and three dimensions.

It is handy to apply absolute coordinates in this derivation where the fractional coordinates and absolute coordinates X are related by

$$\mathrm{x} = \left(\frac{\mathrm{X}}{\mathrm{a}}\right)$$

The electron densities of a one-dimensional system at two points; specifically X and X+U are given by

$$\rho(\mathrm{X}) = \frac{1}{\mathrm{a}}\sum_{\mathrm{h}} \mathrm{F_h}\, \mathrm{e}^{\frac{-\mathrm{i}2\pi \mathrm{hX}}{\mathrm{a}}} \quad (1.\,3)$$

$$\rho(\mathrm{X}+\mathrm{U}) = \frac{1}{\mathrm{a}}\sum_{\mathrm{h}} \mathrm{F_h}\, \mathrm{e}^{\frac{-\mathrm{i}2\pi \mathrm{h(X+U)}}{\mathrm{a}}} \quad (1.4)$$

Multiplying eq(1.3) and eq(1.4), we get the product of two-electron densities inside the identical crystal separated by a chosen interval U. If this product ρ(X) ρ(X+U) is integrated with respect to X throughout X, i.e., from X = 0 to X = a; it affords a measure of the product of electron density which is separated from other electron density by the close interval U.

$$\mathrm{P(U)} = \int_0^{\mathrm{a}} \rho(\mathrm{X})\, \rho(\mathrm{X}+\mathrm{U})\mathrm{dX} \quad (1.\,5)$$

$$= \int_0^{\mathrm{a}} \left[\frac{1}{\mathrm{a}}\sum_{\mathrm{h}} \mathrm{F_h}\, \mathrm{e}^{\frac{-\mathrm{i}2\pi \mathrm{hX}}{\mathrm{a}}}\right] \left[\frac{1}{\mathrm{a}}\sum \mathrm{F_h} \mathrm{e}^{\frac{-\mathrm{i}2\pi \mathrm{h(X+U)}}{\mathrm{a}}}\right] \mathrm{dX} \quad (1.6)$$

This is the integral of a sum of terms. The separate terms in this product, in general, have different indices h. Designating these as m and q and separating the variable part of the exponential in (1.6).

$$\mathrm{P(U)} = \int_0^{\mathrm{a}} \left[\frac{1}{\mathrm{a}}\sum_{\mathrm{m}} \mathrm{F_m}\, \mathrm{e}^{\frac{-\mathrm{i}2\pi \mathrm{mX}}{\mathrm{a}}}\right] \left[\frac{1}{\mathrm{a}}\sum_{\mathrm{q}} \mathrm{F_q}\, \mathrm{e}^{\frac{-\mathrm{i}2\pi \mathrm{(X+U)q}}{\mathrm{a}}}\right] \mathrm{dX} \quad (1.\,7)$$

$$= \frac{1}{\mathrm{a}^2}\sum_{\mathrm{m}}\sum_{\mathrm{q}} \mathrm{F_m F_q} \mathrm{e}^{\frac{-\mathrm{i}2\pi \mathrm{qU}}{\mathrm{a}}} \int_0^{\mathrm{a}} \mathrm{e}^{\frac{-\mathrm{i}2\pi \mathrm{(m+q)X}}{\mathrm{a}}} \mathrm{dX} \quad (1.8)$$

The integral part in (1.8) vanishes except when q ≠ –m, whereas for q = –m, the integral part in (1.8) becomes a.

Eq(1.8) can be written as

$$\mathrm{P(U)} = \frac{1}{\mathrm{a}^2}\sum_{\mathrm{h}} \mathrm{F_h F_{-h}} \mathrm{e}^{\frac{-\mathrm{i}2\pi(-\mathrm{h})\mathrm{U}}{\mathrm{a}}}\, a$$

$$= \frac{1}{\mathrm{a}}\sum_{\mathrm{h}} \mathrm{F_h F_{-h}} \mathrm{e}^{\frac{\mathrm{i}2\pi \mathrm{hU}}{\mathrm{a}}} \qquad (1.9)$$

Expressing the fractional coordinates u=U/a,

$$\mathrm{P(U)} = \frac{1}{\mathrm{a}}\sum_{\mathrm{h}} |\mathrm{F_h}|^2\, \mathrm{e}^{\mathrm{i}2\pi \mathrm{hu}} \qquad (1.10)$$

This result can be further simplified by expanding the exponential term in (1.10)

$$\mathrm{P(U)} = \frac{1}{\mathrm{a}}\sum_{\mathrm{h}} |\mathrm{F_h}|^2\, (\cos 2\pi \mathrm{hu} + \mathrm{i}\,\sin 2\pi \mathrm{hu}) \qquad (1.11)$$

Now according to Friedel's law, $|\mathrm{F_h}|^2 = |\mathrm{F_{-h}}|^2$

Now the summation over h in eq(1.11) gives to paired terms in (+h) and (–h):

For (–h), $|\mathrm{F_h}|^2\cos 2\pi \mathrm{hu}$ becomes

$|\mathrm{F_{-h}}|^2\cos 2\pi(-\mathrm{h})\mathrm{u} = |\mathrm{F_h}|^2\cos 2\pi \mathrm{hu}$

and for (–h), $\mathrm{i}|\mathrm{F_h}|^2\sin 2\pi \mathrm{hu}$ becomes-

$\mathrm{i}|\mathrm{F_{-h}}|^2\sin 2\pi(-\mathrm{h})\mathrm{u} = -\mathrm{i}|\mathrm{F_h}|^2\cos 2\pi \mathrm{hu}$

So the sine terms in eq(1.11) cancel in pairs, leaving

$$\mathrm{P(U)} = \frac{1}{\mathrm{a}}\sum_{\mathrm{h}} |\mathrm{F_h}|^2\, (\cos 2\pi \mathrm{hu}) \qquad (1.12)$$

This shows that the Patterson function has the same value for +u and –u, so it's far symmetrical in origin. Hence all Patterson functions have a centre of symmetry in origin, irrespective of whether the crystal is centrosymmetric or not.

The two and three-dimensional formulas of (1.12) are

$$\mathrm{P(uv)} = \frac{1}{\mathrm{A}}\sum_{\mathrm{h}}\sum_{\mathrm{k}} |\mathrm{F_{hk}}|^2 \cos 2\pi(\mathrm{hu} + \mathrm{kv})$$

$$\mathrm{P(uvw)} = \frac{1}{\mathrm{V}}\sum_{\mathrm{h}}\sum_{\mathrm{k}}\sum_{\mathrm{l}} |\mathrm{F_{hkl}}|^2 \cos 2\pi(\mathrm{hu} + \mathrm{kv} + \mathrm{lw}) \qquad (1.13)$$

Where A is the area of the two-dimensional cell and V is the volume of the three-dimensional cell.

This function shows that each peak in the Patterson map corresponds to an interatomic vector in the crystal structure, with the magnitude of the peak being proportional to the product of electron densities of the corresponding pair of atoms. The Patterson method [1] is compelling and valuable for finding the heavy atom in a structure because the peaks due to heavy atom – heavy atom interaction could predominate in a map computed from (1.13), and the atomic positions of the heavy atom(s) may be analyzed. However, for the lighter atom, the X-ray intensities are less sensitive to the nature and positions than the heavy atoms. One would like to replace 'Direct methods' to overcome this problem.

1.2.3b. Direct method

In this method, the phase angles of reflections are derived directly from the observed structure factor amplitudes via mathematical relationships among intensities and indices of the reflections. The relationships are based on two physical properties of crystal:

(i) The electron density is non-negative wherever in the unit cell [$\rho(x,y,z) \geq 0$ for all (x, y, z)].

(ii) The structure consists of almost spherical atoms spread evenly throughout the unit cell volume.

Since the electron density $\rho(r)$, is associated with the structure factors F(h) by a Fourier transformation (Eqn. 1.1), any constraints on the electron density impose corresponding constraints on the structure factors. As the structure amplitudes are known, most constraints restrict the values of the structure factors phases and, in favorable cases, are sufficient to determine the phase values directly. Some constraints on the electron density that have been utilized in structure determination are listed in Table 1.1.

Table 1.1. Constraints on the electron density

Constraints	*How Used*
1. Atomicity of $\rho(r)$	Normalized structure factors [2]
2. Positivity of $\rho(r)$	Inequalities and determinants [3, 4]
3. $\int\rho^3(r)\,dv$ =max	Phase relationship and Tangent formula [5,6]
4. Equal atoms	Sayre's equation [7]
5. $\int\rho(r)\ln\rho(r)\,dv$ =max	Maximum entropy methods
6. Partial structure	Modification of probability equations
7. Multiple motifs	Molecular replacement

The discrete atom condition in Table 1.1 is used in defining the normalized structure factor, E as

$$|E_{\mathbf{h}}|^2 = I_{\mathbf{h}} / \varepsilon_{\mathbf{h}} \langle I \rangle \qquad (1.14)$$

The constraints indexed in Table 1.1 leads to the general inequalities of Karle and Hauptman [4], probability relationships among the phases [5], and the tangent formula [6], which can be expressed as

$$\tan\Phi_{\mathbf{h}} \approx \frac{\sum_{\mathbf{k}} |E_{\mathbf{k}}\, E_{(\mathbf{h}-\mathbf{k})}|\sin[\Phi_{\mathbf{k}} + \Phi_{(\mathbf{h}-\mathbf{k})}]]}{\sum_{\mathbf{k}} |E_{\mathbf{k}}\, E_{(\mathbf{h}-\mathbf{k})}|\cos[\Phi_{\mathbf{k}} + \Phi_{(\mathbf{h}-\mathbf{k})}]} \qquad (1.15)$$

where the symbol ≈ means 'probably equals'. Sayre [7] used the 'equal atoms' constraint to give an exact relationship among the structure factors

$$F_{\mathbf{h}} = \theta_{\mathbf{h}} \sum_{\mathbf{k}} F_{\mathbf{k}} F_{(\mathbf{h}-\mathbf{k})} \qquad (1.16)$$

where θ_h depends on the shape of the atom. Equations (1.15) and (1.16) can be rewritten as

$$\phi_h \approx \text{phase of } [E_k\, E_{h-k}]$$

$$\approx \phi_k + \phi_{h-k}$$

which can be rearranged to give the well-known triple phase relationship

$$\phi_h + \phi_k + \phi_{h-k} \approx 0 \qquad (1.17)$$

Direct structure determination methods have become popular because they can be automated and are, consequently, easy to use. The direct methods have been implemented in several computer programs like SHELXS97 [8], and SIR2004 [9]. The program generates random phase sets, then refines the phases using the phase annealing and tangent formula methods. In 1987 M. M. Woolfson published a review on the history and development of direct methods [10]. An in-depth discussion on the principles of direct methods and the way they may be carried out in practice are summarized in the books of Dunitz [11], Stout and Jensen [12], Ladd and Palmer [13] etc.

1.2.4. Structure refinement

When the partial structure is attained via both the Patterson or Direct methods, the main impediment has been left at the back, and it is a routine matter to refine this roughly known structure to a precision that the data allow. Numerous methods exist to accomplish this refinement, but the least commonly used technique is the Least-squares method, as described below.

If we define a linear function Φ with X_n variables and P_n parameters as:

$$\Phi = P_1X_1 + P_2X_2 + ... + P_nX_n \qquad (1.18)$$

and, if the values of the function are known at m points with $m > n$; then following least squares principle, the 'best' values for the $P_1, P_2, ... , P_n$ parameters are given by those, which minimize the function

$$\chi^2 = \sum w_i (\Phi_{o,i} - \Phi_{c,i})^2 \qquad (1.19)$$

where $\Phi_{o,i}$ is the observed value of the function at i, $\Phi_{c,i}$ is the calculated value of the function at i, and w_i is an assigned weight for the observed value. In crystallography, the parameters may be refined against either the structure factors, $\Delta = | |Fo| - |Fc| |$, or the intensities, $\Delta = |Fo^2 - Fc^2|$. In either case, the function being minimized is $\sum w \Delta^2$. It's far normal to count on that the trial parameters need only small shifts to attain the correct.

The model structure acquired employing any of the previously mentioned procedures is approximate, and the atomic parameters (positional and thermal) and the scale factor should be refined so that the calculated F_c's agree properly with the observed F_o's. The agreement between the calculated- and actual-structure is evaluated by the residual factors, i.e.,

$$R = \frac{\sum_h \left\| F_o \right| - \left| F_c \right\|}{\sum_h \left| F_o \right|} \qquad (1.20)$$

and

$$wR = \left[\frac{\sum_h w_h \left(\left| F_o{}^2 \right| - \left| F_c{}^2 \right| \right)^2}{\sum_h w_h \left| F_o{}^2 \right|^2} \right]^{1/2} \qquad (1.21)$$

where the weight, $w_h = 1/\sigma^2(F_o)$, $\sigma(F_o)$ being the estimated standard deviation of F_o.

A third statistical parameter, the goodness of fit, 'S', that is 'the standard deviation of an observation with unit weight', displays the reliability of standard deviations of the positional and displacement parameters of the atoms. In case of refinements on F^2, the goodness of fit has the form:

$$S = \{\sum [w(F_o^2 - F_c^2)^2] / (n-p)\}^{1/2} \qquad (1.22)$$

where n is the number of reflections and p is the total number of parameters refined. As soon as the refinement is completed, distinct geometrical parameters, i.e., bond lengths, bond angles, torsion angles, mean planes through selected atoms, etc., may be effortlessly calculated.

1.3. Methodologies for characterization of grown solids

Crystals are a prerequisite for understanding the physics and chemistry of the solid state. Crystals discover crucial uses in research and technology. Therefore, assessing grown solids' physical and chemical perfection is necessary to evaluate their quality. A crystal is thoroughly characterized when its identity, concentration, and position of all its constituent atoms and other related properties are known. Numerous characterization techniques include CHN analysis, Powder X-ray diffraction, FTIR analysis, DTA-TGA, and many others. CHN analysis gives an idea about the empirical formula of the compound. FTIR analysis and X-ray diffraction are used to identify the synthesized material. DTA-TGA analysis gives an idea approximately the thermal stability of the sample.

Diverse methodologies have been implemented for the characterization of the grown solids, which are listed beneath:

- Elemental analysis
- Infrared spectroscopic analysis
- X-ray diffraction (powder and single crystal)
- Thermal analysis

1.3.1. Elemental analysis

Elemental analysis of carbon, hydrogen, and nitrogen is the most essential- and, in many cases, the only investigation performed to characterize and prove an organic sample's elemental composition. In this present thesis work, use has been made of a Perkin Elmer 2400 CHN elemental analyzer. The sample under test is weighed using a tin capsule. The required amount is 2 to 3 mg of organic material and may hardly ever exceed 10 mg if inorganic matter with little carbon content is investigated. The tin capsule enclosing the sample falls into the reactor chamber, where excess O_2 is introduced before. At approximately 990°C, the material is mineralized. The complete oxidation is reached at a tungsten trioxide catalyst that is passed using gaseous reaction products. The resulting mixture should thus consist of CO_2, H_2O, and NO_x. The product gas mixture flows through a silica tube packed with copper granules. In this zone, at about 500°C, remaining oxygen is bound, and nitric/nitrous oxides are reduced. The leaving gas stream includes the analytically important species CO_2, H_2O, and N_2. High-quality helium (Quality 5.0) is used as carrier gas. Subsequently, the gas mixture is brought to a defined pressure state and is passed to a gas chromatographic system containing a packing material. The packing material first adsorbs the gases, desorbing them separately, depending upon the affinity between the analid and packing material. The thermal conductivity of each coming out from the chromatographic column is measured and compared with a standard sample (acetanilide) from which the amount of each element (μV/μg) is observed. Detailed results of our work on CHN analysis have been included in appropriate chapters.

1.3.2. Infrared spectroscopic analysis

Infrared spectroscopy is one of the most vital analytical techniques for scientists. The underlying basis of applied infrared spectroscopy is that almost all organic substances possess selective absorption at unique frequencies in the infrared portion of the electromagnetic spectrum. A spectrometer determines the percent transmission or absorption of the sample at a series of narrow frequency intervals throughout a chosen part of the spectrum. A plot of these transmission or absorption values versus frequency or wavelength units constitutes an infrared spectrum characteristic of the sample under study. A molecule to show infrared absorption must possess a specific feature, i.e., an electric dipole must change during the vibration. The more significant the change, the more intense will be the absorption. Vibrations can involve either a change in bond length (stretching) or bond angle (bending). A few bonds can stretch in phase (symmetrical stretching) or out of phase (asymmetric stretching).

The infrared spectrometer consists essentially of

(i) A source
(ii) Optical path and monochromator
(iii) Detector and amplifier

The source is usually a filament maintained at red or white heat through an electric current. Nernst filament made of rare-earth oxides, or globar filament, made of carborundum, is used as source filament. The source beam is focused on the sample with the help of a mirror silvered on the surface. Monochromators are usually rotatable grating that could produce radiation of preferred frequency. The detectors may be of two types, one senses the heating effect of radiation, and the other depends on photoconductivity. In the first type, the radiation falls on a small cell containing air; temperature changes are measured in terms of pressure changes within the cell, which may be recorded directly as transmittance. Photoconductors are usually semiconductors, and PbS, sensitive to infrared radiation, is used as a detector. A type of Wheatstone bridge network can measure the conductivity of the material. The sample is ground to a fine powder with KBr, after which pressed into a transparent disk. It is then located directly inside the infrared beam in a suitable holder.

1.3.3. X-ray diffraction analysis

X-ray diffraction is a vital technique in materials characterization to obtain information on an atomic scale from crystalline and noncrystalline materials. X-rays lie in the electromagnetic spectrum between ultraviolet light and gamma radiation and have an approximate wavelength of about 1 Å (1–10 nm), about the identical size of an atom. X-ray diffraction has been utilized in two main areas: the fingerprint characterization of crystalline materials and their structure determination. Although X-ray single-crystal and powder-crystal diffraction patterns contain the same basic information, in the former case, this information is distributed in three-dimensional space (Figure 1.1a). In contrast, in the latter case, the three-dimensional diffraction data are compressed into one dimension (Figure 1.1b), leading to numerous peaks overlapping in the powder diffraction pattern. Such peak overlap obscures information on the intensities of individual diffraction maxima and constitutes the main reason for difficulties in solving crystal structures directly from powder diffraction data.

1.3.3a Powder X-ray diffraction

Generally, the powder method is used to identify the materials under investigation. Each crystalline solid has its specific characteristic X-ray powder pattern, which can be used as a "fingerprint" for its identification. When a monochromatic X-ray beam is incident on the surface of a crystal, it is reflected. However, the reflection occurs only when the incidence angle has specific values. Those values rely upon the wavelength and lattice constants of the crystal. The crystal is represented by a set of parallel planes corresponding to the atomic planes. The incident beam is reflected partially at each of these planes, which act as mirrors, and the reflected rays are then collected simultaneously at a distant detector. The reflected rays interfere with the detector, and, according to physical optics, the interference is constructive only if the difference between the paths of any two consecutive rays is an integral multiple of the wavelength, i.e., $n\lambda = 2d\sin\theta$. This is the well-known Bragg's law where n is an integer, λ is the wavelength in Å, d is the interatomic spacing, and θ is the diffraction angle in degrees.

The X-ray diffraction experiment requires an X-ray diffractometer that incorporates an X-ray source, the sample under investigation, and a detector to select the diffracted X-rays. An automatic counter serves as the cause for measuring the intensity of X-ray diffraction. The diffracted intensities are counted directly, and the angular setting at which they occur helps us ascertain the cell geometry by applying Bragg's law and determining crystal structure. The powder method derives its name from a polycrystal sample, which may take many physical forms but is usually a powder. In this method, the sample is ground to a fine powder and put in a glass or metal plate groove. The sample's surface is made smooth by pressing the surface with the help of a glass slide. Uniform packing of the sample is essential to get a reproducible result. The sample is then put inside a goniometer of a powder X-ray diffractometer. The intensity of X-ray diffraction is then recorded on a paper chart recorder. The goniometer and the paper chart recorder are switched on simultaneously, and at each Bragg angle, the diffracted beam's intensity seems like a line having a certain width on the paper chart, or the number of the counts is recorded directly by using a computer. From the positions of those diffraction lines, 2θ and therefore d can be known, and miller indices can be calculated using the computer program POWD [14].

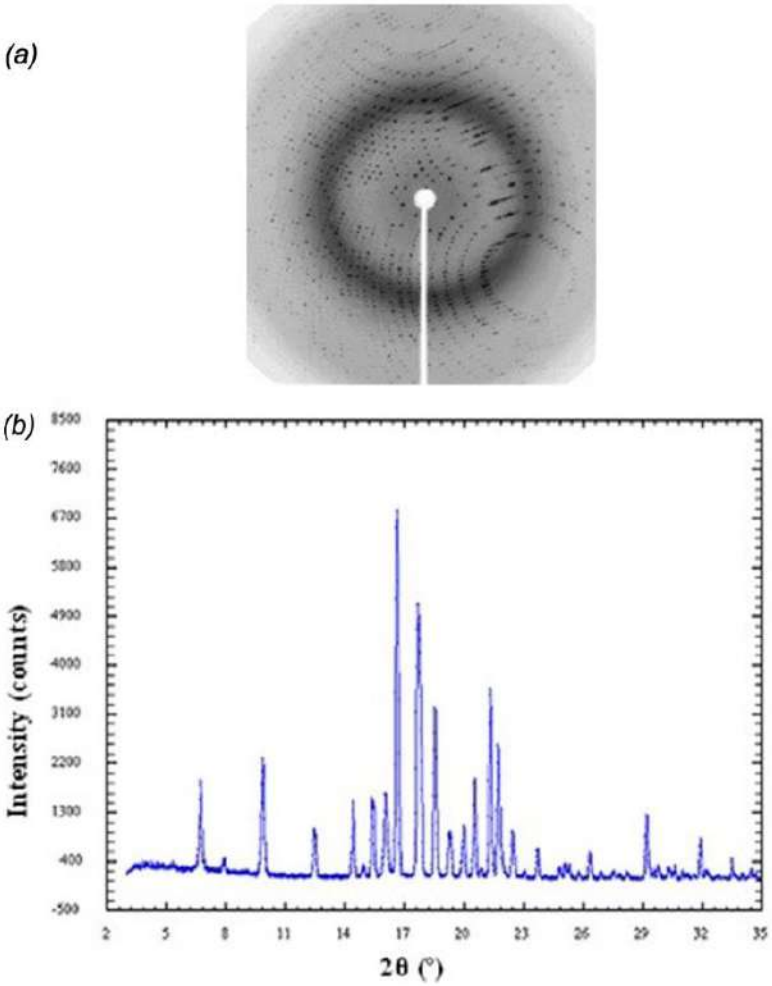

Figure 1.1. (a) Single crystal X-ray diffraction pattern; (b) powder X-ray diffraction pattern.

1.3.3b Single crystal X-ray diffraction: Crystallographic analysis

Single crystal X-ray diffraction measurements of the grown solids were carried out on a Bruker APEX II Kappa CCD single crystal diffractometer equipped with a graphite monochromator. MoKα radiation (λ = 0.71073 Å) was used for all of the collections that were controlled by APEX2 [15], with data collected at various temperatures. Data were corrected for Lorentz and polarization effects using SAINT [15], and multi-scan absorption corrections were applied using SADABS [15]. The structures were solved by direct methods (SHELXS-2016) [16] and refined using full-matrix least-squares procedures using the SHELXL-2016/6 program [16]. All non-hydrogen atoms were refined anisotropically, all hydrogen atoms bound to carbon were placed in the calculated positions, and their thermal parameters were refined isotropically with $U_{eq} = 1.2 - 1.5U_{eq}(C)$. The N–H hydrogen atoms were located in difference Fourier maps, and their coordinates were refined with $U_{eq} = 1.2U_{eq}(N)$. All molecular plots and packing diagrams were drawn using Mercury [17], and additional metrical data were calculated using PLATON [18,19]. Tables were prepared using WINGX [20].

A detailed methodology has been appended below for crystallographic analysis.

- ***Sample selection and preparation***

  Samples for single-crystal diffraction need to be selected from unfractured, optically clear crystals. This could be decided by viewing the samples under crossed polars on a petrographic microscope. Crystals can be broken off into a larger sample and the best fragment selected. Samples ought to be between 30 and 300 microns, with perfect crystals averaging 150–250 microns in size. To minimize the absorption effects, equant crystals are desired. Spherical crystals may be created using a small, air-powered crystal tumbler; however, without difficulty, cleaved minerals can break during this technique. Consequently, minerals lacking cleavage are the best choice for this step. If the sample is inequant, this must be corrected for absorption corrections to the data.

- ***Sample Mounting***

  Samples are mounted on a thin glass fiber's tip using epoxy or cement. Care must be taken to use just enough epoxy to secure the sample without embedding it in the mounting compound. The fiber can be ground to minimize absorption by means of glass. This fiber is connected to a brass mounting pin, commonly using modeling clay, and the pin is inserted into the goniometer head.

❖ *Sample Centering*

The goniometer head and sample are then affixed to the diffractometer. Samples may be centered by viewing the sample under an attached microscope or video camera and adjusting the X, Y, and Z directions until the sample is centered under the crosshairs for all crystal orientations.

❖ *Data Collection*

Once the crystal is centered, a preliminary rotational image is often collected from screening the sample quality and selecting parameters for later steps. An automatic collection routine can then collect a preliminary set of frames to determine the unit cell. Reflections from these frames are auto-indexed to select the reduced primitive cell and calculate the orientation matrix (which relates the unit cell to the actual crystal position within the beam). The primitive unit cell is refined using least-squares and converted to the appropriate crystal system and Bravias lattice. This new cell is also refined using least-squares to determine the final orientation matrix for the sample.

After the refined cell and orientation matrix have been determined, intensity data is collected. Typically, this is accomplished by collecting a sphere or hemisphere of data using an incremental scan method, collecting frames in 0.1° to 0.3° increments (over certain angles while others are held constant). For highly symmetric materials, collection can be constrained symmetrically to reduce the collection time. Data is typically collected between 4° and 60° 2θ for molybdenum radiation. A complete data collection might also require anywhere between 4–12 hours, depending on the specimen and the diffractometer. Exposure times of 4–20 seconds per frame for a hemisphere of data would require total run times of 4–10 hours. Older diffractometers with non-CCD detectors may additionally require 4–5 days for a complete collection run.

- ***Corrections for Background, Absorption, etc.***

  After accumulated data, corrections for instrumental factors, polarization effects, X-ray absorption, and (potentially) crystal decomposition have to be implemented to the complete data set. This integration technique reduces raw frame data to a smaller set of individual integrated intensities. These correction and processing procedures are commonly part of the software package that controls and runs the data collection.

- ***Phase problem and Fourier transformation***

  As soon as the data have been collected, the phase problem needs to be solved to find the unique set of phases that may be combined with the structure factors to determine the electron density and, consequently, the crystal structure. Several different procedures exist to solve the phase problem, but the most common approach currently, due to the prevalence of high-speed computers, is using direct methods and least-squares, initially assigning phases to strong reflections and iterating to produce a refined fit.

- ***Structure solution***

  The solution to the phase problem leads to the initial electron density map. Elements can be assigned to intensity centers, with heavier elements associated with higher intensities. Distances and angles among intensity centers also can be used for atom assignment based on possible coordination. A template may be used for the initial solution if the sample is of a known material.

- ***Structure Refinement***

  Once the initial crystal structure is solved, various steps can be carried out to obtain the best fit between the observed and calculated crystal structure. The final structure solution might be presented with an *R*-value, which gives the percent variant among the calculated and observed structures.

1.3.4. Thermal analysis

Thermal analysis measures and interprets the relationship between a sample's physical and chemical properties and its temperature. Several thermal analysis methods depend on the property to be measured. Herein the details of differential thermal analysis (DTA) and thermogravimetric analysis (TGA) have been discussed.

1.3.4a. Differential thermal analysis

Differential thermal analysis (DTA) records the difference in temperature between a substance and a reference material, as the two specimens are subjected to identical temperature regimes in an environment heated or cooled at a controlled rate. The DTA curve is obtained by plotting ΔT against T. Endotherms are plotted downward, and exothermic peaks are plotted upward. Experimentally, that is finished through a furnace containing a sample holder or block and two symmetrically located and identical chambers. Every chamber contains an identical thermocouple (Platinum-Platinum 10% Rhodium) or a different temperature detection device. The sample to be investigated is placed in one chamber, and a thermally inert substance, having a similar heat capacity such as α-alumina (Al_2O_3), is placed in the other. The sample and α-alumina are then heated at a uniform rate by the furnace, and the temperature difference (ΔT) between them, as detected by temperature detection devices, is recorded as a function of t or T.

1.3.4b. Thermogravimetric analysis

It is the branch of thermal analysis that examines the mass change of a sample as a function of temperature in the scanning mode or as a function of time in the isothermal mode. Thermogravimetric (TG) analysis is used to characterize the materials' decomposition and thermal stability under diverse conditions and to examine the kinetics of the physio-chemical processes occurring in the sample. The mass change characteristics of a material are strongly dependent on the experimental conditions together with sample mass, volume, and physical form, the shape and nature of the sample holder, the nature and pressure of the atmosphere in the sample chamber, and the scanning rate. The TG curves generally are plotted with the mass change (Δm) expressed as a percentage on the vertical axis and temperature (T) or time (t) on the horizontal axis.

The instrument for TGA consists of a balance, a furnace programmed for a linear rise of temperature with time at which the heating rate can be varied, and a recorder. A small but accurately known sample mass is heated in a crucible on an analytical balance during controlled heating. An inert reference material (often alumina) treated simultaneously ensures that any drift of the instrument can be correlated. Several gas atmospheres (air, N_2, CO_2) can be chosen. Any difference in the weight of the sample (loss or gain) is recorded versus temperature during controlled heating. The approach is acceptable for many solid substances, although limitations can also arise regarding possible reactions with the crucible material or corrosive gases emitted by the sample.

1.4. Molecular recognition

Molecular recognition is an idea of fundamental importance in structural chemistry and materials science. The knowledge of molecular recognition is an exceptionally new area dating to 1967 when C. J. Pedersen discovered crown ether that turned into observed to bind alkali metal ions to form highly structured complexes [21]. D. J. Cram (1988) also refers to molecular recognition chemistry as 'host-guest' chemistry [22], at the same time as Lehn (1988) calls it supramolecular chemistry [23]. It is a phenomenon in which a receptor or a 'host' molecule (generally large) forms a stable complex with one or more 'guest' molecules (generally small) through weak directional forces operating within various subunits of the component molecules. Cram (1988) has defined host and guest as follows: the host is any molecule or ion whose binding sites converge in the complex, while the guest is any molecule or ion whose binding sites diverge.

The molecular complex or supermolecule is a noticeably established assembly of host and guest molecules complementing each other both sterically and stereo electronically via multiple contact points on common surfaces [21–23]. A 'host' molecule (a receptor) forms a complex with one or more 'guest' molecules via weak directional forces operating within the component molecules. Molecular recognition can be categorized into static molecular recognition and dynamic molecular recognition (Figure 1.2). Static molecular recognition is associated with the interaction between a key and a keyhole. This is a 1:1 type complexation reaction between a host molecule and a guest molecule to generate a host-guest complex. In dynamic molecular recognition, the first guest molecule binds to the host molecule's first binding site, affecting the association constant of a second guest with a second binding site [24]. Dynamic molecular recognition is applicable in highly functional chemical sensors and molecular devices.

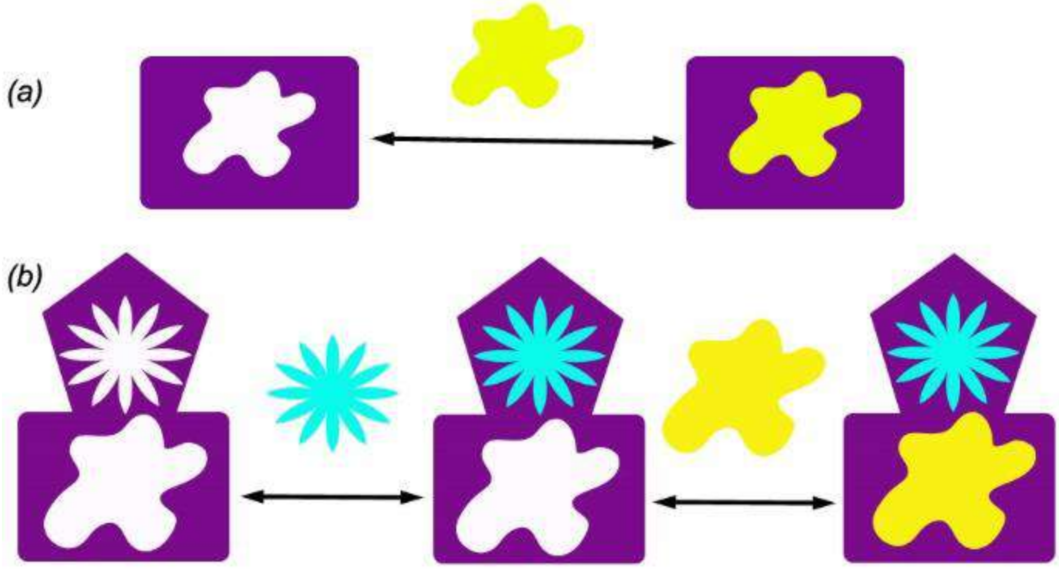

Figure 1.2. Static (a) and dynamic (b) recognition between guest and host molecules.

Preorganization and complementarity dictate the stability of the "host-guest" complexes. In preorganization, the host and the guest are arranged for binding and for low solvation before being combined. Complementarity or structural recognition requires the guest to be accommodated in a cavity or cavities formed in the host, and binding sites must cooperate [25-28]. The cavity of the host must be well matched with the size and shape of the guest to minimize steric interaction. Additionally, the binding sites of the host and guest molecules need to be aligned well to obtain minimal stereo electronic interaction. Consequently, the host and guest molecules recognize each other by molecular recognition. The system will become more ordered through the molecular recognition process. As a result, the system's entropy is reduced through the process. However, the adverse thermodynamic consequences are more than compensated by noncovalent binding interactions.

1.5. Self-assembly

The process of self-assembly involves the spontaneous association of small molecules to form stable, large, and structurally well-defined aggregates. Assembling components into an ordered pattern is called self-assembly [29]. There are two types of self-assembly, static and dynamic. When systems are in equilibrium, static self-assembly occurs. The patterns of previous components are ordered by particular local interactions in the case of dynamic self-assembly. Supramolecular self-organization is the key process in the spontaneous but regulated assembly of structurally structured and functionally integrated molecular systems [30]. It is guided by information stored in molecular components and read out through their unique interactions.

Additionally, it is possible to think of supramolecular self-assembly as a collection of ordered self-assemblies that (i) contain systems that spontaneously develop order in either space or time or both; (ii) include non-linear chemical processes, energy flow, and the arrow of time to include the spatial and temporal order of both equilibrium structures and of non-equilibrium, dissipative structures; (iii) only the noncovalent, supramolecular level; (iv) be multicomponent and produce polymolecular assemblies with supramolecular organization and long-range order due to specific interactions acting either through recognition events between the molecular components or in a dynamic process. The self-assembly of organic supramolecular architectures is caused by supramolecular properties seen in proteins, nucleic acids, and molecular complexes, such as electrostatic, hydrogen bonding, van der Waals, stacking, or donor-acceptor effects [31-35]. The steric factors associated with the organic molecular components control how organic supramolecules self-assemble. Creating organic molecule building blocks that can self-assemble into supramolecular entities with the desired architectural and functional properties is essential for the spontaneous generation of organized structures.

1.6. Crystal engineering

The rational design of functional molecular solids is known as crystal engineering [36,37]. Modern chemists and crystal engineers interested in modeling, designing, synthesizing, and using crystalline solids with predetermined and preferred aggregation of molecules and ions engage in this lucrative area of research [38,39]. For scientists working on the design of structured phases and assemblies, this topic is crucial and of significant interest to solid-state and structural chemists. The crystal engineering principles can be applied to intermolecular self-assembly [36].

The literature claims that for the first time in 1955, R. Pepinsky coined the term "crystal engineering" [40]. Schmidt, however, used the term "Crystal Engineering" in 1971 about photodimerization processes in crystalline cinnamic acids [41]. Since its initial application, the term has significantly expanded to encompass a variety of features of solid-state supramolecular chemistry. In 1989, 'crystal engineering' was defined by G. R. Desiraju as "*the understanding of intermolecular interactions in the context of crystal packing and the utilization of such understanding in the design of new solids with desired physical and chemical properties"* [36]. Despite being a nearly 50-year-old field, crystal engineering has significantly contributed to the interface between solid-state sciences and supramolecular chemistry [42]. The "top-down" and "bottom-up" approaches towards materials design and fabrication meet. Since many conventional fields of science, including chemistry, crystallography, and crystal growth, contribute to crystal engineering, it is a highly multidisciplinary field of study. Due to the need to create complex devices and discover how to govern molecular recognition and self-assembly, this area of research is attracting a growing number of scientists. This is mainly an effort to comprehend the underlying fundamental problems with nucleation and crystal growth [43]. The appearance of crystal engineering as a "stand-alone" science results from several significant circumstances. For instance: (i) the achievement of supramolecular chemistry has given scientists access to a suitable research environment [44]; (ii) instead of molecular-based chemistry, the study of molecular aggregates is becoming more and more popular; (iii) The ability to solve theoretical and experimental issues of enormous complexity on a modest time scale is demonstrated by the development of computing and diffraction techniques; (iv) Due of widespread funding limits for fundamental investigations, crystal engineering satisfies the urge for more practical goals for the chemical sciences [45].

Crystal engineering is known to design and synthesize molecular structures in the solid-state with desired features based on knowledge of and exploitation of intermolecular interactions. The two primary methods for crystal engineering currently in use are coordination complexation and hydrogen bonding. Important ideas like the secondary building unit and the supramolecular synthon may be understood. In the solid-state studies of "self-assembly," crystal engineering of supramolecular frameworks connected by intermolecular interactions is a crucial subject [46–50]. The main objective of crystal engineering is to control the topology of crystal packing for functional solids through covalent and noncovalent interactions, as the successful incorporation of desirable structural units into a crystal may lead to the development of innovative materials [51–53]. The critical challenge facing the crystal engineer is the rational assembly of molecular components into 3-D arrays controlling the whole gamut of intermolecular interactions. The task would be easier if not for molecules' inherent conformational flexibility. One would like to forecast the resulting supramolecular self-associations of a collection of molecules in crystals [54–57]. The crystal structure prediction is difficult; therefore, the prediction problem is often limited to recognizing patterns or supramolecular synthons. A productive strategy for predicting synthons relies on strong and weak interactions as they accurately reflect the hierarchy of intermolecular interactions [58]. The penultimate result is created by a succession of intricate recognition processes between the parts, and control over this assembly is referred to as "crystal engineering." A closely related discipline called "crystal structure prediction" also depends on it for its success. The planned quick advancement in these fields has been slowed down by the subtle and intricate nature of the "self-assembly" process, which is overly sensitive to several physicochemical parameters.

1.7. Supramolecular synthon

Corey [59] first proposed the definition of synthon. A supramolecular synthon is a structural unit formed by intermolecular interactions within a crystal. The smallest structural units, known as supramolecular synthons [60], contain all the information necessary for molecules to recognize one another and create solid-state supermolecules, or crystals (see Figure 1.3). Supramolecular synthons set up the conceptual relationship between crystal engineering and organic synthesis. Prof. Desiraju has described the main features of the supramolecular synthon approach in crystal engineering [54]. For successful crystal engineering, structural chemists, and crystallographers, can now use the novel ideas of supramolecular strategy, target identification, and synthetic methodology. In this context, it is possible to define a supramolecular “synthon” as *a smallest structural unit which contain all the information inherent in the recognition events through which molecules assemble into supermolecules* [54]. Thus, these synthons are the algorithms that link supramolecular and molecular structure.

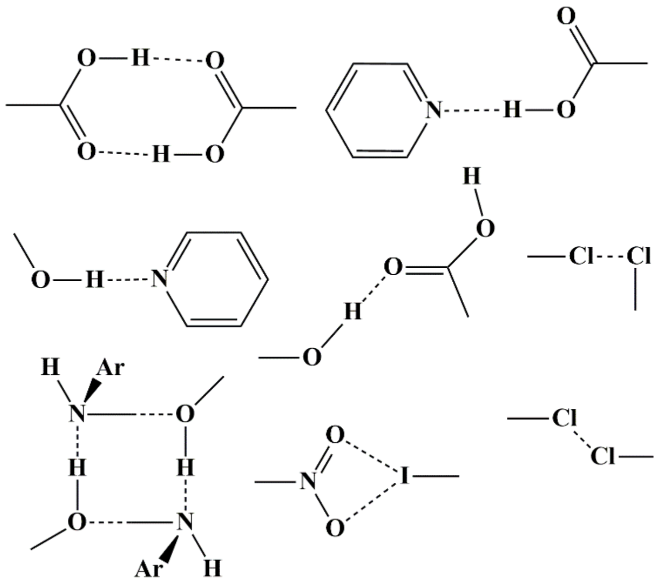

Figure 1.3. Representative example of some synthons [60].

Two categories of supramolecular synthons are recognized; for instance: (i) same self-complementary functionalities are combined in a supramolecular homosynthon and (ii) different yet complementary functionalities make up supramolecular heterosynthon [61]. Supramolecular homosynthons can continue supramolecular assemblages where single components make up the functional groups [62]. Contrarily, when other complementary functional groups are present in the assemblages, supramolecular heterosynthons may predominate [63-66] (see the Figure 1.4). Supramolecular synthons are identified by identifying several kinds of unique intermolecular connections, and this method is very successful when the molecule contains several strong interactions. However, sometimes recognizing it can be exceedingly challenging, particularly in crystals with weak hydrogen bonding contacts. As a result, for these kinds of crystals, rationalizing the relationship becomes exceedingly challenging. A geometrical approach to determining certain intermolecular interactions that contribute to the formation of supramolecular synthons is one of the key reasons of this difficulty. It should be kept in mind that the energy of general dispersion and electrostatic contacts may be comparable to the energy of specific interactions in larger molecules [67]. However, discussing and analyzing supramolecular synthons in terms of weak intermolecular interactions has practically become standard practice in recent years. The majority of interactions are not very stable, and the molecular structure and crystallization circumstances both have an impact on how they occur and are related to it. The objective should be to identify and design synthons that are robust enough to be exchanged between different network structures [68].

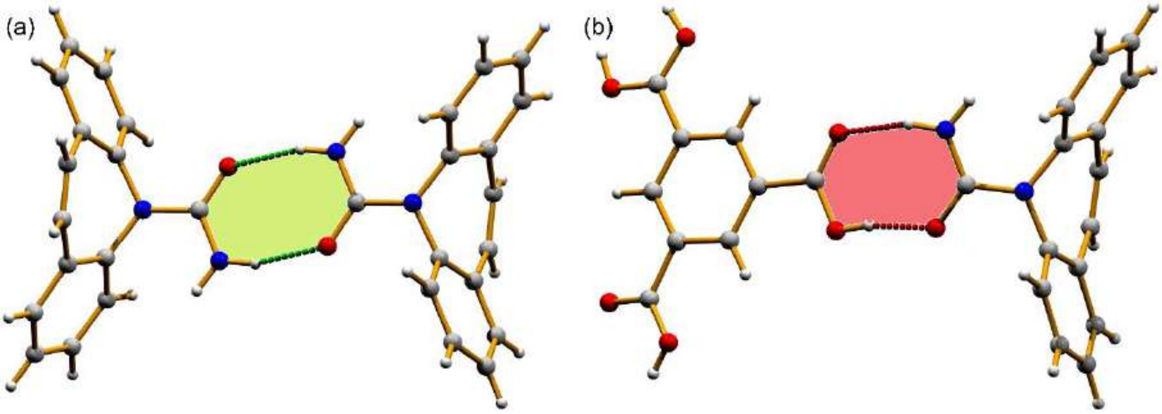

Figure 1.4. (a) Supramolecular homosynthon observed in cocrystal [65]; (b) Supramolecular heterosynthon observed in cocrystal [65].

The numerous and weak interactions that govern crystal formations present a significant challenge for crystal engineering. Concern has been raised about the deformability of intermolecular interactions, which can cause closely related molecules to create crystal structures with quite different properties. As a result, the robustness of supramolecular synthons is a crucial issue, and unless robustness holds, the whole concept of a supramolecular synthon would not be of any practical benefit. The methods for creating a particular set of contacts can only be generalized from one molecule to the next if supramolecular synthons are robust [69–73].

1.8. Non-covalent interactions

Noncovalent bonding refers to attractive intermolecular forces that are not covalent in nature. Noncovalent bonds are a form of chemical bond, usually between macromolecules, that do not share pairs of electrons but instead involve more diffused electromagnetic interactions. In supermolecular chemistry, the noncovalent bond is the most common type of bond between supermolecules.

Noncovalent forces are dominant in supramolecular chemistry. Noncovalent bonds are critical in maintaining the three-dimensional structure of large molecules. The noncovalent interactions include ionic bonds, hydrophobic interactions, hydrogen bonds and van der Waals forces (dispersion attractions, dipole-dipole and dipole-induced dipole interactions). Noncovalent bonds are weak and must work together to have a significant effect. In addition, the combined bond strength is greater than the sum of the individual bonds. This is because the free energy of multiple bonds between two molecules is greater than the sum of the enthalpies of each bond due to entropic effects [74-78]. In this dissertation the following three main types of noncovalent interactions have been presented.

i) Hydrogen bonding
ii) Salt-bridge (SB) interaction
iii) Interaction involving aryl rings

1.8.1. Hydrogen bonding interactions

Even though the hydrogen bond was discovered about a century ago, it continues to be an important area of scientific study. The fundamental significance of hydrogen bonding for the structure, function, and dynamics of a wide range of chemical systems, from inorganic to biological chemistry, accounts for this persistent interest. There are many different scientific disciplines involved, such as biochemistry, molecular medicine, pharmacy, general inorganic and organic chemistry, supramolecular chemistry, mineralogy, and material science. Particularly in recent years, research on hydrogen-bonds has significantly risen in breadth and depth, new ideas have emerged, and the complexity of the phenomena under consideration has grown significantly [79]. A hydrogen bond is the attractive interaction of a hydrogen atom with an electronegative atom, such as nitrogen, oxygen or fluorine that comes from another molecule or chemical group. To create the bond, the hydrogen must be covalently bonded to another electronegative atom. These bonds can occur between molecules (intermolecularly), or within different parts of a single molecule (intramolecularly).

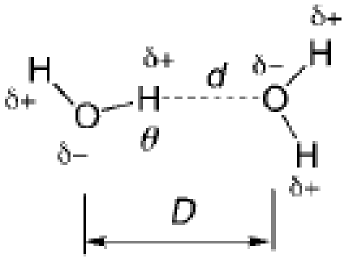

Figure 1.5. Prototype of a hydrogen bond: the water dimer. Definitions of geometrical parameters: d = H···O distance, D = O···O distance, θ = O–H···O angle.

An X–H···A interaction is called a "hydrogen bond", if (i) it constitutes a local bond, and (ii) X–H acts as proton donor to A (where X stands for donor and A stands for acceptor). The second condition, which has to do with the acid/base characteristics of X–H and A, chemically implies that a hydrogen bond can be viewed as the beginning of a proton-transfer reaction from X–H to A. For instance, it disallows B-H-B bridges, agostic interactions, and pure van der Waals contacts. Point (ii) should actually be read broadly enough to include symmetric hydrogen bonds, such as X-H-X, in which the donor and acceptor cannot be separated. In a hydrogen bond, the formal or actual electron transfer occurs in the opposite direction to the proton donation [79, 80]. For automated data treatment processes to discover hydrogen bonds, the practical scientist frequently needs a technical definition. It is simply indicated that the van der Waals cutoff definition [81,82] which stipulates that the H–A distance must be considerably shorter than the sum of the van der Waals radii of H and A, should no longer be used to identify hydrogen bonds on a structural basis. If distance cutoff limits be used, X–H···A interactions with H···A distances up to 3.0 or even 3.2 Å should be considered as potentially hydrogen bonding [81,82]. A cutoff angle can be set at > 90° or, in a more conservative manner, > 110°. Positive directionality preference, or the statistical preference for linear X–H···A angles over curved ones, is an essential geometric criterion for hydrogen bonding [83]. In nature, hydrogen bonds are both composite and complex. The complexity results from numerous atom interactions, at least three (D, H, and A). Its varied covalent, electrostatic, and van der Waals characteristics are manifestations of the composite nature. The nature of D and A, their conformations and combinations, and the enormous environmental diversity all contribute to this unpredictability. As a result, the interaction is chemically "tunable," and consequently, one anticipates the potential of fine-tuning the material properties. About -0.2 to -40 Kcalmol^{-1} appears to be the range of hydrogen bond energies, which spans more than two orders of magnitude [84-86].

Depending on the chemical, conformational and configurational nature of X and A of hydrogen bond (X–H···A), the interaction pattern of the hydrogen bonding changes (Figure 1.6). As a result, the supramolecule has hydrogen bonding interactions shows different types of structural patterns when different X and A are present within the supramolecule. In general, the energies of the hydrogen bonding interactions lie in range of 0.25-40 kcal mol^{-1} [87-91]. The energy ranges of different type hydrogen bonding interactions are included in Table 1.2.

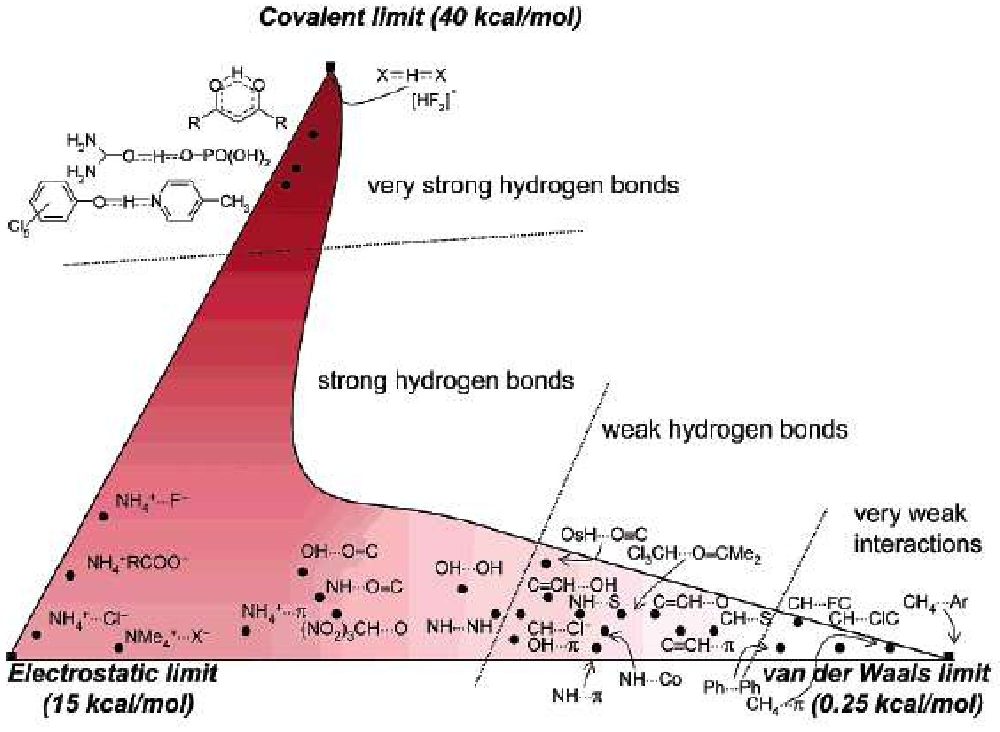

Figure 1.6. Various weak and strong hydrogen bonds [Courtesy: Prof. G. R. Desiraju].

Table 1.2. Energy ranges of different hydrogen bonding interactions.

Kind of interactions	**Energy (kcal mol^{-1})**
Hydrogen bonds	~0.25-40
Weak H–bonds	~1-4
Moderate H–bonds	~ 4-15
Strong H–bonds	~15-40

1.8.1a. Bifurcated hydrogen bonds

A donor creates hydrogen bonds with multiple acceptors at once in a multifurcated hydrogen bond. A high density of acceptors is necessary for multifurcated hydrogen bonding, at least locally. In carbohydrates, more than 25% of all O-H-O hydrogen bonds are multifurcated, and this percentage is significantly greater in amino acids [92]. Multifurcated hydrogen bonds are also widely distributed in proteins [93]. When angles are small and/or some of the putative acceptors are compelled by stereochemistry to be near to the donor, it might be challenging to demonstrate that all of the components are bonding. However, bond routes in the theoretical electron density have been demonstrated for both components for a number of bifurcated bonds [94]. In the majority of multifurcated hydrogen bonds, a stronger ("major") component can be distinguished readily, but not always. Sometimes even trifurcated hydrogen bonds with a symmetric geometry can be found. The three hydroxy O atoms in the triethanolammonium cation, for instance, always condense toward the N^+–H donor and are observed in very identical bowl-shaped conformations in crystal structures [95, 96]. Frequently, the A1 and A2 types are the two acceptors in a bifurcated hydrogen bond. It might be challenging to determine whether one is genuinely of any structural consequence if it is significantly weaker than the other (for example, when A1 = O, N, and A2 = Hal-C, etc.). Even though the interaction geometry favors the weaker acceptor, multiple cases of bifurcated hydrogen bonds have been discovered with both strong and weak acceptors [97-99].

1.8.1b. σ-bond cooperativity

An X–H group becomes more polar if an X–H···A hydrogen bond develops. The same holds true if it accepts the Y–H···X–H hydrogen bond. As a result, both hydrogen bonds in the chain Y–H···X–H···A become stronger. Since the charges move across the X–H bonds, the phenomenon is frequently referred to as "σ-bond cooperativity," [92] but the terms "polarization-enhanced hydrogen bonding" [100] or "polarization-assisted hydrogen bonding" [101] have also been proposed. σ-Bond cooperativity efforts the clustering of polar groups. This leads to the formation of X–H···X–H···X–H chains and rings in the condensed phases, especially for X–O but also for X–N or S. Double donors, such as water, and/or double acceptors can connect rings and chains to build intricate networks. The topology of such networks for O–H-rich carbohydrates has been extensively studied [102,103].

1.8.1c. π-bond cooperativity or Resonance-Assisted Hydrogen Bonding (RAHB)

Charge flow through bonds has the potential to polarize X–H groups as well. For instance, if the amide O atom accepts a hydrogen bond, X–H···O=C–N–H, the amide N–H group becomes a stronger donor. This happens as a result of the stabilization of the zwitterionic resonance. Thio- and selenoamides have the exact same action [104]. Due to their potential as both donors and acceptors, amide units frequently form hydrogen-bonded chains or rings, such as in the secondary structure of proteins. Since polarization happens through π-bonds, the phenomenon is frequently referred to as π-bond cooperativity [92]. "Resonance assisted hydrogen bonding" (RAHB) is the name given to this action by Gilli et al. based on research on intramolecular hydrogen bonds in β-diketone enolates [105]. In the β-diketone enolates, a short hydrogen bond is connected to a charge flow through the conjugated double bond system. The C=O and C=C bonds are weakened while the C–O and C–C bonds acquire partial double bond characteristics and are shortened. Conjugated double bond longer chains with intra- and intermolecular hydrogen bonds exhibit completely analogous effects [106]. The carboxylic acid dimer is the most well-known example. The effect will also be visible in any other suitable donor-acceptor pair connected by a resonant π-system. The cases N–H···O and O–H···N [107], N–H···S/Se [104], O–H···S [108], and S–H···S [109] provide as examples of the range of situations in which experimental proof of the π-bond cooperativity is available.

1.8.1d. Strong and weak hydrogen bonds

High electronegativity atoms act as the donor and acceptor in a strong hydrogen bond. Historically, F, O, and N atoms have been regarded as either acceptors or donors in this group. Strong hydrogen bonds have an energy between 15 and 40 kcal/mole. Weak hydrogen bonds have an energy range of 0.25 to 4 kcal/mole and can be comprised of the interactions C–H···O, C–H···N, C–H···S, N–H···S, S–H···N, S–H···O, and S–H···S. The C–H···O hydrogen bond has the highest abundance since the C-H group is so prevalent in organic molecules. Initial doubts about the presence of the C–H···O hydrogen bond [110] have been dispelled, although this has taken extensive research by Desiraju and others [111-114]. Since the latter can be constructed not only with strong hydrogen bonds like O–H···O and N–H···O but also with weak C–H···O bonds, a significant effort has already been made to assess the viability of the C–H···O bond. Because all hydrogen bonds are electrostatic and thus long-range, this is the case. Since the C–H···O hydrogen bond is weaker than the conventional N–H···O or O–H···O bonds, the topic of whether one might construct crystal structures using C–H···O and other weak hydrogen bonds was raised at first. According to Desiraju et al., these interactions' effects on crystal packing can be categorized as innocuous, useful, or intrusive [115]. Innocent interactions are significantly weak and have no part in the creation of the structure. Although supportive C–H···O interactions are not very weak, their directional preferences are satisfied by the stronger interactions' geometrical constraints. The patterns and topologies created by the stronger interactions are disturbed by intrusive interactions. When the strong interaction is absent or acts in a direction that is orthogonal to the direction of the C–H···O bonding in the crystal [116], crystal engineering employing the C–H···O interaction has been documented in the literature. The typical energies and geometries for the majority of weak interactions are gathered in Table 1.3.

Table 1.3. Interaction energies and geometries of various noncovalent forces.

Interaction	**Energy (kcal/mole)**	**Typical H···A distance (Å)**	**Typical D–A distance (Å)**
O–H···O	3-8	1.51	2.78
O–H···C	1.79	2.66	3.30
O–H···S	4	2.49	3.25
N–H···O	6	1.80	2.81
N–H···C	3	2.61	3.30
N–H···N	6	1.92	2.83
N–H···S	3	2.60	3.12
O/N–H···π	2-4	2.45	3.30
C–H···π	~1	2.36	3.20
C–H···O	~2	2.60	3.50
C–H···N	2	2.51	3.41
C–H···S	1.5	2.70	3.66
C–H···Se	1.84	2.81	3.25
C–H···F	2.2	2.53	3.47
C–H···F-C	2.2	2.60	3.50
C–H···C	.33	2.74	3.59
S–H···N	1.5-3.5	2.80	3.70
S–H···S	1.1	2.16	3.48

1.8.2 Salt-bridge (SB) interaction

An interaction between two groups of opposite charges in which at least one pair of heavy atoms is within hydrogen bonding range is known as a salt bridge (SB). Though substantial strides have been made [117, 118], salt bridges are challenging to correctly predict and model. Predicting salt bridge interactions is particularly difficult due to the high cost of dehydrating a basic residue and a carboxylate to form a salt bridge as well as the strict geometric constraints imposed by the electrostatic and hydrogen-bonding interactions. The salt bridge (SB) can be defined as an interaction between two groups of opposite charge where the protonated and deprotonated residues interact directly [119-121]. Therefore, salt bridges are hydrogen bonded ion pairs, which are important for the stabilization of molecular conformations. The hydrogen bonding of the SBs shows stronger binding compared to the normal hydrogen bonding interactions due to the zwitterionic charges (charge assisted hydrogen bond) [122]. The formation of salt bridges is one of the significant noncovalent interactions that has been used to construct self-assembled structures in organic solvents [123, 124]. In protein chemistry, SBs played a crucial role in substrate bonding, activity of catalytic triads, secondary-structure stabilization and stability of thermophilic proteins [125, 126]. To generate new supramolecular systems, [127,128] intermolecular salt bridges are often used while biological systems such as proteins often comprise SBs that control their structure and function [129]. However, due to the geometric constraints placed by the electrostatic and H-bonding interactions, predicting SB interactions remains uniquely challenging. The influence of salt bridges on cation–π interaction had been investigated by computational analysis and synthetic studies [130, 131]. However, a comprehensive study of the interaction between a planar salt bridge and aromatic rings and cooperativity of other noncovalent forces with SBs is not well explored. As depicted in Seth et al. [132] (see Figure 1.7), the SBs are very rich as binding motifs due to their dual character that makes it adequate for establishing a great deal of noncovalent interactions.

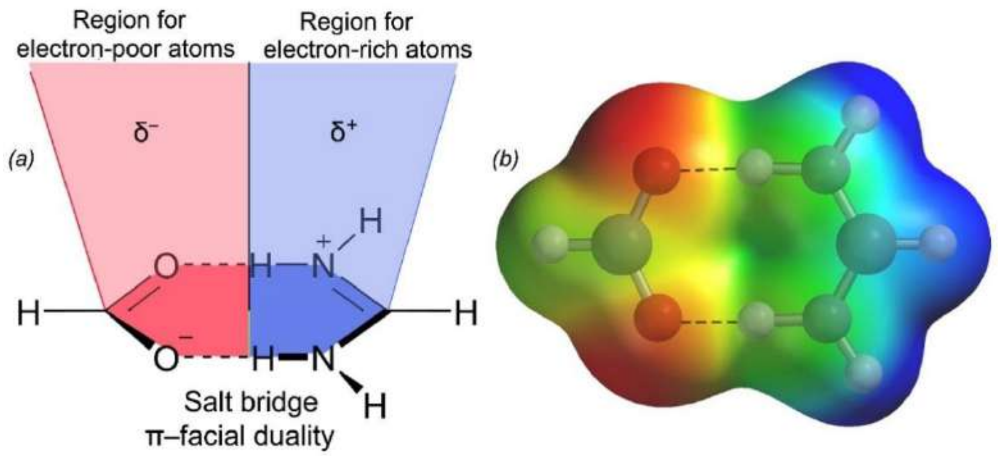

Figure 1.7. (a) Schematic representation of a salt-bridge and its expected dual behaviour as electron donor and acceptor. (b) MEP surface of the salt-bridge model system.

1.8.3. Conventional C–H···π(aryl) interaction

The term "C–H···π interaction" refers to the interactions between an aliphatic/aromatic -C–H group and an aromatic π-electrons system (or any delocalized π-system). Various weak nonclassical hydrogen-bonding interactions constitute this phenomenon [104, 133]. The scientific community is very interested in these interactions since they are ubiquitous despite their weak character. These C–H···π interactions have been extensively researched in a variety of fields including supramolecular chemistry [134], crystal packing [135], molecular aggregates [136], protein and other biomolecule structure [137], and rational drug design [138]. Umezawa et. al. conducted a detailed analysis of the crystal structure database and discovered that roughly 40% of organic crystals include C–H···π interactions [139]. The importance of C–H···π interaction in the synthesis of streoselective metal complexes was initially demonstrated by Okawa [140-143]. The effects of C–H···π interaction in organometallic and coordination chemistry have drawn significant attention and have been thoroughly studied by scientists [144, 145].

The C–H···π interaction between C–H groups (soft acids) and electron pairs (bases) in a system can alternatively be thought of as the weakest of hydrogen bonds. The thermochemical observations [146] and spectroscopic results [147] were the first to demonstrate the attraction of the interaction between CHs and π-systems. Iitaka et al. published crystallographic findings on the proximity of the phenyl group at the other terminal of the same molecule to the t-butyl group in a pair of sulfoxide diastereoisomers ($C_6H_5CHCH_3SO$-t-C_4H_9) [148]. A variety of techniques can be used to gather proof of the CH/π interaction [144]. AIM (atoms in molecules) investigations have verified that the CH/π interaction is a hydrogen-bond interaction [149]. Bagno et al. described on the through-space spin–spin coupling in CH/π interacting systems [150]. Going from sp^3-CH to sp^2-CH and finally to sp-CH results in a rise in the electrostatic energy proportion [151]. According to Nakagawa and Nikki, it is crucial for the C-H dipole and aromatic quadrupole to interact [152]. According to Hirota [153], depending on the interaction system, the energy of the CH/π hydrogen bond involving $CHCl_3$ and aromatic hydrocarbons ranges from 1.5 to 3 kcal mol^{-1}. The stabilizing impact increases with the CH's capacity to donate protons. As a result, the following order is obtained: sp-CH > sp^2-CH > sp^3-CH; $CHX_3 > CH_2X_2 > CH_3X$ (X: any electron withdrawing atom or group). In the same order, the CH/acceptor distance increases. Aliphatic CH interactions are weaker than aromatic CH interactions. According to theoretical simulations the dispersion force is primarily responsible for stabilizing the CH/π bond. The thorough analysis of Prof. Motohiro Nishio can provide additional understanding of the CH/π interaction [154].

1.8.4. Unconventional C–H···π(chelate) interaction

Chelate rings [155] are cyclic systems with π-electron delocalization that are created in metal-organic complexes by the coordination of organic ligands to a metal ion. These aromatic-like chelate rings can participate in weak noncovalent interactions due to their delocalized π-bonds [156]. It had been thought that the interaction between the metal-ligand aromatic cation···π was an X–H···π (X = N, O, C) interaction [157-159]. Chelate rings' delocalized π-systems can exhibit aromatic character [160]. It has recently been demonstrated that various kinds of

X–H···π interactions can entail chelate rings with π-electron delocalization [161, 162]. The chelate rings can participate in stacking interactions because of the planarity and delocalization of the π-system [163-165]. The C–H···π interactions, which take place between a soft acid C-H and a soft or intermediate base π-system, are thought to be the weakest of all X–H···π interactions [154, 166]. It is important to note that aromatic rings that have C–H bonds that are perpendicular to the chelate ring's π-system can interact with the chelate ring through the C–H···π (chelate) pathway [161]. The evidence of C–H···π interaction with the π-cloud of a six-membered chelate ring was reported by Zaric and co-workers [167]. It was revealed by Niclo's-Gutie'rrez and co-worker that there was intramolecular C–H···π(chelate) interaction [168]. The Tiekink group has also provided evidence for the C–H···π(quasi-chelate ring) interaction, showing that six-membered quasi-chelate rings can be produced by a strong hydrogen bonding contact [169]. In addition, the Tiekink group has demonstrated C–H···π(chelate) interaction in solid-state structures of Pd complexes with four-membered chelate rings [170]. Based on structures found in the CSD database, Zaric and colleagues recently published significant evidence of stacking interactions involving chelate rings [171]. This research reveals that chelate-chelate interactions are even more powerful than chelate-aryl stacking interactions [168]. In the context of crystal engineering, interest is rising in several noncovalent interactions involving the π-cloud of chelate rings, such as π(aryl)···π(chelate), π(chelate)···π(chelate), and C–H···π(chelate) [172-174].

1.8.5. π···π stacking interaction

A noncovalent interaction between aromatic molecules is called a "π–π interaction." In π-conjugated systems, intermolecular π-orbital overlap is what causes the "π–π interaction”. As the number of π-electrons rises, this kind of contact becomes stronger. Since benzene is unquestionably the optimum system, interactions between aromatic and aromatic packing have been theoretically investigated [175].

Benzene has a constant quadrupole moment instead of a dipole moment [176]. An essential force in regulating the solid-state architecture of molecules with phenyl rings is provided by such quadrupole (Figure 1.8). The benzene dimer [177] can have either a parallel-displaced face-to-face structure or a T-shaped edge-to-face structure (Figure 1.9). C–H···π interaction results from the benzene dimer's T-shaped structure. Hunter and Sanders have devised a set of rules based on a simple model of the charge distribution in a π system to understand and analyze aromatic-aromatic interactions. They differentiated between the σ framework and the π electrons, supposing that π–π interactions originate from π–σ attractions overcoming π–π repulsions [178]. According to these "Hunter-Sanders" rules, non-polarized π-systems should:

- Rule 1: π–π repulsion dominates in a face-to-face π-stacked geometry.
- Rule 2: π–σ attraction dominates in an edge on or T-shaped geometry.
- Rule 3: π–σ attraction dominates in an offset π-stacked geometry. For polarized π systems there are an additional three rules, which are stated here in the form of a requirement for face-to-face π stacking.
- Rule 4: For interaction between highly charged atoms, charge–charge interaction dominates.
- Rule 5: A favorable (face-to-face) interaction with a neutral or weakly polarized site requires as a π polarization a π-deficient atom (in the aromatic ring).
- Rule 6: A favorable (face-to-face) interaction with a neutral or weakly polarized site requires, as a σ polarization, a positively charged atom (in the aromatic ring).

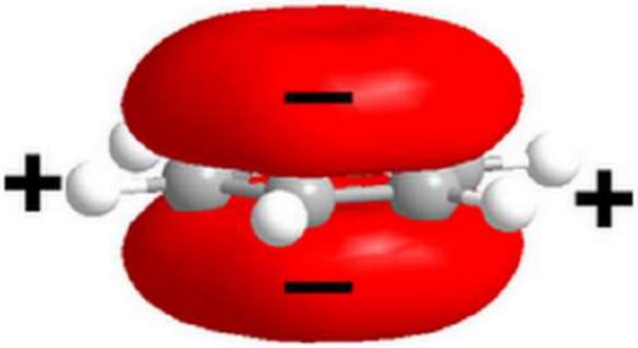

Figure 1.8. The π system above and below the benzene ring leads to a quadrupole charge distribution.

When an electron-withdrawing substituent is attached to the aromatic ring, the π-electron density in the aromatic ring decreases, which decreases the π–π electron repulsion. The effectiveness of the "π–π interaction" is increased by the electron-withdrawing substituents associated to the aromatic system, whereas the "π–π interaction" is adversely affected by the electron-donating substituents attached to the aromatic system. π-deficient - π-deficient > π-deficient - π-rich > π-rich - π-rich is the decreasing stability order of π-interactions between two π-systems [177, 179]. Consequently, the pyridine, bipyridines, and other aromatic nitrogen heterocycles with low π-electron densities exhibit effective π–π interactions [180].

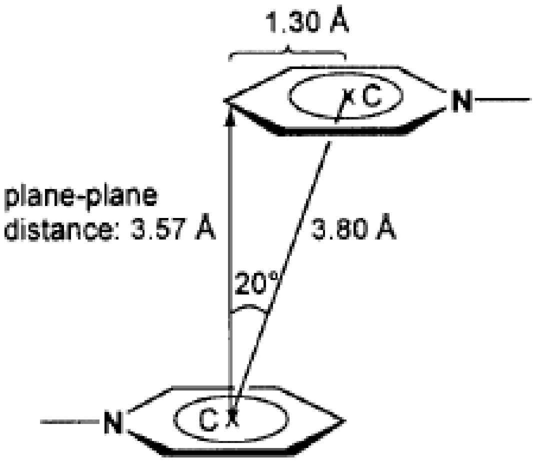

Figure 1.9. Graphical presentation of usual offset or slipped π interaction (Courtesy: Christoph Janiak).

Short centroid-centroid contacts (Cg···Cg < 3.8 Å), modest slip angles (β, γ < 25°), and vertical displacements (d[a] < 1.5 Å), which result in significant overlap of the π-electron clouds and are indicative of strong π-stacking interactions, have been demonstrated by Janiak and coworkers (Figure 1.10) [181].

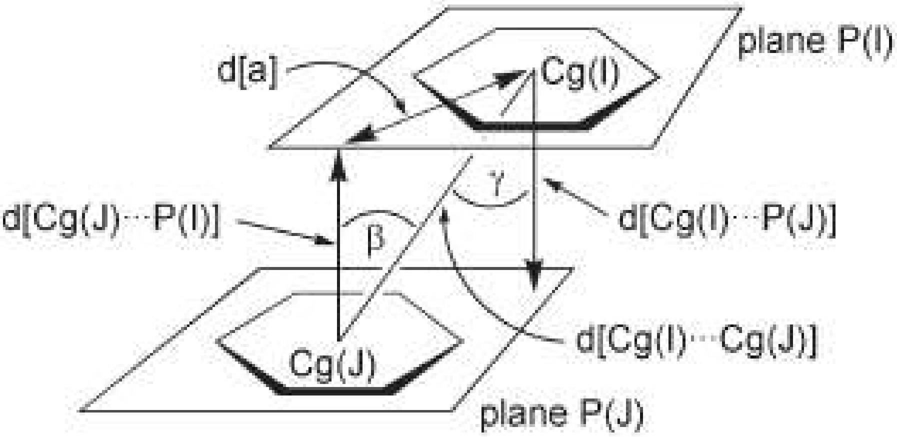

Figure 1.10. Graphical presentation of the parameters usually used to describe π–π stacking. d[Cg(I)···Cg(J)] = Centroid–centroid distance; α = Dihedral angle between the ring planes; β = Angle between the centroid vector Cg(I)···Cg(J) and the normal to the plane I; γ = Angle between the centroid vector Cg(I)···Cg(J) and the normal to the plane J; d[Cg(I)···P(J)] = Perpendicular distance of Cg(I) on ring plane J; d[Cg(J)···P(I)] = Perpendicular distance of Cg(J) on ring plane I; d[a] = Vertical displacement between ring centroids. (Courtesy: Christoph Janiak)

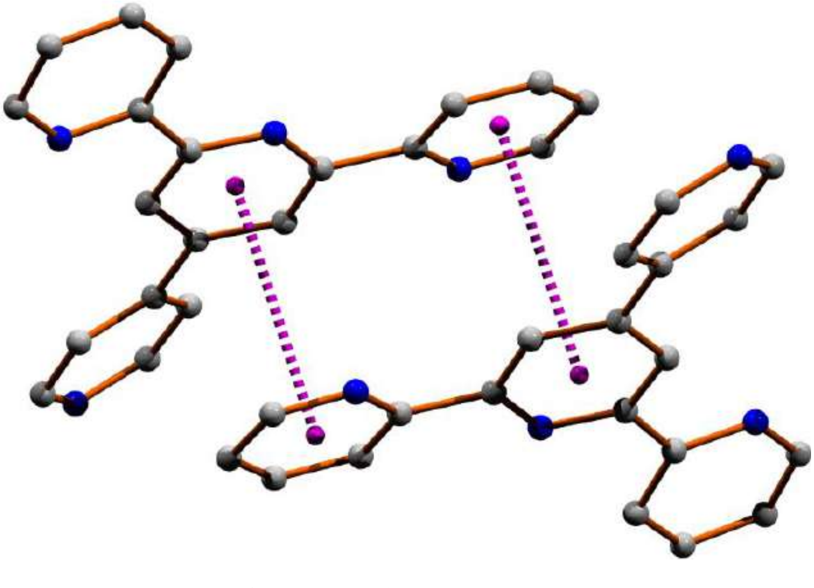

Figure 1.11. Supramolecular framework generated through π–π stacking interactions (pink dotted lines) [182].

1.8.6. Anion···π interaction

Anion···π interactions are characterized as noncovalent contacts between an anion and an electron-deficient (π-acidic) aromatic system (Figure 1.12) [183]. The anion–electrostatic and anion-induced polarization contributions control π interaction [183-185]. An increasing number of chemical and biological processes now recognize and value anion-π interactions for their critical role. The anion-π contact is therefore particularly useful in both environmental and medical applications [186].

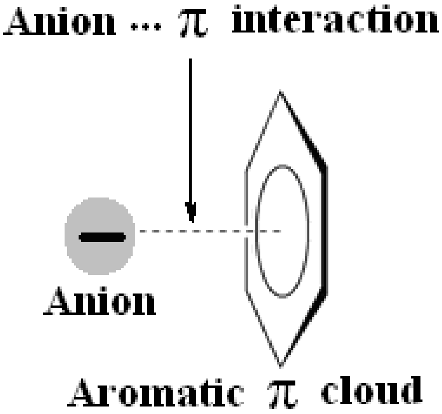

Figure. 1.12. Anion–π interaction.

Since any interaction between anions and neutral aromatic π-clouds should be repulsive, anions are naturally not expected to do so. However, once the electron-withdrawing groups bind to the aromatic π-clouds, the aromatic system turns acidic (i.e. electron-deficient). As a result, there are fewer repulsive interactions between anions and electron-deficient aromatic systems. Anion-π interactions are advantageous in such a circumstance [187]. These interactions are energetically advantageous and fall within the energy range of 20–50 kJ mol^{-1}, according to a number of significant theoretical investigations [184, 188, 189]. A substantial number of experimental evidence [190-192] supports the value of anion-π interactions in science.

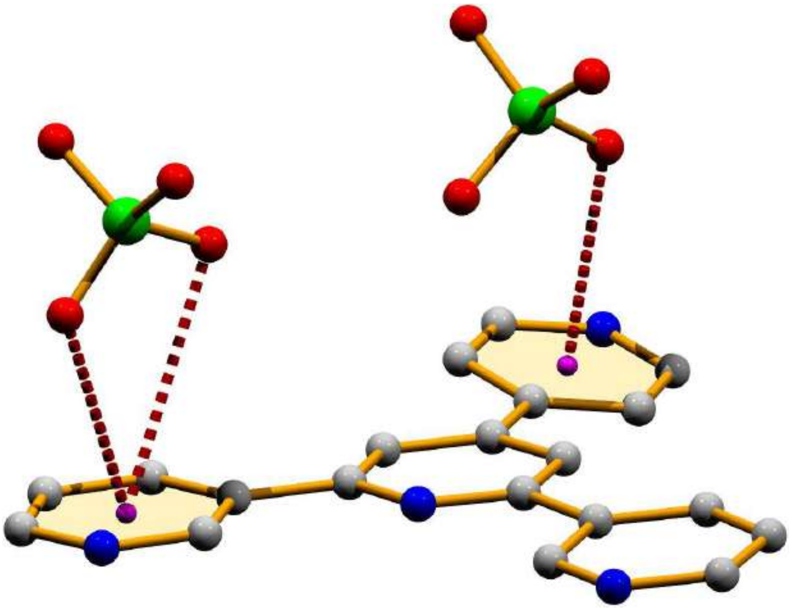

Figure 1.13. Anion···π interactions (dotted lines) in solid-state structure [193].

1.8.7. Cation···π interactions

First, Kebarle and his coworkers [194] performed experiments to establish the validity of cation-interaction. A cationic species interacts with the π-clouds of aromatic rings in cation···π interaction (Figure 1.14). An adjacent cation, such as Li^+ or Na^+, and the face of an electron-rich π-system, such as benzene or ethylene, interact via a noncovalent molecular interaction known as cation···π interaction. This unique interaction between a monopole (cation) and a quadrupole (π-system) is an example of noncovalent interaction. The same order of magnitude as hydrogen bonds or salt bridges, cation···π interaction energies are important for molecular recognition.

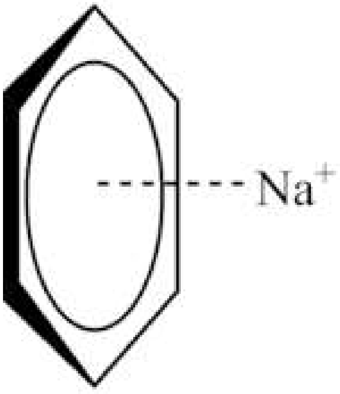

Figure 1.14. Cation–π interaction between benzene and a sodium cation.

Since the contributions of the weakly polar carbon-hydrogen bonds cancel due to molecular symmetry, benzene, the model π-system, lacks a stable dipole moment. However, a partial negative charge is present in the electron-rich π-system above and below the benzene ring. A positive charge is connected to this sandwiching negative charge within the plane in which all benzene atoms are arranged. A pair of dipoles that don't cancel each other out create an electric quadrupole (Figure 1.8). The positively charged ions can then interact well with the negatively charged π-system. Similar to hydrogen bonding in strength, the cation-π interaction often acts as a strong intermolecular force. The nature of cation, the constituents of the π-system, and the solvent are three factors that affect the strength of the bonding. The structure and function of biomolecules are significantly influenced by numerous examples of cation-π interactions that are frequently observed in nature [195-200].

1.8.8. Carbonyl (lone pair)···π interactions

An significant type of supramolecular interaction between a neutral electron-rich molecule and an electron-deficient π-ring (see Figure 1.15) is the lone pair···π interaction [201]. Various biological systems place a great deal of importance on the lone-pair···π interaction [202, 203]. The stability of biological macromolecules is greatly aided by lone-pair···π interactions [204, 205].

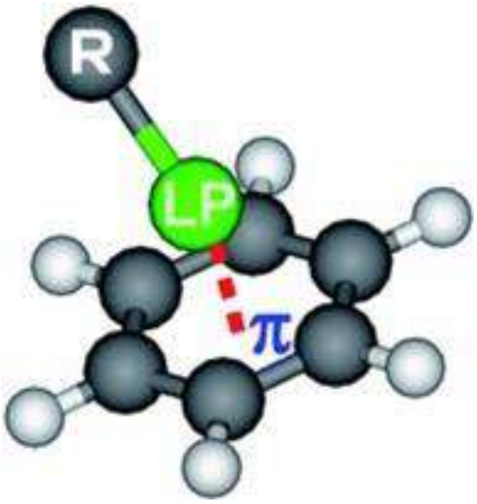

Fig. 1.15. The lone pair–π interaction [95].

According to a methodical analysis by Sankararamakrishnan and coworkers, the ideal lone-pair···π interaction occurs when an aromatic acceptor center and a lone-pair donor are located within 3.5Å of one another [206]. Lone-pair···π interaction is favorable for electron-deficient π-systems, according to ab initio research [207-209]. In addition to these, a great deal of computational research has shown that the interaction between a lone-pair donor and an aromatic acceptor (i.e., π-system) can be energetically favorable [210-2012]. Numerous molecular host-guest systems have also been reported to have the lone-pair···π bonding contacts [213-216].

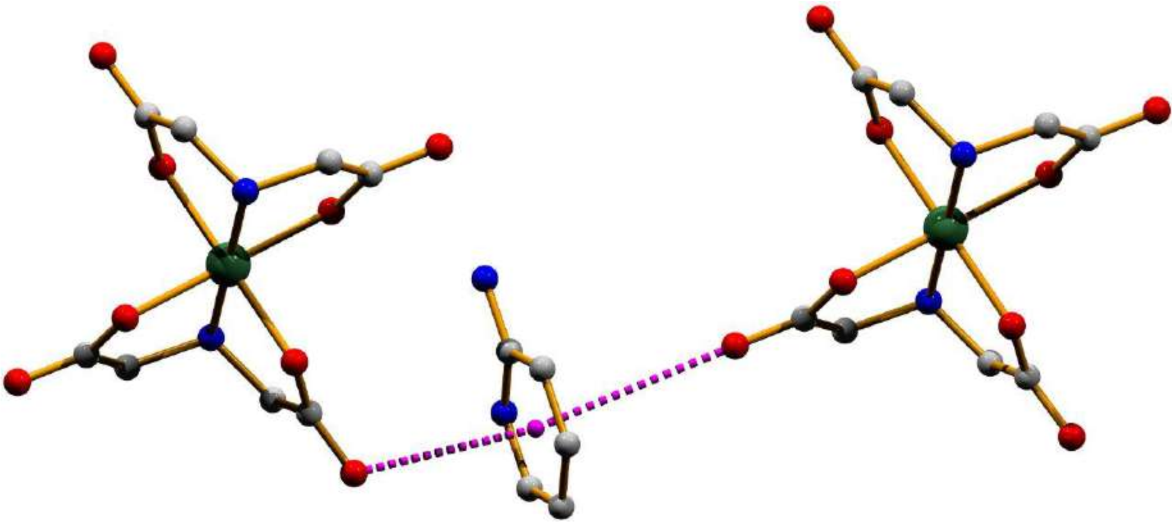

Figure 1.16. The lone-pair···π/π···lone-pair interaction (pink dotted lines) in the solid-state [217].

1.9. Hirshfeld surface

Due to the stockholder partitioning' scheme, the molecular surfaces were given names in accordance with F. L. Hirshfeld [218]. Hirshfeld surfaces [218-223] have only lately been used to divide molecular crystals into molecular regions for electron density integration [224]. Molecular Hirshfeld surfaces are created by dividing up space in the crystal into areas where the electron distribution of a sum of spherical atoms for the molecule (the promolecule) outweighs the equivalent sum over the crystal (the procrystal). Hirshfeld [218] states that a weighting function *w*(r) for a specific molecule is defined as

$$W(\boldsymbol{r}) = \sum_{a \in molecule} \rho_a(\boldsymbol{r}) \Big/ \sum_{a \in crystal} \rho_a(\boldsymbol{r})$$

$$= \rho_{promolecule}(\boldsymbol{r})/\rho_{procrystal}(\boldsymbol{r})$$

$$\simeq \rho_{molecule}(\boldsymbol{r})/\rho_{crystal}(\boldsymbol{r}), \qquad (1.23)$$

Since the Hirshfeld surface is specified by w(r) = 0.5, it follows that the volume where the promolecule predominates the procrystal electron density is that area where w(r) ≥ 0.5. The ratio between promolecule and procrystal electron densities can be considered an approximation to the ratio between the true molecule and crystal electron densities in this situation where $\rho(\mathbf{r})$ is a spherically averaged Hartree-Fock atomic electron density function [225] centered on the nucleus. For computational purposes the sum over the crystal is condensed to a group of molecules only around 10 Å away from the target molecule. The isosurface defined by w(r) = 0.5 is unique for a given crystal structure and set of atomic electron densities, although changes in the atomic electron densities result in very slight changes in the resulting surface.

Hirshfeld surfaces, in contrast to other molecular volumes and surfaces [226], are defined only inside the crystal and represent the interaction between various atomic sizes and intermolecular interactions within the crystal. It should be determined whether Hirshfeld surfaces do this quantitatively or qualitatively. Hirshfeld surfaces and volumes are significantly larger than conventional ones [227]; typically, they fill at least 95% of the crystal volume, as opposed to typical packing coefficients, which range from 0.65 to 0.80 [228]. Hirshfeld surfaces pack very densely in the crystal, never overlapping and just occasionally touching.

The points where the electron density contribution from the molecule of interest equals the combined contribution from all other molecules constitute the Hirshfeld surface that encloses the molecule. Two distances are specified for each place on that isosurface: d_e, the distance to the closest nucleus outside the surface, and d_i, the distance to the closest nucleus inside the surface. The normalized contact distance (d_{norm}) based on the atom's *vdW* radii, d_e and d_i, given by the equation

$$d_{norm} = \frac{d_i - r_i^{vdw}}{r_i^{vdw}} + \frac{d_e - r_e^{vdw}}{r_e^{vdw}} \qquad (1.24)$$

allows for identifying the areas that are especially important for intermolecular interactions [219]. When intermolecular interactions are either shorter or longer than vdW separations, the value of the d_{norm} is either negative or positive, respectively. Due to the symmetry between d_e and d_i in the expression of d_{norm}, a red spot with the same color intensity, size and shape will appear where two Hirshfeld surfaces touch. The intermolecular interactions in the crystal [219] are summarized by the combination of d_e and d_i as a fingerprint plot [229]. d_{norm}-mapped molecular Hirshfeld surfaces are represented graphically as red, white, and blue plots where blue is used for longer contacts, white is used for contacts near the vdW separation, and red is used to highlight shorter contacts. Furthermore, based on the local curvature of the surface, two additional colored attributes (Shape index and Curvedness) can be specified [230].

Shape index, which quantifies "which shape", is sensitive to the smallest changes in surface shape, especially in areas with very low curvature. The function defines shape index

$$S = \left(\frac{2}{\pi}\right) \arctan\left[\frac{k_1 + k_2}{k_1 - k_2}\right] \qquad (1.25)$$

Where k_1 and k_2 are the surface curvatures of the molecule. The formal range of S is [-1, +1]. S has several intriguing attributes that have been extensively discussed in the literature. The shape-index surface's adjacent red and blue triangles characterize the solid-state structure's π–π stacking interaction. Red triangles show concave regions because of carbon atoms of the π-stacked molecule above it, whereas blue triangles represent convex regions because of ring carbon atoms of the molecule inside the surface. The pattern of symmetrically alternating red and blue triangles shows offset π–π stacking interactions typical of layers.

Curvedness is a measure of "how much shape" while regions of sharp curvature have a high curvedness and tend to partition the surface into patches associated with contacts between surrounding molecules, low values of curvedness are linked with completely flat areas of the surface. Curvedness is defined by

$$C = \left(\frac{2}{\pi}\right) ln[(k_1^2 + k_2^2)/2]^{1/2} \qquad (1.26)$$

C is obviously a function of the r.m.s. curvature of the surface, and although the formal range of C is (-∞, +∞), it has been discovered that in practice a mapping from -4.0 to +0.4 (with $k1$ and $k2$ in a.u.$^{-1}$), is most useful with molecular Hirshfeld surfaces. The pattern and large flat region of the curvedness surface also characterize π–π stacking interaction.

1.10. References

[1] A.L. Patterson, Phys. Rev. 46 (1934) 372–376.

[2] A.J.C. Wilson, Nature (London) 150 (1942) 151–152.

[3] D. Harker, J.S. Kasper, Acta Cryst. 3 (1948) 374–378.

[4] J. Karle, H. Hauptman, Acta Cryst. 3 (1950) 181–187.

[5] W. Cochran, Acta Cryst. 8 (1955) 473–478.

[6] J. Karle, H. Hauptman, Acta Cryst. 9 (1956) 635–651.

[7] D. Sayre, Acta Cryst. 5 (1952) 60–65.

[8] G.M. Sheldrick, SHELXS-97: Program for crystal structure solution, University of Göttingen, Germany, 1997.

[9] M.C. Burla, R. Caliandro, M. Camalli, B. Carrozzini, G.L. Cascarano, L. De Caro, C. Giacovazzo, G. Polidori, R. Spagna, J. Appl. Cryst. 38 (2005) 381–388.

[10] M.M. Woolfson, Acta Cryst. A 43 (1987) 593–612.

[11] J.D. Dunitz, X-ray Analysis and structure of Organic Molecules, Cornell University Press: Ithaca, 1979.

[12] G.H. Stout, L. H. Jensen, X-ray Structure Determination: A Practical Guide, John Wiley and Sons: New York, 1989.

[13] M.F.C. Ladd, R. H. Palmer, Structure determination by X-Ray Crystallography, Plenum, New York, 1985.

[14] E. Wu, J. Appl. Crystallogr. 22 (1989) 506–510.

[15] Bruker APEX2, SAINT and SADABS, Bruker AXS Inc., Madison, Wisconsin, USA, 2011.

[16] G. Sheldrick, Crystal Structure Refinement with SHELXL. Acta Crystallogr. Sect. C 71 (2015) 3–8.

[17] C.F. Macrae, L. Sovago, S.J. Cottrell, P.T.A. Galek, P. McCabe, E. Pidcock, M. Platings, G.P. Shields, J.S. Stevens, M. Towler, P. Wood, A. Mercury 4.0: From Visualization to Analysis, Design and Prediction. J. Appl. Crystallogr. 53 (2020) 226–235.

[18] A. Spek, Structure Validation in Chemical Crystallography. Acta Crystallogr. Sect. D 65 (2009) 148–155.

[19] A. Spek, CheckCIF Validation ALERTS: What They Mean and How to Respond. Acta Crystallogr. Sect. E 76 (2020) 1–11.

[20] L.J. Farrugia, J. Appl. Crystallogr. 45 (2012) 849–854.

[21] C.J. Pedersen, J. Am. Chem. Soc. 89 (1967) 7017–7036.

[22] D.J. Cram, Angew. Chem. Int. Ed. 27 (1988) 1009.

[23] J.-M. Lehn, Angew. Chem. Int. Ed. 27 (1988) 89.

[24] S. Shinkai, M. Ikeda, A. Sugasaki, M. Takeuchi, Acc. Chem. Res. 34 (2001) 494–503.

[25] C.J. Pedersen, Angew. Chem. Int. Ed. 27 (1988) 1021–1027.

[26] J. M. Lehn, Struct. Bonding 16 (1973) 1–69.

[27] J.-M. Lehn, Pure Appl Chem. 50 (1978) 871–892.

[28] J.-M. Lehn, Science 295 (2002) 2400–2403.

[29] G.M. Whitesides, B. Grzybowski, Science 295 (2002) 2418–2421.

[30] J.-M. Lehn, Proc. Natl. Acad. Sci. U. S. A. 99 (2002) 4763–4768.

[31] G.M. Whitesides, B. Grzybowski, Science 295 (2002) 2418–2421.

[32] R. Custelcean, C. Afloroaei, M. Vlassa, M. Polverejan, Angew. Chem. Int. Ed. 39 (2000) 3094–3096.

[33] H. Yin, G. Hummer, J.C. Rasaiah, J. Am. Chem. Soc. 129 (2007) 7369–7377.

[34] C. Meier, U. Ziener, K. Landfester, P. Weihrich, J. Phys. Chem. B 109 (2005) 21015–21027.

[35] B. K. Saha, A. Nangia, Chem. Commun. (2005) 3024–3026.

[36] G.R. Desiraju, Crystal Engineering: The Design of Organic Solids, Materials Science Monographs, Elsevier, Amsterdam 54,1989.

[37] G.R. Desiraju, Angew. Chem. Int. Ed. 46 (2007) 8342–8356.

[38] D. Braga, J. Chem. Soc. Dalton Trans. (2000) 3705–3713.

[39] D. Braga, F. Grepioni, G.R. Desiraju, Chem. Rev. 98 (1998) 1375–1406.

[40] R. Pepinsky, Crystal engineering-new concept in crystallography In Physical Review, vol. 100, no. 3, pp. 971–971. ONE PHYSICS ELLIPSE, COLLEGE PK, MD 20740-3844 USA: AMERICAN PHYSICAL SOC, 1955.

[41] G.M.J. Schmidt, Pure Appl. Chem. 27 (1971) 647–678.

[42] M. Lusi, Cryst. Growth Des. 18 (2018) 3704–3712.

[43] D. Braga, G.R. Desiraju, J.S. Miller, A.G. Orpend, S.L. Price, CrystEngComm 4 (2002) 500–509.

[44] J.M. Lehn, Supramolecular Chemistry: Concepts and Perspectives. VCH: Weinheim, 1995.

[45] D. Braga, F. Grepioni, Acc. Chem. Res. *33* (2000) 601–608.

[46] B. Moulton, M. J. Zaworotko, Chem. Rev. 101 (2001) 1629–1658.

[47] D. Braga, G. Desiraju, J. Miller, A. Orpen, S. Price, CrystEngComm 4 (2002) 500–509.

[48] D. Braga, Chem. Commun. 22 (2003) 2751–2754.

[49] D. Braga, L. Brammer, N.R. Champness, CrystEngComm 7 (2005) 1–19.

[50] P. Kanoo, K.L. Gurunatha, T.K. Maji, Cryst. Growth Des. 9 (2009) 4147–4156.

[51] L. Brammer, Chem. Soc. Rev. 33 (2004) 476–489.

[52] S. Kitagawa, K. Uemura, Chem. Soc. Rev. 34 (2005) 109–119.

[53] M.W. Hosseini, Acc. Chem. Res. 38 (2005) 313–323.

[54] G.R. Desiraju, Angew. Chem. Int. Ed. 34 (1995) 2311–2327.

[55] V.R. Vangala, B.R. Bhogala, A. Dey, G.R. Desiraju, C.K. Broder, P.S. Smith, R. Mondal, J.A.K. Howard, C.C. Wilson, J. Am. Chem. Soc. 125 (2003) 14495–14509.

[56] B.R. Bhogala, A. Nangia, Cryst. Growth Des. 3 (2003) 547–554.

[57] K. Biradha, New J. Chem. 32 (2008) 1673–1676.

[58] M.C. Etter, Acc. Chem. Res. 23 (1990) 120–126.

[59] E. Corey, J. Pure Appl. Chem. 14 (1967) 19−38.

[60] O.V. Shishkin, R.I. Zubatyuk, S.V. Shishkina, V.V. Dyakonenko, V.V. Medviediev, Phys. Chem. Chem. Phys. 16 (2014) 6773−6786.

[61] R.D. Bailey Walsh, M.W. Bradner, S. Fleischman, L.A. Morales, B. Moulton, N. Rodríguez-Hornedob, M. J. Zaworotko, Chem Comm. (2003) 186−187.

[62] M. Mohana, P. T. Muthiaha, C. D. McMillen, Acta Cryst. C 73 (2017) 259–263.

[63] C. Chen, K. Zhang, Y. Sun, S. Xiang, Y. Geng, K. Liu, L. Wang, J. Mol. Struct. 1170 (2018) 60–69.

[64] T.K. Adalder, R. Sankolli, P. Dastidar, Cryst. Growth & Des. 12 (2012) 2533–2542.

[65] S.G. Fleischman, S.S. Kuduva, J.A. McMahon, B. Moulton, R.D. Bailey Walsh, N. Rodríguez-Hornedo, M.J. Zaworotko, Cryst. Growth Des. 3 (2003) 909–919.

[66] J.A. McMahon, J.A. Bis, P. Vishweshwar, T.R. Shattock, O.L. McLaughlin, M.J.Z. Zaworotko, Kristallogr. 220 (2005) 340−350.

[67] O.V. Shishkin, Chem. Phys. Lett. 458 (2008) 96−100.

[68] K. Merz, V. Vasylyeva, CrystEngComm 12 (2010) 3989−4002.

[69] M.J. Zaworotko, Cryst. Growth Des. 7 (2007) 4–9.

[70] K. Biradha, CrystEngComm 5 (2003) 374–384.

[71] L. Brammer, Chem. Soc. Rev. 33 (2004) 476–489.

[72] D. Braga, L. Brammer, N. R. Champness, CrystEngComm 7 (2005) 1–19.

[73] S. Goswami, S. Jana, A. Hazra, H.-K Fun, S. Anjum, A.-U. Rahman CrystEngComm 8 (2006) 712–718.

[74] J. L. Atwood, J. E. D. Davies, D. D. MacNicol, F. Vögtle, J.-M. Lehn, Comprehensive Supramolecular Chemistry; Pergamon: Oxford, 1996.

[75] G. R. Desiraju, C. V. K. Sharma, Perspectives in Supramolecular Chemistry; Wiley: Chichester, 1995.

[76] J. Steed, J. L. Atwood, J. L. Supramolecular Chemistry; Wiley, New York 2000.

[77] L. Lindoy, F.I.M. Atkinson, Self-Assembly in Supramolecular Systems; Royal Society of Chemistry, Cambridge, 2000.

[78] J.-M. Lehn, Proc. Natl. Acad. Sci. U. S. A. 99 (2002) 4763–4768.

[79] T. Steiner, Angew. Chem. Int. Ed. 41 (2002) 48–76.

[80] S.–i. Noro, T. Akutagawa, T. Nakamura, Cryst. Growth Des. 7 (2007) 1205–1208.

[81] R.S. Rowland, T. Taylor, J. Phys. Chem. 100 (1996) 7384–7391.

[82] G.A. Jeffrey, W. Saenger, Hydrogen Bonding in Biological Structures; Springer, Berlin (1991).

[83] T. Steiner, G.R. Desiraju, Chem. Commun. 8 (1998) 891–892.

[84] S. Scheiner, Hydrogen Bonding. A Theoretical Perspective; Oxford University Press: Oxford (1997).

[85] A.K. Rappé, E.R.Bernstein, J. Phys. Chem. A 104 (2000) 6117–6128.

[86] K. M. Dethlefs, P. Hobza, Chem. Rev. 100 (2000) 143–168.

[87] S.L.R. MacGillivray, J.L. Atwood, Nature 389 (1997) 469–472.

[88] L. J. Childs, N. W. Alcock, M. Hannon, Angew. Chem. Int. Ed. 40 (2001) 1079–1081.

[89] M. Kidowaki, N. Tamaoki, Chem. Commun. 2 (2003) 290–291.

[90] K. Biradha, M.J. Zaworotko, J. Am. Chem. Soc. 120 (1998) 6431–6432.

[91] A.D. Bond, Chem. Commun. 16 (2002) 1664–1665.

[92] G.A. Jeffrey, An Introduction to Hydrogen Bonding; Oxford University Press: Oxford, 1997.

[93] R. Preibner, U. Egner, W. Saenger, FEBS Lett. 288 (1991) 192–196.

[94] I. Rozas, I. Alkorta, J. Elguero, J. Phys. Chem. A 102 (1998) 9925–9932.

[95] T. Steiner, A.M.M. Schreurs, M. Lutz, J. Kroon, New J. Chem. 25 (2001) 174–178.

[96] T. Steiner, S.A. Mason, Z. Kristallogr. 18 (2001) 93.

[97] H.S. Rzepa, M.H. Smith, M.L. Webb, J. Chem. Soc., Perkin Trans. 2 (1994) 703–707.

[98] M. Pilkington, J.D. Wallis, S. Larsen, J. Chem. Soc., Chem. Commun. 15 (1995) 1499–1500.

[99] P.K. Bakshi, A. Linden, B.R. Vincent, S.P. Roe, D. Adhikesavalu, T.S. Cameron, O. Knop, O. Can. J. Chem. 72 (1994) 1273–1293.

[100] G.A. Jeffrey, Crystallogr. Rev. 3 (1995) 213–254.

[101] G. Gilli, P. Gilli, J. Mol. Struct. 552 (2000) 1–15.

[102] G.A. Jeffrey, J. Mitra, Acta Crystallogr. B 39 (1983) 469–480.

[103] T. Steiner, S.A. Mason, W. Saenger, J. Am. Chem. Soc. 113 (1991) 5676–5687.

[104] G.R. Desiraju, T. Steiner, The Weak Hydrogen Bond in Structural Chemistry and Biology; Oxford University Press, Oxford, 1999.

[105] G. Gilli, F. Bellucci, V. Ferretti, V. Bertolasi, J. Am. Chem. Soc. 111 (1989) 1023–1028.

[106] V. Bertolasi, P. Gilli, V. Verretti, G. Gilli, Chem. Eur. J. 2 (1996) 925–934.

[107] V. Bertolasi, P. Gilli, V. Ferretti, G. Gilli, Acta Crystallogr. B51 (1995) 1004–1015.

[108] P. Gilli, V. Bertolasi, V. Ferretti, G. Gilli, J. Am. Chem. Soc. 122 (2000) 10405–10417.

[109] T. Steiner, Chem. Commun. 3 (1998) 411–412.

[110] T. Steiner, Chem. Commun. 8 (1997) 727–734.

[111] G.R. Desiraju, Acc. Chem. Res. 24 (1991) 290–296.

[112] G.R. Desiraju, J. Chem. Soc., Chem. Commun. 3 (1989) 179–180.

[113] G.R. Desiraju, J. Chem. Soc., Chem. Commun. 6 (1990) 454–455.

[114] M. Czugler, N. Báthori, CrystEngComm 6 (2004) 495–503.

[115] G.R. Desiraju, Acc. Chem. Res. 29 (1996) 441–449.

[116] H. Hofmeier, U.S. Schubert, Chem. Commun. 19 (2005) 2423–2432.

[117] S. Kumar, R. Nussinov , J Mol Biol. 293 (1999) 1241–1255.

[118] S Kumar, R. Nussinov, Biophys J. 83 (2002) 1595–1612.

[119] F.O. Tzul, K.L. Schweiker G.I. Makhatadze, Proc. Natl. Acad. Sci. U. S. A., 112 (2015) E259–E266.

[120] M.P. Williamson, A.M. Hounslow, J. Ford, K. Fowler, M. Hebditch, P.E. Hansen, Chem. Commun. 49 (2013) 9824–9826.

[121] I. Gitlin, J.D. Carbeck, G. M. Whitesides, Angew. Chem. Int. Ed. 45 (2006) 3022–3060.

[122] V. Ferretti, V. Bertolasi, L. Pretto, New J. Chem. 28 (2004) 646–651.

[123] E. Yashima, K. Maeda, Y. Furusho, Acc. Chem. Res. 41 (2008) 1166–1180.

[124] H. Katagiri, Y. Tanaka, Y. Furusho and E. Yashima, Angew. Chem. Int. Ed. 46 (2007) 2435–2439.

[125] A. Warshel, P. K. Sharma, M. Kato, W. W. Parson, Biochim. Biophys. Acta-Proteins Proteomics 1764 (2006) 1647–1676.

[126] Q. Xu, H. Guo, A. Wlodawer, H. Guo, J. Am. Chem. Soc. 128 (2006) 5994–5995.

[127] B. Kuberski, A. Szumna, Chem. Commun. 15 (2009) 1959–1961.

[128] L.E.R. O'Leary, J.A. Fallas, E.L. Bakota, M.K. Kang, J.D. Hartgerink, Nat. Chem. 3 (2011) 821–828.

[129] J.M. Christie, A.S. Arvai, K.J. Baxter, M. Heilmann, A.J. Pratt, A. O'Hara, S.M. Kelly, M. Hothorn, B.O. Smith, K. Hitomi, G.I. Jenkins, E.D. Getzoff, Science 335 (2012) 1492–1496.

[130] V. Dvornikovs, D.B. Smithrud, J. Org. Chem. 67 (2002) 2160–2167.

[131] P.-O. Norrby, T. Liljefors, J. Am. Chem. Soc. 121 (1999) 2303–2306.

[132] S.K. Seth, A. Bauza, A. Frontera, New J. Chem. 2018, (2018) 12134–12142.

[133] D. Sadhukhan, M. Maiti, G. Pilet, A. Bauzá, A. Frontera, S. Mitra, Eur. J. Inorg. Chem. 2015 (2015) 1958−1972.

[134] M. Kaufmann, M. Gisler, C.J. Leumann, Angew. Chem. Int. Ed. 48 (2009) 3810−3813.

[135] L. Berg, M.S. Niemiec, W. Qian, C.D. Andersson, P. Wittung- Stafshede, F. Ekström, A. Linusson, Angew. Chem. Int. Ed. 51 (2012) 12716−12720.

[136] M. Majumder, B.K. Mishra, N. Sathyamurthy, Chem. Phys. Lett. 557 (2013) 59−65.

[137] J. Černyý, M. Kabeláč, P. Hobza, J. Am. Chem. Soc. 130 (2008) 16055−16059.

[138] R.K. Raju, N.A. Burton, I.H. Hillier, Phys. Chem. Chem. Phys. 12 (2010) 7117−7125.

[139] Y. Umezawa, S. Tsuboyama, K. Honda, J. Uzawa, M. Nishio, Bull. Chem. Soc. Jpn. 71 (1998) 1207−1213.

[140] H. Okawa, Y. Numata, A. Mio, S. Kida, S. Bull. Chem. Soc. Jpn. 53 (1980) 2248−2251.

[141] H. Okawa, K. Ueda, S. Kida, Inorg. Chem. 21 (1982) 1594−1598.

[142] M. Nakamura, H. Okawa, T. Inazu, S. Kida, Bull. Chem. Soc. Jpn. 55 (1982) 2400−2403.

[143] M. Nakamura, H. Okawa, T. Ito, M. Kato, S. Kida, Bull. Chem. Soc. Jpn. 60 (1987) 539−543.

[144] M. Nishio, M. Hirota, Y. Umezawa, The CH/π Interaction−Evidence, Nature, and Consequences. Wiley-VCH, New York, 1998.

[145] H. Okawa, Coord. Chem. Rev. 92 (1988) 1−28.

[146] M. Tamres, J. Am. Chem. Soc. 74 (1952) 3375–3378.

[147] J.C.D. Brand, G. Eglinton, J. Tyrrell, J. Chem. Soc. (1965) 5914–5919.

[148] Y. Iitaka, Y. Kodama, K. Nishihata, M. Nishio, Chem. Commun. 10 (1974) 389–390.

[149] J.J. Novoa, F. Mota, Chem. Phys. Lett. 318 (2000) 345–354.

[150] A. Bagno, G. Saielli, G. Scorrano, Angew. Chem. Int. Ed. 40 (2001) 2532–2534.

[151] S. Tsuzuki, K. Honda, T. Uchimaru, M. Mikami, K. Tanabe, J. Phys. Chem. A 106 (2002) 4423–4428.

[152] N. Kunio, N. Naoya, Bull. Chem. Soc. Jpn. 51 (1978) 3267–3272.

[153] R. Ehama, A. Yokoo, M. Tsushima, T. Yuzuri, H. Suezawa, M. Hirota, Bull. Chem. Soc. Jpn. 66 (1993) 814–818.

[154] M. Nishio, CrystEngComm 6 (2004) 130–158.

[155] T. Maity, H. Mandal, A. Bauzá, B. C. Samanta, A. Frontera, S. K. Seth, New J. Chem. 42 (2018) 10202–10213.

[156] Z. D. Tomić, S. B. Novaković, S. D. Zarić, Eur. J. Inorg. Chem. 2004 (2004) 2215–2218.

[157] H. Tsubaki, S. Tohyama, K. Koike, H. Saitoh, O. Ishitani, Dalton Trans. 2005 385–395.

[158] H. Kumita, T. Kato, K. Jitsukawa, H. Einaga, H. Masuda, Inorg. Chem. 40 (2001) 3936–3942.

[159] H. Suezawa, T. Yoshida, Y. Umezawa, S. Tsuboyama, M. Nishio, Eur. J. Inorg. Chem. 2002 (2002) 3148–3155.

[160] H. Masui, Coord. Chem. Rev. 219 (2001) 957–992.

[161] M. K. Milčič, V. B. Medaković, D. N. Sredojević, N. O. Juranić, S. D. Zarić, Inorg. Chem. 45 (2006) 4755–4763.

[162] S. D. Stojanović, V. B. Medaković, G. Predović, M. Beljanski, S. D. Zarić, J. Biol. Inorg. Chem. 12 (2007) 1063–1071.

[163] D. N. Sredojević, D. B. Ninković, G. V. Janjić, J. Zhou, M. B. Hall, S. D. Zarić, ChemPhysChem 14 (2013) 1797–1800.

[164] D. P. Malenov, D. B. Ninković, D. N. Sredojević, S. D. Zarić, ChemPhysChem 15 (2014) 2458–2461.

[165] S. Jana, S. Khan, A. Bauza, A. Frontera, S. Chattopadhyay, J. Mol. Struct. 1127 (2017) 355–360.

[166] C. Janiak, J. Chem. Soc., Dalton Trans. 21 (2000) 3885–3896.

[167] G. A. Bogdanović, A. S. Biré, S. D. Zarić, Eur. J. Inorg. Chem. 2002 (2002) 1599–1602.

[168] Y.-F. Jiang, C.-J. Xi, Y.-Z. Liu, J. Niclós-Gutiérrez, D. Choquesillo-Lazarte, Eur. J. Inorg. Chem. (2005) 1585–1588.

[169] C. I. Yeo, S. N. A. Halim, S. W. Ng, S. L. Tan, J. Zukerman-Schpector, M. A. B. Ferreira, E. R. T. Tiekink, Chem. Commun. 50 (2014) 5984–5986.

[170] Y. S. Tan, S. N. A. Halim, K. C. Molloy, A. L. Sudlow, A. Otero-de-la-Roza, E. R. T. Tiekink, CrystEngComm 18 (2016) 1105–1117.

[171] D.P. Malenov, G.V. Janjić, V.B. Medaković, M.B. Hall, S.D. Zarić, Coord. Chem. Rev. 34 (2017) 318–341.

[172] M. Nishio, Y. Umezawa, K. Honda, S. Tsuboyama, H. Suezawa, CrystEngComm 11 (2009) 1757–1788.

[173] T. R. Cook, Y. R. Zheng, P. J. Stang, Chem. Rev. 113 (2013) 734–777.

[174] C.I. Yeo, S.N.A. Halim, S.W. Ng, S.L. Tan, J. Zukerman-Schpector, M.A. B. Ferreira, E.R.T. Tiekink, Chem. Commun. 50 (2014) 5984–5986.

[175] K. Müller-Dethlefs, P. Hobza, Chem. Rev. 100 (2000) 143–168.

[176] C.A. Hunter, K.R. Lawson, J. Perkins, C.J. Urch, J. Chem. Soc., Perkin Trans. 2 (2001) 651–669.

[177] C.A. Hunter, J.K.M. Sanders, J. Am. Chem. Soc. 112 (1990) 5525–5534.

[178] C. Janiak, J. Chem. Soc., Dalton Trans. (2000) 3885–3896.

[179] F. Cozzi, M. Cinquini, R. Annuziata, J.S. Siegel, J. Am. Chem. Soc. 115 (1993) 5330–5331.

180. D.B. Amabilino, J.F. Stoddart, Chem. Rev. 95 (1995) 2725–2828.

[181] T. Dorn, C. Janiak, K. Abu-Shandi, CrystEngComm 7 (2005) 633–641.

[182] S. Tripathi, A. Hossain, S.K. Seth, S. Mukhopadhyay, J. Mol. Struct. 1226 (2021) 129254.

[183] B.L. Schottel, H.T. Chifotides, K.R. Dunbar Chem. Soc. Rev. 37 (2008) 68–83.

[184] D. Quiñonero, C. Garau, C. Rotger, A. Frontera, P. Ballester, A. Costa, P.M. Deyà, Angew. Chem. Int. Ed. 41 (2002) 3389–3392.

[185] C. Garau, A. Frontera, D. Quiñonero, P. Ballester, A. Costa, P.M. Deyà, ChemPhysChem 4 (2003) 1344–1348.

[186] P. Gamez, T.J. Mooibroek, S.J. Teat, J. Reedijk, Acc. Chem. Res. 40 (2007) 435–444.

[187] R. Robson, B.F. Abrahams, S.R. Batten, R.W. Gable, B.F. Hoskins, B. F.; Liu, J. Supramolecular Architecture, ACS Publications, Washington, DC,1992.

[188] I. Alkorta, I. Rozas, J. Elguero, J. Am. Chem. Soc.124 (2002) 8593–8598.

[189] M. Mascal, A. Armstrong, M.D. Bartberger, J. Am. Chem. Soc. 124 (2002) 6274–6276.

[190] C.A. Black, L.R. Hanton, M.D. Spicer, Chem. Commun. (2007) 3171–3173.

[191] S.R. Choudhury, P. Gamez, A. Robertazzi, C.-Y. Chen, H.M. Lee, S. Mukhopadhyay, Cryst. Growth Des. 8 (2008) 3773–3784.

[192] Z.-F. Tian, H.-B. Duan, H. Zhou, X.-M. Ren, H. Zhang, Q.-J Meng, Inorg. Chem. Commun. 12 (2009) 148–150.

[193] P. Manna, S.K. Seth, M. Mitra, S.R. Choudhury, A. Bauzá, A. Frontera, S. Mukhopadhyay, Cryst. Growth Des. 14 (2014) 5812−5821.

[194] J. Sunner, K. Nishizawa, P. Kebarle, J. Phys. Chem. 85 (1981) 1814–1820.

[195] J. C. Ma, D.A. Dougherty Chem. Rev. 97 (1997) 1303–1324.

[196] G.W. Gokel, L.J. Barbour, S.L.D. Wall, E.S. Meadows, Coord. Chem. Rev. 222 (2001) 127–154.

[197] G.W. Gokel, L.J. Barbour, R. Ferdani, J. Hu Acc. Chem. Res. 35 (2002) 878–886.

[198] E.A. Meyer, R.K. Castellano, F. Diederich, Angew. Chem. Int. Ed. 42 (2003) 1210–1250.

[199] V. Kuusk, W.S. McIntire, J. Biol. Chem. 269 (1994) 26136–26143.

[200] A.R.C. Raine, C.-C.Yang, L.C. Packman, S.A. White, F.S. Mathews, N.S. Scrutton, Protein Sci. 4 (1995) 2625–2628.

[201] T.J. Mooibroek, P. Gamez, J. Reedijk, CrystEngComm 10 (2008) 1501−1515.

[202] M. Egli, S. Sarkhel, Acc. Chem. Res. 40 (2007) 197–205.

[203] S. Sarkhel, A. Rich, M. Egli, J. Am. Chem. Soc. 125 (2003) 8998−8999.

[204] J.C. Calabrese, D.B. Jordan, A. Boodhoo, S. Sariaslani, T. Vannelli, Biochemistry 43 (2004) 11403−11416.

[205] E.J. Stollar, J.L. Gelpi, S. Velankar, A. Golovin, M. Orozco, B.F. Luisi, Proteins 57 (2004) 1−8.

[206] A. Jain, C.S. Purohit, S. Verma, R. Sankararamakrishnan, J. Phys. Chem. B 111 (2007) 8680−8683.

[207] J.P. Gallivan, D.A. Dougherty, Org. Lett. 1 (1999) 103−106.

[208] Y. Danten, T. Tassaing, M. Besnard, J. Phys. Chem. A 103 (1999) 3530−3534.

[209] S. Scheiner, T. Kar, J. Pattanayak, J. Am. Chem. Soc. 124 (2002) 13257−13264.

[210] B.W. Gung, X.W. Xue, H.J. Reich, J. Org. Chem. 70 (2005) 7232−7237.

[211] B.W. Gung, Y. Zou, Z.G. Xu, J.C. Amicangelo, D.G. Irwin, S.Q. Ma, H.C. Zhou, J. Org. Chem. 73 (2008) 689−693.

[212] J.C. Amicangelo, B.W. Gung, D.G. Irwin, N.C. Romano, Phys. Chem. Chem. Phys. 10 (2008) 2695−2705.

[213] T.J. Mooibroek, S.J. Teat, C. Massera, P. Gamez, J. Reedijk, Cryst. Growth Des. 6 (2006) 1569−1574.

[214] Z.L. Lu, P. Gamez, I. Mutikainen, U. Turpeinen, J. Reedijk, Cryst. Growth Des. 7 (2007) 1669−1671.

[215] P.J. Kitson, Y.F. Song, P. Gamez, P. de Hoog, D.L. Long, A.D.C. Parenty, J. Reedijk, L. Cronin, Inorg. Chem. 47 (2008) 1883−1885.

[216] C.Q. Wan, X.D. Chen, T.C.W Mak, CrystEngComm 10 (2008) 475−478.

[217] S.K. Seth, I. Saha, C. Estarellas, A. Frontera, T. Kar, S. Mukhopadhyay, Cryst. Growth Des. 11 (2011) 3250–3265.

[218] F.L. Hirshfeld, Theor. Chim. Acta 44 (1977) 129–138.

[219] M.A. Spackman, J.J. McKinnon, CrystEngComm 4 (2002) 378–392.

[220] J.J. McKinnon, D. Jayatilaka, M.A. Spackman, Chem. Commun. (2007) 3814–3816.

[221] M.A. Spackman, J.J. McKinnon, D. Jayatilaka, CrystEngComm. 10 (2008) 377–388.

[222] M.A. Spackman, D. Jayatilaka, CrystEngComm 11 (2009) 19–32.

[223] H.F. Clausen, M.S. Chevallier, M.A. Spackman, B.B. Iversen, New. J. Chem. 34 (2010) 193–199.

[224] M.A. Spackman, P.G. Byrom, Chem. Phys. Lett. 267 (1997) 215–220.

[225] E. Clementi, C. Roetti, At. Data Nucl. Data Tables 14 (1974) 177–478.

[226] P.G. Mezey, Rev. Comput. Chem. 1 (1990) 265–294.

[227] J.J. McKinnon, A.S. Mitchell, M.A. Spackman, Chem. Eur. J. 4 (1998) 2136–2141.

[228] A.I. Kitaigorodsky, Molecular Crystals and Molecules. New York: Academic Press, 1973.

[229] A.L. Rohl, M. Moret, W. Kaminsky, K. Claborn, J.J. Mckinnon, B. Kahr, Cryst. Growth Des. 8 (2008) 4517–4525.

[230] J.J. Koenderink, A.J. van Doorn, Image Vision Comput. 10 (1992) 557–564.

Chapter 2

Quantitative investigation of a mixed-ligand Co(III) complex

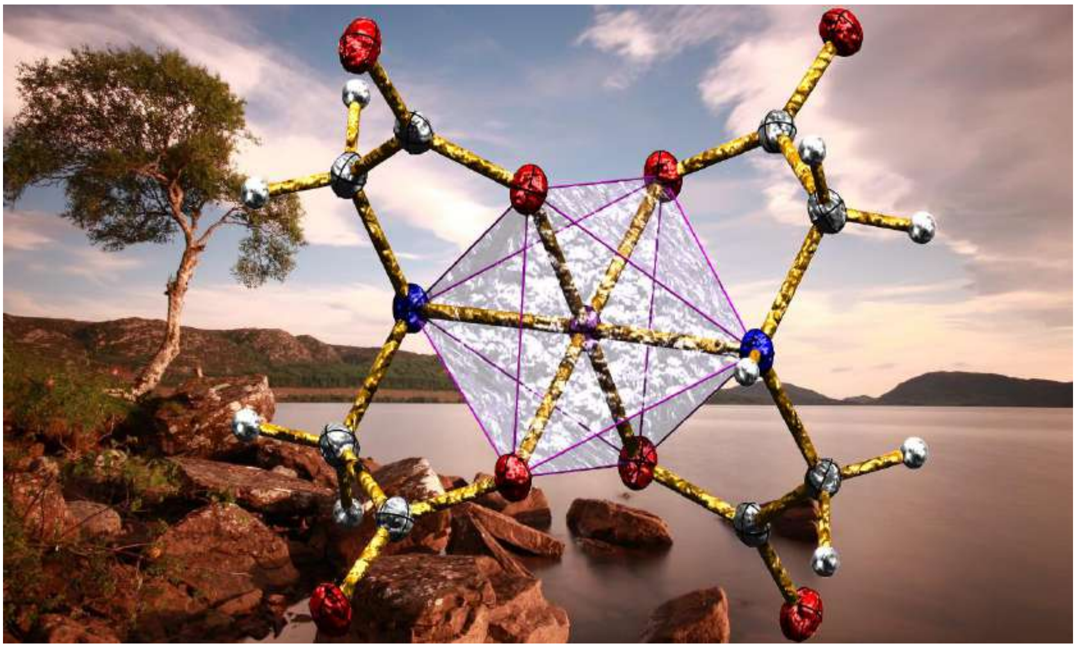

Published in: *Journal of Molecular Structure* 1216 (2020) 128207

2.1. Introduction

In crystal engineering, self-assembly is the essential molecular recognition process that deals with the control over the organization of molecular moieties in solid-state [1,2]. Crystals are assembled in spontaneous process that proceeds through a series of molecular recognition events. A recognition event among the molecular moieties is the outcome of the mutual interaction through several forces that are in operation. Therefore, the study and detail understanding of noncovalent forces are essential for the development of different applications in supramolecular chemistry [3,4]. Nevertheless, engineering supramolecular architecture is problematic due to the subtle nature of the noncovalent interactions [5]. Supramolecular chemistry relies on weak noncovalent interactions and the interactions involving aromatic systems are extremely significant due to their colossal influence in chemical and biological processes [6,7]. Hydrogen bonds and π–π stacking interactions are two vital adhesive and cohesive forces in the crystal structures of small molecules. Various weak dispersive π-interactions including C–H···π [8-10], π-stacking [11-14], anion···π [15-18] and lone pair···π [19,20] interactions have been widely used in building various supramolecular architectures. However, π^+–π and π^+–π^+ stacking interactions are much stronger than conventional π–π interaction [13, 14, 21-23]. These interactions are quite different in terms of their magnitude and directionality. The proper understanding of these interactions and their cooperativity are extremely important not only for rationalizing the solid-state networks but also to predict new supramolecular architectures.

Iminodiacetic acid (H_2IDA) is a promising candidate in coordination chemistry, since it is a tridentate ligand bearing imino and carboxyl electron-donating groups that could bind mono or multiple metal ions to exhibit structural diversity in the solid-state [24-26]. The carboxylic acid protons of iminodiacetic acid dissociate to give iminodiacetato dianion that reacts with metal ions to form diverse metal iminodiacetate complexes. X-ray structures of the ternary complexes with iminodiacetato as primary and N-donors as secondary ligands have been a subject of continuous investigation in the context of crystal engineering due to its variety of supramolecular structures.

In continuation of our previous work [19, 27-29], prompted by the supramolecular behavior of the M-IDA complexes, it was contemplated to design synthesis of mixed-ligand 5-ethyl-2-methylpyridinium trans-bis(iminodiacetato-k^3O,N,O′)cobaltate(III) complex and to explore its solid-state structure in detail. The structural description have been corroborated with theoretical calculations and the intermolecular interactions have been quantified by Hirshfeld surface analysis. The noncovalent interactions have been further characterized by using the Bader's theory of "atoms in molecule" (AIM) and "noncovalent interaction" (NCI) plot.

2.2. Experimental sections

2.2.1. Materials

The reagents Cobalt(II) chloride hexahydrate, Iminodiacetic acid and 5-ethyl-2-methylpyridine were readily available from commercial sources (Sigma-Aldrich, India) and used as received without further purification.

2.2.2. Synthesis

$CoCl_2.6H_2O$ (0.238g, 1 mmol) was reacted with iminodiacetic acid (0.266 g, 2.0 mmol) in water (25 mL) nearly at 60°C until a clear solution resulted in open glassware. A warm (~40°C) methanolic solution (15 mL) of 5-ethyl-2-methylpyridine (0.363 g, 3mmol) was added dropwise to the above solution. The mixture was stirred for 1h at 60°C, then stirred for 2h at normal laboratory temperature (~30°C), and then filtered. The dark-red filtrate was kept undisturbed at ambient temperature and covered with paraffin film and a few small holes were made using a needle to allow the solvent evaporate slowly. After 6-7 weeks, dark-red colored; block shaped single crystals of the title complex was formed. Anal. Calcd. for $C_{16}H_{22}CoN_3O_8$ (MW = 443.257 and melting point = 304ºC): C, 43.35; H, 4.99; N, 9.47%. Found: C, 43.31; H, 4.95; N, 9.51%. Main IR absorption bands observed for **1** (KBr pellet, cm^{-1}, Figure 2.1): 3181(S), 3041(s), 2969(s), 1644(s), 1610(s), 1468(s), 1437(s), 1381(s), 1358(s), 1313(s), 1297(s), 1248(s), 1156(s), 1126(s), 1069(s), 1029(s), 1000(s), 964(s), 917(s), 898(s), 880(s), 784(s), 761(s), 725(s), 645(s), 613(s), 595(s), 565(s), 534(s), 516(s), 455(s), 441(s). ^{1}H NMR (DMSO-d$_6$, 300 MHz, Figure 2.2) δ in ppm: 8.69-8.74 (m, 2H), 8.61 (s, 2H), 8.26 (d, 1H), 7.75 (d, 1H), 3.13 (d, 8H), 2.72 (q, 2H), 2.62 (s, 3H), 1.20 (t, 3H).

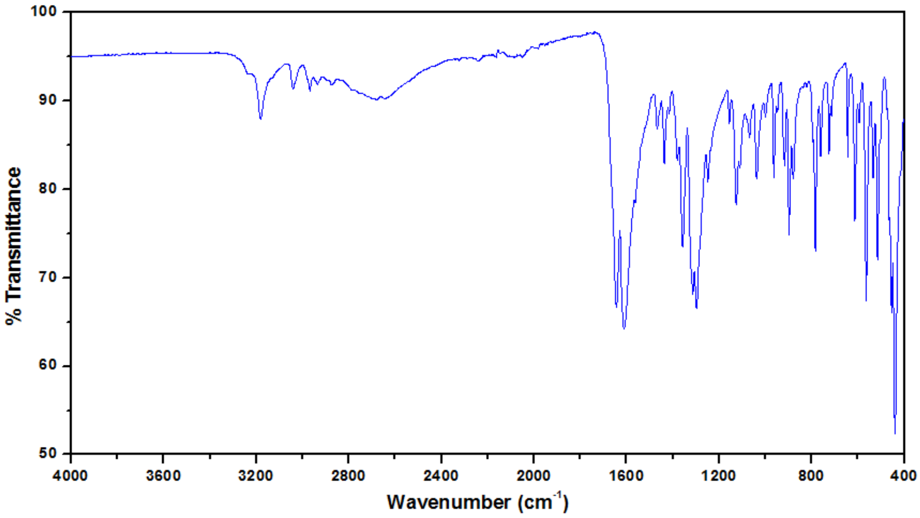

Figure 2.1. IR spectrum of the title complex.

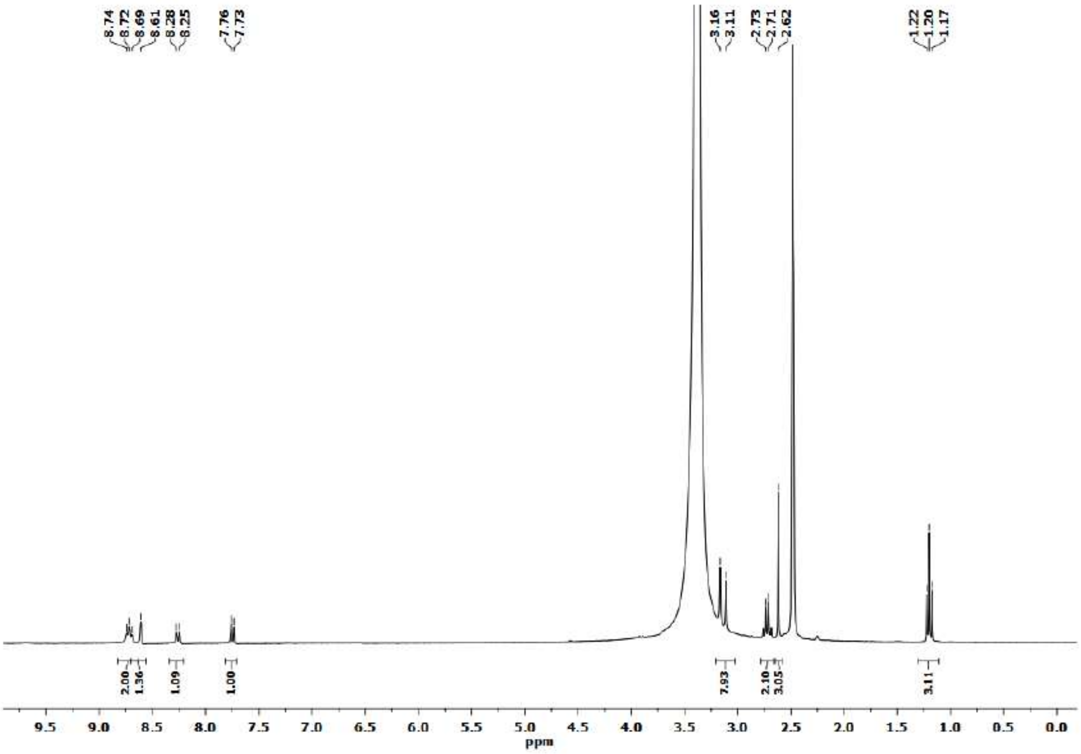

Figure 2.2. ^{1}H NMR spectrum of the title complex.

2.2.3. *X-ray crystal structure determination*

Single crystal X-ray diffraction intensity data of the title complex was collected at 150(2) K using a Bruker APEX-II CCD diffractometer equipped with graphite monochromated MoKα radiation (λ = 0.71073 Å). Data reduction was carried out using the program Bruker SAINT [30] and an empirical absorption correction was applied based on multi-scan method [31]. The structure of the title complex was solved by direct method and refined by the full-matrix least-square technique on F^2 with anisotropic thermal parameters to describe the thermal motions of all non-hydrogen atoms using the programs (SHELXS-14) [32] and (SHELXL-18) [33], respectively. All hydrogen atoms were placed at their geometrically idealized positions and refined isotropically. All calculations were carried out using WinGX system V2014.1 [34] and PLATON [35]. The summary of crystal data and relevant structure refinement parameters [36] are given in Table 2.1. CCDC 1945765 contains the supplementary crystallographic data.

2.2.4. *Hirshfeld surface analysis*

The Hirshfeld surface [37-40] of the title complex has been generated based on electron distribution of the molecule and are calculated as the sum of spherical atom electron densities [41,42]. Hirshfeld surface is distinctive for the investigating structure and a set of spherical atomic electron densities [43]. The normalized contact distance (d_{norm}) is based on d_e, d_i and the vd*W* radii of the atom. d_e and d_i are defined as the distance from the point to the nearest nucleus external and internal to the surface respectively. The 2D fingerprint plot provides summary of intermolecular contacts in the crystal [43-45]. The Hirshfeld surface analysis has been carried out using Crystal Explorer program [46].

Table 2.1. Crystal data and structure refinement parameters for the title complex.

Structure	(**1**)
Crystal data	
Empirical formula	$C_{16}H_{22}CoN_3O_8$
M_r	443.29
Crystal system, space group	Triclinic, $P\bar{1}$
Temperature (K)	150(2)
a, b, c (Å)	8.574(5), 10.010(3), 11.351(5)
α, β, γ (°)	105.040(2), 101.856(5), 91.557(3)
V (Å^3)	917.4(7)
Z	2
Radiation type	Mo $K\alpha$
μ (mm^{-1})	0.987
Crystal size (mm)	0.16 × 0.11 × 0.08
Data collection	
Diffractometer	Bruker *SMART APEX* II CCD area-detector
Absorption correction	Multi-scan, *SADABS*
$T_{\min}$, $T_{\max}$	0.88, 0.92
No. of measured, independent and observed [$I > 2\sigma(I)$] reflections	8645, 3207, 3038
R_{int}	0.019
$(\sin \theta/\lambda)_{\max}$ (Å^{-1})	0.595
Refinement	1
$R[F^2 > 2\sigma(F^2)]$, $wR(F^2)$, S	0.028, 0.082, 1.06
No. of reflections	3207
No. of parameters	255
H-atom treatment	H-atom parameters constrained
$\Delta\rho_{\max}$, $\Delta\rho_{\min}$ (e Å^{-3})	0.42, −0.37

2.2.5. *Theoretical methods*

We have performed the calculations for the wave function analysis by using Gaussian09 calculation package [47] at the B3LYP level with a large basis set 6-311++G(d,p). The crystallographic coordinates have been used for the theoretical analysis of the noncovalent interactions present in the solid state. The Bader's "Atoms in molecules" theory [48] has been used for analyzing the noncovalent interactions by means of the AIMall calculation package [49]. The topological properties of the charge density (ϱ(r)) is characterized by their critical points (CPs) and it's Laplacian. The Laplacian is expressed in terms of L(r) = $-\nabla^2$(ϱ(r)) that are calculated using the Atom In Molecule (AIM) theory [50]. The electron density is concentrated where ∇^2(ϱ(r))< 0 and it is depleted where ∇^2(ϱ(r)) > 0. The NCI plot [51] is a visualization index based on the electron density and its derivatives. The NCI plot isosurfaces have been used to characterize the noncovalent interactions. Since the isosurfaces represent the noncovalent interactions instead of critical points, it permits proficient visualization and identification. The isosurfaces correspond to both favorable and unfavorable interactions, as differentiated by the sign of the second density Hessian eigenvalue and defined by the isosurface color. The color scheme is a red-yellow-green-blue scale with red for ρ^{+}cut (repulsive) and blue for ρ^{-}cut (attractive) [52]. Yellow and green surfaces correspond to weak repulsive and weak attractive interactions, respectively.

2.3. Results and discussion

2.3.1. Structural description

The molecular structure of the title compound is shown in Figure 2.3 that comprised of one cationic moiety namely 5-ethyl-2-methylpyridinium and an anionic moiety namely *trans*-bis(iminodiacetato-*N,O,O′*)cobaltate(III). In the anionic moiety, the Co atom is coordinated by two different tridentate IDA ligands through their six donor (two nitrogen and four oxygen) atoms with a distorted octahedral geometry {CoN_2O_4}. The IDA ligands binds the metal ion in *fac*-chelating arrangement where two nitrogen atoms occupies *trans* positions. The Co–O bonding distances vary between 1.8777(14) and 1.9015(14) Å, while the Co–N bond lengths are 1.9283(16) and 1.9432(16)Å (Table 2.2). As expected, these bonding distances are in normal range and comparable to those in other Co(III) iminodiacetates reported earlier [53–56]. The rest bond distances are considered normal and correlate well with those reported compounds.

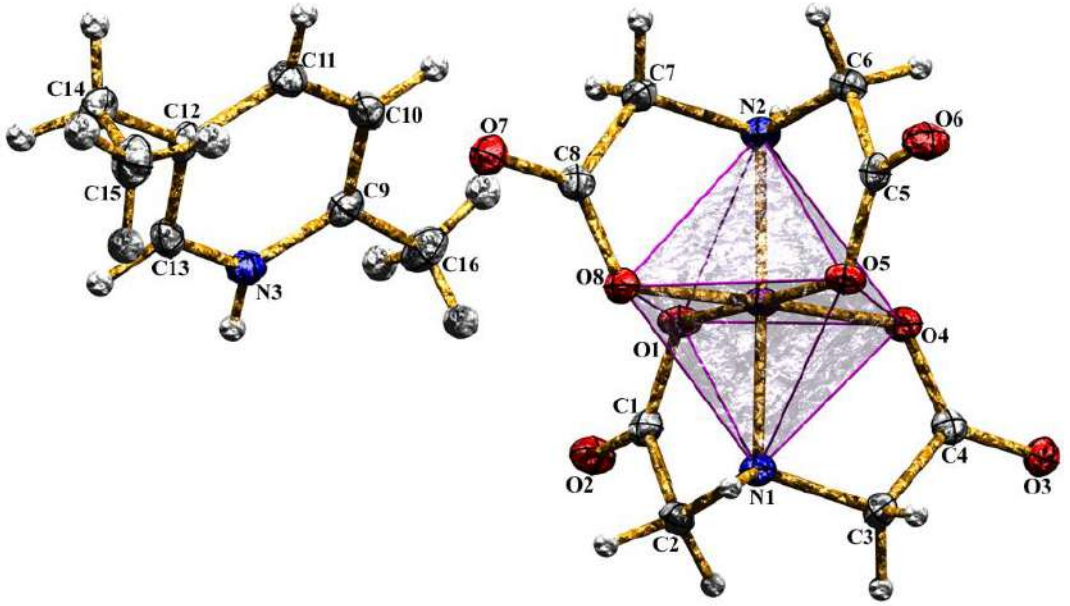

Figure 2.3. View of the asymmetric unit with atom numbering of the title compound. Displacement ellipsoids (Granite stone) are drawn at 30% probability.

The deviation around Co ion from octahedral geometry is noteworthy. The N–Co–O bond angles are the most distorted that varying between 86.53(6)° and 94.78(6)°, while the O–Co–O angles vary between 88.51(6)° and 92.09(6)°. The values of the trans bond angles O–Co–O and N–Co–N are 177.83(6)°, 178.41(6)° and 178.62(7)° (Table 2.2). In either five membered chelating rings Co1–O1–C1–C2–N1; Co1–O4–C4–C3–N1; Co1–O5–C5–C6–N2 and Co1–O8–C8–C7–N2, all atoms are almost coplanar with C2,N1; N1,C3; N2,C6 and C7,N2 have the largest deviations in opposite directions (Table 2.3) from the least-squares mean planes of the rings. The dihedral angles between the chelating rings (Co1–O1–C1–C2–N1; Co1–O4–C4–C3–N1) and (Co1–O5–C5–C6–N2; Co1–O8–C8–C7–N2) are 86.11(4) and 87.39(4), respectively.

In the solid state, compound (**1**) includes a combination of N–H···O, C–H···O hydrogen bonding, C–H···π and π–π stacking interactions (Tables 2.4, 2.5). In (**1**), the amino N1 atom of one IDA molecule at (x, y, z) acts as donor to the carboxylate oxygen O(5) atom of another IDA unit of the partner molecule at (2-x, -y, 2-z), so generating a centrosymmetric $R_2^2(8)$ dimeric ring (M) centered at (1, 0, 1) (Figure 2.4). Similarly, another amino N2 atom binds the carboxylate oxygen atom of the other IDA moiety in the molecule at (2-x, 1-y, 2-z) that generates another centrosymmetric $R_2^2(8)$ dimeric ring (N) centered at (1, ½, 1). The two types of $R_2^2(8)$ dimeric rings are alternately linked into infinite MNMNMN… chain that propagating along [010] direction (Figure 2.4). In between two parallel MNMN… chains, the cationic moieties are juxtaposed through C–H···π and π–π stacking interactions. The methyl carbon C(15) of the cationic unit in the molecules at (x, y, z) acts as donor to the centroid of the pyridine ring at (1-x, -y, 1-z) with a separation distance of 2.91Å, thus generating a centrosymmetric dimeric unit. In either side of the dimeric unit, the pyridine rings of the molecule at (x, y, z) and (1-x, 1-y, 1-z) are anti-parallel, with an interplanar spacing of 3.417(1)Å, and a ring centroid separation of 4.113(3)Å, corresponding to a ring offset of 2.289Å. The combination of C–H···π and π–π stacking interactions leads the molecules to generate an infinite chain along [010] direction (Figure 2.4). Finally, these anionic MNMN… chains and cationic chains are interconnected through N–H···O H-bond. The pyridine ring nitrogen N(3) atom from the cationic chain acts as donor to the carbonyl oxygen O(6) atom of the anionic chain at (x, y, -1+z), thus interconnects the two types of parallel chains by generating a two-dimensional supramolecular network in (011) plane (Figure 2.4).

Table 2.2. Selected bond lengths (Å) and bond angles (°).

Co(1)–O(1)	1.878(2)	Co(1)–O(5)	1.902(2)
Co(1)–O(4)	1.896(2)	Co(1)–O(8)	1.881(2)
Co(1)–N(1)	1.928(2)	Co(1)–N(2)	1.943(2)
O(1)–Co(1)–O(8)	92.09(6)	O(4)–Co(1)–N(1)	86.53(6)
O(1)–Co(1)–O(4)	88.86(6)	O(5)–Co(1)–N(1)	93.50(6)
O(8)–Co(1)–O(4)	177.83(6)	O(1)–Co(1)–N(2)	91.64(6)
O(1)–Co(1)–O(5)	178.41(6)	O(8)–Co(1)–N(2)	87.14(6)
O(8)–Co(1)–O(5)	88.51(6)	O(4)–Co(1)–N(2)	94.78(6)
O(4)–Co(1)–O(5)	90.58(6)	O(5)–Co(1)–N(2)	86.92(6)
O(1)–Co(1)–N(1)	87.96(6)	N(1)–Co(1)–N(2)	178.62(7)
O(8)–Co(1)–N(1)	91.56(6)		

Table 3.3. Distances of atoms of the chelate rings from the ring planes (Å).

Plane	Co distance	N distance	O distance	C (carboxylate) distance	C (methylene) distance
Co1–O1–C1–C2–N1	0.006(4)	-0.093(2)	-0.047(2)	0.006(2)	0.111(2)
Co1–O4–C4–C3–N1	-0.009(4)	0.208(2)	0.106(2)	-0.032(2)	-0.241(2)
Co1–O5–C5–C6–N2	-0.007(4)	0.126(2)	0.048(2)	0.016(2)	-0.171(2)
Co1–O8–C8–C7–N2	0.007(4)	-0.165(2)	-0.072(2)	-0.005(2)	0.218(2)

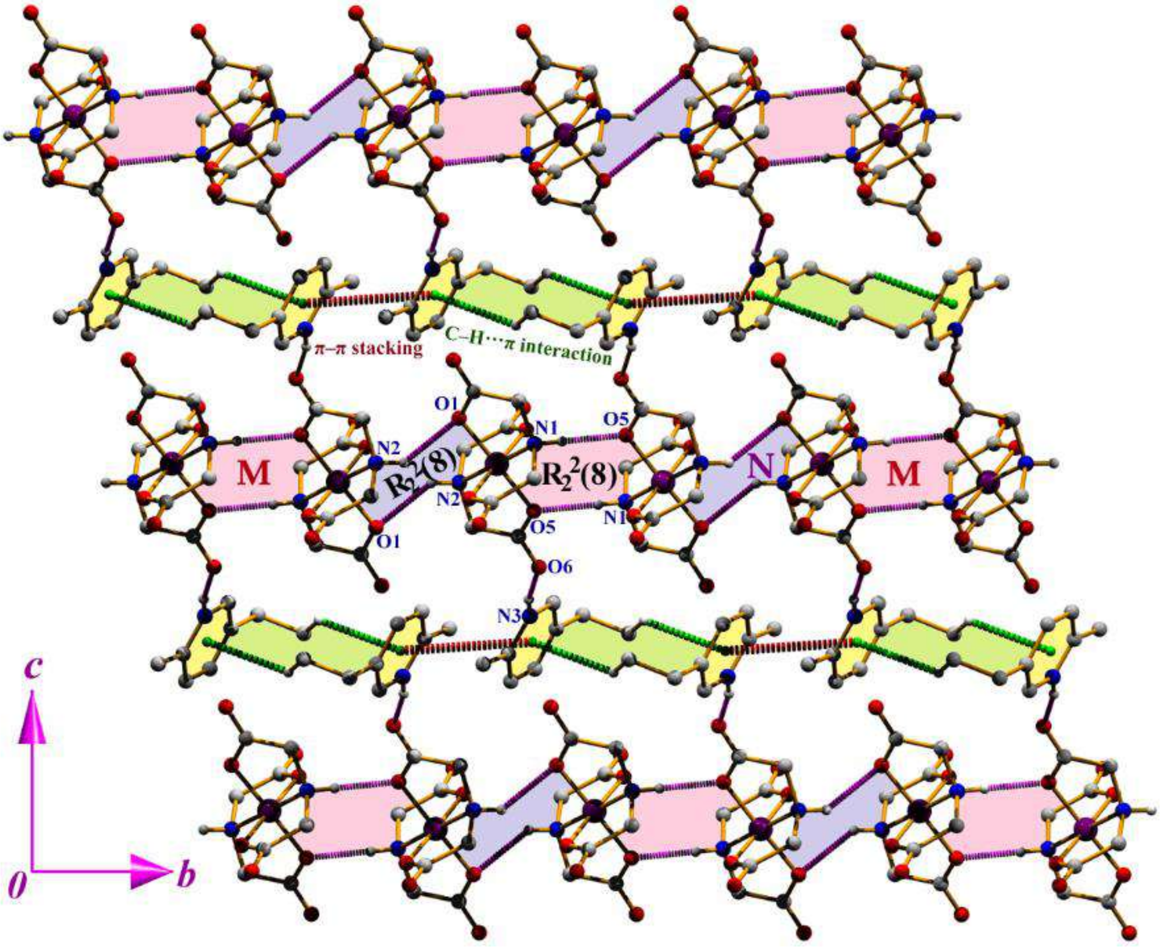

Figure 2.4. Perspective view of the supramolecular network in (011) plane.

Table 2.4. Hydrogen-bond geometry (Å, °).

D–H···A	D–H	H···A	D···A	D–H···A	Symmetry
N(1)–H(1)···O(5)	0.91	2.01	2.904(3)	168	2-x, -y, 2-z
N(2)–H(2)···O(1)	0.91	2.31	3.097(3)	144	2-x, 1-y, 2-z
N(2)–H(2)···O(4)	0.91	2.30	3.083(3)	144	2-x, 1-y, 2-z
N(3)–H(3)···O(6)	0.86	1.86	2.709(3)	167	x, y, -1+z
C(2)–H(2B)···O(7)	0.97	2.37	3.333(3)	172	1+x, y, z
C(3)–H(3B)···O(8)	0.97	2.51	3.399(3)	152	2-x, -y, 2-z
C(6)–H(6A)···O(3)	0.97	2.42	3.370(3)	167	-1+x, y, z
C(6)–H(6B)···O(2)	0.97	2.49	3.333(3)	145	2-x, 1-y, 2-z
C(10)–H(10)···O(3)	0.93	2.36	3.268(3)	165	2-x, 1-y, 2-z
C(11)–H(11)···O(2)	0.93	2.34	3.212(3)	156	-1+x, y, z
C(13)–H(13)···O(7)	0.93	2.46	3.275(3)	146	1-x, -y, 1-z
C(16)–H(16A)···O(2)	0.96	2.37	3.300(3)	162	---
C(15)–H(15A)···Cg(5)		2.91	3.563(3)	126	1-x, -y, 1-z

Cg(5) is the centroid of the pyridine ring.

Table 2.5. Geometrical parameters (Å, °) for π-stacking interactions.

Rings i–j	Rc	R1v	R2v	α	β	γ	Slippage
Cg(5)–Cg(5)$^{(i)}$	4.112(3)	-3.4170(8)	-3.4169(8)	0.0	33.82	33.82	2.289

[Symmetry codes: (i) (1-x, 1-y, 1-z)]. Cg(5) is the centroids of the pyridine (N3/C9–C13) ring.

Again, the weak C–H···O H-bonds also played significant role in building supramolecular assemblies. The carbon atoms C(2) and C(6) of the IDA unit acts as donor to the carbonyl oxygen atoms O(7) and O(3) in the molecules at (1+x, y, z) and (-1+x, y, z) respectively, therefore generating a dimeric $R_2^2(12)$ ring. These hydrogen bonds leads the molecules of the anionic moiety to propagate an infinite chain along [100] direction (Figure 2.5). The parallel infinite chains of the anionic moieties are further interacts with the cationic moieties. The pyridine ring carbon atom, substituted methyl carbon atom and ring nitrogen atom acts as donor to the carbonyl oxygen atoms of the anionic chain, thus generating a two-dimensional self-assembled network in (101) plane (Figure 2.5).

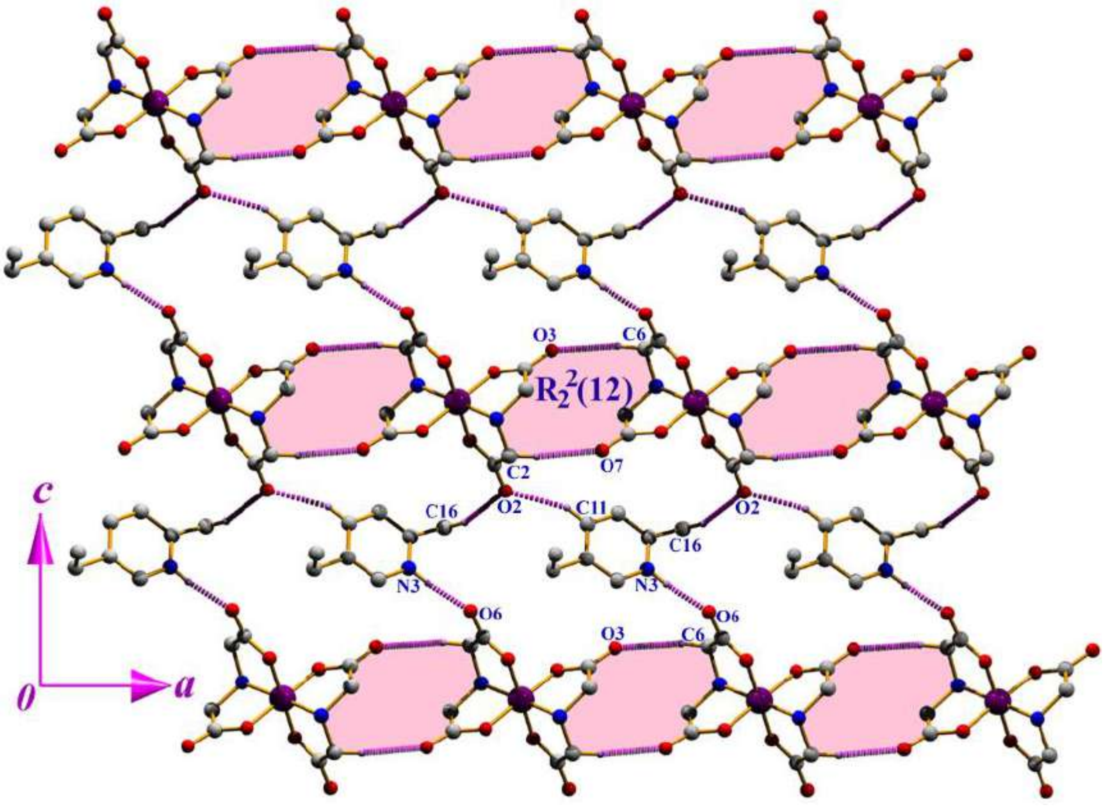

Figure 2.5. View of the self-assembly in (101) plane.

2.3.2. NMR spectroscopic observations and Bond Valence Sum (BVS) calculation

NMR spectroscopic analysis reveals that the complex contains diamagnetic Cobalt in 3+ oxidation state (Figure 2.2). Further, Bond Valence Sum (BVS) calculation was performed to establish the oxidation state of cobalt [57-58]. This calculation includes following equations:

$$s_{ij} = \exp[(r_o - r_{ij})/\mathrm{b}] \tag{1}$$

where, i = donor centre, j = metal centre, r_o = reported bond length between i and j, r_{ij} = the observed bond length, s_{ij} = the valence of a bond between two atoms i and j, and b is usually taken to be 0.37. The Pauling's valence sum rule (Pauling's second rule) is defined as

$$z_j = \sum_i Sij \tag{2}$$

where, z_j is the valence of atom j connecting i–j bonds with all neighbouring i atoms.

Table 2.6. Bond valence sum calculation and related parameters for complex (1).

i–j (reported)	r_o	*i–j* (complex **1**)	r_{ij}	s_{ij}	z_j
O^{2-}–Co^{3+}	1.637	O(1)–Co(1)	1.878(2)	0.521	3.052
O^{2-}–Co^{3+}	1.637	O(4)–Co(1)	1.896(2)	0.496	
O^{2-}–Co^{3+}	1.637	O(5)–Co(1)	1.902(2)	0.488	
O^{2-}–Co^{3+}	1.637	O(8)–Co(1)	1.881(2)	0.517	
N^{3-}–Co^{3+}	1.690	N(1)–Co(1)	1.928(2)	0.525	
N^{3-}–Co^{3+}	1.690	N(2)–Co(1)	1.943(2)	0.505	

From the BVS calculation, it is confirmed that complex (**1**) contain cobalt in 3+ oxidation state as the z_j value is around ~3. The slight deviation of the BVS from an integer value usually appears due to excessive thermal motion, possible steric constraints, and problems with the crystal structure report or some combination of all of these effects [59].

2.3.3. Hirshfeld surface

In this study, we have estimated the contribution of various available contacts that are contributed in the crystal packing. We have analyzed the Hirshfeld surface [37-39] of both anionic and cationic moieties separately and that are mapped with d_{norm}, shape-index, d_e and curvedness. The d_{norm} mapping (-0.6922 to 1.2777 Å) of the molecular aggregate is shown in Figure 2.6. The protuberant hydrogen-bonding interactions are clearly identified from the circular depressions (red spots) on the d_{norm} surface that are dominated by the strong N–H···O (carboxylate) hydrogen bonds. Fingerprint plots are the key tool for the quantification of the available intermolecular contacts and can be decomposed to quantify individual contributions of the interactions [43,44]. The O···H/H···O interactions in the anionic moiety are clearly evident by two distinct spikes in the region of (d_i=1.031Å; d_e=0.676Å) and (d_e=1.121 Å; d_i=0.771 Å) respectively that comprises 67.8% of the total Hirshfeld surface area (Figure 2.7). In contrast, there is no signature of the O···H interaction in the cationic moiety of the title complex.

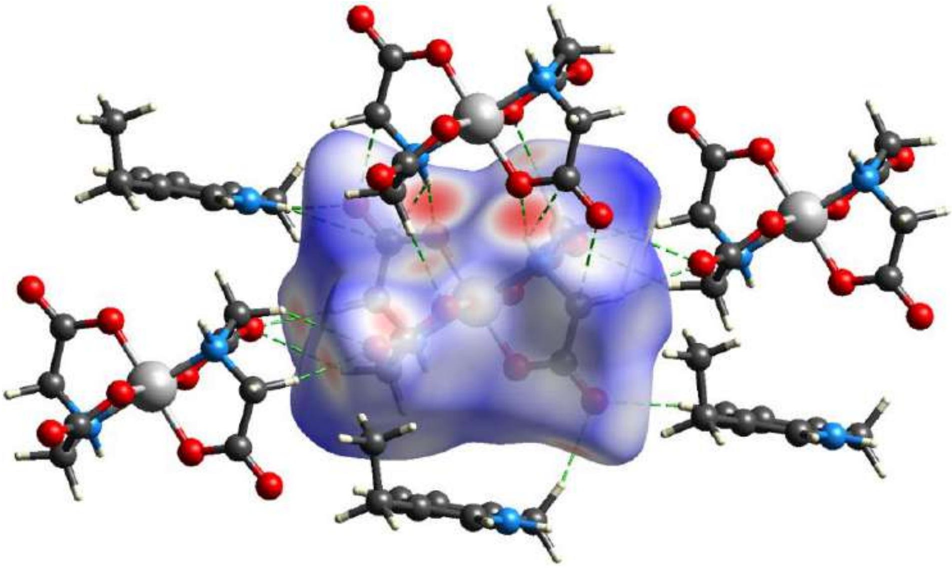

Figure 2.6. Hirshfeld surface mapped with d_{norm} for the anionic moiety illustrating the interactions with partner molecules through hydrogen bonding interactions (green dotted lines).

The only available spike in the region of (d_i = 0.681Å; d_e = 1.031Å) is for H···O contribution that comprises 30.7% to the total Hirshfeld surface area (Figure 2.8). The N···H/H···N contributions are visible in the fingerprint plot of the cationic moiety that are represented by the wings in the region of (d_i = 2.069Å; d_e = 1.232Å) and (d_e = 2.049 Å; d_i = 1.227 Å). The N···H contacts contributed more (1.9%) compare to the H···N counterpart (1.7%); consequently, the N···H/H···N contacts contributed 3.6% to the total Hirshfeld surface of the molecule (Figure 2.8). The C···H/H···C contacts are evident in the anionic moiety by the discrete spots as a spike that contributed 5.2% to the total Hirshfeld surface area (Figure 2.7) whereas the C···H/H···C contacts are distinctly evident by the wings in the donor and acceptor region (Figure 2.8) of the breakdown fingerprint plot. The wings in the region of (d_i = 2.063; d_e = 1.222) comprised 7.1% and the counterpart part H···C contact (d_i= 1.222; d_e = 2.068) comprises 7.7% and as whole the C···H/H···C contact comprised of 14.8% to the total Hirshfeld surface area of the cationic moiety (Figure 2.8).

As expected, the C–H···π interactions are clearly visible on the d_e and shape-index surfaces of the cationic moiety (Figure 2.9). The bright-orange depression above the π electron cloud of the pyridine ring and greenish-blue patch on the C–H donor site of the d_e surface are the indicator of C–H···π interactions (Figure 2.9a). The donors and acceptors of intermolecular C–H···π interactions are further recognized by the red and blue regions around the participating atoms of the π-cloud and C–H donor respectively, on the shape-index surface (Figure 2.9b).

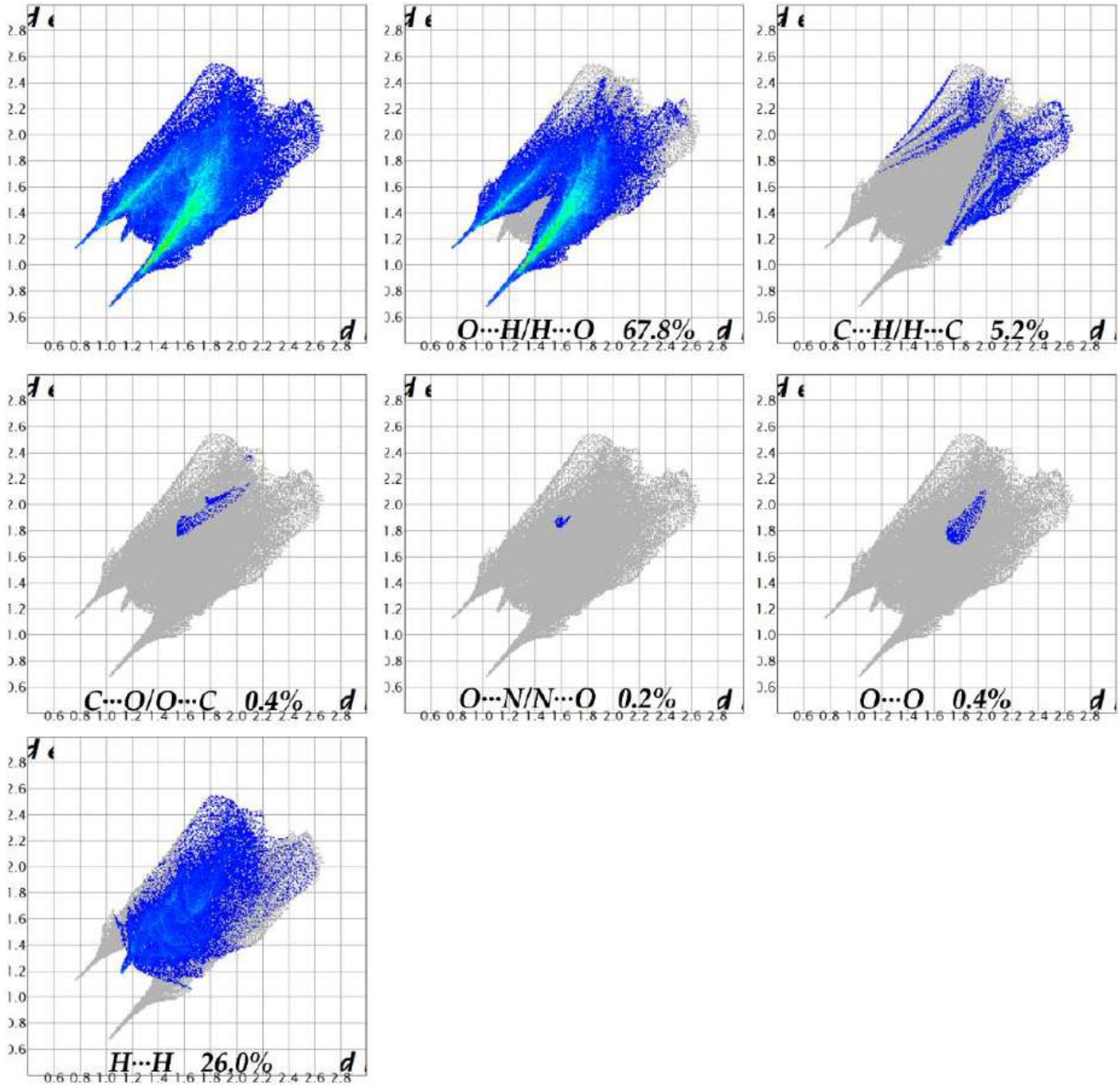

Figure 2.7. Fingerprint plot (Full) and resolved into various interaction of the anionic moiety of the title complex.

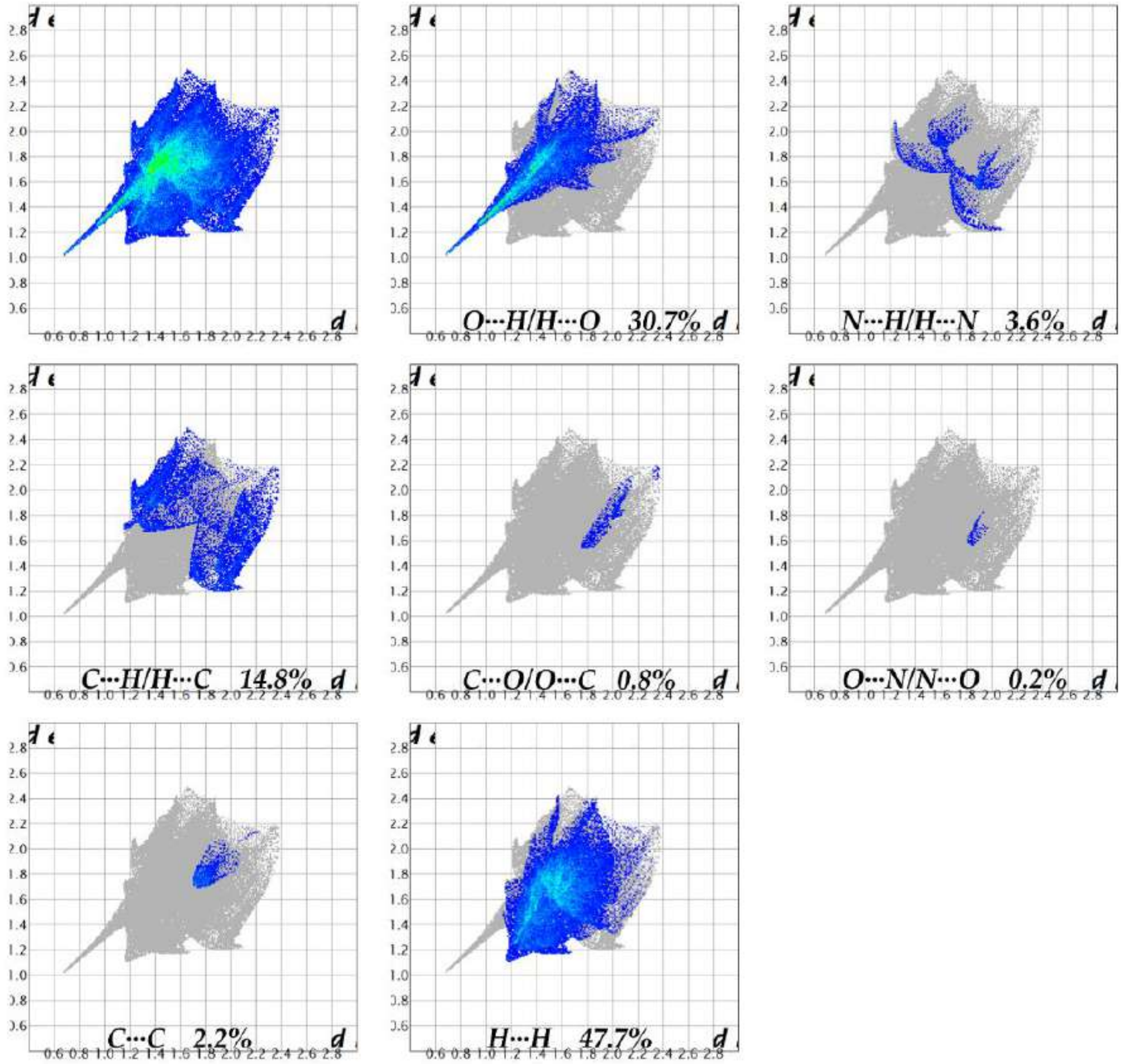

Figure 2.8. Fingerprint plot (Full) and resolved into various interaction of the cationic moiety of (**1**).

To examine the impact of π–π stacking interaction on the molecular packing, we have analyzed the Hirshfeld surface by mapping over shape-index and curvedness (Figure 2.9c-d). From the mapped Hirshfeld surfaces, it is clear that the protonated pyridine rings are related to one another through π–π stacking interaction. The π–π stacking between the rings is displayed by the red and blue triangles on the same region of the shape-index surface (Figure 2.9c). The blue triangle denotes the convex regions resulting from the pyridine ring of the molecule inside the surface, while the red triangle signifies concave regions caused by pyridine ring atoms of the π-stacked molecule above it. The pattern of the red-blue triangle characterizes the anti-parallel π-stacking interaction of the cationic moiety (Figure 2.9c). Moreover, the large flat region of the curvedness surface across the π-cloud of the pyridine ring of the cationic moiety further characterized the anti-parallel π-stacking interactions (Figure 2.9d). The fingerprint plot corresponding to π–π stacking is shown as a blue region on the diagonal at around $d_i = d_e = 1.708$ Å (Figure 2.8). All other available contacts are further quantified by the fingerprint plot and are depicted in Figures 2.7 and 2.8 for anionic and cationic moiety, respectively. A significant difference between the molecular interactions in terms of H···H contacts (Figures 2.7, 2.8) are reflected in the distribution of scattered points in the region ($d_i = 1.116$ Å, $d_e = 1.176$ Å) in anionic moiety and ($d_i = 1.161$ Å, $d_e = 1.111$ Å) in cationic moiety.

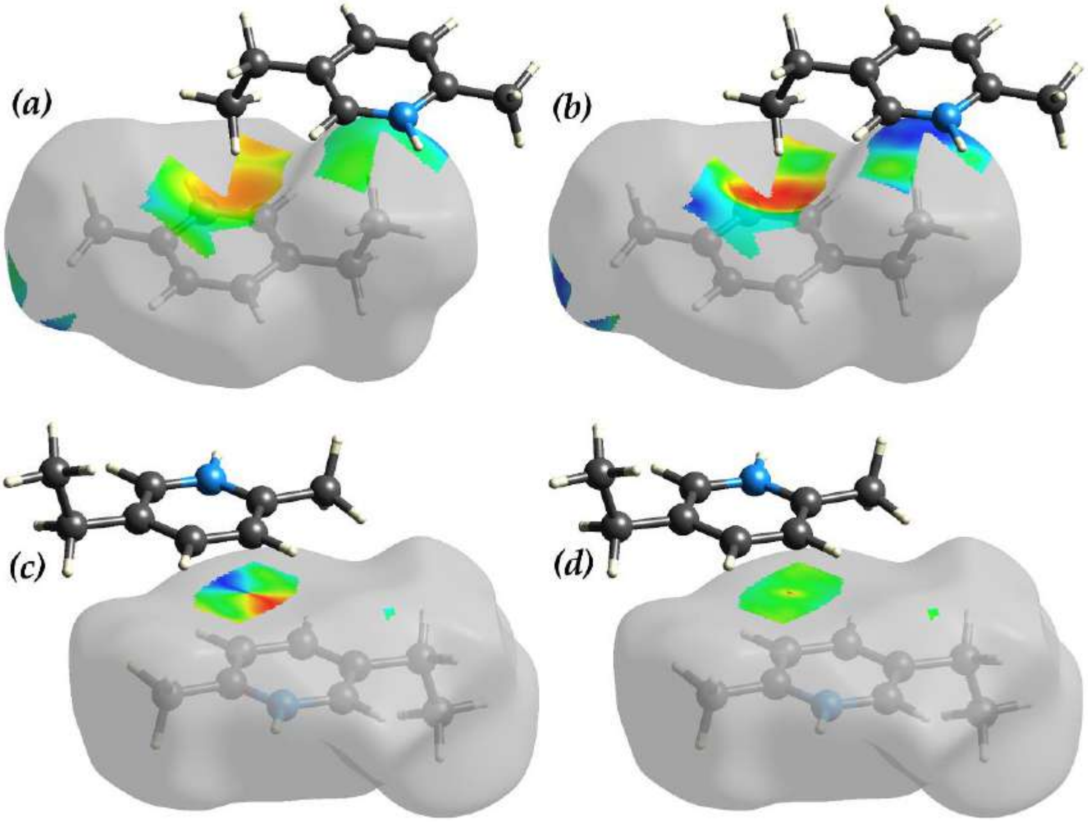

Figure 2.9. Perspective view of the decomposed Hirshfeld surface mapped with d_e (a) and shape-index (b) property illustrating C–H···π/π···H–C contacts. The Hirshfeld surface mapped with shape-index (c) and curvedness (d) property illustrating π–π stacking contacts in the crystal of the title complex.

2.3.4. *Theoretical analysis*

The Bader's theory of atoms in molecules (AIM) analysis [49] has been performed with the self-assembled dimeric units of the title compound. AIM analysis has been included for visualization and characterization of the noncovalent interactions that are involved within the structure through the distribution of bond critical points and the bond paths. The bond critical point (CP) and bond path that connects two atoms evidenced the existence of interaction between two atoms [48]. In Figure 2.10, we represent the distribution of CPs and bond paths of the several self-assembled networks of the title compound. In the first model of Figure 2.10, we used the molecular moiety of dimeric ring motif M (See Figure 2.4). The bond paths connecting the H atom of two amine nitrogen and the carboxylate oxygen atoms designate the N–H···O bonding interaction.

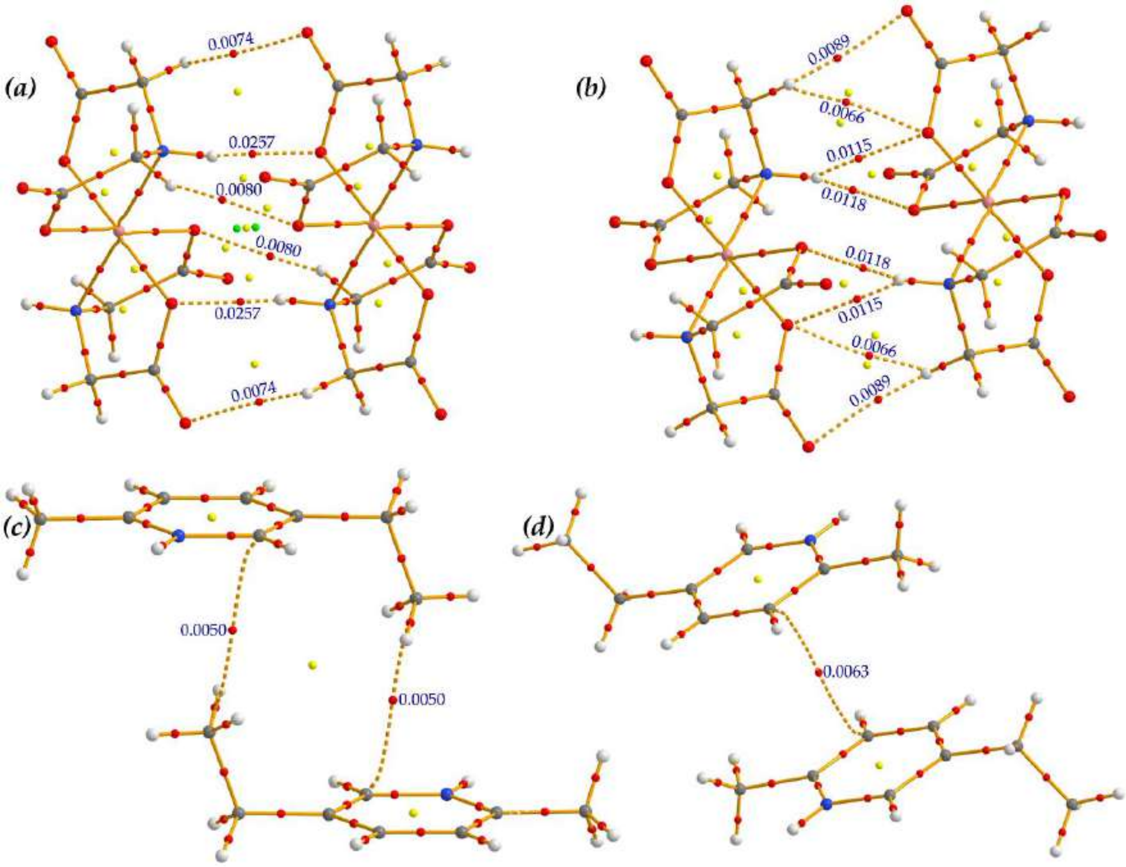

Figure 2.10. Distribution of the critical points of various self-assembled networks of the title compound (*a-d*). Red, yellow and green spheres represent bond, ring and cage critical points, respectively.

The ring CP that is presented by yellow sphere further characterize the dimeric ring M. Further, we analyzed the ϱ(r) values of the bond CPs to verify the strength of the interaction [50] that are included in Figure 2.10. The $\rho_{BCP} = 0.0094$ a.u. value characterize the N–H···O H-bonding (Figure 2.10a). Moreover, two different carbon atom from the IDA unit interacts with the carboxylate and carbonyl oxygen atom and are characterized by the bond paths and ρ_{BCP} values (0.0080 a.u. and 0.0074 a.u.). In model 2 (Figure 2.10b), the dimeric ring N (see Figure 2.4) is characterized by the bond path connecting the hydrogen atom of the parent amine nitrogen and carboxylate oxygen atom having ρ_{BCP} (0.0118 a.u.). It is noteworthy that the ϱ(r) values of the bond CPs for in centrosymmetric ring M is larger (0.0094 a.u.) in comparison to the N ring (0.0118 a.u.). Therefore, it can be concluded that the N–H···O hydrogen bonds that generates ring M are stronger that the N–H···O bond of ring N that is in agreement with the geometrical parameters of X-ray structure (Table 2.4). In model 3, we have analyzed the C–H···π interaction. The bond critical point and the bond path connecting the hydrogen atom of the methyl carbon and the pyridine ring carbon atom characterizes the C–H···π interaction where the ρ_{BCP} is 0.0050 a.u. (Figure 2.10c). The bond paths between two carbon atoms of the pyridine rings characterize the π–π interaction ($\rho_{BCPs} = 0.0063$ a.u.) (Figure 2.10d).

Finally, we further characterized the noncovalent interactions using NCI plot index computational tool [51,52]. It permits an easy assessment of host-guest complementarity and the extent to which weak interactions stabilize the investigating structure. In Figure 2.11, the NCI plot of the self-assembled structure (see Figure 2.4) of the title complex has been presented. Various noncovalent interactions are clearly evident by the green, blue isosurfaces. The two types of ring motif M and N that are formed by the strong N–H···O bonding are clearly observed by the blue isosurfaces between amine nitrogen and carboxylate oxygen of the anionic moiety. The weak C–H···O H-bonds are observed as small green isosurface between two anionic moieties. In the same figure, the cooperativity of the C–H···π and π–π interaction between cationic moieties are represented. The presence of dual large green isosurface between methyl hydrogen atom and π-cloud of the pyridine ring clearly designate the C–H···π interaction. The isosurface that characterizes the π–π interaction embraces the pyridine ring and the ethyl groups. The large region and the greenish-blue color on the isosurface indicates that the π–π interaction is stronger than the C–H···π interaction in agreement with the ϱ(r) values at the bond CPs mentioned above (see Figure 2.10). It is worth mentioning the existence of strong blue isosurfaces between the cationic and anionic layers. These strong blue isosurfaces between the protonated pyridine ring nitrogen atom and the carbonyl oxygen atom of the IDA ligand clearly shows how the cationic and anionic layers are interconnected through the N–H···O bonds.

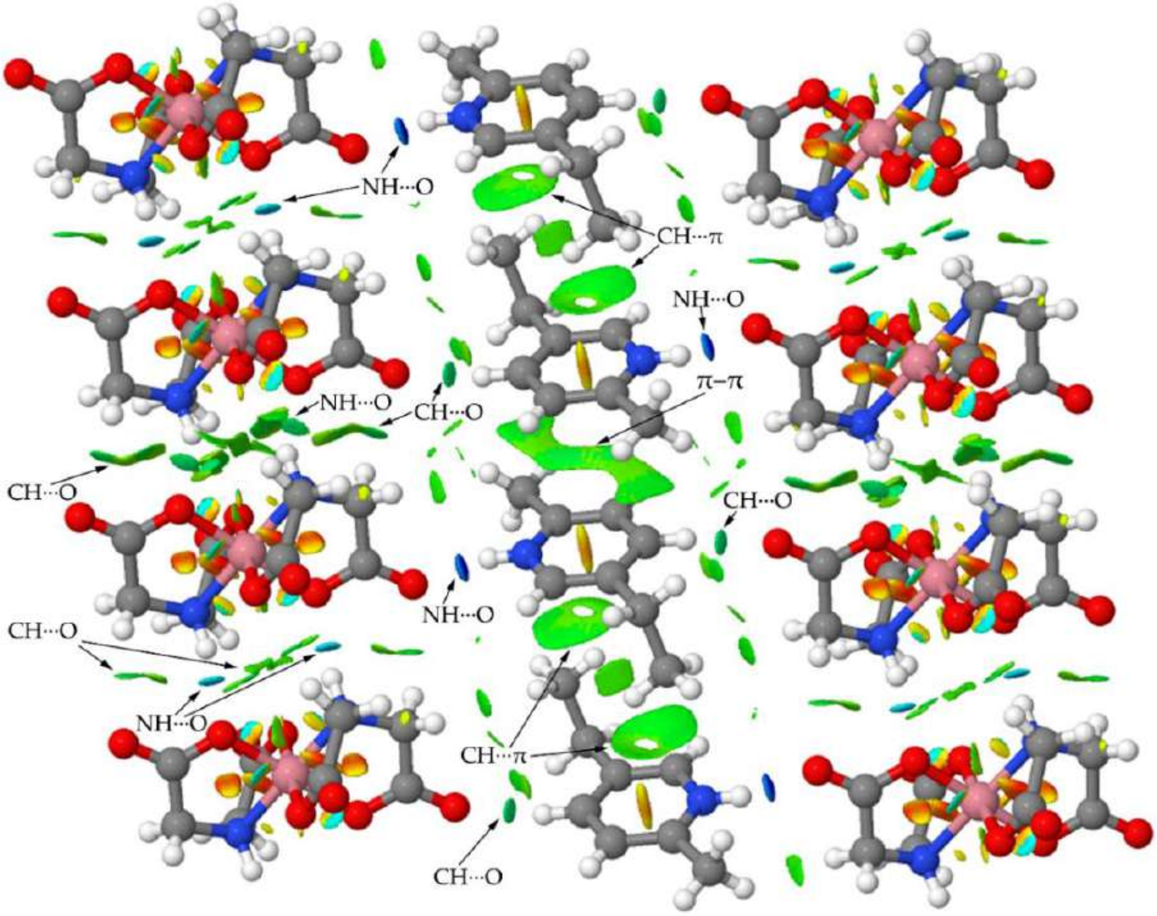

Figure 2.11. NCI plot of the self-assembly in (**1**). The gradient cut-off is s = 0.35 au, and the color scale is $-0.04 < \varrho < 0.04$ au.

2.4. Conclusions

In summary, a new octahedral mixed-ligand complex has been synthesized and structurally characterized. The cooperativity of weak noncovalent interactions in building supramolecular structures have been analyzed in detail and quantified by Hirshfeld surface analysis. Finally, these noncovalent interactions have been characterized theoretically by Bader's theory of "atoms-in-molecules" and also have been analyzed by NCI plot index. The computational study of energy framework, allowed us to estimate the topology of noncovalent interactions in the self-assembly. The theoretical investigations based on DFT functional, AIM and NCI analyses supports the experimental findings of the intricate combination of intermolecular interactions that characterized the studied complex. The results reported herein are expected to be useful for understanding of cooperativity effect of noncovalent interactions in the context of crystal engineering.

2.5. References

[1] G.R. Desiraju, J. Am. Chem. Soc. 135 (2013) 9952–9967.

[2] N.H. Evans, P.D. Beer, Angew. Chem. Int. Ed. 53 (2014) 11716–11754.

[3] J.W. Steed, J.L. Atwood, *Supramolecular Chemistry*, Wiley, Chichester, 2nd edn, 2009

[4] J.L. Atwood, G.W. Gokel, L.J. Barbour, *Comprehensive Supramolecular Chemistry II*, ed. Elsevier, 2017.

[5] A. Bauza, S.K. Seth, A. Frontera, Coord. Chem. Rev. 384 (2019) 107–125.

[6] M.M. Watt, M.S. Collins, D.W. Johnson, Acc. Chem. Res., 46 (2012) 955–966.

[7] K.E. Riley, P. Hobza, Acc. Chem. Res. 46 (2012) 927–936.

[8] P. Seth, A. Bauzá, A. Frontera, C. Massera, P. Gamez, A. Ghosh, CrystEngComm 15 (2013) 3031–3039.

[9] S.K. Seth, J. Mol. Struct. 1070 (2014) 65–74.

[10] T. Maity, H. Mandal, A. Bauzá, B.C. Samanta, A. Frontera, S.K. Seth, New J. Chem. 42 (2018) 10202–10213.

[11] J.W.G. Bloom, S.E. Wheeler, Angew. Chem. Int. Ed. 50 (2011) 7847–7849.

[12] S.K. Seth, D. Sarkar, T. Kar, CrystEngComm 13 (2011) 4528–4535.

[13] S.K. Seth, P. Manna, N.J. Singh, M. Mitra, A.D. Jana, A. Das, S.R. Choudhury, T. Kar, S. Mukhopadhyay, K.S. Kim, CrystEngComm 15 (2013) 1285–1288.

[14] P. Manna, S.K. Seth, M. Mitra, A. Das, N.J. Singh, S.R. Choudhury, T. Kar, S. Mukhopadhyay, CrystEngComm 15 (2013) 7879–7886.

[15] A. Frontera, P. Gamez, M. Mascal, T.J. Mooibroek, J. Reedijk, Angew. Chem. Int. Ed. 50 (2011) 9564–9583.

[16] P. Manna, S.K. Seth, M. Mitra, S.R. Choudhury, A. Bauzá, A. Frontera, S. Mukhopadhyay, Cryst. Growth Des. 14 (2014) 5812–5821.

[17] P. Manna, S.K. Seth, A. Bauzá, M. Mitra, S.R. Choudhury, A. Frontera, S. Mukhopadhyay, Cryst. Growth Des. 14 (2014) 747–755.

[18] M. Mitra, P. Manna, A. Bauzá, P. Ballester, S.K. Seth, S.R. Choudhury, A. Frontera, S. Mukhopadhyay, J. Phys. Chem. B 118 (2014) 14713–14726.

[19] S.K. Seth, I. Saha, C. Estarellas, A. Frontera, T. Kar, S. Mukhopadhyay, Cryst. Growth Des. 11 (2011) 3250–3265.

[20] P. Manna, S.K. Seth, A. Das, J. Hemming, R. Prendergast, M. Helliwell, S.R. Choudhury, A. Frontera, S. Mukhopadhyay, Inorg. Chem. 51 (2012) 3557–3571.

[21] I. Geronimo, E.C. Lee, N.J. Singh, K.S. Kim, J. Chem. Theory Comput. 6 (2010) 1931–1934.

[22] A. Das, A.D. Jana, S.K. Seth, B. Dey, S.R. Choudhury, T. Kar, S. Mukhopadhyay, N.J. Singh, I.C. Hwang, K.S. Kim, J. Phys. Chem. B 114 (2010) 4166–4170.

[23] M.B. -Oliver, B.A. Baquero, A. Bauzá, A.G. -Raso, A. Terrón, I. Mata, E. Molins, A. Frontera, CrystEngComm 14 (2012) 5777–5784.

[24] M.P. Brandi-Blanco, J.M. Gonzalez-Perez, D.C. Lazarte, R. Carballo, A. Castinereiras, J. Niclos-Gutierrez, Inorg. Chem. Commun. 6 (2003) 270–273.

[25] I. Yousuf, M. Zeeshan, F. Arjmand, M.A. Rizvi, S. Tabassum, Inorg. Chem. Commun. 106 (2019) 48–53.

[26] S.-J. Liu, X.-R. Xie, T.-F Zheng, J. Bao, J.-S. Liao, J.-L. Chen, H.-R. Wen, CrystEngComm 17 (2015) 7270–7275.

[27] S.K. Seth, B. Dey, T. Kar, S. Mukhopadhyay, J. Mol. Struct. 973 (2010) 81–88.

[28] S.K. Seth, A. Bauza, A. Frontera, CrystEngComm 20 (2018) 746–754.

[29] S.K. Seth, Crystals 8 (2018) 455.

[30] Bruker, *SAINT*, Version 6.36a, Bruker AXS Inc., Madison, Wisconsin, USA, 2002.

[31] Bruker, *SMART*, Version 5.625 and *SADABS*, Version 2.03a, Bruker AXS Inc., Madison, Wisconsin, USA, 2001.

[32] G.M. Sheldrick, ActaCryst. A 64 (2008) 112–122.

[33] G.M. Sheldrick, ActaCryst. C 71 (2015) 3–8.

[34] L.J. Farrugia, J. Appl. Cryst. 45 (2012) 849–854.

[35] A.L. Spek, J. Appl. Crystallogr. 36 (2003) 7–13.

[36] M. Tahmasebi, M. Mirzaei, H. Eshtiagh-Hosseini, J. T. Mague, A. Bauzá, A. Frontera, Acta Cryst. C75 (2019) 469–477.

[37] M.A. Spackman, J.J. McKinnon, CrystEngComm 4 (2002) 378–392.

[38] J.J. McKinnon, D. Jayatilaka, M.A. Spackman, Chem. Commun. (2007) 3814–3816

[39] F.P.A. Fabbiani, L.T. Byrne, J.J. McKinnon, M.A. Spackman, CrystEngComm 9 (2007) 728–731.

[40] S.K. Seth, CrystEngComm 15 (2013) 1772–1781.

[41] M.A. Spackman, P.G. Byrom, Chem. Phys. Lett. 267 (1997) 215–220.

[42] J.J. McKinnon, A.S. Mitchell, M.A. Spackman, Chem.–Eur. J. 4 (1998) 2136–2141.

[43] J.J. McKinnon, M.A. Spackman, A.S. Mitchell, Acta Crystallogr. Sect. B 60 (2004) 627–668.

[44] A.L. Rohl, M. Moret, W. Kaminsky, K. Claborn, J.J. Mckinnon, B. Kahr, Cryst. Growth Des. 8 (2008) 4517–4525.

[45] S.K. Seth, Acta Cryst. E74 (2018) 600–606.

[46] M.J. Turner, J.J. McKinnon, S.K. Wolff, D.J. Grimwood, P.R. Spackman, D. Jayatilaka, M.A. Spackman, *CrystalExplorer17*; University of Western Australia, 2017.

[47] M.J. Frisch, G.W. Trucks, H.B. Schlegel, G.E. Scuseria, M.A. Robb, J.R. Cheeseman, G. Scalmani, V. Barone, G.A. Petersson, H. Nakatsuji, et al. *Gaussian 09*, Revision *C.01*; Gaussian, Inc.: Wallingford, CT, USA, 2009.

[48] R.F.W. Bader, Chem. Rev. 91 (1991) 893–928.

[49] T.A. Keith, AIMAll, Version 13.05.06; TK Gristmill Software: Overland Park, KS, USA, 2013.

[50] R.F.W. Bader, Atoms in Molecules, a Quantum Theory; Oxford University Press: New York, NY, USA, 1990.

[51] J. Contreras-García, E.R. Johnson, S. Keinan, R. Chaudret, J.P. Piquemal, D.N. Beratan, W. Yang, J. Chem. Theory Comput. 7 (2011) 625–632.

[52] E.R. Johnson, S. Keinan, P. Mori-Sanchez, J. Contreras-Garcia, A.J. Cohen, W. Yang, J. Am. Chem. Soc. 132 (2010) 6498–6506.

[53] P.C. Junk, M.K. Smith, J. Coord. Chem. 55 (2002) 1091–1096.

[54] Q.-Z. Zhang, X. He, Y.-Q. Yu, S.-M. Chen, C.-Z. Lu, Z. Anorg. Allg. Chem. 631 (2005) 798–802.

[55] X-L. Gao, L-P Lu, M-L Zhu, Acta Cryst. E65 (2009) m561.

[56] Q.-Z. Zhang, C.-Z. Lu, W.-B. Yang, J. Coord. Chem. 59 (2006) 837–844.

[57] I. D. Brown, D. Altermatt, Acta Crystallogr. B 41 (1985) 244−247.

[58] H. H. Thorp, Inorg. Chem. 31 (1992) 1585−1588.

[59] T. Basak, K. Ghosh, C. J. Gómez-García, S. Chattopadhyay, Polyhedron 146 (2018) 42−54.

Chapter 3

Bipolar behaviour of salt-bridges: a combined theoretical and X-ray study

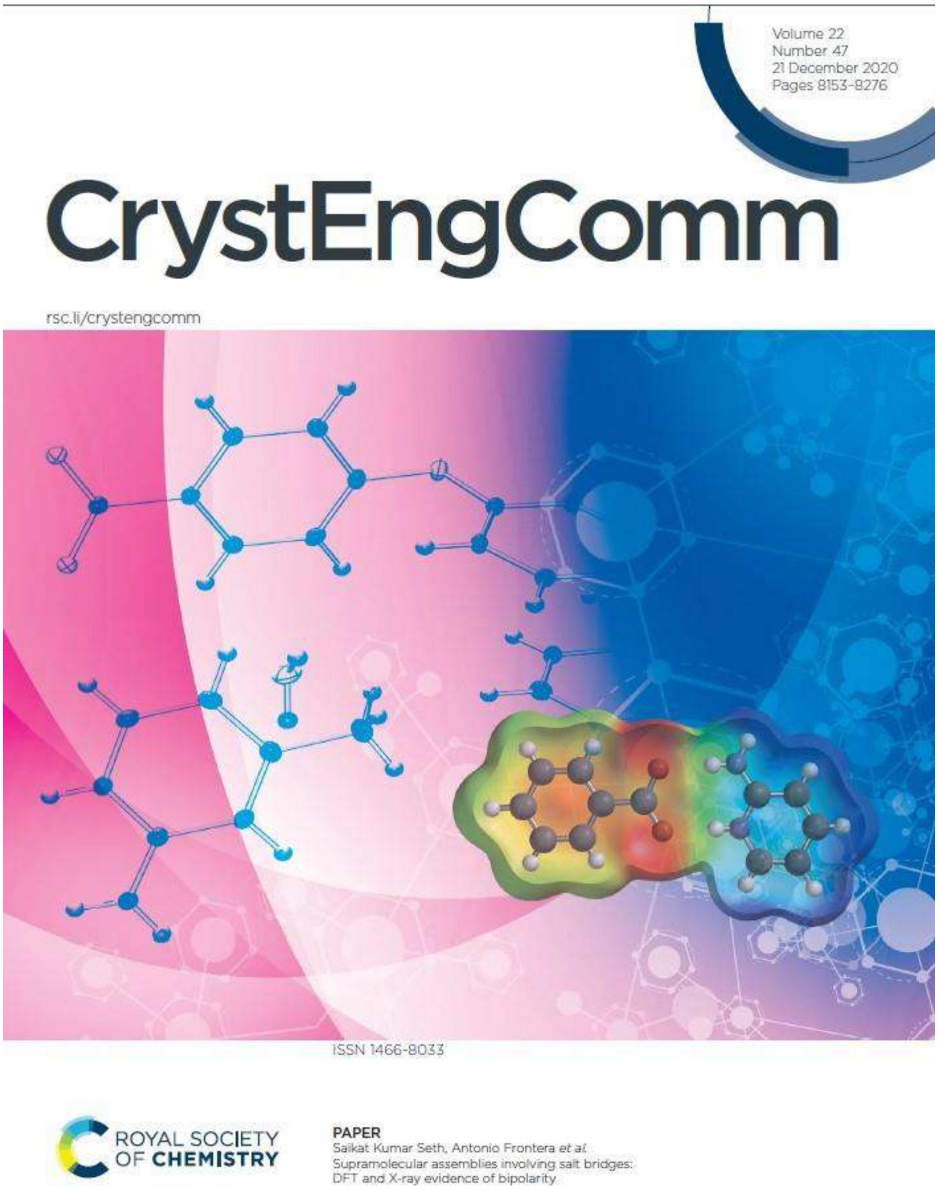

Volume 22
Number 47
21 December 2020
Pages 8153-8276

CrystEngComm

rsc.li/crystengcomm

ISSN 1466-8033

ROYAL SOCIETY OF CHEMISTRY

PAPER
Saikat Kumar Seth, Antonio Frontera *et al.*
Supramolecular assemblies involving salt bridges: DFT and X-ray evidence of bipolarity

Published in: *CrystEngComm* 22 (2020) 8153-8153

Published as Front Cover Page: 10.1039/D0CE90171G

3.1. Introduction

The challenge of a systematic and thorough bulk analysis of factors directing packing geometry of solid crystalline materials was raised by Desiraju over two decades ago [1]. The packing persuading features are described by strong and classic intermolecular interactions. To predict the actual crystal structure, precise understanding and complete control over the interplay of intermolecular interactions is required [2-4]. Therefore, accurate relationship between crystal packing structures, in addition to molecular structures are essential for structural design. Weak noncovalent forces direct the formation of self-assembled supramolecular networks. The noncovalent forces like C–H···π [5], π···stacking [6-9], cation···π [10], anion···π [11-14], and lone pair···π [15-18] interactions are prominent binding forces that have been used successfully to build solid-state networks [19]. Apart from these weak noncovalent interactions, hydrogen bonding plays a crucial role in crystal engineering due to specific, highly directive and relatively strong interactions [20]. The driving force that is predominant in the formation of synthon is hydrogen bonding and the supramolecular synthon serves as backbone of the crystal structure by providing articulate explanation of the entire structure [21].

The salt bridge (SB) can be defined as an interaction between two groups of opposite charge where the protonated and deprotonated residues interact directly [22-24]. Therefore, salt bridges are hydrogen bonded ion pairs, which are important for the stabilization of the molecular conformations. The hydrogen bonding of the SBs shows stronger binding compared to the normal hydrogen bonding interactions due to the zwitterionic charges (charge assisted hydrogen bond) [25]. The formation of salt-bridge is one of the significant noncovalent interactions that has been used to construct self-assembled structures in organic solvents [26, 27]. In protein chemistry, SBs played a crucial role in substrate bonding, activity of catalytic triads, secondary-structure stabilization and stability of thermophilic proteins [28, 29]. To generate new supramolecular systems [30, 31], intermolecular salt bridges are often used while biological systems such as proteins often comprise SBs that control their structure and function [32]. However, due to the geometric constraints placed by the electrostatic and H-bonding interactions, predicting SB interactions remains uniquely challenging.

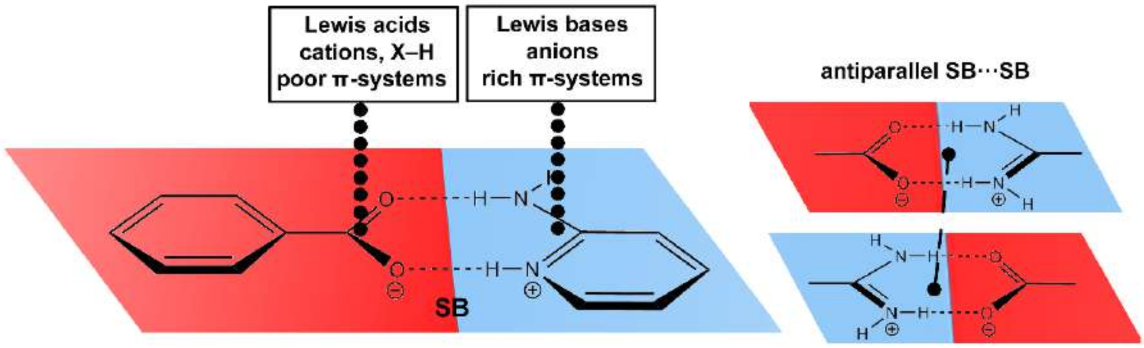

Scheme 3.1. Dual character of salt bridges (negative part in red and positive part in blue) and some of the interactions described herein.

We are particularly interested to explore the associative network structures involving salt-bridge. The influence of salt-bridges on cation-π interaction had been investigated by computational analysis and synthetic studies [33, 34]. However, a comprehensive study of the interaction between a planar salt-bridge and aromatic rings and cooperativity of other noncovalent forces with SBs are not well explored. As depicted in Scheme 3.1, the SBs are very rich as binding motif due to its dual character that makes it adequate for establishing a great deal of noncovalent interactions. As a matter of fact, we reported salt-bridge(SB)···π interaction by providing both experimental evidence and theoretical calculations [35]. Herein, we analyze salt-bridge interaction of three salts and their self-assembled structures involving charged aromatic ring and other noncovalent interactions, by means of experimental and theoretical calculations. The structural analyses of these compounds revealed the formation of completely new and extended supramolecular networks by the formation of salt-bridge interactions. The unique combinations of weak forces in building the extended networks [lone-pair(l.p)···(SB)/(SB)···π^+ in (**1**), C–H···(SB)/(SB)···π in (**2**) and

$\pi^+\cdots$(SB)/(SB)$\cdots$(SB)/(SB)$\cdots\pi^+$ and C–H$\cdots$(SB)/(SB)$\cdots$H–C in (**3**)] are the first evidence of crystalline solids. The solid-state structure of these compounds are described in detail, including theoretical calculations. The binding energies of the networks have been calculated using theoretical DFT calculations and the noncovalent interactions have been analyzed by using Bader's theory of "atoms in molecules" (AIM).

3.2. Experimental sections

3.2.1. Materials

The reagents [4,4′-oxybis(benzoic acid), 2-amino-5-methylpyridine and 2-amino-4-methylpyridine)] and solvents [N,N-dimethylformamide (DMF), dimethyl sulfoxide (DMSO)] were purchased from commercial sources (Sigma-Aldrich, India) and used without further purification.

3.2.2. Syntheses

Compounds (**1–3**) were prepared by reacting stoichiometric amounts of 4,4′-oxybis(benzoic acid) molecule with substituted aminopyridine ligands. 4,4′-oxybis(benzoic acid) (0.258 g, 1.0 mmol) was dissolved in 20 ml of DMF for (**1–2**) and DMSO for (**3**) and heated at 50°C that resulting a clear solution. Then, 2.0 mmol (0.216 g) of 2-amino-5-methylpyridine, 1 mmol (0.108 g) of 2-Amino-4-methylpyridine and 2 mmol (0.216 g) of 2-amino-4-methylpyridine was added to 10 ml of water-methanol (1:1) for (**1–3**) respectively. These solutions were added drop wise to the acid solution with continuous stirring. The solution mixtures obtained were heated at 50°C for 1 h with continuous stirring. The resulting solutions were kept undisturbed at ambient temperature and covered with paraffin film and a few small holes were made using a needle to allow the solvent evaporate slowly. After 6–8 weeks, testable single crystals were grown.

3.2.3. *X-ray crystal structure determination*

Single crystal X-ray diffraction intensity data of the title compounds were collected at 150(2)K for (**1**) and 120(2)K for (**2–3**) using a Bruker APEX-II CCD diffractometer by using graphite monochromated MoKα radiation (λ = 0.71073 Å). Data reduction was performed by using the program Bruker SAINT [36] and empirical absorption correction was applied [37]. The structures were solved by direct method and refined by the full-matrix least-square technique on F^2 with anisotropic thermal parameters by describing the thermal motions of all non-hydrogen atoms using the programs SHELXS-14 [38] and SHELXL-18 [39], respectively. The hydrogen atoms were positioned from difference Fourier map and consequently refined isotropically. The calculations were performed using WinGX system V2014.1 [40] and PLATON [41]. The summary of crystal data and relevant structure refinement parameters for the title compounds are included in Table 3.1. CCDC 1831105–1831107 contain the supplementary crystallographic data of (**1–3**).

3.2.4. *Theoretical methods*

We have used the BP86-D3/def2-TZVP level of theory to compute the energies of the H-bonding interactions by means of the program TURBOMOLE version 7.0. [42]. The crystallographic coordinates have been used for the theoretical calculations. The binding energies were computed applying the correction for the BSSE (basis set superposition error) by means of the counterpoise technique developed by the Boys–Bernardi [43]. The AIMall calculation package [44] was employed to analyze the interactions studied using the Bader's "atoms-in-molecules" (AIM) theory [45]. The Molecular Electrostatic Potential (MEP) surfaces have been calculated using the SPARTAN10 program [46]. The calculations for the wavefunction analysis have been carried out at the BP86-D/def2TZVP level of theory using Gaussian-09 software [47].

Table 3.1. Crystal data and structure refinement parameters of (**1**–**3**).

Structure	**(1)**	**(2)**	**(3)**
Empirical formula	$C_{26}H_{28}N_4O_6$	$C_{20}H_{18}N_2O_5$	$C_{26}H_{28}N_4O_6$
Formula Weight	492.52	366.36	492.52
Temperature (K)	150(2)	120(2)	120(2)
Wavelength (Å)	0.71073	0.71073	0.71073
Crystal system	Monoclinic	Monoclinic	Triclinic
space group	C2/c	$P2_1/n$	P-1
a, b, c (Å)	13.864(11), 12.086(11), 14.994(12)	7.075(3), 19.857(2), 12.811(2)	6.855(4), 7.642(3), 24.281(4)
α, β, γ (°)	90, 111.62(2), 90	90, 94.991(2), 90	90.019(3), 2.555(2), 107.022(4)
Volume ($Å^3$)	2336(3)	1793.0(8)	1214.9(9)
Z / Density (calc.) (Mg/m^3)	4 / 1.401	4 / 1.357	2 / 1.346
Absorption coefficient (mm^{-1})	0.101	0.099	0.097
F(000)	1040	768	520
Crystal size (mm^3)	0.18 × 0.11 × 0.06	0.19 × 0.11 × 0.05	0.19 × 0.15 × 0.09
Limiting indices	$-16 \le h \le 16$, $-14 \le k \le 14$, $-17 \le l \le 17$	$-8 \le h \le 8$, $-23 \le k \le 23$, $-15 \le l \le 15$	$-8 \le h \le 8$, $-9 \le k \le 9$, $-28 \le l \le 28$
Reflections collected / unique	9037 / 2021 [R(int) = 0.0741]	20967 / 3155 [R(int) = 0.0363]	11530 / 4260 [R(int) = 0.0238]
Completeness to θ (%)	98.7	100.0	99.8
Absorption correction	Semi-empirical from equivalents	Semi-empirical from equivalents	Semi-empirical from equivalents
Max. and min. transmission	0.99 and 0.98	0.99 and 0.98	0.99 and 0.98
Refinement method	Full-matrix least-squares on F^2	Full-matrix least-squares on F^2	Full-matrix least-squares on F^2
Data/ parameters	2021 / 166	3155 / 245	4260 / 328
Goodness-of - fit on F^2	1.084	1.040	1.047
Final R indices [$I > 2\sigma(I)$]	$R_1 = 0.0494$, $wR_2 = 0.1320$	$R_1 = 0.0355$, $wR_2 = 0.0927$	$R_1 = 0.0339$, $wR_2 = 0.0910$
R indices (all data)	$R_1 = 0.0540$, $wR_2 = 0.1371$	$R_1 = 0.0435$, $wR_2 = 0.0995$	$R_1 = 0.0388$, $wR_2 = 0.0947$
Largest diff. peak and hole ($e.Å^{-3}$)	0.218 and -0.313	0.224 and -0.205	0.220 and -0.167

$R_1 = \sum||F_o|-|F_c||/\sum|F_o|$, $wR_2 = [\sum\{(F_o^2-F_c^2)^2\}/\sum\{w(F_o^2)^2\}]^{1/2}$, $w = 1/\{\sigma^2(F_o^2) + (aP)^2 + bP\}$, where a = 0.0845 and b = 0.6212 for (**1**), a = 0.0506 and b = 0.5361 for (**2**) and a = 0.0461 and b = 0.3636 for (**3**). $P = (F_o^2 + 2F_c^2)/3$ for all structures.

3.3. Results and discussion

3.3.1. Structural description

The ORTEP view of the title compounds (**1–3**) are shown in Figure 3.1. In compounds (**1**) and (**3**), 4,4′-oxybis(benzoic acid) is fully deprotonated with two 2-Amino-5-methylpyridinium and 2-Amino-4-methylpyridinium cations respectively with one solvent water molecule. However, in (**2**), the 4,4′-oxybis(benzoic acid) is partly deprotonated with one 2-amino-4-methylpyridinium cation. In (**1**), the oxygen atom O(3) lies on the inversion centre (-x+2, y, -z+1/2) and thus generates symmetric counterpart (see Figure 3.1a).

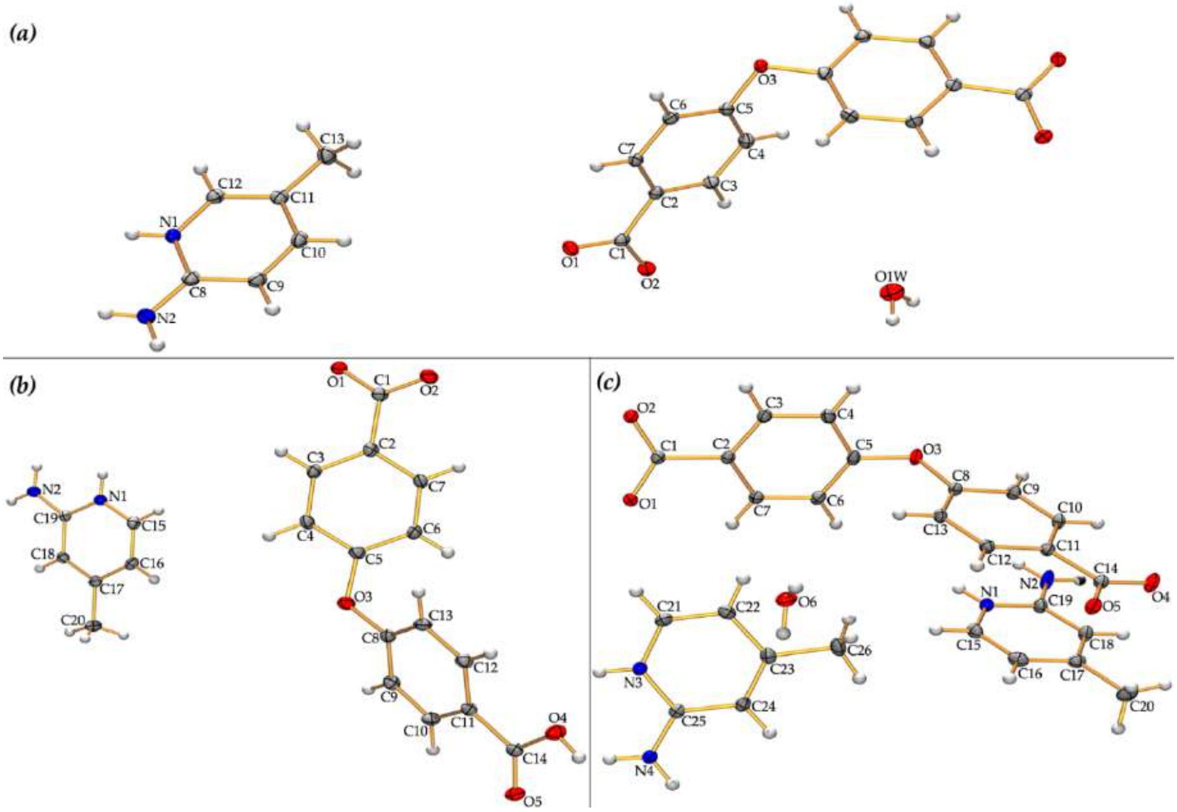

Figure 3.1. Molecular view (ORTEP) of the asymmetric unit of the title compounds (**1–3**) (a–c) with atom numbering scheme. In compound (1), the unlabelled counterpart has been generated through the symmetry operation (-x+2, y, -z+1/2). The thermal ellipsoids are drawn at 30% probability level.

In (**1**), the pyridinum and amine nitrogen atoms N(1) and N(2) act as donors to the carboxylate oxygen atoms at (½-x, -½+y, ½-z), thus forming a $R_2^2(8)$ dimeric ring that termed as salt-bridge (SB) (Figure 3.2) (Table 3.2). Two nearby dimeric rings are interconnected by further interaction in between amine nitrogen and carboxylate oxygen atoms. This hydrogen bond leads the molecules to form a $R_4^2(8)$ ring motif (Figure 3.2). Again the solvent water molecule acts as double donor to the carboxylate oxygen atom O(1) at (3/2-x, ½+y, ½-z); thus interconnects the ring motifs and leading to the formation of two-dimensional assembly in (101) plane (Figure 3.2). In another substructure, the aryl ring carbon atom C(6) acts as donor to the carboxylate oxygen atom O(2) in the molecule at (3/2-x, -½+y, ½-z) to form a two-dimensional anionic network in (110) plane (Figure 3.3).

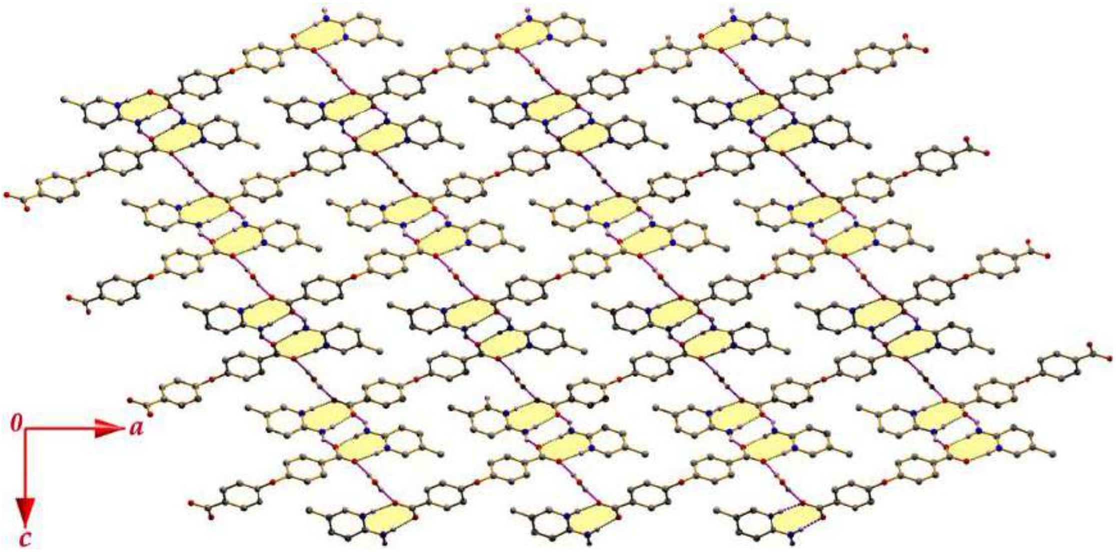

Figure 3.2. Supramolecular network in (101) plane of (**1**).

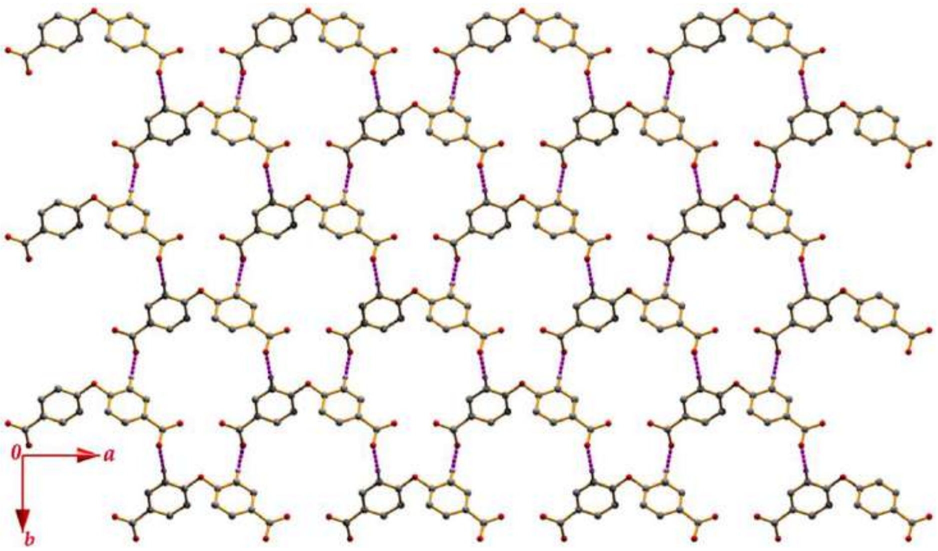

Figure 3.3. Network through C–H···O bond in (110) plane in (**1**).

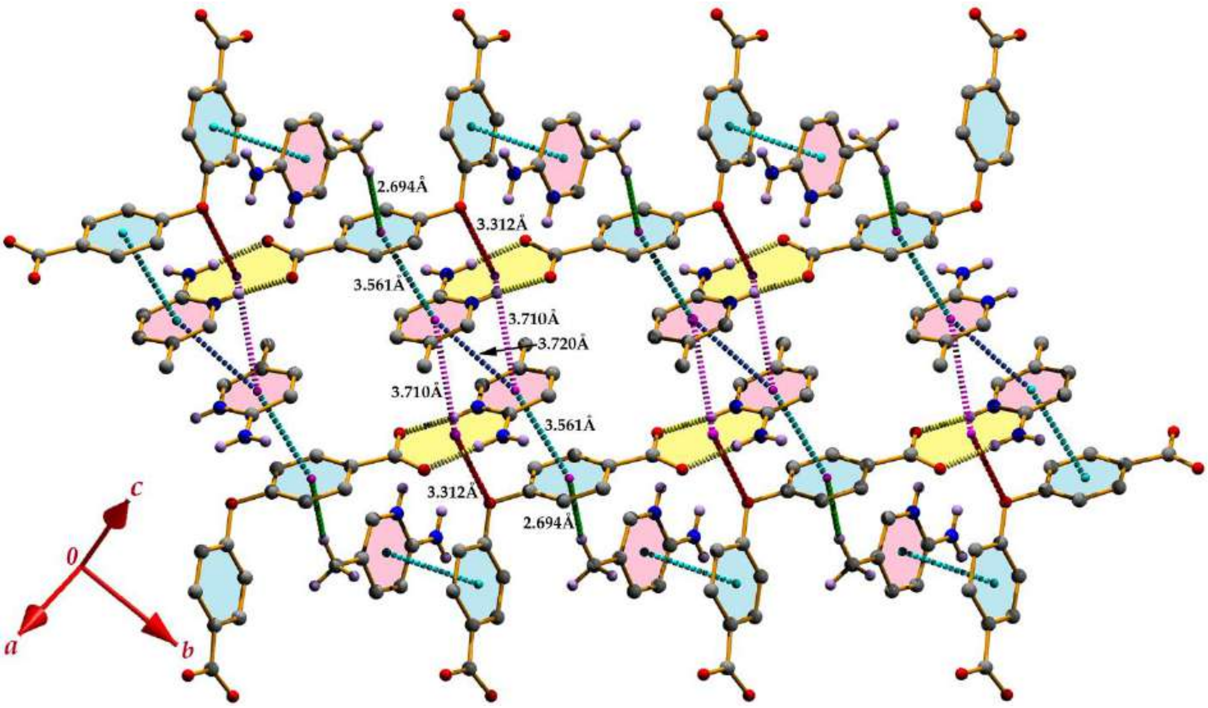

Figure 3.4. Perspective view of the extended lone-pair (l.p)···SB/SB···π^+ network in (**1**). The SB unit is highlighted by yellow colour whereas the π^+ and π moieties are shown by pink and turquoise colour respectively.

Interestingly, the lone-pair of the oxygen atom O(3) is oriented toward the salt-bridge unit with a separation distance of 3.312Å. In the opposite side, the π-face of the pyridinium moiety is juxtaposed to the SB unit with a separation distance of 3.710Å; thus, dual bridging of SB···π^+ network is observed where the two-pyridinium moieties are also optimized (Figure 3.4). The pyridine rings at (x, y, z) and (-x, -y, -z) are anti-parallel, with an interplanar spacing of 3.272Å, and a ring centroid separation of 3.720(3)Å, corresponding to a ring offset of 1.77Å. Thus a lone-pair (l.p)···SB/SB···π^+ is observed in (**1**) (Figure 3.4). Again, the pyridinium ring and aryl ring of the acid moiety is optimized further in the molecule at (1-x, y, ½-z) with a separation distance of 3.561(3)Å. Thus, the molecules of (**1**) generates an extended unique network lone-pair(l.p)···(SB)/(SB)···π^+ through SB unit (Figure 3.4).

Table 3.2. Relevant Hydrogen Bonding Parameters in (**1–3**).

D–H···A	D–H	H···A	D···A	D–H···A	Symmetry
Compound (1)					
N(1)–H(1)···O(1)	0.86	1.86	2.712(3)	173	1/2-x, -1/2+y, 1/2-z
N(2)–H(2A)···O(2)	0.86	1.90	2.762(3)	179	1/2-x, -1/2+y, 1/2-z
N(2)–H(2B)···O(2)	0.86	2.06	2.839(3)	150	-1+x, 1-y, -1/2+z
O(1w)–H(1w)···O(1)	0.82	2.00	2.813(3)	170	3/2-x, 1/2+y, 1/2-z
C(6)–H(6)···O(2)	0.93	2.49	3.404(3)	168	3/2-x, -1/2+y, 1/2-z
C(13)–H(13C)···Cg(1)	0.93	2.70	3.565(4)	150	-1/2+x, -1/2+y, z
Compound (2)					
N(1)–H(1)···O(3)	0.86	1.92	2.774(2)	172	-x, 1-y, 2-z
N(2)–H(2A)···O(4)	0.86	1.93	2.790(2)	174	-x, 1-y, 2-z
N(2)–H(2B)···O(3)	0.86	2.25	2.865(2)	129	1+x, 1+y, z
O(2)–H(2)···O(1)	0.82	1.78	2.585(2)	169	1/2-x, -1/2+y, 3/2-z
C(5)–H(5)···O(4)	0.93	2.44	3.298(2)	154	-1/2+x, 1/2-y, 1/2+z
Compound (3)					
N(1)–H(1)···O(5)	0.86	1.84	2.698(2)	172	x, -1+y, z
N(2)–H(2A)···O(4)	0.86	1.88	2.737(2)	172	x, -1+y, z
N(2)–H(2B)···O(4)	0.86	2.08	2.848(2)	148	1-x, 1-y, -z
N(3)–H(3)···O(1)	0.86	1.81	2.654(2)	165	1-x, -y, 1-z
N(4)–H(4A)···O(2)	0.86	2.04	2.899(2)	173	1-x, -y, 1-z
N(4)–H(4B)···O(6)	0.86	2.11	2.899(2)	153	1+x, y, z
O(6)–H(6A)···O(1)	0.83	1.98	2.794(2)	169	x, 1+y, z
O(6)–H(6B)···O(2)	0.83	1.95	2.775(2)	174	1+x, 1+y, z
C(6)–H(6)···O(5)	0.93	2.54	3.400(3)	154	x, -1+y, z
C(21)–H(21)···O(1)	0.93	2.57	3.313(3)	137	---

In (**1**), Cg(1) is the centroid of the (C2–C7) ring.

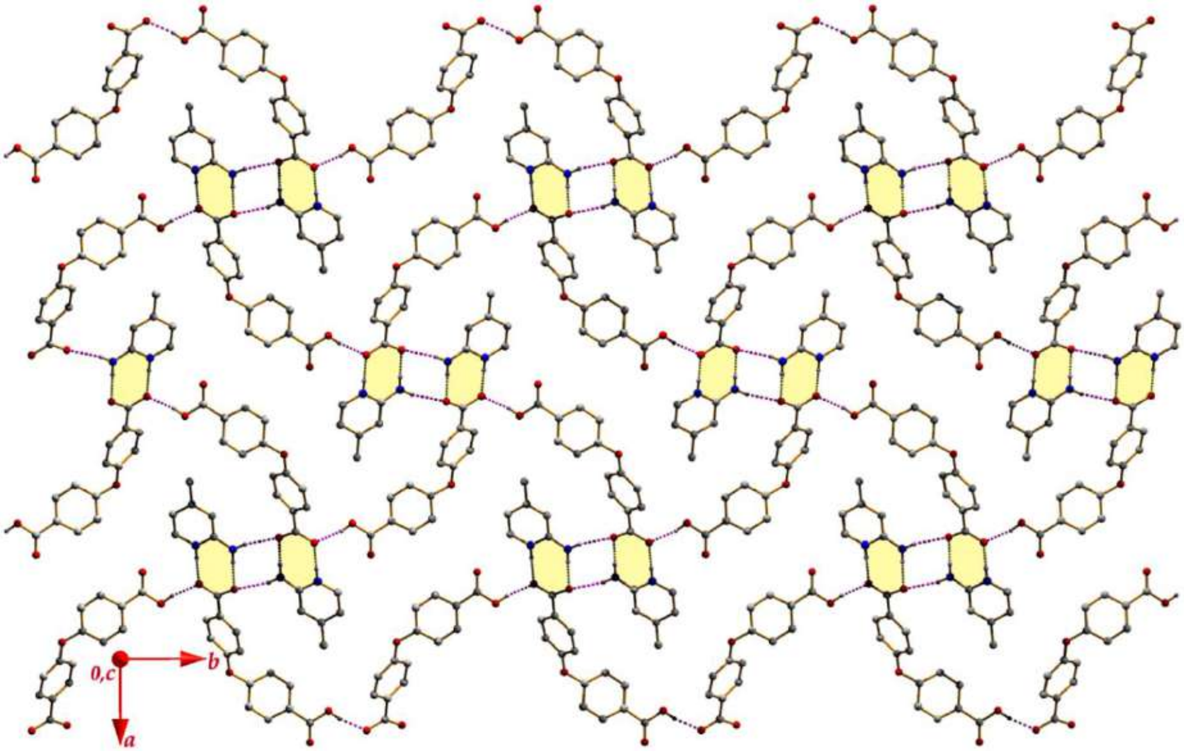

Figure 3.5. Two-dimensional assembly of (**2**) in (110) plane.

In (**2**), the pyridinium and amine nitrogen atoms N(1) and N(2) act as donors to the carboxylate oxygen atoms O(1) and O(2) respectively (see Table 3.2) in the molecule at (-x, 1-y, 2-z) to form the SB unit $R_2^2(8)$ (Figure 3.5). Again the amine hydrogen atom acts as secondary donor to the carboxylate oxygen atom at (1+x, 1+y, z); thus forming a $R_4^2(8)$ ring. Due to the self-complementarity, the non-protonated carboxy oxygen atom O4 acting as donor to the protonate carboxylate oxygen atom O1 and interconnect the ring motifs to build a two-dimensional framework in (110) plane (Figure 3.5). In another substructure, the methyl carbon atom of the pyridinium moiety is in contact with the SB unit with a separation distance of 2.912Å. On the other side of the SB unit, the π-cloud of the aryl ring is oriented towards the SB unit with a separation distance of 2.060Å. Thus, a unique C–H···SB/SB···π network is observed in (**2**) (Figure 3.6).

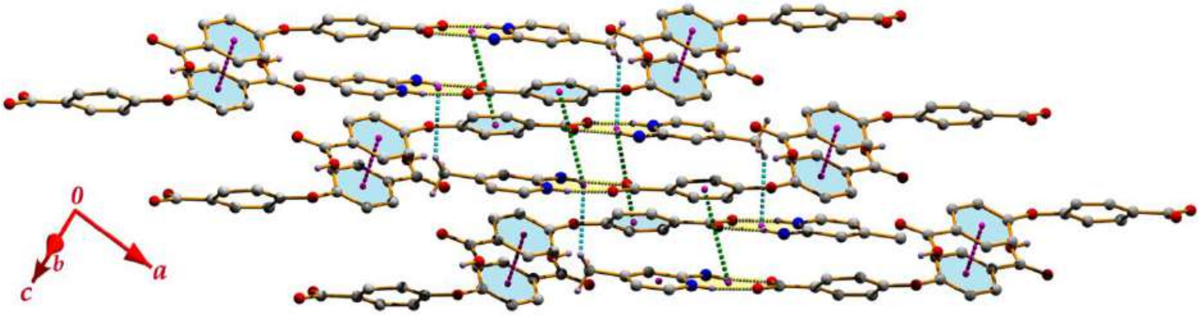

Figure 3.6. Extended C–H···SB/SB···π network in (**2**). The SB, C–H···SB, SB···π and π–π stacking interactions are represented by the yellow, turquoise, green and pink dotted lines respectively.

In (**3**), two SB units [$R_2^2(8)$ ring motifs] are generated through the N–H···O hydrogen bonding interactions (Table 3.2). These two SB units are interconnected by CH···O hydrogen bonds thus propagating into a one-dimensional chain along [010] direction (Figure 3.7). The parallel chains are further interconnected by hydrogen bonds between the amine nitrogen and carboxylate oxygen atoms. This combination of interactions leads the molecules to generate a two-dimensional framework in (011) plane (Figure 3.7).

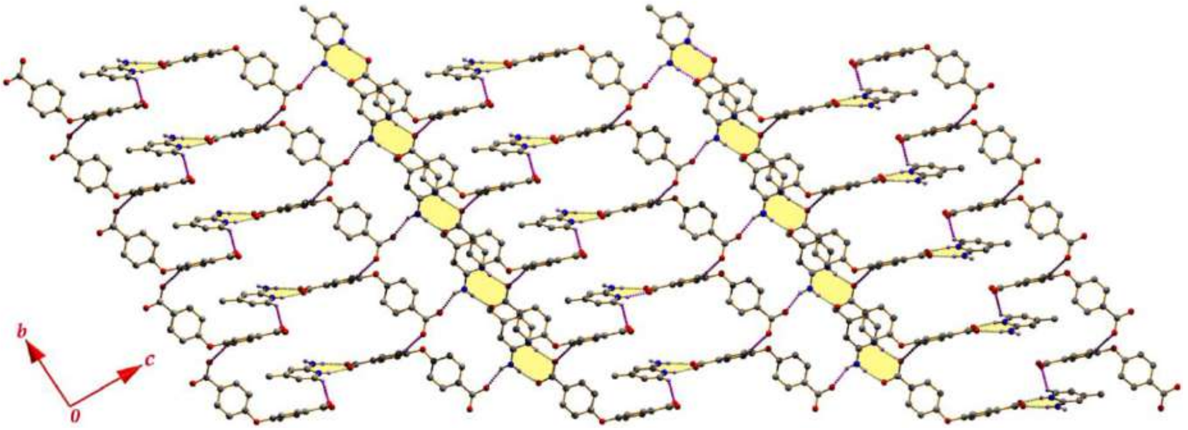

Figure 3.7. Layer network of (**3**) in (011) plane.

In another substructure, one SB unit is in contact with the solvent water molecule where the amine nitrogen atom acts as donor to the water oxygen atom and the water oxygen atom acts as donor to the carboxylate oxygen atom. Thus, the mutual interactions of N–H···O and O–H···O hydrogen bonds generates $R_6^4(12)$ ring motif that leads the molecules to propagate along [100] direction (Figure 3.8). In other side of the carboxylate anion, the SB is interconnected with another SB of the partner molecule through N–H···O hydrogen bond and generates a supramolecular layered assembly in (110) plane (Figure 3.8).

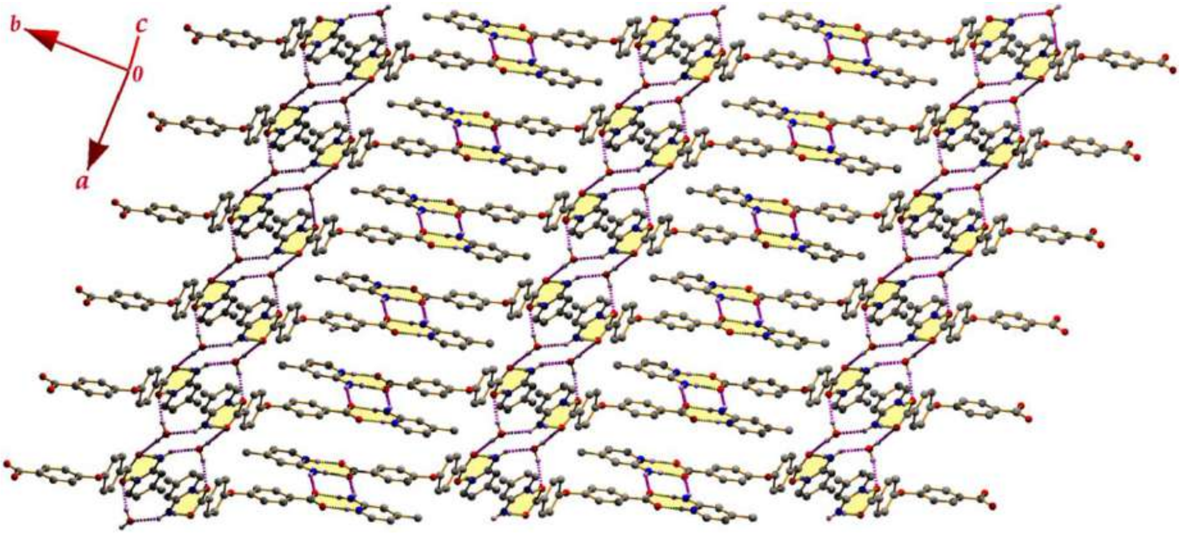

Figure 3.8. Supramolecular layered assembly in (**3**).

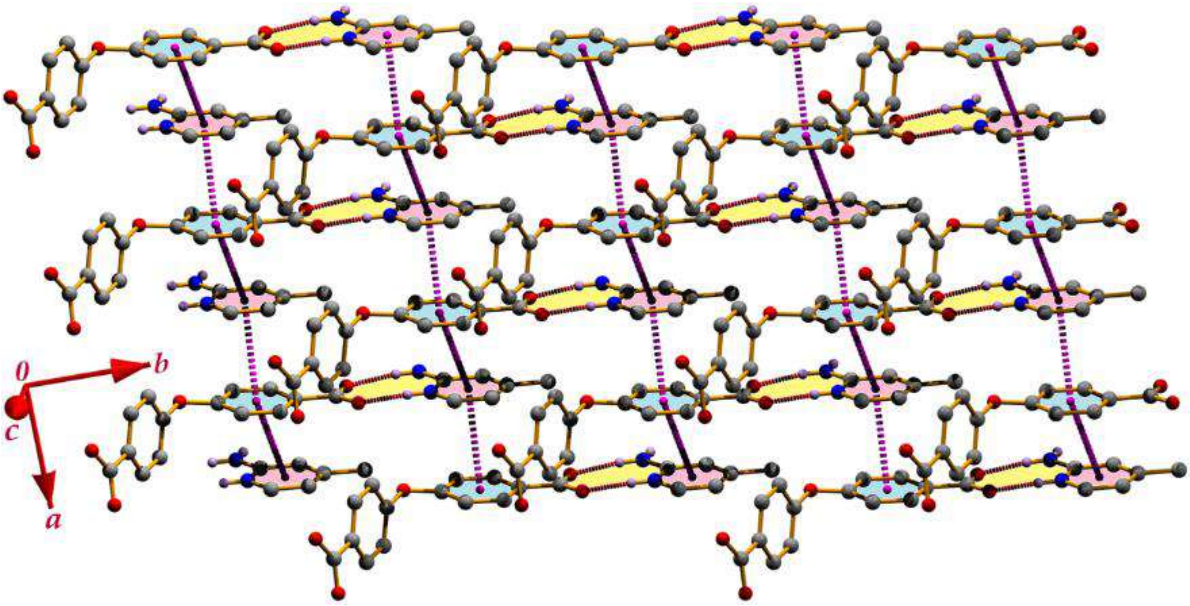

Figure 3.9. Supramolecular layered assembly in (**3**) through π-stacking interactions.

In another substructure, the aryl ring of the acid moiety is oriented towards the π-cloud of the pyridine ring with an interplanar spacing of 3.426 Å with an intercentroid separation of 3.805 Å. Again the pyridine ring is juxtaposed to the aryl ring of the acid moiety through π-stacking interaction with a separation distance of 3.667 Å. Repetition of the π-π^+/π^+-π network leads the molecules to propagate into a one-dimensional ribbon along [100] direction (Figure 3.9). These parallel ribbons are interconnected through the SB unit and generate a supramolecular layered assembly in (110) plane (Figure 3.9).

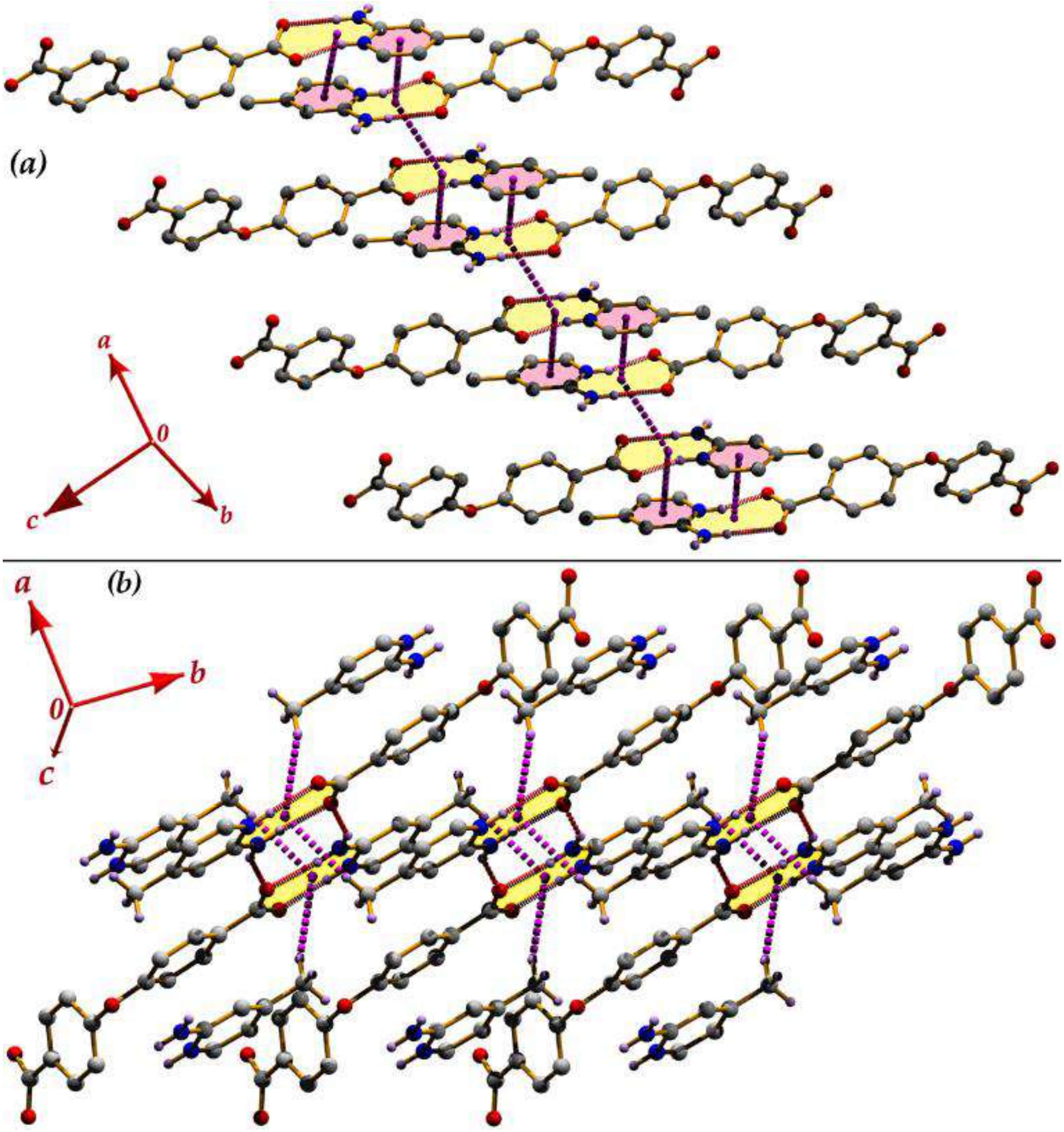

Figure 3.10. Perspective view of $\pi^+\cdots$SB/SB$\cdots$SB/SB$\cdots\pi^+$ network (a) and CH$\cdots$SB/SB$\cdots$HC network in (**3**). The SB units are highlighted by yellow colour whereas the π^+ moieties are shown in pink colour.

Compound (**3**) exhibits two distinctly different supramolecular networks involving the SB unit. In one substructure, the SB unit lies just above the π-cloud of the pyridine ring with a separation distance of 3.754Å. Thus a face-to-face dual SB$\cdots\pi^+$ unit is generated (Figure 3.10a). Two adjacent dual SB$\cdots\pi^+$ units are juxtaposed through SB···SB interaction with a separation distance of 3.616Å. Thus, an extended π⁺···SB/SB···SB/SB···π⁺ network is generated in (**3**) (Figure 3.10a). In another substructure, the second SB unit that is generated through second carboxylate unit also takes part in building extended network. The methyl carbon atom of the pyridine moiety is oriented towards the SB unit with a separation distance of 3.237Å (Figure 3.10b). Another methyl carbon from the aminopyridine moiety is in contact with the SB unit with a separation distance of 2.840Å. Thus a CH···SB/SB···HC network is generated in (**3**) (Figure 3.10b). These unique and extended two distinct networks are also observed in a supramolecular-layered assembly (Figure 3.11).

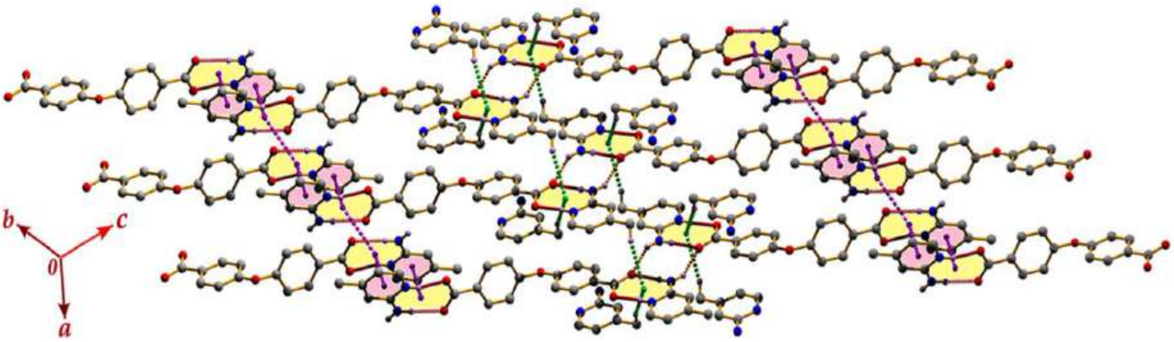

Figure 3.11. Extended supramolecular layered network generated through π⁺···SB/SB···SB/SB···π⁺ and CH···SB/SB···HC networks in (**3**).

3.3.2. Theoretical calculations

We have executed the computational study using DFT-D3 calculations to analyze the noncovalent interactions involved in the interesting architectures of compounds (**1–3**). We are particularly interested to perform the calculations of the extended networks involving the salt bridge unit. We have focused our efforts in two main issues. First, we have studied the energetic features of the noncovalent interactions and, second we have analyzed the interplay between them and characterized the interactions using Bader's theory of ''atoms-in-molecules'' (AIM). The crystallographic coordinates have been used in theoretical models/calculations and in some cases, we have modified the small fragments to evaluate the contributions for the formation of the self-assembly.

First of all, we have computed the MEP surface of the 2-aminopyridinium-benzoate slat bridge as model of compounds (**1–3**) in order to illustrate the dual donor-acceptor ability of the salt bridge. Figure 3.12 depicts the MEP surface where the most positive MEP value is located at the H-atom of the amino group (+57 kcal/mol) and the most negative at the O-atom of the carboxylate group (–52 kcal/mol). Interestingly, the surface clearly confirms the existence of two different halves of the salt bridge, one electron poor and the other electron rich, as illustrated by the opposite values over the center of the aromatic ring. Consequently, the large dipole moment (11.7 D) and the planarity of the system also facilitates the formation of antiparallel stacking interactions, either with itself or any other planar system with large dipole moments like charged aromatic rings.

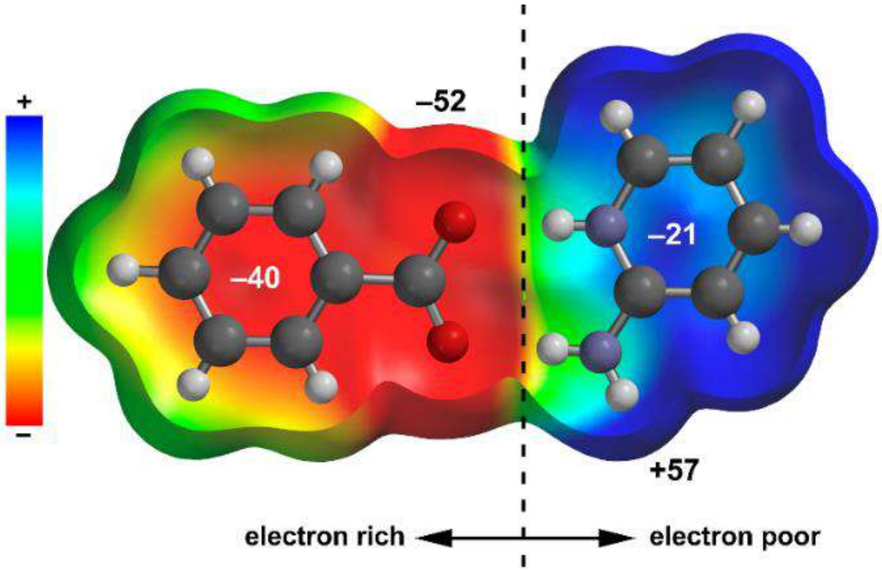

Figure 3.12. MEP surface of aminopyridinium-benzoate slat bridge using the 0.001 a.u. isosurface. The values are selected points of the surface are indicated in kcal/mol.

For compound (**1**), we have prepared some models (following Figure 3.4) to evaluate the formation energies (see Figure 3.13). In Figure 3.13a, the acid moiety is simplified (see the red arrow) in which the formation energy of the salt bridge (SB) is $\Delta E_1 = -110.6$ kcal/mol. Due to the ion-pair nature of the interaction, the formation energy ΔE_1 is very large. In the model shown in Figure 3.13b, the carboxylate units are modified (see the pink arrows) to make the model neutral. The formation energy of the cooperative interactions [lone-pair (l.p)···SB, π–π^+ and CH···O H-bonding] is moderately strong $\Delta E_2 = -13.5$ kcal/mol. We have used several theoretical models to evaluate the contribution of each interaction separately. In this context, we prepared two models where the benzoic acid moiety is simplified: (i) to avoid C–H···O interaction in Figure 3.13c and (ii) to avoid π–π^+ interaction in Figure 3.13d. The first model where the lone-pair (l.p)···SB and π–π^+ are evaluated exhibits a formation energy of $\Delta E_3 = -9.8$ kcal/mol. So, the binding energy of the CH···O interaction can be evaluated as a difference, i.e. $\Delta E_2 - \Delta E_3 = -3.7$ kcal/mol. The formation energy of the second model where lone-pair (l.p)···SB and CH···O interactions are estimated is $\Delta E_4 = -4.9$ kcal/mol (see Figure 3.13d). So, the formation energy of the π–π^+ interaction can be also deduced by difference, which is $\Delta E_2 - \Delta E_4 = -8.6$ kcal/mol. The energy of the lone-pair (l.p)···SB interaction is (-4.9 + 3.7 = –1.2) kcal/mol. Moreover, we have used the neutral aminopyridine moiety (see the blue arrows in Figure 3.13e) to estimate the energy of the π-stacking interaction in the absence of the strong electrostatic repulsion between the cationic arenes. Finally, the model dimer shown in Figure 3.13f is crucial to understand the π^+···SB/SB···SB/SB···π^+ network discussed above in Figure 3.10a. The formation energy of the model shown in Figure 3.13f, where two SB···π^+ and one π^+–π^+ interactions are acting mutually is very large $\Delta E_6 = -26.67$ kcal/mol, thus confirming that it is a strong binding motif. In order to estimate the contribution of both SB···π^+ interactions, we have subtracted the energy of the π–π interaction evaluated in Figure 3.13e to the formation energy of the assembly, which is ($\Delta E_6 - \Delta E_5$) = –21.36 kcal/mol, thus evidencing that each SB···π^+ interaction is moderately strong (-10.68 kcal/mol).

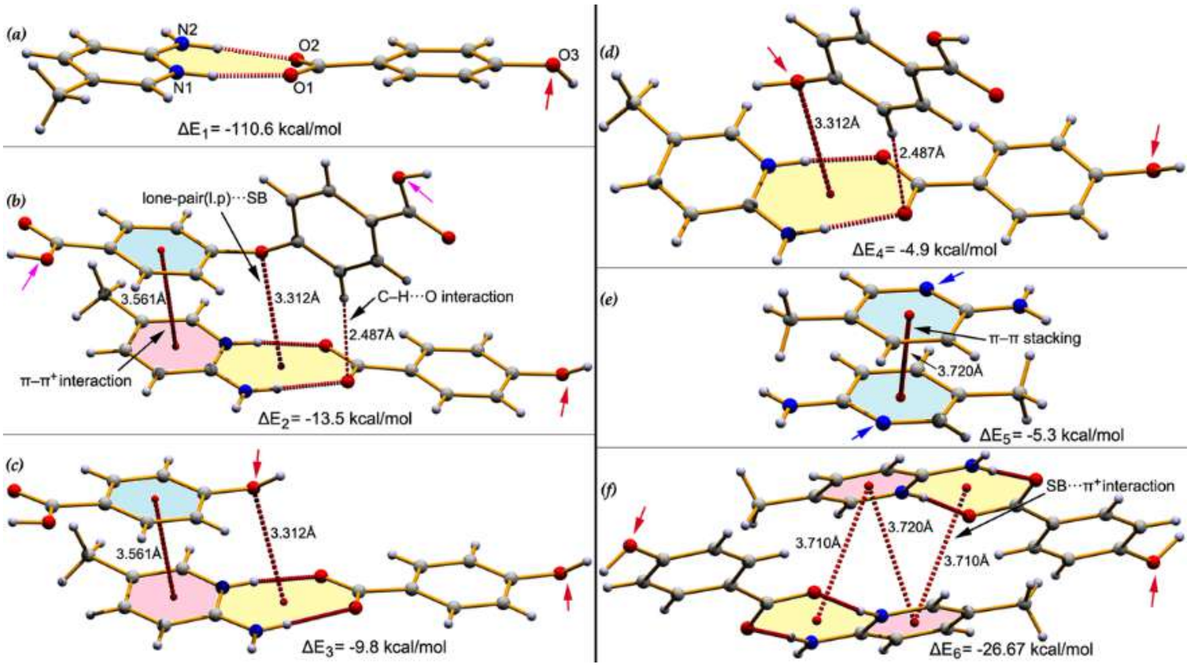

Figure 3.13. Various theoretical models used to analyse the noncovalent interactions observed in the supramolecular assembly observed in the solid state structure of compound (**1**).

For compound (**2**), the models used to compute the formation energies are shown in Figure 3.14. We have used formate ions (see the red arrow) as a model of 4,4′-oxybis(benzoic acid) in building the SB unit. This model allows us to study the stacking interaction between the neutral moieties (formate and protonated aminopyridine ion-pairs). The formation energy of the SB is higher ($\Delta E_7 = -114.3$ kcal/mol) compared to compound (**1**). We have used the neutral models to evaluate the formation energy of the CH···SB interaction ($\Delta E_8 = -7.0$ kcal/mol) (Figure 3.14b). Following Figure 3.6, we have calculated the formation energy of the SB···π interaction using the model where the acid moiety is simplified (see the pink arrow in Figure 3.14c). The formation energy of the SB···π interaction in (**2**) is $\Delta E_9 = -10.0$ kcal/mol which is comparable to the energy value of SB···π^+ interaction of compound (**1**) (–10.68 kcal/mol).

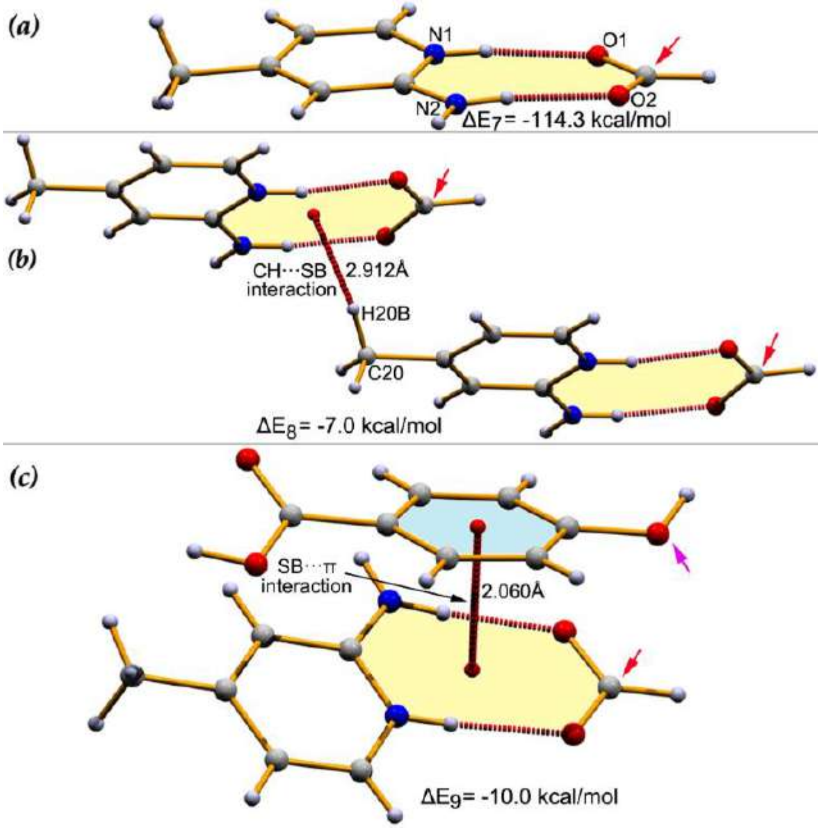

Figure 3.14. The different interactions observed in the self-assembly of compound (**2**) are shown by the models which are used for theoretical computation.

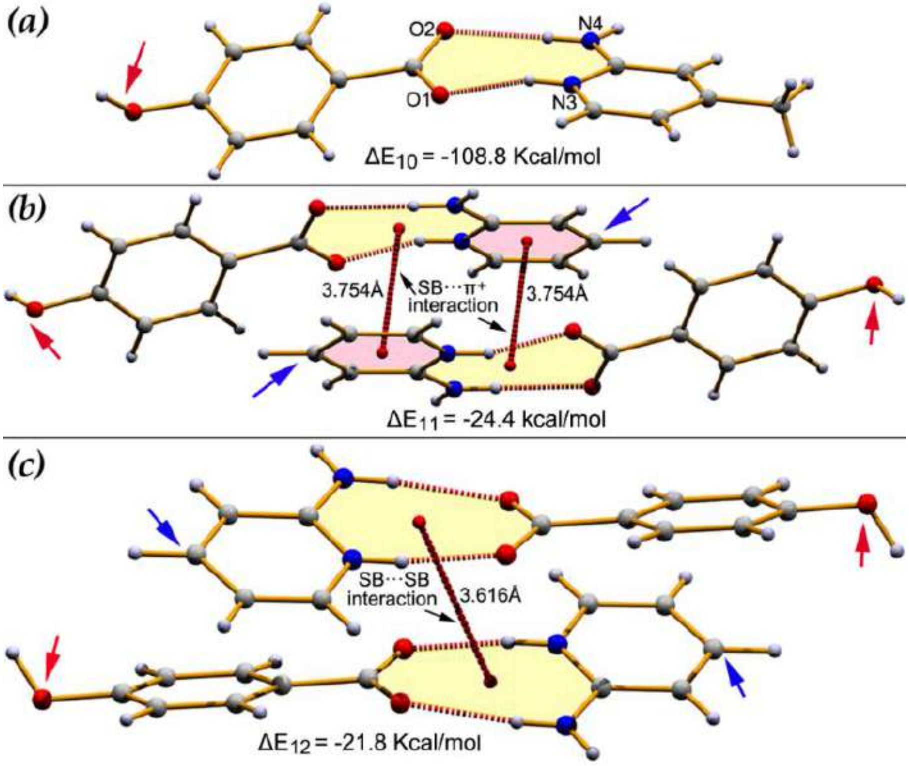

Figure 3.15. Theoretical models of compound (**3**) and their interactions energies.

In compound (**3**), two SB units are generated by the two-protonated carboxylate groups of 4,4′-oxybis(benzoic acid). Therefore, two distinctly different networks are generated involving the SB units. We have simplified the model (see red arrow in Figure 3.15a) to calculate the formation energy of the SB, which is ΔE_{10} = -108.8 kcal/mol. It is slightly weaker than those of compounds (**1**) and (**2**). In another model (Figure 3.15b), we have used 2-aminopyridine instead of 2-amino-4-methylpyridine to avoid the CH contacts with partner molecule (see the blue arrows). The binding energy of the dual SB···π^+ interaction is strong (ΔE_{11} = –24.4 kcal/mol). Finally, we have computed the binding energy of SB···SB interaction, which is also strong (ΔE_{12} = –21.8 kcal/mol). Therefore, the antiparallel SB···SB interaction is much more favorable in comparison to SB···π^+ interaction (-12.2 kcal/mol) due to the dual ion-pair interaction. These large interaction energies confirm the importance of both interactions in building π^+···SB/SB···SB/SB···π^+ network shown in Figure 3.10a.

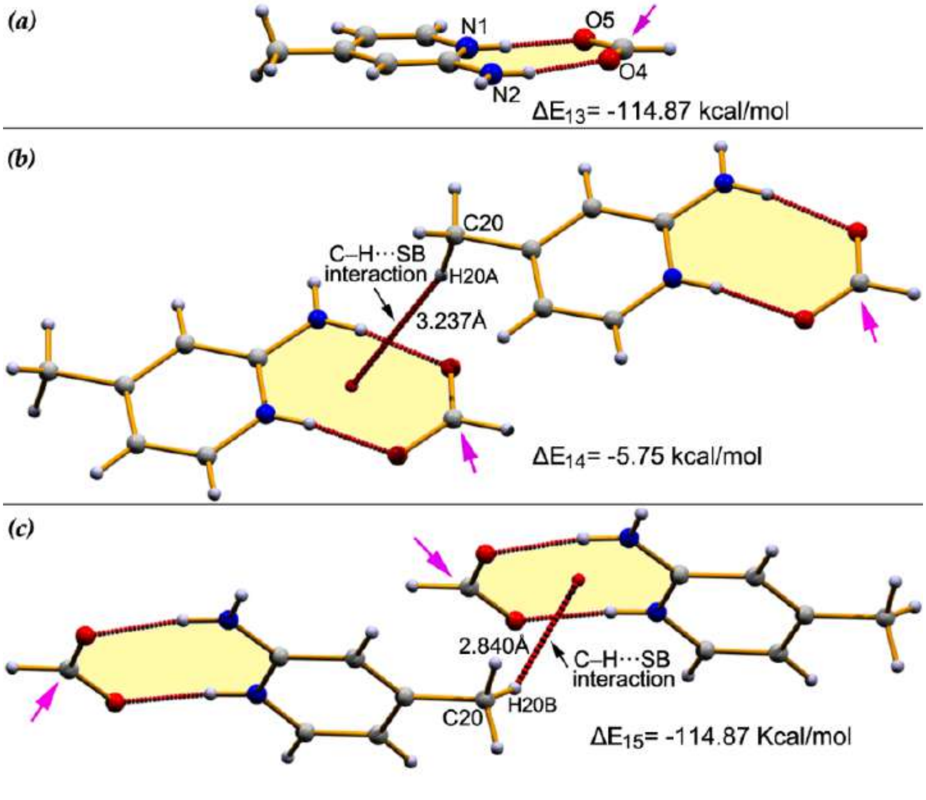

Figure 3.16. Theoretical models of compound (**3**) to explore the formation energies of CH···SB/SB···HC network.

To calculate the formation energy of the SB unit, we have used formate ion to simplify the model (see the pink arrow of Figure 3.16a). The formation energy of the SB is ΔE_{13} = -114.87 kcal/mol and comparable to the formation energy of compound (**2**). Finally, to confirm the importance of the CH···SB/SB···HC network as shown in Figure 3.10b, we have calculated the formation energies of the CH···SB and SB···HC interactions (-5.75 kcal/mol and -7.23 kcal/mol) (see Figures 3.16b and 3.16c).

We have performed the Bader's theory of atoms in molecules (AIM) [45] analysis of the self-assembled network structures of compounds (**1–3**) by using the models described above. The AIM is used to visualize and characterize the noncovalent interactions involved within the structures by paying attention to the distribution of the critical points and bond paths. The existence of a bond critical point (CP) and bond path connecting two atoms is a clear evidence of interaction, since it indicates that electron density is accumulated between the nuclei that are linked by the associated atomic interaction line [44]. AIM analysis has been recently used to rationalize similar noncovalent interactions [48-51]. In Figure 3.17, we represent the distribution of CPs and bond paths of the extended networks of compounds (**1**–**3**). The CH···SB/SB···HC network of compound (**3**) is shown in Figure 3.18. In all cases, the SB is characterized by the presence of the two bond CPs (represented as red spheres in Figure 3.17) and bond paths connecting the H atoms of the aminopyridine and the carboxylate oxygen atoms (Figures 3.17 and 3.18). A ring CP (yellow sphere) further characterizes the SBs due to the formation of a supramolecular ring. The $\varrho(r)$ values at the bond CPs are indicated the Figure 3.17. For the SBs of all compounds, the $\varrho(r)$ values at the bond CPs that characterize the pyridine $N^{+}H\cdots O$ bond are larger than those of the amine $NH\cdots O$ bonds that is in agreement with their shorter distances. Therefore, it can be concluded that the protonated pyridine N$^+$H···O hydrogen bond is stronger than the exocyclic NH···O bond.

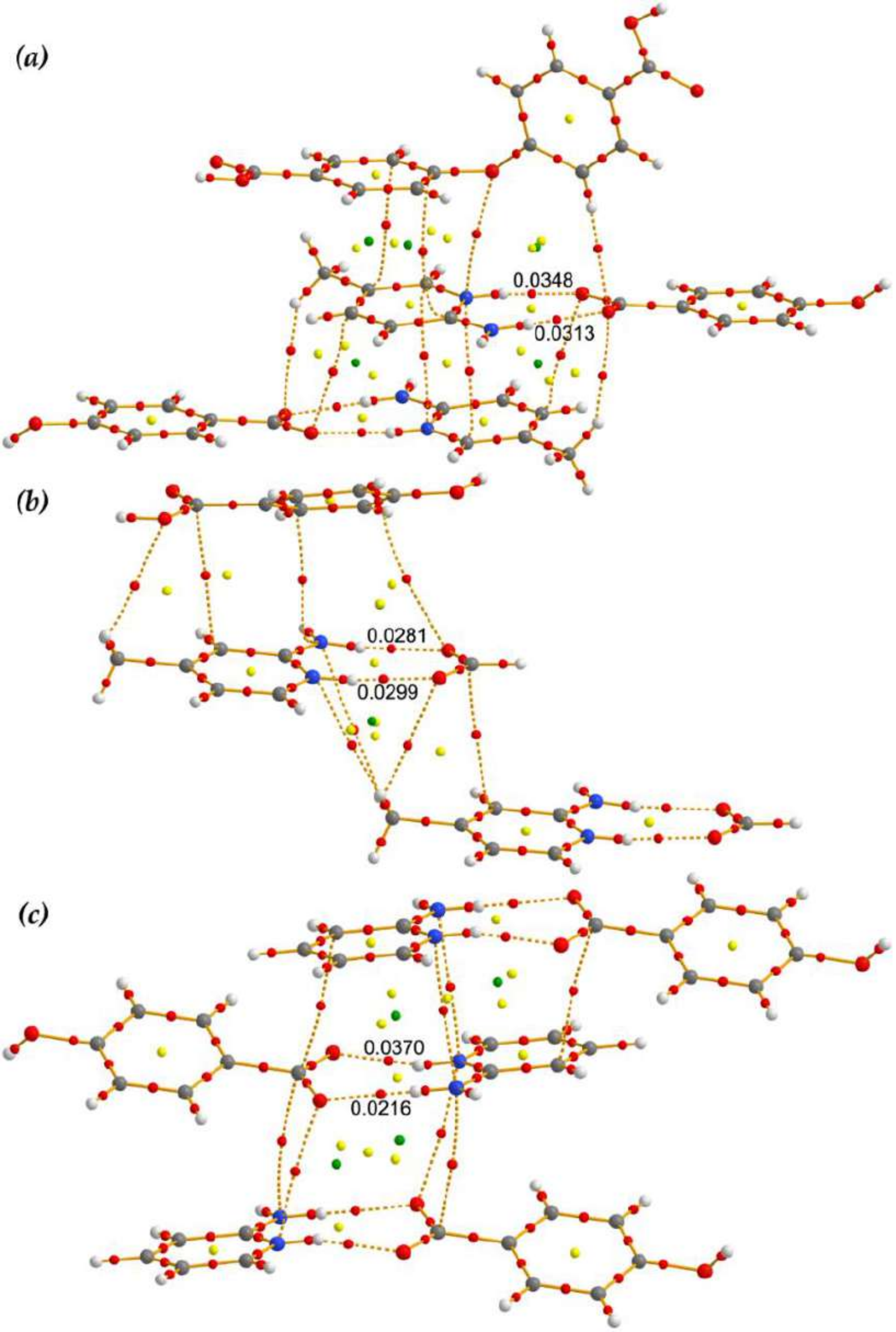

Figure 3.17. Distribution of the critical points of the self-assembled extended networks of compounds (**1**–**3**) (a-c). Red, yellow and green spheres represent bond, ring and cage critical points, respectively.

For compound (**1**), the interactions shown in Figure 3.13b are clearly evident by the distribution of bond CPs of and bond paths (Figure 3.17a). The lone-pair(l.p)···SB interaction is characterized by a bond CP (red sphere) and bond path connecting the O and pyridine N atom of the SB unit (ρ_{BCP} = 0.0054 a.u.). The CH···O H bond is also characterized by the corresponding BCP (ρ_{BCP} = 0.0094 a.u.) and bond path. The π–π^+ interaction (ρ_{BCPs} = 0.0064 and 0.0052 a.u.) is characterized by the presence of two BCPs and bond paths interconnecting two carbon atoms of the aryl and pyridine rings (Figure 3.17a). The Sb···π^+ interaction (see Figure 3.13f) is characterized by two BCPs where one bond path connects one carbon atom of the pyridine ring and nitrogen atom of the pyridine ring (ρ_{BCP} = 0.0063 a.u.) and another bond path connects the pyridine ring carbon atom and carboxylate oxygen atom (ρ_{BCP} = 0.0063 a.u.). In compound (**2**), the ϱ(r) values of the SB and bond paths are shown in Figure 3.17b. The BCP and bond path connecting amine nitrogen and carbon atom of the aryl ring characterizes the extended SB···π interaction where the ρ_{BCP} is 0.0058 a.u. The CH···SB interaction in (**2**) is characterized by two BCPs and bond paths connecting one hydrogen atom of the methyl group with one carboxylate oxygen and pyridine ring nitrogen atom (ρ_{BCPs} = 0.0039 and 0.0033 a.u. respectively) (See Figure 3.17b). An additional bond path connects another hydrogen atom of the methyl group and amine nitrogen atom that further characterizes the CH···SB interaction (ρ_{BCP} = 0.0013 a.u.). In compound (**3**), two SBs are evidenced and the associated networks are depicted in Figures 3.17c and 3.18. The Sb···π^+ interaction is characterized by two BCPs and where one bond path connects the carbon atoms of the pyridine ring and carboxylate moiety (ρ_{BCP} = 0.0046 a.u.) whereas another bond path connects the pyridine ring nitrogen and amine nitrogen atom (ρ_{BCP} = 0.0052 a.u.). Four BCPs and bond paths characterize the SB···SB interaction (Figure 3.17c). The CH···SB/SB···HC network is characterized by two BCPs and two bond paths connecting methyl hydrogen atoms with carboxylate oxygen atom where the ϱ(r) values are 0.0073 and 0.0062 (see Figure 3.18).

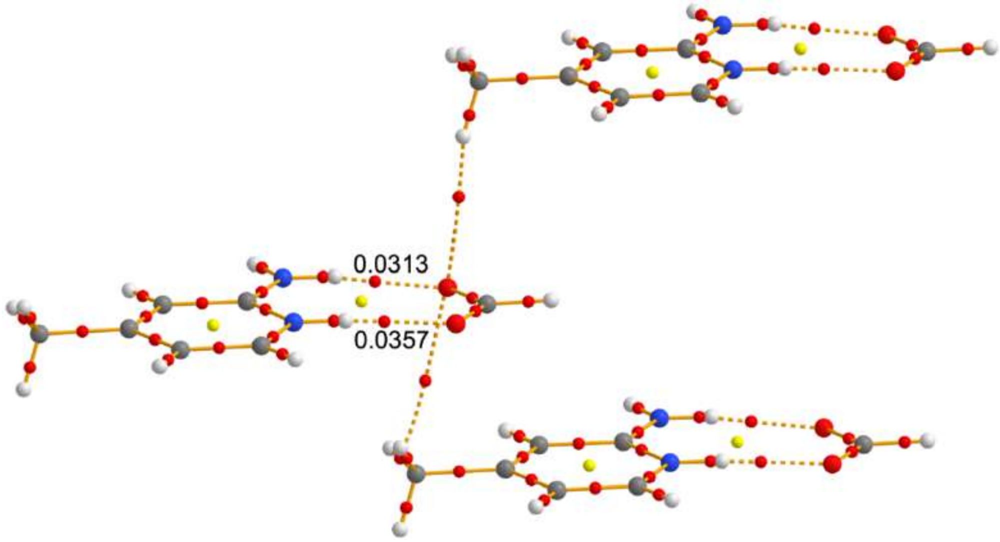

Figure 3.18. Distribution of the critical points of the self-assembled CH···SB/SB···HC network of compound (**3**). Red and yellow spheres represent bond and ring critical points, respectively.

3.4. Conclusions

Three new aminopyridinium/4,4'-oxydibenzoate salts have been synthesized and their structures determined by single-crystal X-ray diffraction. A common feature of these compounds in the formation of salt bridges aminopyridinium cations and the 4,4'-oxydibenzoate succinate anions. They participate in a great variety of interactions due to the dual nature of the salt-bridge. These interactions determine the crystal packing architecture of all salts and have been evaluated using theoretical calculations and AIM analysis that confirm the existence of the interactions. We have evaluated the contribution of several interactions to the total formation energy of the assemblies, showing that the SB···π and antiparallel SB···SB interactions are very strong. Since salt-bridge formation between the side chain of aspartate or glutamate and arginine is very common in protein and enzymes, π-facial interactions with the side chain or aromatic amino-acids or substrates can be very common, thus suggesting that more research in this direction is needed.

3.5. References

[1] G. R. Desiraju, *Chem. Commun.*, 1997, 1475–1482.

[2] J.Y. Lee, B.H. Hong, W.Y. Kim, S.K. Min, Y. Kim, M.V. Jouravlev, R. Bose, K.S. Kim, I.-C. Hwang, L.J. Kaufman, C.W. Wong, P. Kim, K.S. Kim, *Nature*, 2009, **460**, 498–501.

[3] T.S. Thakur, G.R. Desiraju, *Cryst. Growth Des.*, 2008, **8**, 4031.

[4] S.L. Price, *Acc. Chem. Res.*, 2009, **42**, 117–126.

[5] P. Seth, A. Bauzá, A. Frontera, C. Massera, P. Gamez, A. Ghosh, *CrystEngComm*, 2013, **15**, 3031–3039.

[6] J.W.G. Bloom, S.E. Wheeler, Angew. Chem. Int. Ed., 2011, **50**, 7847–7849.

[7] S. K. Seth, D. Sarkar, T. Kar, CrystEngComm, 2011, **13**, 4528–4535.

[8] S. K. Seth, D. Sarkar, A. D. Jana, T. Kar, Cryst. Growth Des., 2011, **11**, 4837–4849.

[9] S. K. Seth, P. Manna, N.J. Singh, M. Mitra, A.D. Jana, A. Das, S.R. Choudhury, T. Kar, S. Mukhopadhyaya, K.S. Kim, CrystEngComm, 2013, **15**, 1285–1288.

[10] J.C. Ma, D.A. Dougherty, *Chem. Rev.*, 1997, **97**, 1303–1324.

[11] A. Frontera, P. Gamez, M. Mascal, T.J. Mooibroek, J. Reedijk, *Angew. Chem. Int. Ed.*, 2011, **50**, 9564–9583.

[12] P. Manna, S.K. Seth, M. Mitra, S.R. Choudhury, A. Bauzá, A. Frontera, S. Mukhopadhyay, *Cryst. Growth Des.*, 2014, **14**, 5812–5821.

[13] P. Manna, S.K. Seth, A. Bauzá, M. Mitra, S.R. Choudhury, A. Frontera, S. Mukhopadhyay, *Cryst. Growth Des.*, 2014, **14**, 747–755.

[14] M. Mitra, P. Manna, A. Bauzá, P. Ballester, S.K. Seth, S.R. Choudhury, A. Frontera, S. Mukhopadhyay, *J. Phys. Chem. B*, 2014, **118**, 14713–14726.

[15] B. Notash, N. Safari, H.R. Khavasi, *CrystEngComm*, 2012, **14**, 6788–6796.

[16] S.K. Seth, I. Saha, C. Estarellas, A. Frontera, T. Kar, S. Mukhopadhyay, *Cryst. Growth Des.*, 2011, **11**, 3250–3265.

[17] P. Manna, S.K. Seth, A. Das, J. Hemming, R. Prendergast, M. Helliwell, S.R. Choudhury, A. Frontera, S. Mukhopadhyay, *Inorg. Chem.*, 2012, **51**, 3557–3571.

[18] I. Alkorta, F. Blanco, P.M. Deya, J. Elguero, C. Estarellas, A. Frontera, D. Quinonero, *Theor. Chem. Acc.*, 2010, **126**, 1–14.

[19] J.W. Steed, D.R. Turner, K.J. Wallace, *Core Concepts in Supramolecular Chemistry and Nanochemistry*; John Wiley & Sons, Ltd.: Chichester, UK, 2007; pp. 194–228.

[20] M. R. Shimpi, S. P. Velaga, F. U. Shah, O. N. Antzutkin, *Cryst. Growth Des.*, 2017, **17**, 1729–1734.

[21] G. R. Desiraju, *Angew. Chem., Int. Ed.*, 2007, **46**, 8342–8356.

[22] F. O. Tzul, K. L. Schweiker, G. I. Makhatadze, *Proc. Natl. Acad. Sci.* U. S. A., 2015, **112**, E259–66.

[23] M. P. Williamson, A. M. Hounslow, J. Ford, K. Fowler, M. Hebditch, P. E. Hansen, *Chem. Commun.*, 2013, **49**, 9824–9826.

[24] I. Gitlin, J. D. Carbeck, G. M. Whitesides, *Angew. Chem., Int. Ed. Engl.*, 2006, **45**, 3022–3060.

[25] V. Ferretti, V. Bertolasi, L. Pretto, *New J. Chem.*, 2004, **28**, 646–651.

[26] E. Yashima, K. Maeda, Y. Furusho, *Acc. Chem. Res.*, 2008, **41**, 1166–1180.

[27] H. Katagiri, Y. Tanaka, Y. Furusho, E. Yashima, *Angew. Chem., Int. Ed.*, 2007, **46**, 2435–2439.

[28] A. Warshel, P. K. Sharma, M. Kato, W. W. Parson, *Biochim. Biophys. Acta, Proteins Proteomics*, 2006, **1764**, 1647–1676.

[29] Q. Xu, H. Guo, A. Wlodawer, H. Guo, *J. Am. Chem. Soc.*, 2006, **128**, 5994–5995.

[30] B. Kuberski, A. Szumna, *Chem. Commun.*, 2009, 1959–1961.

[31] L.E.R. O'Leary, J. A. Fallas, E. L. Bakota, M. K. Kang, J. D. Hartgerink, *Nature Chem.*, 2011, **3**, 821–828.

[32] J. M. Christie, A. S. Arvai, K. J. Baxter, M. Heilmann, A. J. Pratt, A. O'Hara, S. M. Kelly, M. Hothorn, B. O. Smith, K. Hitomi, G. I. Jenkins, E. D. Getzoff, *Science*, 2012, **335**, 1492–1496.

[33] V. Dvornikovs, D. B. Smithrud, *J. Org. Chem.*, 2002, **67**, 2160–2167.

[34] P.-O. Norrby, T. Liljefors, *J. Am. Chem. Soc.*, 1999, **121**, 2303–2306.

[35] M. Mitra, P. Manna, S.K. Seth, A. Das, J. Meredith, M. Helliwell, A. Bauzá, S.R. Choudhury, A. Frontera, S. Mukhopadhyay, *CrystEngComm*, 2013, **15**, 686–696.

[36] Bruker, *SAINT*, Version 6.36a, Bruker AXS Inc., Madison, Wisconsin, USA, 2002.

[37] Bruker, *SMART*, Version 5.625 and *SADABS*, Version 2.03a, Bruker AXS Inc., Madison, Wisconsin, USA, 2001.

[38] G.M. Sheldrick, *Acta Cryst. A*, 2008, **64**, 112–122.

[39] G. M. Sheldrick, *Acta Cryst. C*, 2015, **71**, 3–8.

[40] L.J. Farrugia, *J. Appl. Cryst.*, 2012, **45**, 849–854.

[41] A. L. Spek, *J. Appl. Crystallogr.*, 2003, **36**, 7–13.

[42] R. Ahlrichs, M. Bär, M. Hacer, H. Horn, C. Kömel, *Chem. Phys. Lett.*, 1989, **162**, 165–169.

[43] S.B. Boys, F. Bernardi, *Mol. Phys*. 1970, **19**, 553–566.

[44] R.F.W. Bader, *Chem. Rev*. 1991, **91**, 893–928.

[45] T. A. Keith, AIMAll (Version 13.05.06), TK Gristmill Software, Overland Park KS, USA, 2013.

[46] Y. Shao, L.F. Molnar, Y. Jung, J. Kussmann, C. Ochsenfeld, S.T. Brown, A.T.B. Gilbert, L.V. Slipchenko, S.V. Levchenko, D.P. O'Neill, R.A. DiStasio Jr., R.C. Lochan, T. Wang, G.J.O. Beran, N.A. Besley, J.M. Herbert, C.Y. Lin, T. Van Voorhis, S.H. Chien, A. Sodt, R.P. Steele, V.A. Rassolov, P.E. Maslen, P.P. Korambath, R.D. Adamson, B. Austin, J. Baker, E.F.C. Byrd, H. Dachsel, R.J. Doerksen, A. Dreuw, B.D. Dunietz, A.D. Dutoi, T.R. Furlani, S.R. Gwaltney, A. Heyden, S. Hirata, C-P. Hsu, G. Kedziora, R.Z. Khalliulin, P. Klunzinger, A.M. Lee, M.S. Lee, W.Z. Liang, I. Lotan, N. Nair, B. Peters, E.I. Proynov, P.A. Pieniazek, Y.M. Rhee, J. Ritchie, E. Rosta, C.D. Sherrill, A.C. Simmonett, J.E. Subotnik, H.L. Woodcock III, W. Zhang, A.T. Bell, A.K. Chakraborty, D.M. Chipman, F.J. Keil, A. Warshel, W.J. Hehre, H.F. Schaefer, J. Kong, A.I. Krylov, P.M.W. Gill, M. Head-Gordon, *Phys. Chem. Chem. Phys.*, 2006, **8**, 3172.

[47] M.J. Frisch, G.W. Trucks, H.B. Schlegel, G.E. Scuseria, M.A. Robb, J.R. Cheeseman, G. Scalmani, V. Barone, G.A. Petersson, H. Nakatsuji, et al. *Gaussian 09*, Revision *C.01*; Gaussian, Inc.: Wallingford, CT, USA, 2009.

[48] A. Hossain, S. K. Seth, A. Bauzá, S. Mukhopadhyay, *Polymers*, 2018, **10**, 182.

[49] S.K. Seth, A. Bauzá, A.Frontera, *CrystEngComm*, 2018, **20**, 746–754.

[50] T. Maity, H. Mandal, A. Bauzá, B. C. Samanta, A. Frontera, S. K. Seth, *New. J. Chem.*, 2018, **42**, 10202–10213.

[51] G. Mahmoudi, S. K. Seth, A. Bauzá, F. I. Zubkov, A. V. Gurbanov, J. White, V. Stilinović, T. Doert, A, Frontera, CrystEngComm, 2018, **20**, 2812–282.

Chapter 4

Quantifying weak interactions of 4′-functionalized 2,2′:6′,2″-terpyridines

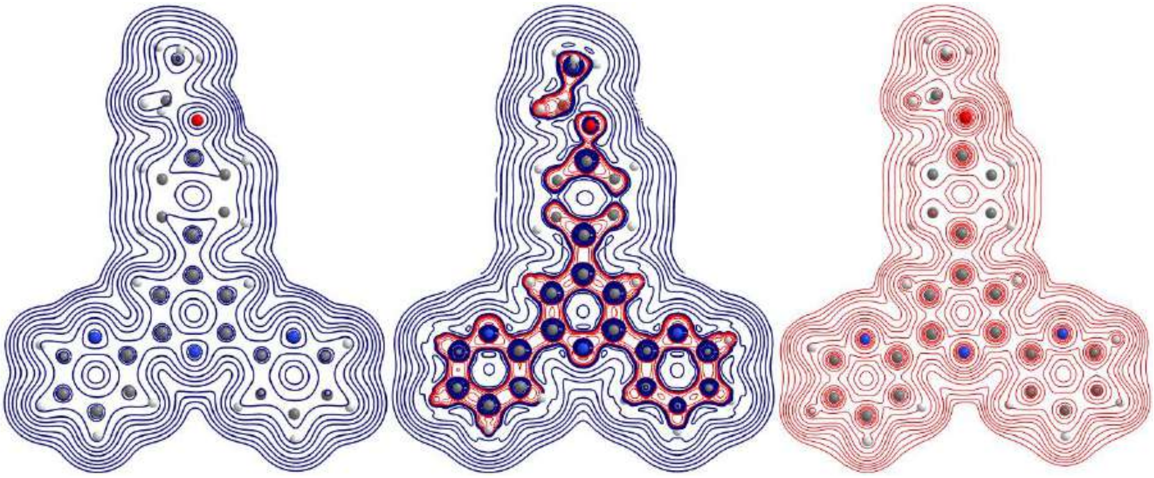

Published in: *Journal of Molecular Structure* 1226 (2021) 129254

4.1. Introduction

Terpyridine compounds are treated as most significant ligand in the fields ranging from chemical synthesis [1-3] to supramolecular design [4-10]. Morgan and Burstall published first synthesis of terpyridine around 80 years back [11]. Since that time, the chemistry of terpyridine corresponds to the maturity of supramolecular chemistry [12-15]. Terpyridine compounds containing N-donor heterocyclic rings is a tridentate NNN-type Pincer ligand that have attracted widespread significant attention as building blocks in coordination chemistry and for preparation of functional materials [16,17]. Terpyridine ligands have been extensively investigated, modified and utilized in the area of supramolecular chemistry [18-20] due to ease of synthesizing [19,21] and various properties. Substitution of terpyridine moiety with various groups induces altered physical properties [22] and exhibit good nonlinear optical property [23-25]. Among terpyridine compounds, the 2,2′:6′,2″-terpyridine is one enthralling ligand that has caught substantial attentions over the past decades for various applications [20, 26-29]. These compounds are used as photosensitizers in Dye-Sensitized Solar Cells (DSSCs) [30] in materials science, as an antitumor [31] and chemotherapy agent [32,33] in medicinal chemistry. Moreover, the 2,2′:6′,2″-terpyridines with the substituent at 4′ position have also been investigated extensively [6-10,34-37]. The 4′-position offers a broad range of substituents that permits us to modify inductive influence largely [38,39]. Moreover, substitution of aromatic ring at the 4′-position of terpyridine leads the molecules to form a conjugated system with moderate planar structure through π–π stacking interactions. Therefore, Structural design of molecular architectures is extremely important that offers an opportunity to control properties of the desired products at the molecular level.

Supramolecular architectures involving organic ligands have become an important research topic in the field of crystal engineering due to its wide applications [40,41]. Crystal engineering is the purposeful design of new crystalline solids with emphasis on finding plans to regulate their properties by exploring crystal structure prediction [42-44]. The noncovalent interactions have attracted widespread interest in exploring the influence of the interactions in determining the structures and properties of molecular assemblies in the field of supramolecular chemistry and materials science [45-49]. In crystal engineering, proper understanding and utilization of noncovalent interactions are extremely important to control the supramolecular association since they are composed of a combination of interactions [50,51]. Noncovalent interactions, including hydrogen bonding and other dispersive π-interactions like C-H···π [52-54], π-π [6-8,55,56], anion···π [9,10,57,58], lp···π [59-61] etc. are ubiquitous interactions that played a pivotal role in crystal engineering. The dispersive π-π stacking interactions play a crucial role in crystal engineering and molecular recognition [57,62,63]. Moreover, the molecular entities of π-systems having π^{+}/π^{-} moieties is an intriguing subject in the study of π-π interactions [6-10,64]. Since the cooperativity of intermolecular interactions significantly pretentious to the final solid-state structures, it is desirable to explore the quantitative contribution of the cooperative effect of noncovalent interactions in the design of supramolecular frameworks [65,66].

Keeping in mind the above facts, in continuation of our effort to further advanced the supramolecular behavior of 2,2′:6′,2″-terpyridines [6-10], herein three terpyridine compounds have been structurally characterized. Apart from reporting the crystal structures, the weak noncovalent interactions that govern the stability of the structures have been analyzed. The intermolecular interactions have been inspected critically and quantified by Hirshfeld surface analysis. The characteristics of the noncovalent interactions are studied theoretically using Bader's theory of "atoms-in-molecules" (AIM). Moreover, theoretical noncovalent interaction (NCI) plot index analyses have been performed in detail to confirm and characterize the noncovalent interactions in a novel visual manner.

4.2. Experimental sections

4.2.1. Materials

All reactions were carried out in ethanol medium and in aerobic condition. All chemicals used were of reagent grade quality, purchased from Sigma Aldrich Chemical Co.

4.2.2. Syntheses

4.2.2a. 4′-(4-ethoxyphenyl)- 2,2′:6′,2″-terpyridine (1).

The terpyridine ligand was prepared following the literature method [67]. In order to synthesize the title compound, 2-acetylpyridine (1 mmol, 0.12 gm) was first taken in a round-bottom flask in 200 ml ethanol and then 4-ethoxybenzaldehyde (2 mmol, 0.30 gm) was added. To this reaction mixture excess of KOH bead (8 mmol, 0.448 gm) was then added and stirred at room temperature for 15 minute. Finally, 25 ml of ammonia was added and stirred at room temperature for another four hours. Pale yellow powdered product obtained was filtered, washed with distilled water and dried in air. Single crystal suitable for X-ray analysis was obtained by dissolving the synthesized compound (0.176 gm, 0.5 mmol) in ethanol (150 ml) and slow evaporation of the solvent at room temperature for about 25 days. The chemical structure of the compound has shown in Scheme 1.

4.2.2b. 4′-(4-methoxyphenyl)- 2,2′:6′,2″-terpyridine (2).

Title compound (**2**) was synthesized previously by two different ways [67-69,6]. Here, we prepared the compound using the reported Hanan's method [67,6]. Single crystal suitable for X-ray analysis was obtained by dissolving the synthesized compound (0.170 gm, 0.5 mmol) in ethanol (150 ml) and slow evaporation of the solvent at room temperature for 25 days. The chemical structure of compound (**2**) has shown in Scheme 4.1.

4.2.2c. 4′-(pyridyl)- 2,2′:6′,2″-terpyridine (3).

Compound (**3**) was also prepared by the reported one step Hanan's method [67,70,7]. Single crystal suitable for X-ray analysis was obtained by dissolving the synthesized compound (0.155 gm, 0.5 mmol) in ethanol (150 ml) and slow evaporation of the solvent at room temperature for about 25 days. Scheme 1 shows the chemical structure of the title compound.

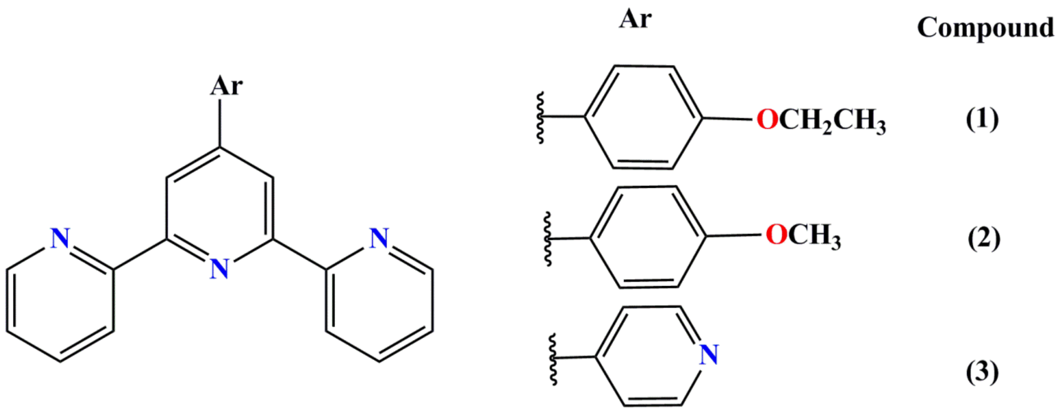

Scheme 4.1 Schematic representation of the chemical structure of the title compounds.

4.2.3. X-ray crystal structure determination

Single crystal X-ray diffraction data was collected by using Bruker APEX-II CCD diffractometer with graphite monochromated MoKα radiation ($\lambda = 0.71073$ Å) at 150(2)K, 293(2)K and 150(2)K of compounds (**1**–**3**) respectively. The program Bruker SAINT [71] was used for data reduction process. Then, an empirical absorption correction was used based on multi-scan method [72]. The structure of the title compounds were solved by direct method and refined by the full-matrix least-square technique on F^2 using the programs (SHELXS-14) [73] and (SHELXL-18) [74], respectively. The hydrogen atoms were placed at their geometrically idealized positions and refined isotropically. The structure solution of the title compounds were carried out by using WinGX program V2014.1 [75] and geometrically analyzed by PLATON [76]. The details of crystal data and structure refinement parameters are included in Table 4.1. CCDC 2003133–2003135 contain the supplementary crystallographic data of (**1–3**).

Table 4.1. Crystal data and structure refinement parameters of (**1**–**3**).

Structure	**(1)**	**(2)**	**(3)**
Empirical formula	$C_{23}H_{19}N_{3}O_{1}$	$C_{22}H_{17}N_{3}O_{1}$	$C_{20}H_{14}N_{4}$
Formula Weight	353.41	339.38	310.35
Temperature (K)	150(2)	293(2)	150(2)
Wavelength (Å)	0.71073	0.71073	0.71073
Crystal system	Monoclinic	Monoclinic	Orthorhombic
space group	$P2_1/c$	$P2_1/c$	Pbcn
a (Å)	9.3390(18)	19.0733(13)	11.0196(6)
b (Å)	37.293(7)	5.2262(3)	11.3966(6)
c (Å)	11.227(2)	17.3887(11)	12.0792(7)
α (°)	90	90	90
β (°)	113.566(4)	91.695(2)	90
γ (°)	90	90	90
Volume (Å^3)	3583.9(12)	1732.56(19)	1516.98(14)
Z / Density (calc.) (Mg/m^3)	8/1.310	4/ 1.301	4/1.359
Absorption coefficient (mm^{-1})	0.082	0.082	0.084
F(000)	1488	712	648
Crystal size (mm^3)	0.15 × 0.11 × 0.07	0.12 × 0.08 × 0.05	0.18 × 0.13 × 0.09
θ range for data collection (º)	1.092–24.999	2.136–24.996	2.571–24.990
Limiting indices	$-11 \leq h \leq 10$ $-44 \leq k \leq 44$ $-13 \leq l \leq 13$	$-22 \leq h \leq 22$ $-6 \leq k \leq 6$ $-19 \leq l \leq 18$	$-13 \leq h \leq 13$ $-13 \leq k \leq 13$ $-14 \leq l \leq 14$
Reflections collected / unique	33796 / 6318 [R(int) = 0.0603]	15103 / 2885 [R(int) = 0.0437]	16321 / 1341 [R(int) = 0.0246]
Completeness to θ (%)	100.0	94.4	100.0
Absorption correction	Semi-empirical from equivalents	Semi-empirical from equivalents	Semi-empirical from equivalents
Max. and min. transmission	0.99 and 0.98	0.996 and 0.990	0.99 and 0.98
Refinement method	full-matrix least-squares on F^2	full-matrix least-squares on F^2	full-matrix least-squares on F^2
Data/ restraints/ parameters	6318/0/490	2885/0/ 236	1341/0/112
Goodness-of - fit on F^2	1.054	1.048	1.074
Final R indices [$I > 2\sigma(I)$]	$R_1 = 0.0433$ $wR_2 = 0.1061$	$R_1 = 0.0494$ $wR_2 = 0.1375$	$R_1 = 0.0308$ $wR_2 = 0.0822$
R indices (all data)	$R_1 = 0.0646$ $wR_2 = 0.1170$	$R_1 = 0.0735$ $wR_2 = 0.1588$	$R_1 = 0.0335$ $wR_2 = 0.0851$
Largest diff. peak and hole (e.Å^{-3})	0.214 and -0.194	0.175 and -0.207	0.186 and -0.171

$R_1 = \sum||F_o|-|F_c||/\sum|F_o|$, $wR_2 = [\sum\{(F_o^2-F_c^2)^2\}/\sum\{w(F_o^2)^2\}]^{1/2}$, $w = 1/\{\sigma^2(F_o^2) + (aP)^2 + bP\}$, where, a = 0.0556 and b = 0.2925 for (**1**); a = 0.0877 and b = 0.1428 for (**2**); a = 0.0425 and b = 0.4574 for (**3**).

4.2.4. Hirshfeld surface analysis

The Hirshfeld surface [77–80] of compounds (**1**–**3**) have been carried out based on electron distribution of the molecules and are calculated as the sum of spherical atom electron densities [81,82]. Hirshfeld surface is unique for the investigating molecule and a set of spherical atomic electron densities [83]. The normalized contact distance (d_{norm}) is generated based on d_e, d_i and the vd*W* radii of the atom where d_e and d_i are defined as the distance from the point to the nearest nucleus external and internal to the surface respectively. The 2D fingerprint plot [83-86] is generated by using the d_e and d_i parameters that provides summary of intermolecular contacts in the crystal structures. The Hirshfeld surface analyses have been carried out using the program *Crystal Explorer17* [87].

4.2.5. Theoretical methods

The wave function analyses have been performed by using Gaussian09 calculation package [88] at the B3LYP level with a large basis set 6-311++G(d,p). We have used the crystallographic coordinates for the theoretical calculations by using the models that are generated from the supramolecular networks. We have used Bader's "Atoms in molecules" theory [89] to analyze the weak noncovalent interactions by AIMall calculation package [90]. The charge density ($\varrho(r)$) is characterized by their critical points (CPs) and it's Laplacian that is expressed in terms of $L(r) = -\nabla^2(\varrho(r))$ and are calculated using the Atom In Molecule (AIM) theory [91]. According to the topological properties, electron density is concentrated over $\nabla^2(\varrho(r)) < 0$ and is depleted for $\nabla^2(\varrho(r)) > 0$. The theoretical NCI plot [92] is a visualization index that has been used for the characterization of noncovalent interactions. The noncovalent interactions are represented by isosurfaces instead of critical points. These isosurfaces represent both favorable and unfavorable interactions and are differentiated by the isosurface colour scheme with red-yellow-green-blue scale. The red and blue surfaces represent ρ^{+}cut (repulsive) and ρ^{-}cut (attractive) interactions [93] respectively. However, weak repulsive and weak attractive interactions are represented by the yellow and green colour respectively.

4.3. Results and discussion

4.3.1. *Molecular structure*

The molecular view of the title compounds (**1**–**3**) are included in Figure 4.1. In (**1**), the asymmetric unit consists of two molecular moieties whereas there are one moiety in compounds (**2**) and (**3**). The terpyridine unit has an 4-ethoxyphenyl, 4-methoxyphenyl and pyridyl substituent in (**1**–**3**) respectively at the 4′-position of the central pyridyl ring. The structure of compound (**2**) was determined at low temperature (100 K) by Anthonysamy et al. [68] with an R value of 0.056 and later the structure was re-determined by Emmerling et al. [69] with an R value of 0.058 at room temperature (293 K). The structure of compounds (**2**) and (**3**) were reported earlier [68–70] and we are reporting the re-determination of the structures with highest precision with an *R*-value of 0.0494 and 0.0308 respectively. In (**1**–**3**), the terminal pyridine rings of the terpyridine unit adopt *trans-trans* conformation with respect to the interannular C–C bonds. Various terpyridine ligands have *trans-trans* geometry [94-96] in the X-ray structure that are energetically more favorable in comparison to other conformations [97]. The interannular bond distances varies from 1.489(3)Å to 1.493(2)Å (Table 4.2) which are in the normal range and comparable with the averaged values of 1.49(1)Å [94,98]. The molecular conformation of the title compounds are determined by the dihedral angles between the plane of central pyridine ring with terminal pyridine rings and the ring of the substituent group.

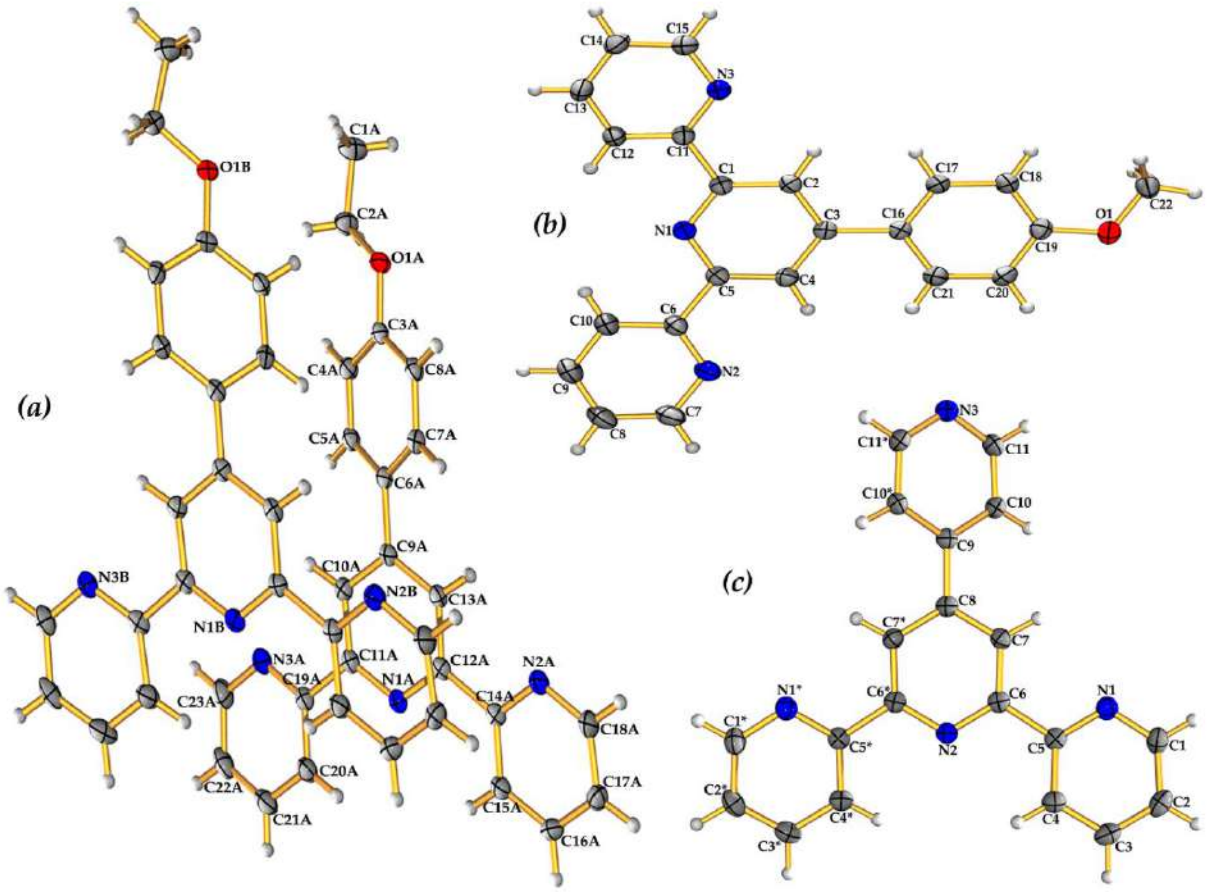

Figure 4.1. ORTEP view and atom-numbering scheme of the title compounds (**1**–**3**)(*a*–*c*). The thermal ellipsoids are drawn at 50% probability level. Symmetry transformations used to generate equivalent atoms in compound (**3**) (* = -x+1, y, -z+1/2).

Table 4.2. Selected bond distances and angles (Å, °) of compounds (**1**–**3**).

Compound (**1**) (Moiety A)		Compound (**1**) (Moiety B)		Compound (**2**)		Compound (**3**)	
C(11A)–C(19A)	1.492(2)	C(11B)–C(19B)	1.490(2)	C(1)–C(11)	1.489(3)	C(5)–C(6)	1.492(2)
C(12A)–C(14A)	1.493(2)	C(12B)–C(14B)	1.492(2)	C(5)–C(6)	1.490(3)	C(5)*–C(6)*	1.492(2)
C(6A)–C(9A)	1.482(2)	C(6B)–C(9B)	1.483(2)	C(3)–C(16)	1.493(3)	C(8)–C(9)	1.491(2)
N(3A)–C(19A)–C(11A)	116.51(15)	N(3B)–C(19B)–C(11B)	116.87(15)	N(3)–C(11)–C(1)	117.59(16)	N(1)–C(5)–C(6)	116.36(10)
C(11A)–N(1A)–C(12A)	117.55(14)	C(11B)–N(1B)–C(12B)	117.66(14)	C(1)–N(1)–C(5)	117.58(15)	C(6)–N(2)–C(6)*	117.97(13)
C(12A)–C(14A)–N(2A)	116.61(14)	C(12B)–C(14B)–N(2B)	117.48(14)	C(5)–C(6)–N(2)	117.24(17)	C(6)*–C(5)*–N(1)*	116.36(10)

The terpyridine unit of both moieties in (**1**) and in (**2**–**3**) are almost planar with small dihedral angles between the planes of central pyridine ring and terminal pyridine rings. The aryl ring of the ethoxyphenyl and methoxyphenyl substituent in (**1**–**2**) and pyridyl ring substituent in (**3**) is slightly twisted. The dihedral angle between the central pyridine ring and the aryl ring in (**1**) is 29.34(6)° and 27.93(5)° in moieties A and B respectively, whereas the angles are 5.72(4)° and 18.62(3)° in (**2**) and (**3**) respectively. These dihedral angles are in normal range and comparable with the related structures reported earlier [94,96,99,100]. In (**1**), the C(20A) and C(23A) atoms of moiety-A, C(18B) and C(15B) atoms of moiety-B have the largest deviations in opposite direction from the mean plane generated through the atoms of the terpyridine unit. The atoms C(3A) and C(1A) of moiety-A, C(2B) and C(1B) from moiety-B have the largest deviations from the least square mean planes generated through the atoms of the ethoxyphenyl group. In (**2**), C(14) and C(12) atoms of the terpyridine unit and C(22) and O(1) atoms of the substituent group have the largest deviations in opposite directions. In (**3**), C(1) and C(4) atoms of the terpyridine unit and C(10) and C(11) atoms of the substituent pyridyl ring have the largest deviations in opposite directions from the least-square mean plane generated through the atoms of the terpyridine unit and substituent unit respectively.

4.3.2. Supramolecular assembly

Compound (**1**) is stabilized through intermolecular C–H···π and π–π stacking interactions (Tables 4.3, 4.4). Due to the self-complementarity nature, the centroid of the aryl ring of moiety A is juxtaposed from both sides by two B moieties through C–H···π interactions. The carbon atoms C(4B) and C(7B) of the aryl ring of 4-ethoxyphenyl group from moiety B in the molecules at (-1+x, y, z) and (x, y, z) binds the centroid of the aryl ring of the same group of moiety A with separation distances of 3.540(2)Å and 3.417(2)Å respectively (Table 4.3). The aryl ring carbon atom C(4A) is again juxtaposed the centroid of the aryl ring of moiety

B in the molecule at (1-x, -y, -z) through C–H···π interaction (Figure 4.2). The packing in compound (**1**) is such that the π–π stacking interactions between the terminal pyridine rings of one moiety with the central pyridine ring of another moiety of adjacent layers are optimized. The terminal pyridine ring of moiety A and the central ring of moiety B at (x, y, z) and (1+x, y, z) are juxtaposed through π–π stacking, with an interplanar spacing of 3.470Å, and a ring centroid separation of 3.666(2)Å (Table 4.4). In another layer, the central ring of moiety A and terminal ring of moiety B are in contact through π stacking with a ring centroid separation of 3.685(2)Å. The combination of C–H···π and π–π stacking interactions results in a two-dimensional layered assembly in (**1**) (Figure 4.2).

Table 4.3. Geometrical Parameters for C–H···π Interaction

X–H···Cg	H···Cg	X···Cg	H···Perp	X-H···Cg	Symmetry
*Compound (**1**)*					
C(4A)–(H4A)···Cg(8)	2.91	3.689(2)	2.88	143	1-x, -y, -z
C(4B)–(H4B)···Cg(4)	2.84	3.540(2)	2.83	133	-1+x, y, z
C(7B)–(H7B)···Cg(4)	2.71	3.417(2)	2.69	133	x, y, z
*Compound (**3**)*					
C(10)–(H10)···Cg(1)	2.68	3.4726(12)	2.670	144	1/2+x, -1/2+y, 1/2-z

Cg(4), Cg(8) and Cg(1) are the centroids of the [C(3A)–C(8A)], [C(3B)–C(8B)] and [N(1)/C(1)–C(5)] rings respectively.

Compound (**2**) is stabilized through intermolecular π–π interactions (Table 4.4). The hydrogen bonding interactions that were explored by Anthonysamy et al [68] in the previously reported structure of the compound are not found in the investigating structure. In the solid-state, the title structure is optimized through dual π-interactions that are exhibited in between the central pyridine ring and two terminal pyridine rings. The central ring and terminal ring at (x, y, z) and (x, -1+y, z) are juxtaposed through a intercentroid separation distance of 3.999Å. The molecular assembly that is generated through the π–π interactions is depicted in Figure 4.3.

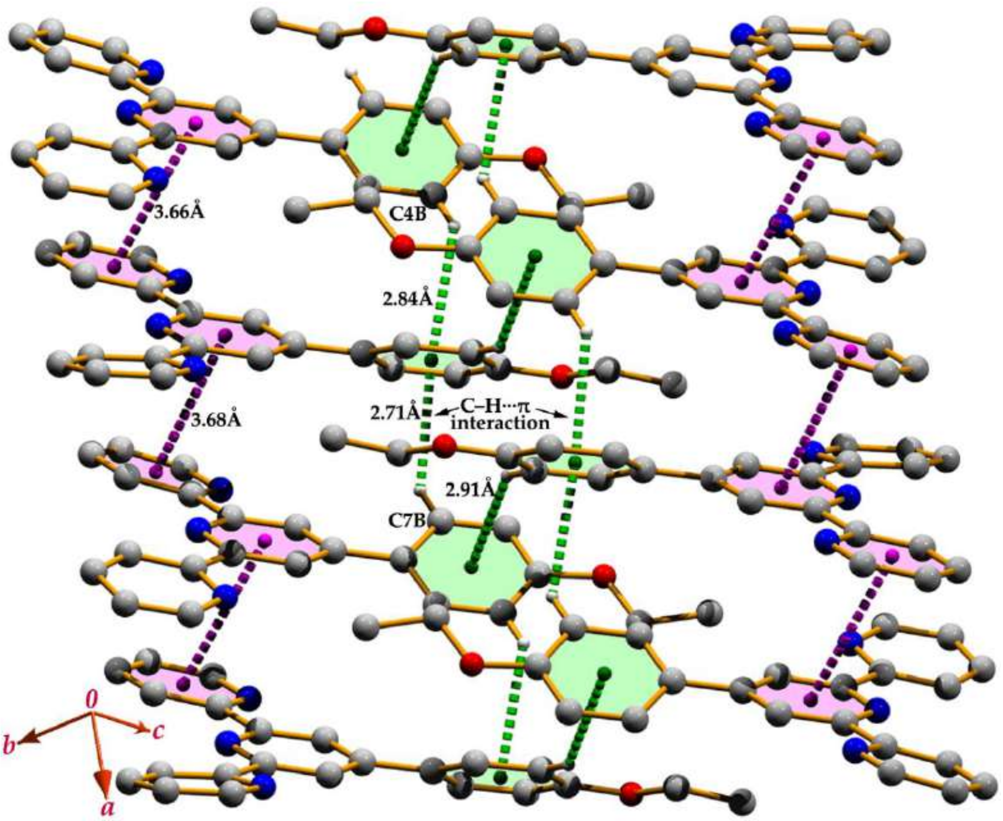

Figure 4.2. Supramolecular network generated through dual C–H···π and π–π stacking interactions in (**1**). The C–H···π and π–π contacts are shown as green and pink dotted lines respectively.

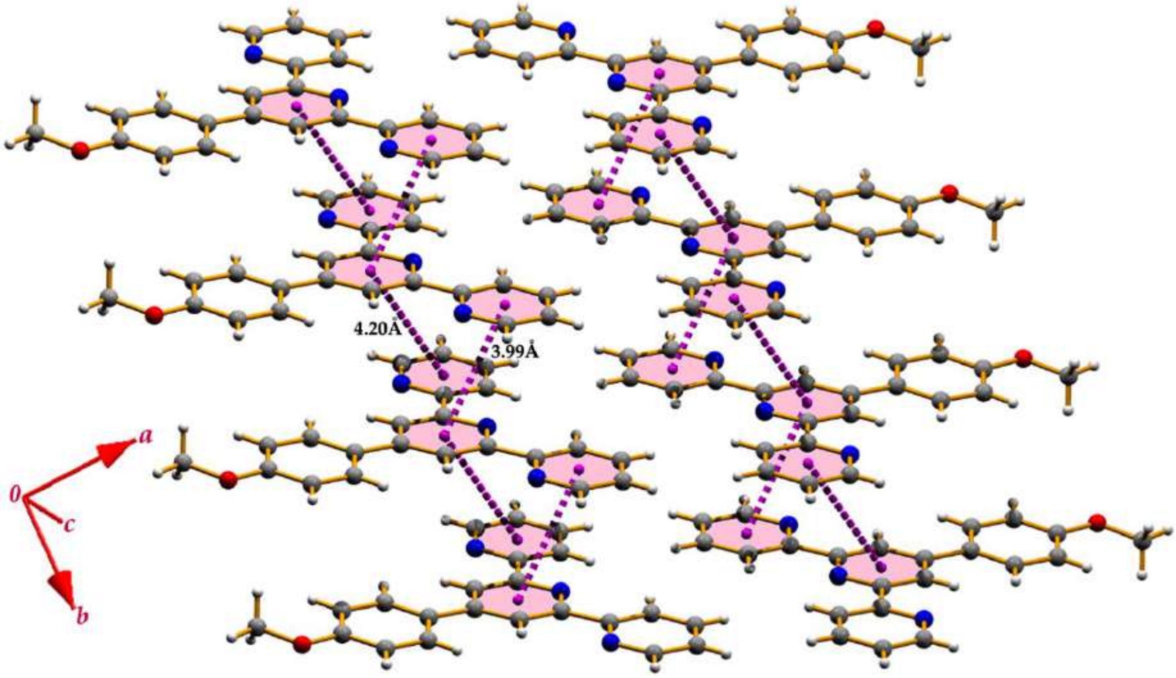

Figure 4.3. Perspective view of the molecular assembly of (**2**) that is generated through π–π stacking interactions. Pink dotted lines show the π–π contacts.

Table 4.4. Geometrical Parameters for π-Stacking Interactions.

Rings *i–j*[a]	**Rc[b]**	**R1v[c]**	**R2v[d]**	**α[e]**	**β[f]**	**γ[g]**	**symmetry**
***Compound* (1)**							
Cg(1)–Cg(6)	3.6849(12)	3.450	3.447	8.87	20.71	20.58	x, y, z
Cg(2)–Cg(5)	3.6665(12)	3.470	3.518	5.18	16.39	18.83	1+x, y, z
Cg(2)–Cg(2)	3.6666(12)	3.518	3.470	5.18	18.83	16.39	-1+x, y, z
Cg(6)–Cg(1)	3.6848(12)	3.447	3.450	8.87	20.58	20.71	x, y, z
***Compound* (2)**							
Cg(1)–Cg(2)	3.9994(12)	3.423	3.447	1.45	30.5	31.2	x, -1+y, z
Cg(1)–Cg(3)	4.2043(12)	3.437	3.446	1.60	34.9	35.2	x, 1+y, z
Cg(2)–Cg(1)	3.9993(12)	3.447	3.423	1.45	31.2	30.5	x, 1+y, z
***Compound* (3)**							
Cg(1)–Cg(2)	4.0416(6)	3.276	3.669	11.23	24.79	35.85	1-x, -y, 1-z
Cg(1)–Cg(2)	4.0416(6)	3.276	3.669	11.23	24.79	35.85	x, -y, 1/2+z
Cg(2)–Cg(1)	4.0416(6)	3.669	3.276	11.23	35.85	24.79	1-x, -y, 1-z
Cg(2)–Cg(1)	4.0416(6)	3.669	3.276	11.23	35.85	24.79	x, -y, -1/2+z

For compound (**1**): Cg(1), Cg(2), Cg(5), and Cg(6) are the centroids of the [N(1A)/C(9A)–C(13A)], [N(2A)/C(14A)–C(18A)], [N(1B)/C(9B)–C(13B)] and [N(2B)/C(14B)–C(18B)] rings, respectively. For compound (**2**): Cg(1), Cg(2) and Cg(3) are the centroids of the [N(1)/C(1)–C(5)], [N(2)/C(6)–C(10)] and [N(3)/C(11)–C(15)] rings respectively. For compound (**3**): Cg(1) and Cg(2) are the centroids of the [N(1)/C(1)–C(5)] and [N(2)/C(6)/C(7)/C(8)/C(7*)/C(6*)] rings respectively.

[b]Centroid distance between ring *i* and ring *j*. [c]Vertical distance from ring centroid *i* to ring *j*. [d]Vertical distance from ring centroid *j* to ring *i*. [e]Dihedral angle between the first ring mean plane and the second ring mean plane of the partner molecule. [f]Angle between centroids of first ring and second ring mean planes. [g]Angle between the centroid of the first ring and the normal to the second ring mean plane of the partner molecule.

Despite the similarity between compounds (**1**) and (**2**) in terms of their general composition and detailed molecular geometries, compound (**3**) have some substantial alterations in the nature of the supramolecular aggregation. The molecules of (**3**) are linked into different molecular framework by a combination of C–H···π and π–π stacking interactions. In the first sub-structure, both the carbon atom C(10) and C(10)* of the substituted pyridine ring (see Figure 4.1c) are in contact with the centroids of the terminal pyridine rings of the terpyridine moiety in the molecule at (1/2+x, -1/2+y, 1/2-z) with a separation distance of 2.68Å.

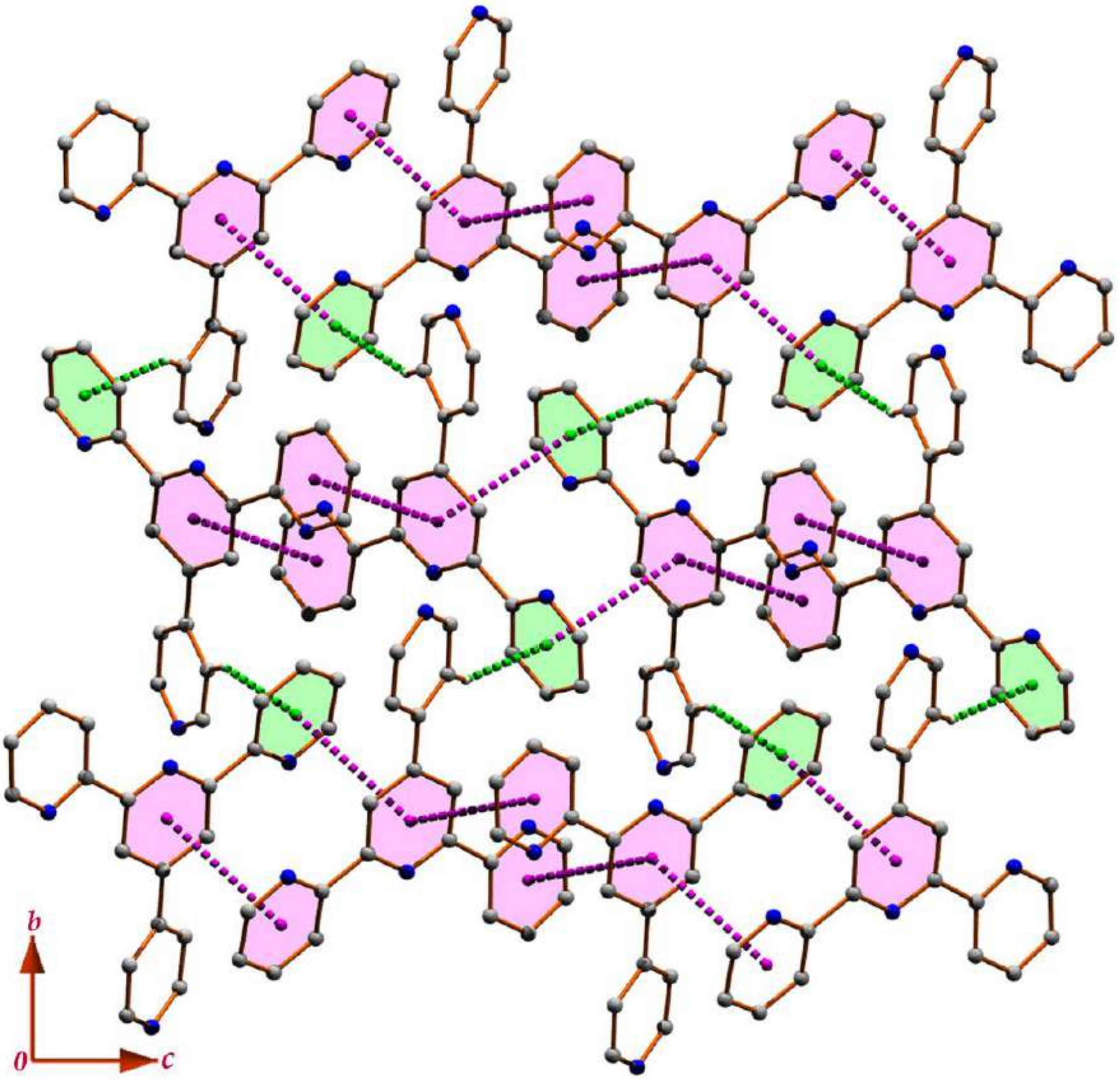

Figure 4.4. Supramolecular framework generated through C–H···π and π–π stacking interactions in (**3**). The C–H···π and π–π contacts are shown as green and pink dotted lines respectively.

Due to the inversion symmetry, the substituted pyridine ring carbon atoms of the parent molecule binds two-partner molecules in both side of the ring through C–H···π interaction. Accordingly, a two-dimensional supramolecular layered assembly is generated in the (110) plane. In the final structure, the central and terminal pyridine rings are optimized through π–π stacking interaction. In one side, the central ring and terminal ring at (x, y, z) and (1-x, -y, 1-z) are juxtaposed with an intercentroid separation of 3.99Å. In the other side of the central ring at (x, y, z), symmetrically generated terminal ring at (x, -y, 1/2+z) of another partner molecule is in contact through π–π stacking interaction.

Consequently, the central pyridine ring is sandwiched through the dual π–π stacking interaction (Figure 4.4). Finally, the substituted pyridine ring carbon atom is in contact with the terminal pyridine through C–H···π interaction. Therefore, a unique C–H···π/π–π/π–π network is self-generated to build the supramolecular assembly in (011) plane (Figure 4.4).

4.3.3. Hirshfeld Surface

The similarities of the title structures (**1**–**3**) in terms of their molecular geometries and the pattern of the noncovalent interactions encouraged us to quantify the contribution of the interactions. In this context, we have calculated Hirshfeld surface [77-80] of the title compounds that are illustrated in Figure 4.5. In compound (**1**), two molecular moieties (A and B) have been calculated separately. We have analyzed various surfaces for the title compounds that have been mapped over d_{norm}, d_e, shape-index, curvedness and fragment patches (see Figure 4.5). No large circular depressions are evident on the d_{norm} surfaces due to absence of strong hydrogen bonding contacts. The weak interactions like C–H···π and π–π contacts that are involved within the structures are examined and evidenced by different surfaces. Moreover, the 2D fingerprint plot [83-86] represent all intermolecular interactions that are involved within the structures (Figure 4.6). To quantify each individual contacts, we have decomposed the full-fingerprint plots in unique visual mode. The O···H/H···O contacts are evidenced by the spoon like tips in the region ($d_i + d_e \approx 2.653$Å) of both moieties of compound (**1**), whereas in (**2**) the tips are located in the region ($d_i + d_e \approx 2.828$Å) (Figure 4.6). The O···H/H···O contacts contributed 4.0% and 3.5% in moiety A and B respectively of (**1**) whereas the contribution is 5.2% to the total Hirshfeld surface area of (**2**). The N···H/H···N contacts varies from 6.1% in (**2**) to 18.4% in (**3**). The sharp tips in the (d_i, d_e) region of (1.462Å, 1.076Å) and (1.457Å, 1.066Å) designate the N···H/H···N interaction in compounds (**2**) and (**3**) respectively (Figure 4.6).

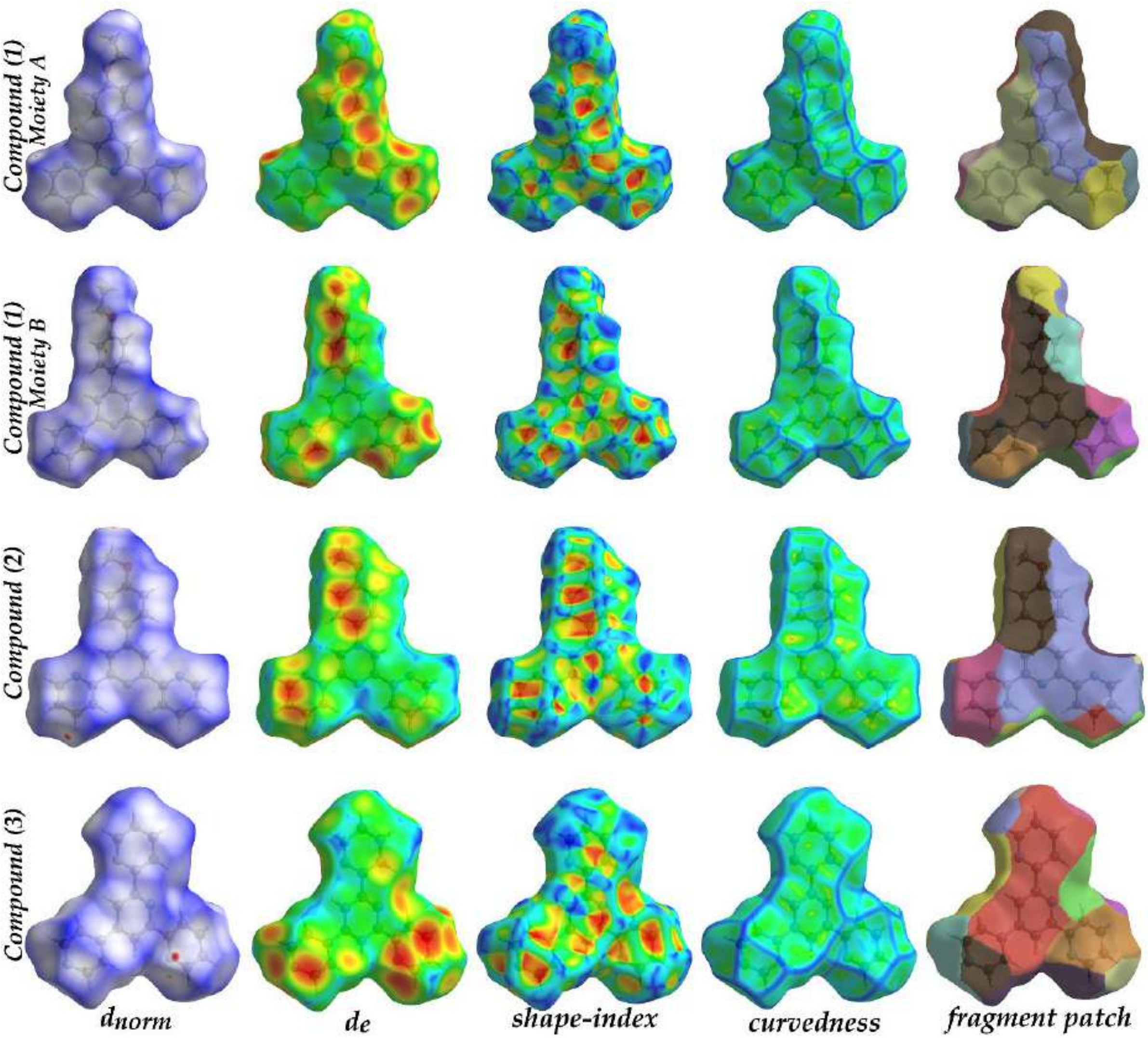

Figure 4.5. Hirshfeld surfaces mapped with d_{norm}, d_e, shape-index, curvedness and fragment patches for compounds (**1**–**3**).

The C–H···π contacts are evidenced by the bright-orange spots on the d_e surface which is also viewed as distinct 'wings' in the fingerprint plots [101]. As evidenced and discussed in the X-ray structural discussion section, the bright-orange spots are evidenced on the substituted aryl ring of both moieties of compound (**1**) and symmetrically generated terminal pyridine rings in (**3**) that are the characteristics feature of C–H···π interaction. The 'wings' are other characteristics of C–H···π interaction which are evidenced in the bottom right [(d_i, d_e) = (2.088Å, 1.197Å)], top left [(d_i, d_e) = (1.192Å, 2.088Å)] and both sides [(d_i, d_e) = (1.943Å, 1.111Å)] of the fingerprint plots of moiety A, Moiety B (compound **1**) and compound (**3**) respectively (Figure 4.6). The C···N/N···C contacts varies from 3.5% in (**3**) to 4.7% in (**2**). The contribution of N···N close contacts are 0.0 % in (**3**) whereas compound (**2**) contributed the maximum contribution (1.1%). To explore the π–π contacts, we have critically inspected the shape-index and curvedness surfaces. An adjacent red-blue triangle on the π-cloud of a ring and a flat region on both sides of a ring on the shape-index and curvedness surface respectively characterize the π–π stacking interactions [56]. The red-blue triangles and consequently the flat regions are evidenced on the central and terminal pyridine rings of (**1**–**3**) (Figure 4.5). In the decomposed fingerprint plot, the π–π stacking interactions are evidenced by the region of blue/green colour on the diagonal at around $d_i = d_e$ = 1.071Å, $d_i = d_e$ = 1.677Å, $d_i = d_e$ = 1.753Å and $d_i = d_e$ = 1.713Å of compounds (**1**–**3**) respectively. The contribution of C···C contacts varies from 3.2% in (**2**) to 6.7% in (**3**). The visual representation of the fragment patches represents the identification of their closeness to adjacent molecules. (Figure 4.5). A substantial variance is observed for H···H contacts (40.1% in (**3**) to 51.7% in moiety B of (**1**)) that is reflected in the scattered points of the fingerprint plots at $d_i = d_e$ = 1.692Å in moiety A of (**1**), $d_i = d_e$ = 1.091Å in moiety B of (**1**), $d_i = d_e$ = 1.071Å in (**2**) and $d_i = d_e$ = 1.176Å in (**3**) (Figure 4.6). The variety of contacts that are involved within the structures of (**1**–**3**) are quantified and compared in a novel visual manner.

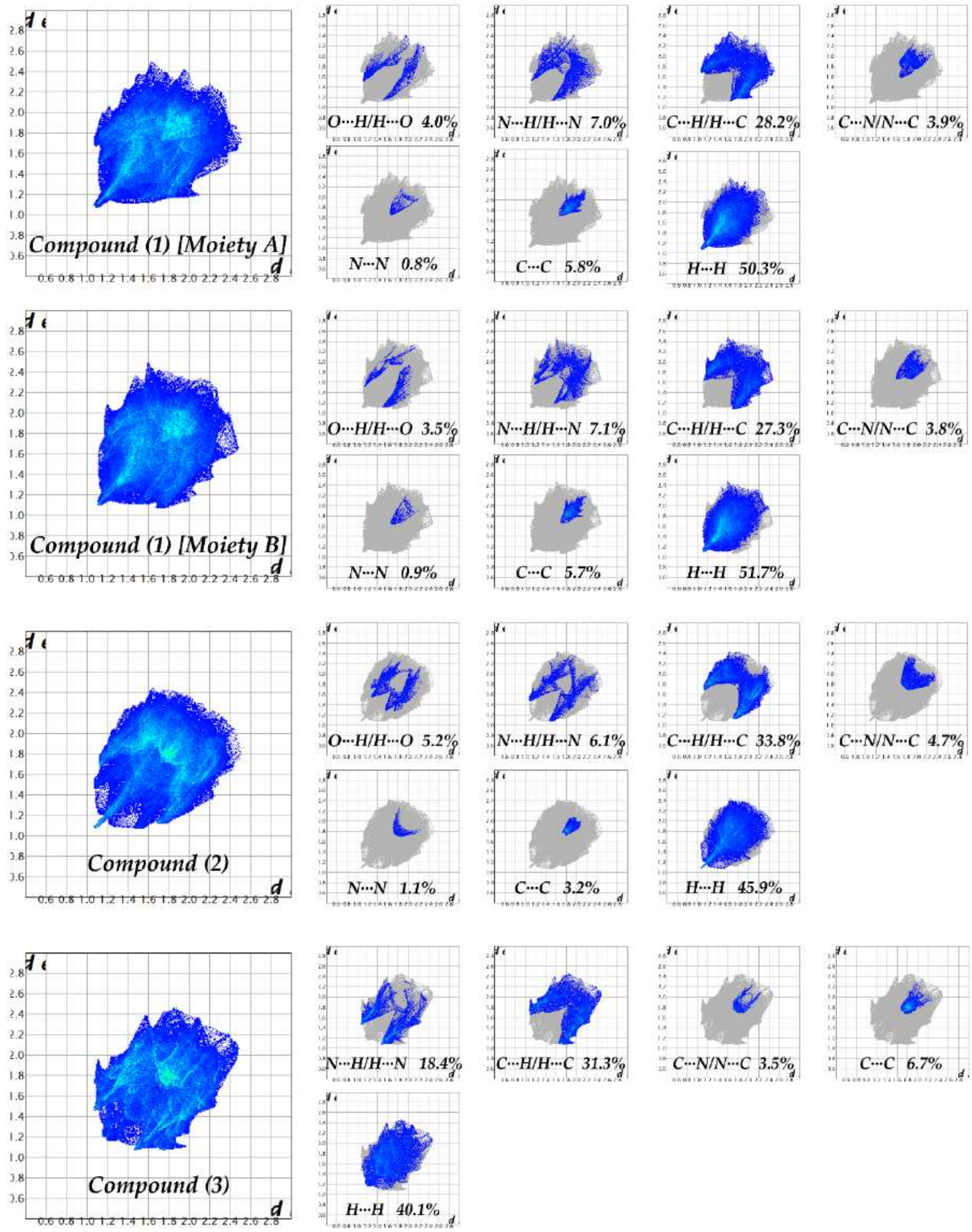

Figure 4.6. Fingerprint plots (Full) and decomposed plots for each individual interactions in (**1**–**3**).

4.3.4. *Theoretical analysis*

We have carried out the Bader's theory of "atoms in molecules"(AIM) of compounds (**1**–**3**). In this calculation, the molecular graph consists of various colored spheres that are shown in Figure 4.7. For compound (**1**), we have used moiety A in this calculation. The white, gray, red and yellow spheres are corresponds to hydrogen nuclei, carbon nuclei, bond critical point (BCP) and ring critical point (RCP) respectively. Black paths are bond paths that originate at BCPs and terminate at nuclei. In Figure 4.7, the RCP to BCP paths are shown as green colored paths whereas RCP attractor paths are shown as yellow dotted paths. We have analyzed the interatomic surface eigen vector (IAS EV) paths for the title compounds (**1**–**3**). The pink colored paths (see Figure 4.8.) that are locally parallel or antiparallel with two negative-eigenvalued eigenvectors of the Hessian of Rho (HessRho) show the IAS EV paths. To get an idea of the shape of the interatomic surface, we have used all bond paths to generate the IAS EV paths where there are four IAS EV paths for each BCP (Figure 4.8). We have analyzed the contour maps of the electron density (ϱ) and Laplacian of the electron density ($\nabla^2\varrho$) (Figure 4.9). The Laplacian of electron density provides the measure of the local charge concentration or depletion for compounds (**1**–**3**) (see Figures. 4.9d-f). The Laplacian of the electron density is extremely important due to two facts: (i) it recovers the shell structure of atoms; (ii) it allows to trace the effects of the chemical bonding in the total charge density. In these contour maps blue and red colour denotes the positive values of the mean local charge depletion and negative values of the mean local charge concentration.

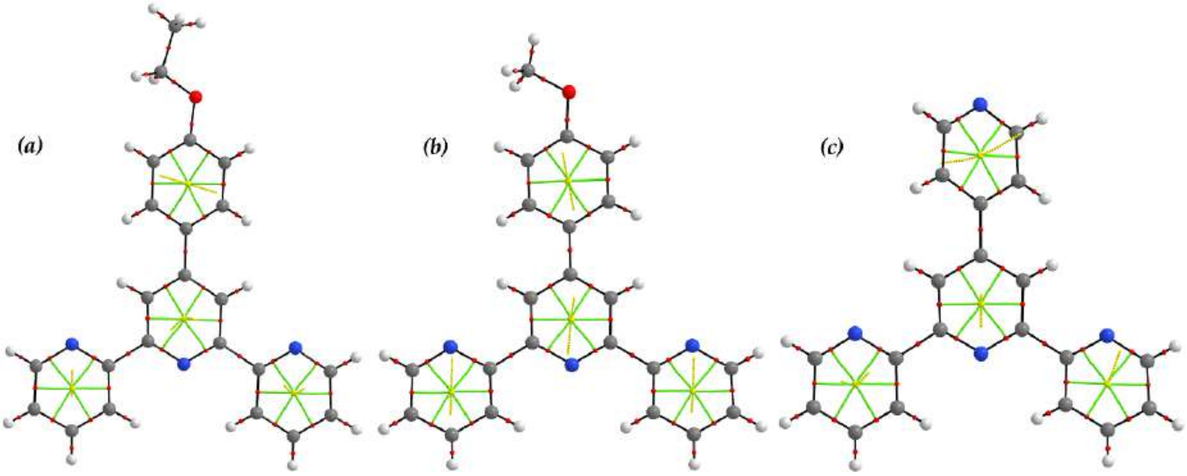

Figure 4.7. RCP to BCP and RCP attractor paths for compounds (*a*-*c*)(**1**–**3**).

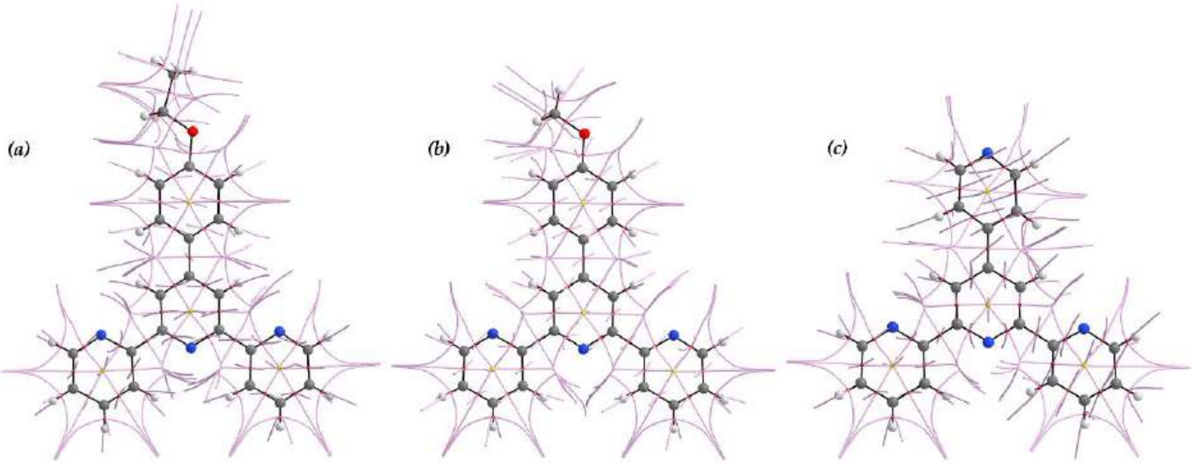

Figure 4.8. IAS EV paths for compounds (**1–3**).

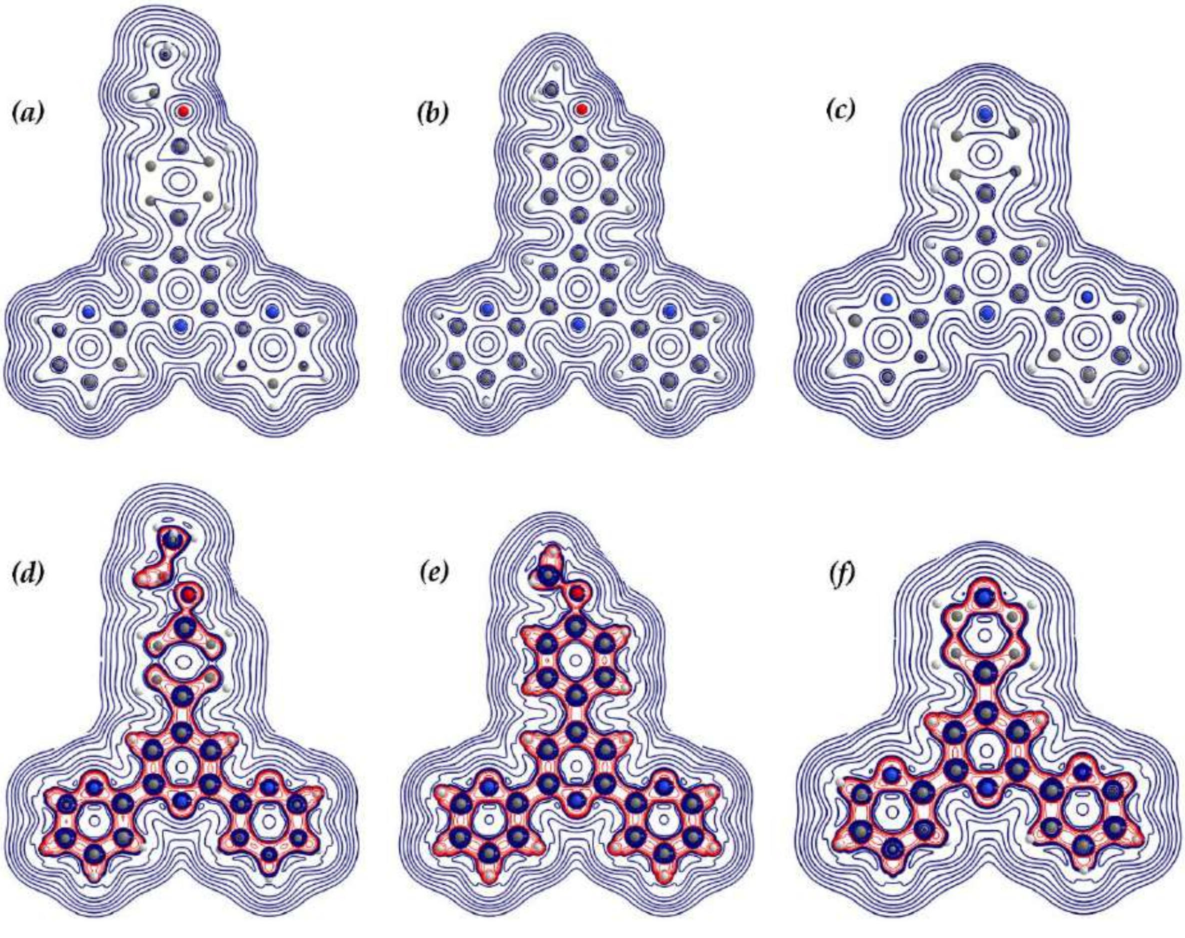

Figure 4.9. Contour maps of the electron density (*a–c*) and Laplacian of the electron density (*d–f*) for compounds (**1–3**) respectively.

Again, we have carried out the AIM calculations by using various models that are depicted in Figure 4.10. These models are generated from the X-ray structure of the title compounds. In this theoretical calculation, the interactions are confirmed through the bond path and a bond critical point that interconnects two atoms [102]. The distribution of critical points displays that the C–H···π interaction (models 1, 2, 4) that is characterized by the presence of a bond CP and bond path connecting the aryl/pyridine H-atom to one of the carbon atoms of the aryl/pyridine ring (Figure 4.10a,b,d). In Table 4.5, we summarize the charge electron density, Laplacian, ellipticity, virial field density, Lagrangian kinetic energy density and Hamiltonian kinetic energy density [ϱ, $\nabla^2\varrho$, ε, V, G and K, respectively] at the BCPs of (**1**–**3**). The π–π stacking interaction (models 1, 3, 5) is characterized by the presence of CP and bond path interconnecting central to terminal and/or terminal to central pyridine rings (Figure 4.10a,c,e). Following Figure 4.2, two models (Figure 4.10a,b) are used for compound (**1**) to characterize the interactions. In Figure 4.10a, one aryl ring of the substituted ethoxyphenyl group is sandwitched through C–H···π interaction where the bond paths are connected between two carbon atoms of the aryl ring and the aromatic H-atom of two rings. Similarly, in Figure 4.10b, the bond path interconnecting the aryl ring carbon and ring hydrogen atom characterized the C–H···π interaction; the charge density $\varrho(r)$ at the bond CPs is included in the Figure 4.10a,b. In compound (**3**), the bond CP (ϱ_{BCP} = 0.0055 a.u.) and bond path connecting substituted pyridine ring H-atom and carbon atom of the terminal pyridine ring characterized the C–H···π interaction (see Figure 4.10d). The BCP and bond paths between pyridine nitrogen and carbon atoms of the pyridine rings characterizes the π–π stacking interactions in compounds (**1**–**3**) (Figure 4.10a,c,e). The inspection of the results indicates that the values of $\varrho(r)$ at the bond CP (ϱ_{BCP} = 0.0068/0.0054 a.u.) in (**1**) are larger in comparison to the other two compounds, in good agreement with the intercentroid separation distances observed from X-ray structures.

Table 4.5. Detailed AIM parameters (ϱ, $\nabla^2\varrho$, ε, V, G and K, a.u.) at the BCPs (See Figure 4.10).

Bond CP	ϱ	$\nabla^2\varrho$	ε	V	G	K
a (CH···π)	0.0060	0.0234	2.2826	-0.0036	0.0047	-0.0011
b (π···π)	0.0033	0.0155	0.9624	-0.0022	0.0030	-0.0009
c (π···π)	0.0068	0.0244	0.7393	-0.0046	0.0053	-0.0008
d (CH···π)	0.0044	0.0175	2.3895	-0.0024	0.0034	-0.0010
e (π···π)	0.0043	0.0148	6.9146	-0.0027	0.0032	-0.0005
f (π···π)	0.0054	0.0174	4.1648	-0.0033	0.0038	-0.0005
g (CH···π)	0.0048	0.0174	1.0454	-0.0028	0.0036	-0.0008
h (π···π)	0.0039	0.0169	1.5800	-0.0024	0.0033	-0.0009
i (π···π)	0.0046	0.0164	1.7373	-0.0027	0.0034	-0.0007
j (CH···π)	0.0055	0.0218	2.3462	-0.0032	0.0043	-0.0011
k (π···π)	0.0047	0.0193	1.0733	-0.0032	0.0040	-0.0008

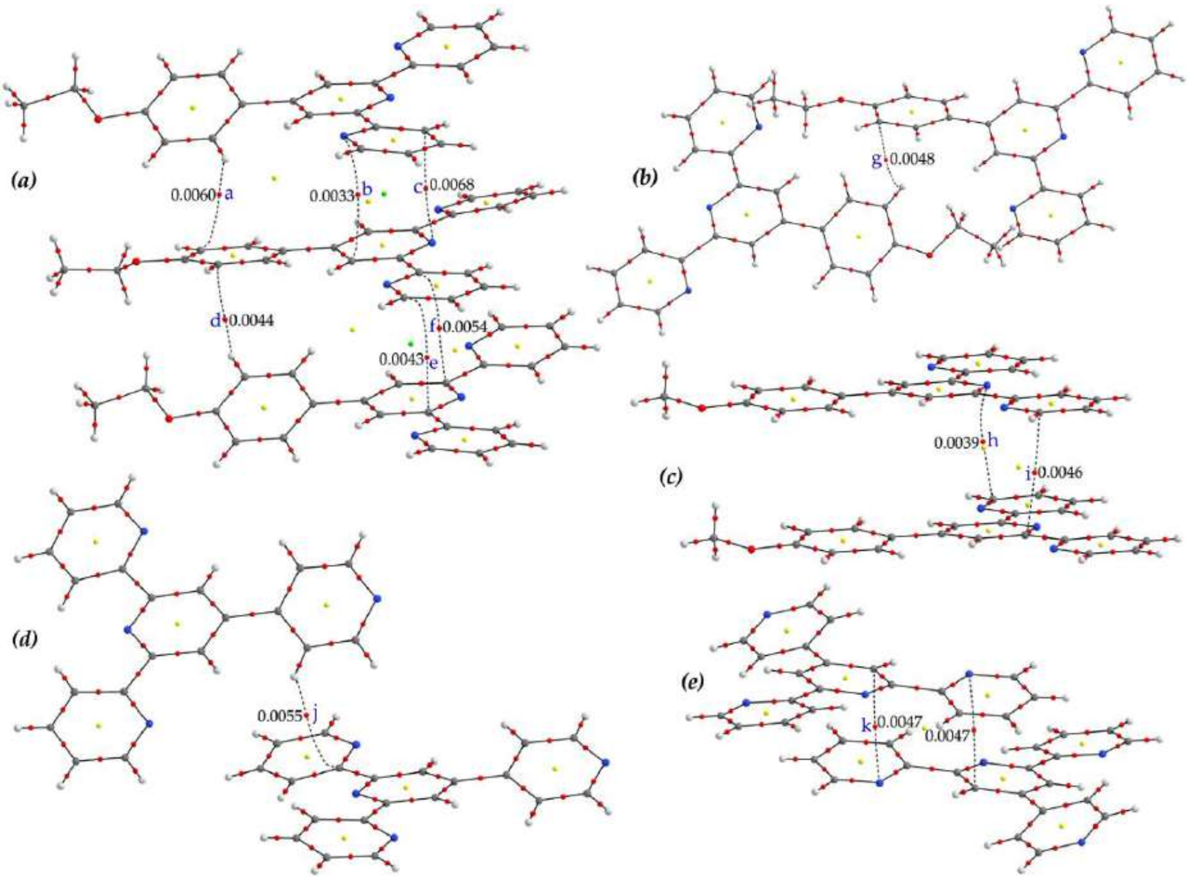

Figure 4.10. AIM analyses of compounds **1**(*a,b*), **2**(*c*), **3**(*d,e*). Red and yellow spheres represent bond and ring critical points, respectively. The $\varrho(r)$ values at the bond critical points are included in atomic units (a.u.).

The noncovalent interactions are further characterized by using 'noncovalent interaction' (NCI) plot computational tool that permits to assess the self-assembled structure. The cooperativity of C–H···π and π–π interactions in (**1–3**) have been characterized by using the same model that were used in AIM calculations (Figure 4.10.acde). The absence of the strong blue isosurface clearly indicates that the title structures do not exhibit strong hydrogen bonds. The large green dual isosurfaces (See Figure 4.11.a) in between the phenyl rings of the substituted ethoxyphenyl groups of the model undoubtedly designate the cooperative C–H···π/π···H–C interactions in (**1**). Similarly, a large green isosurface above the π-cloud of a terminyl pyridine ring (Figure 4.11.c) designate C–H···π interaction in (**3**). The presence of the larger isosurfaces in between terminal to central pyridine ring (Figure 4.11.a,b) and terminal to terminal pyridine ring (Figure 4.11.d) designates the π–π stacking interactions in compounds (**1**–**2**) and (**3**) respectively.

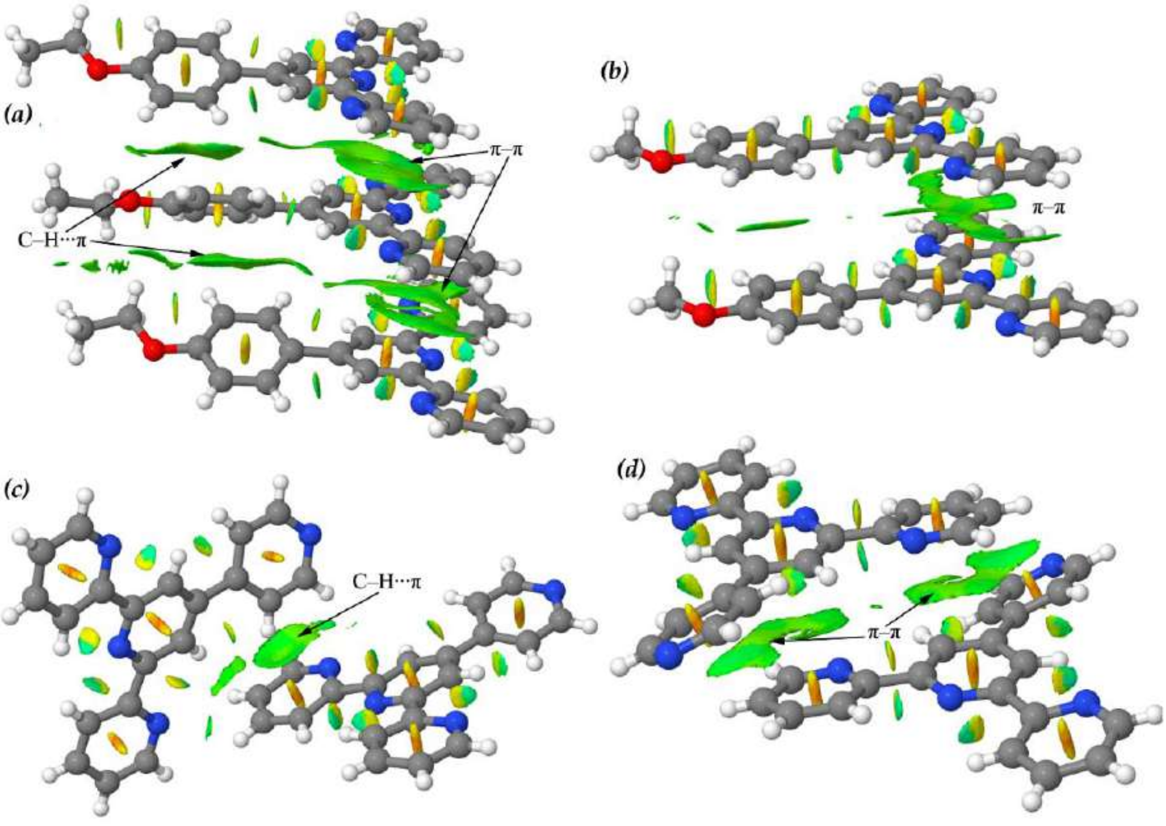

Figure 4.11. NCI plot of the self-assembled structure of compounds (**1**)(*a*), (**2**)(b) and (**3**)(*c,d*).

4.4. Conclusions

In summary, three 4′-functionalized 2,2′:6′,2″-terpyridine compounds (**1**–**3**) have been synthesized and structurally characterized. Compounds (**1**) and (**3**) exhibits both C–H···π and π–π stacking interactions however, compound (**2**) exhibits π–π stacking only. Compounds (**1**) and (**3**) shows cooperative C–H···π/π···H–C and C–H···π/π–π extended networks respectively. Nevertheless, compound (**2**) shows π–π/π–π cooperative network in the solid-state. The entire supramolecular self-assembly and consequent cooperativity of weak noncovalent interactions have been analyzed in detail and further quantified by theoretical Hirshfeld surface analysis. All the interactions are quantified through the infographic fingerprint plots. Additionally, the noncovalent interactions have been characterized by Bader's theory of 'atoms-in-molecules'(AIM). Furthermore, the interplay of the interactions that played significant role in building the final structures have been analyzed by theoretical 'Noncovalent Interaction' (NCI) plot index. The theoretical investigations based on the AIM and NCI analyses verifies the experimental findings by characterizing the intricate combination of intermolecular interactions of the title compounds. Therefore, the results described herein are expected to be beneficial for understanding the cooperativity effect and quantification of noncovalent interactions.

4.5. References

[1] K. Yamamoto, J. Li, J.A.O. Garber, J.D. Rolfes, G.B. Boursalian, J.C. Borghs, C. Genicot, J. Jacq, M. V. Gastel, F. Neese, T. Ritter, Nature 554 (2018) 511–514.

[2] L. An, C. Xu, X. Zhang, Nature Commun. 8 (2017) 1460.

[3] S. Krautwald, M.J. Bezdek, P.J. Chirik, J. Am. Chem. Soc. 139 (2017) 3868–3875.

[4] Y.-J. He, T.-H. Tu, M.-K. Su, C.-W. Yang, K.V. Kong, Y.-T. Chan, J. Am. Chem. Soc. 139 (2017) 4218–4224.

[5] D. Samanta, I. Paul, M. Schmittel, Chem. Commun. 53 (2017) 9709–9712.

[6] A. Das, A. D. Jana, S. K. Seth, B. Dey, S. R. Choudhury, T. Kar, S. Mukhopadhyay, N. J. Singh, I.-C. Hwang, K. S. Kim, J. Phys. Chem. B 114 (2010) 4166–4170.

[7] S. K. Seth, P. Manna, N. J. Singh, M. Mitra, A. D. Jana, A. Das, S. R. Choudhury, T. Kar, S. Mukhopadhyay, K. S. Kim, CrystEngComm 15 (2013) 1285–1288.

[8] P. Manna, S. K. Seth, M. Mitra, A. Das, N. J. Singh, S. R. Choudhury, T. Kar, S. Mukhopadhyay, CrystEngComm 15 (2013) 7879–7886.

[9] P. Manna, S. K. Seth, Antonio Bauzá, M. Mitra, S. R. Choudhury, A. Frontera, S. Mukhopadhyay, Cryst. Growth Des. 14 (2014) 747–755.

[10] P. Manna, S. K. Seth, M. Mitra, S. R. Choudhury, Antonio Bauzá, A. Frontera, S. Mukhopadhyay, Cryst. Growth Des. 14 (2014) 5812–5821.

[11] G.T. Morgan, F.H. Burstall, J. Chem. Soc. (1932) 20–30.

[12] J.M. Lehn, Supramolecular chemistry, Science 260 (1993) 1762–1763.

[13] M.D. Ward, P.R. Raithby, Chem. Soc. Rev. 42 (2013) 1619–1636.

[14] A.K. Pal, G.S. Hanan, Chem. Soc. Rev. 43 (2014) 6184–6197.

[15] A. Sil, D. Giri, S.K. Patra, J. Mater. Chem. C 5 (2017) 11100–11110.

[16] Y. Chi, P.T. Chou, Chem. Soc. Rev. 39 (2010) 638–655.

[17] S. Chakraborty, G.R. Newkome, Chem. Soc. Rev. 47 (2018) 3991–4016.

[18] R. Sakamoto, K.-H. Wu, R. Matsuoka, H. Maeda, H. Nishihara, Chem. Soc. Rev. 44 (2015) 7698–7714.

[19] J. Husson, M. Knorr, Beilstein J. Org. Chem. 8 (2012) 379–389.

[20] A. Wild, A. Winter, F. Schlütter, U.S. Schubert, Chem. Soc. Rev. 40 (2011) 1459–1511.

[21] I. Eryazici, C.N. Moorefield, S. Durmus, G.R. Newkome, J. Org. Chem. 71 (2006) 1009–1014.

[22] S. Romain, C. Baffert, C. Duboc, J.C. Lepretre, A. Deronzier, M.N. Collomb, Inorg. Chem. 48 (2009) 3125–3131.

[23] Q. Zhang, X.H. Tian, H.P. Zhou, J.Y. Wu, Y.P. Tian, Materials 10 (2017) 223.

[24] B.B. Cui, Y.W. Zhong, J. Yao, J. Am. Chem. Soc. 137 (2015) 4058–4061.

[25] R. Sakamoto, S. Katagiri, H. Maeda, H. Nishihara, Coord. Chem. Rev. 257 (2013) 1493–1506.

[26] G. Chelucci, R.P. Thummel, Chem. Rev. 102 (2002) 3129–3170.

[27] G. Zhang, J. Tan, T. Phoenix, D.R. Manke, J.A. Golen, A.L. Rheingold, RSC Adv. 6 (2016) 9270–9277.

[28] D. Zych, A. Slodek, M. Matussek, M. Filapek, G. S-Gorol, S. Maślanka, S. Krompiec, S. Kotowicz, E. S-Balcerzak, K. Smolarek, S. Maćkowski, M. Olejnik, W. Danikiewicz, Dyes Pigments 146 (2017) 331–343.

[29] E.C. Constable, Chem. Soc. Rev. 36 (2007) 246–253.

[30] A. O. Adeloye, P. A. Ajibade, Molecules 19 (2014) 12421–12460.

[31] A. M. Burger, F. Dai, C. M. Schultes, A. P. Reszka, M. J. Moore, J. A. Double, S. Neidle, Cancer Res. 65 (2005) 1489–1496.

[32] D. Mahendiran, R.S. Kumar, V. Viswanathan, D. Velmurugan, A.K. Rahiman, Dalton Trans. 45 (2016) 7794–7814.

[33] D. Mahendiran, R.S. Kumar, A.K. Rahiman, Mater. Sci. Eng. C 76 (2017) 601–615.

[34] C. Wei, Y. He, X. Shi, Z. Song, Coord. Chem. Rev. 385 (2019) 1–19.

[35] D. Zych, A. Slodek, S. Krompiec, K. Malarz, A. Mrozek-Wilczkiewicz, R. Musiol, ChemistrySelect 3 (2018) 7009–7017.

[36] D. Zych, A. Slodek, M. Matussek, M. Filapek, G. Szafraniec-Gorol, S. Krompiec, S. Kotowicz, M. Siwy, E. Schab-Balcerzak, K. Bednarczyk, M. Libera, K. Smolarek, S. Maćkowski, W. Danikiewicz, ChemistrySelect 2 (2017) 8221–8233.

[37] D. Zych, A. Slodek, M. Matussek, M. Filapek, G. Szafraniec-Gorol, S. Maślanka, S. Krompiec, S. Kotowicz, E. Schab-Balcerzak, K. Smolarek, S. Maćkowski, M. Olejnik, W. Danikiewicz, Dyes and Pigments 146 (2017) 331–343.

[38] L. Saghatforoush, K. Adil, M. Hasanzadeh, A. Aminkhani, S. Safarinezhad, Acta Chim. Slov. 59 (2012) 322–330.

[39] J. Schönle, E.C. Constable, C.E. Housecroft, Inorg. Chem. Commun. 53 (2015) 80–83.

[40] D. Maspoch, D. Ruiz-Molina, J. Veciana, Chem. Soc. Rev. 36 (2007) 770–818.

[41] A.Y. Robin, K.M. Fromm, Coord. Chem. Rev. 250 (2006) 2127–2157.

[42] D. Braga, F. Grepioni, L. Maini, S. D'Agostino, IUCrJ 4 (2017) 369–379.

[43] D. Braga, F. Grepioni, L. Maini, S. D'Agostino, Eur. J. Inorg. Chem. 2018 (2018) 3597–3605.

[44] T.S. Thakur, R. Dubey, G.R. Desiraju, Annu. Rev. Phys. Chem. 66 (2015) 21–42.

[45] K.E. Riley, P. Hobza, Acc. Chem. Res. 46 (2013) 927–936.

[46] S. Goyal, A. Chattopadhyay, K. Kasavajhala, U.D. Priyakumar, J. Am. Chem. Soc. 139 (2017) 14931–14946.

[47] C. Sutton, C. Risko, J.-L. Brédas, Chem. Mater. 28 (2016) 3–16.

[48] S. K. Seth, A. Bauzá, A. Frontera, New J. Chem. 42 (2018) 12134–12142.

[49] A. Bauzá, S. K. Seth, A. Frontera, Coord. Chem. Rev. 384 (2019) 107–125.

[50] H.-J. Schneider, Angew. Chem. Int. Ed. 48 (2009) 3924–3977.

[51] H. Eshtiagh-Hosseini, M. Mirzaei, M. Biabani, V. Lippolis, M. Chahkandi, C. Bazzicalupi, CrystEngComm 15 (2013) 6752–6768.

[52] P. Seth, A. Bauzá, A. Frontera, C. Massera, P. Gamez, A. Ghosh, CrystEngComm 15 (2013) 3031–3039.

[53] T. Maity, H. Mandal, A. Bauzá, B. C. Samanta, A. Frontera, S. K. Seth, New J. Chem. 42 (2018) 10202–10213.

[54] S, K, Seth, Crystals 8 (2018) 455.

[55] J. W. G. Bloom, S. E. Wheeler, Angew. Chem. Int. Ed. 50 (2011) 7847–7849.

[56] S. K. Seth, D. Sarkar, T. Kar, CrystEngComm 13 (2011) 4528–4535.

[57] A. Frontera, P. Gamez, M. Mascal, T. J. Mooibroek, J. Reedijk, Angew. Chem. Int. Ed. 50 (2011) 9564–9583.

[58] M. Mitra, P. Manna, A. Bauzá, P. Ballester, S. K. Seth, S. R. Choudhury, A. Frontera, S. Mukhopadhyay, J. Phys. Chem. B 118 (2014) 14713–14726.

[59] S. K. Seth, I. Saha, C. Estarellas, A. Frontera, T. Kar, S. Mukhopadhyay, Cryst. Growth Des. 11 (2011) 3250–3265.

[60] P. Manna, S. K. Seth, A. Das, J. Hemming, R. Prendergast, M. Helliwell, S. R. Choudhury, A. Frontera, S. Mukhopadhyay, Inorg. Chem. 51 (2012) 3557–3571.

[61] A. Bauza, S. K. Seth, A. Frontera, J. Comput. Chem. 39 (2018) 458–463.

[62] Y. Cotelle, S. Benz, A.-J. Avestro, T.R. Ward, N. Sakai, S. Matile, Angew. Chem. Int. Ed. 55 (2016) 4275–4279.

[63] A.-B. Bornhof, A. Bauzá, A. Aster, M. Pupier, A. Frontera, E. Vauthey, N. Sakai, S. Matile, J. Am. Chem. Soc. 140 (2018) 4884–4892.

[64] S.E. Wheeler, K.N. Houk, J. Am. Chem. Soc. 130 (2008) 10854–10855.

[65] E.R.T. Tiekink, Coord. Chem. Rev. 345 (2017) 209–228.

[66] F. Biedermann, H.J. Schneider, Chem. Rev. 116 (2016) 5216–5300.

[67] J. Wang, G. S. Hanan, Synlett. 8 (2005) 1251–1254.

[68] A. Anthonysamy, S. Balasubramanian, K. Chinnakali, H.-K. Fun, Acta Cryst. E63 (2007) o1148–o1150.

[69] F. Emmerling, J. L. Bricks, U. Resch-Genger, W. Kraus, B. Schulz, Y. Q. Li, G. Reck, J. Mol. Struct. 874 (2008) 14–27.

[70] E. C. Constable, C. E. Housecroft, M. Neuburger, D. Phillips, P. R. Raithby, E. Schofield, Emma Sparr, D. A. Tocher, M. Zehnder, Y. Zimmermann, J. Chem. Soc., Dalton Trans., (2000) 2219–2228.

[71] Bruker, *SAINT*, Version 6.36a, Bruker AXS Inc., Madison, Wisconsin, USA, 2002.

[72] Bruker, *SMART*, Version 5.625 and *SADABS*, Version 2.03a, Bruker AXS Inc., Madison, Wisconsin, USA, 2001.

[73] G.M. Sheldrick, Acta Cryst. A 64 (2008) 112–122.

[74] G.M. Sheldrick, Acta Cryst. C 71 (2015) 3–8.

[75] L.J. Farrugia, J. Appl. Cryst. 45 (2012) 849–854.

[76] A.L. Spek, J. Appl. Crystallogr. 36 (2003) 7–13.

[77] M.A. Spackman, J.J. McKinnon, CrystEngComm 4 (2002) 378–392.

[78] J.J. McKinnon, D. Jayatilaka, M.A. Spackman, Chem. Commun. (2007) 3814–3816.

[79] S. K. Seth, A. Bauzá, A. Frontera, CrystEngComm 20 (2018) 746–754.

[80] S.K. Seth, CrystEngComm 15 (2013) 1772–1781.

[81] M.A. Spackman, P.G. Byrom, Chem. Phys. Lett. 267 (1997) 215–220.

[82] J.J. McKinnon, A.S. Mitchell, M.A. Spackman, Chem.–Eur. J. 4 (1998) 2136–2141.

[83] J.J. McKinnon, M.A. Spackman, A.S. Mitchell, Acta Crystallogr. Sect. B 60 (2004) 627–668.

[84] A.L. Rohl, M. Moret, W. Kaminsky, K. Claborn, J.J. Mckinnon, B. Kahr, Cryst. Growth Des. 8 (2008) 4517–4525.

[85] S.K. Seth, Acta Cryst. E74 (2018) 600–606.

[86] S. Tripathi, A. Hossain, S. K. Seth, S. Mukhopadhyay, J. Mol. Struct. 1216 (2020) 128207.

[87] M.J. Turner, J.J. McKinnon, S.K. Wolff, D.J. Grimwood, P.R. Spackman, D. Jayatilaka, M.A. Spackman, *CrystalExplorer17*; University of Western Australia, 2017.

[88] M.J. Frisch, G.W. Trucks, H.B. Schlegel, G.E. Scuseria, M.A. Robb, J.R. Cheeseman, G. Scalmani, V. Barone, G.A. Petersson, H. Nakatsuji, et al. *Gaussian 09*, Revision *C.01*; Gaussian, Inc.: Wallingford, CT, USA, 2009.

[89] R.F.W. Bader, Chem. Rev. 91 (1991) 893–928.

[90] T.A. Keith, AIMAll, Version 13.05.06; TK Gristmill Software: Overland Park, KS, USA, 2013.

[91] R.F.W. Bader, Atoms in Molecules, a Quantum Theory; Oxford University Press: New York, NY, USA, 1990.

[92] J. Contreras-García, E.R. Johnson, S. Keinan, R. Chaudret, J.P. Piquemal, D.N. Beratan, W. Yang, J. Chem. Theory Comput. 7 (2011) 625–632.

[93] E.R. Johnson, S. Keinan, P. Mori-Sanchez, J. Contreras-Garcia, A.J. Cohen, W. Yang, J. Am. Chem. Soc. 132 (2010) 6498–6506.

[94] E. C. Constable, J. Lewis, M. C. Liptrot, P. R. Raithby, Inorg. Chim. Acta, 178 (1990) 47–54.

[95] P. Ledwaba, O. Q. Munro, K. Stewart, Acta Cryst. E65 (2009) o376–o377.

[96] T. Takase, Y. Soga, D. Oyama, IUCrData 1 (2016) x160950.

[97] R. P. Thummel, Y. Jahng, J. Org. Chem., 50 (1985) 2407–2013.

[98] C. A. Bessel, R. F. See, D. L. Jameson, M. R. Churchill, K. J. Takeuchi, J. Chem. Soc., Dalton Trans., (1992) 3223–3228.

[99] E. C. Constable, F. K. Khan, V. E. Marquez, P. R. Raithby, Acta Cryst. C48 (1992) 932–934.

[100] G. D. Storrier, S. B. Colbran, D. C. Craig, J. Chem. Soc. Dalton Trans. (1997) 3011–3028.

[101] S. K. Seth, J. Mol. Struct. 1070 (2014) 65–74.

[102] R.F.W. Bader, J. Phys. Chem. A 102 (1998) 7314–7323.

SUMMARY AND FUTURE PLAN

SUMMARY

The current thesis work aims to synthesis and analyze various functional organic and hybrid inorganic-organic materials by X-ray structural analyses. Since crystal engineering is a new field of study that deals with problems related to intermolecular interactions, it makes perfect sense to discuss the crystallographic analysis of the molecular structures described here in the context of crystal engineering. One would like to predict the supramolecular aggregations of a given set of molecules in crystals. However, predicting the crystal structure is a challenging task that is still a long way from being resolved. As a result, the problem of prediction frequently only applies to supramolecular synthons of various functional groups or recognition patterns. The primary objective of crystal engineering is to control the topology of crystal packing for functional solids through covalent and non-covalent interactions, as the successful incorporation of appropriate structural units into a crystal may result in the development of novel materials.

This thesis work examines the fact that supramolecular constructions can be made not only with strong hydrogen bonds but also with various weak interactions. By rationalizing the packing seen, supramolecular synthons of significance in crystal engineering can be identified. I have concentrated on the idea that weak interactions are essential for creating the structure of compounds under investigation.

In order to improve knowledge in this emerging subject, the research activities described in the thesis aim at systematically examining various noncovalent bonding interactions observed in new crystal structures. Hydrogen bonds are revealed to be the driving force behind the primary structural motifs that constitute the core of the net supramolecular arrangement in the compounds described here, while weaker forces are identified to control the final packing of the molecules in the solid state. The penultimate result of the competitiveness and cooperativity of weaker forces in the organization of substituted groups is the total self-assembly of the crystalline materials described in the title. The crystal structures reported here are excellent illustrations of self-assembled supramolecular structures where this competitiveness and cooperativity has been demonstrated.

The associative interactions of weak forces to build extensive networks and their supramolecular consequences in the solid state are fascinating, even though crystal engineers are more interested in exploring the individual potentiality of weak noncovalent forces. In this context, our serendipititous discovery of lone-pair(l.p)···(SB)/(SB)···π^+, C–H···(SB)/(SB)···π, π^+···(SB)/(SB)···(SB)/(SB)···π^+ and C–H···(SB)/(SB)···H–C supramolecular associations in the solid state structures sheds light on the potentiality of such newly discovered supramolecular forces in organizing and stabilizing molecular components in crystals. The unique combinations of weak forces in building the extended networks are the first evidence of crystalline solids.

Hirshfeld surface have been used to visualize the fidelity of computed crystal structures. Hirshfeld surface analyses make it easier to understand how the title compounds interplay. In addition to providing information about close contacts, the Hirshfeld surface and its fingerprint plots also reveal areas of more distant contacts and weaker interactions. The fingerprint plots are excellent for examining the variations in crystal packing caused by various substitutions in the molecular skeleton because they exhibit all of the intermolecular interactions within the crystal and thus enable a much more thorough investigation in comparison of similar structures. Moreover, the binding energies of the noncovalent interactions have anticipated the usage of DFT calculations. Intricate combinations of these noncovalent interactions are characterized through computational studies by using Bader's theory of "Atoms-in-Molecules" (AIM) and "noncovalent interaction" (NCI) plot index.

FUTURE PLAN

In my continuing effort to understand the role of weak forces in the self-assembly of crystalline solid materials, attempts will be made in near future to explore the robust feature of the cooperativity of very weak non covalent interactions in the context of crystal engineering. In continuation of my work on SB···π/SB···π^+ interaction, attempts will be made in near future to explore more extended networks. These extended networks will be further characterized by high-performance theoretical studies.

LIST OF PUBLICATIONS

1. **Quantitative insights into the crystal structure of a mixed-ligand Co(III) complex: Experimental and theoretical studies**

   Suparna Tripathi, Anowar Hossain, Saikat Kumar Seth, Subrata Mukhopadhyay

   Journal of Molecular Structure 1216 (2020) 128207

2. **Supramolecular assemblies involving salt bridges: DFT and X-ray evidence of bipolarity**

   Suparna Tripathi, Samiul Islam, Saikat Kumar Seth, Antonio Bauzá, Antonio Frontera, Subrata Mukhopadhyay

   CrystEngComm 22 (2020) 8171–8181 (Published as Front Cover Page)

3. **Supramolecular association and quantification of intermolecular interactions of 4′-functionalized 2,2′:6′,2′′-terpyridines: Experimental observation and theoretical studies**

   Suparna Tripathi, Anowar Hossain, Saikat Kumar Seth, Subrata Mukhopadhyay

   Journal of Molecular Structure 1226 (2021) 129254

Publications not included in this thesis

4. **pH-induced structural variations of two new Mg(II)-PDA complexes: experimental and theoretical studies**

   Samiul Islam, **Suparna Tripathi**, Anowar Hossain, Saikat Kumar Seth, Subrata Mukhopadhyay

   Journal of Molecular Structure 1265 (2022) 133373

5. **Exploring Solid-State Supramolecular Architectures of Penta(carboxymethyl)diethylenetriamine: Experimental Observation and Theoretical Studies**

   Samiul Islam, Prantika Das, **Suparna Tripathi**, Subrata Mukhopadhyay, Saikat Kumar Seth

   ChemistrySelect 7 (2022) e202203396

Journal of Molecular Structure 1216 (2020) 128207

Contents lists available at ScienceDirect

Journal of Molecular Structure

journal homepage: http://www.elsevier.com/locate/molstruc

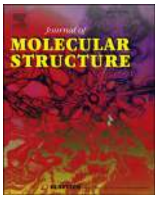

Quantitative insights into the crystal structure of a mixed-ligand Co(III) complex: Experimental and theoretical studies

Suparna Tripathi [a, b], Anowar Hossain [b], Saikat Kumar Seth [a, *], Subrata Mukhopadhyay [b, **]

[a] *Department of Physics, Jadavpur University, Kolkata, 700032, India*
[b] *Department of Chemistry, Jadavpur University, Kolkata, 700032, India*

ARTICLE INFO

Article history:
Received 1 December 2019
Received in revised form
2 April 2020
Accepted 3 April 2020
Available online 22 April 2020

Keywords:
Mixed-ligand complex
Supramolecular layered assembly
Hirshfeld surface
Bader's theory of "atoms-in-molecules" (AIM)
Noncovalent interaction (NCI) plot

ABSTRACT

A new octahedral Co(III) complex namely 5-ethyl-2-methylpyridinium *trans*-bis(iminodiacetato-k^3O,N,O′)cobaltate(III), $(C_8H_{12}N_1)[Co(C_4H_5NO_4)_2]$ (**1**) has been synthesized and structurally characterized by single crystal X-ray diffraction analysis. In the solid state, the structure is stabilized through various hydrogen bonds, C—H···π and π—π stacking interactions that leads the molecules to generate diverse supramolecular architectures. The solid-state supramolecular structure of (**1**) has been corroborated with theoretical calculations. The intermolecular interactions are quantified *via* Hirshfeld surface analysis. The intricate combination of C—H···π and π—π stacking interactions are fully analyzed by computational studies. The noncovalent interactions have been characterized by Bader's theory of "atoms-in-molecules" (AIM) and "noncovalent interaction" (NCI) plot index.

1. Introduction

In crystal engineering, self-assembly is the essential molecular recognition process that deals with the control over the organization of molecular moieties in solid-state [1,2]. Crystals are assembled in spontaneous process that proceeds through a series of molecular recognition events. A recognition event among the molecular moieties is the outcome of the mutual interaction through several forces that are in operation. Therefore, the study and detail understanding of noncovalent forces are essential for the development of different applications in supramolecular chemistry [3,4]. Nevertheless, engineering supramolecular architecture is problematic due to the subtle nature of the noncovalent interactions [5]. Supramolecular chemistry relies on weak noncovalent interactions and the interactions involving aromatic systems are extremely significant due to their colossal influence in chemical and biological processes [6,7]. Hydrogen bonds and π—π stacking interactions are two vital adhesive and cohesive forces in the crystal structures of small molecules. Various weak dispersive π-interactions including C—H•••π [8–10], π-stacking [11–14], anion•••π [15–18] and lone pair•••π [19,20] interactions have been widely used in building various supramolecular architectures. However, π^+—π and π^+—π^+ stacking interactions are much stronger than conventional π—π interaction [13,14,21–23]. These interactions are quite different in terms of their magnitude and directionality. The proper understanding of these interactions and their cooperativity are extremely important not only for rationalizing the solid-state networks but also to predict new supramolecular architectures.

Iminodiacetic acid (H_2IDA) is a promising candidate in coordination chemistry, since it is a tridentate ligand bearing imino and carboxyl electron-donating groups that could bind mono or multiple metal ions to exhibit structural diversity in the solid-state [24–26]. The carboxylic acid protons of iminodiacetic acid dissociate to give iminodiacetato dianion that reacts with metal ions to form diverse metal iminodiacetate complexes. X-ray structures of the ternary complexes with iminodiacetato as primary and N-donors as secondary ligands have been a subject of continuous investigation in the context of crystal engineering due to its variety of supramolecular structures.

In continuation of our previous work [19,27–29], prompted by the supramolecular behavior of the M-IDA complexes, it was

---

* Corresponding author.
** Corresponding author.
E-mail addresses: saikatk.seth@jadavpuruniversity.in, saikatim@yahoo.co.in (S.K. Seth), ju_subrata@yahoo.co.in (S. Mukhopadhyay).

https://doi.org/10.1016/j.molstruc.2020.128207
0022-2860/

contemplated to design synthesis of mixed-ligand 5-ethyl-2-methylpyridinium trans-bis(iminodiacetato-k^3O,N,O′)cobaltate(III) complex and to explore its solid-state structure in detail. The structural description have been corroborated with theoretical calculations and the intermolecular interactions have been quantified by Hirshfeld surface analysis. The noncovalent interactions have been further characterized by using the Bader's theory of "atoms in molecule" (AIM) and "noncovalent interaction" (NCI) plot.

2. Experimental sections

2.1. Materials

The reagents Cobalt(II) chloride hexahydrate, Iminodiacetic acid and 5-ethyl-2-methylpyridine were readily available from commercial sources (Sigma-Aldrich, India) and used as received without further purification.

2.2. Synthesis

$CoCl_2 \cdot 6H_2O$ (0.238 g, 1 mmol) was reacted with iminodiacetic acid (0.266 g, 2.0 mmol) in water (25 mL) nearly at 60 °C until a clear solution resulted in open glassware. A warm (~40 °C) methanolic solution (15 mL) of 5-ethyl-2-methylpyridine (0.363 g, 3 mmol) was added dropwise to the above solution. The mixture was stirred for 1 h at 60 °C, then stirred for 2 h at normal laboratory temperature (~30 °C), and then filtered. The dark-red filtrate was kept undisturbed at ambient temperature and covered with paraffin film and a few small holes were made using a needle to allow the solvent evaporate slowly. After 6–7 weeks, dark-red colored; block shaped single crystals of the title complex was formed. Anal. Calcd. for $C_{16}H_{22}CoN_3O_8$ (MW = 443.257 and melting point = 304 °C): C, 43.35; H, 4.99; N, 9.47%. Found: C, 43.31; H, 4.95; N, 9.51%. Main IR absorption bands observed for **1** (KBr pellet, cm^{-1}, Fig. S1): 3181(S), 3041(s), 2969(s), 1644(s), 1610(s), 1468(s), 1437(s), 1381(s), 1358(s), 1313(s), 1297(s), 1248(s), 1156(s), 1126(s), 1069(s), 1029(s), 1000(s), 964(s), 917(s), 898(s), 880(s), 784(s), 761(s), 725(s), 645(s), 613(s), 595(s), 565(s), 534(s), 516(s), 455(s), 441(s). ^{1}H NMR (DMSO-d_6, 300 MHz, Fig. S2) δ in ppm: 8.69–8.74 (m, 2H), 8.61 (s, 2H), 8.26 (d, 1H), 7.75 (d, 1H), 3.13 (d, 8H), 2.72 (q, 2H), 2.62 (s, 3H), 1.20 (t, 3H).

2.3. X-ray crystal structure determination

Single crystal X-ray diffraction intensity data of the title complex was collected at 150(2) K using a Bruker APEX-II CCD diffractometer equipped with graphite monochromated MoKα radiation (λ = 0.71073 Å). Data reduction was carried out using the program Bruker SAINT [30] and an empirical absorption correction was applied based on multi-scan method [31]. The structure of the title complex was solved by direct method and refined by the full-matrix least-square technique on F^2 with anisotropic thermal parameters to describe the thermal motions of all non-hydrogen atoms using the programs (SHELXS-14) [32] and (SHELXL-18) [33], respectively. All hydrogen atoms were placed at their geometrically idealized positions and refined isotropically. All calculations were carried out using WinGX system V2014.1 [34] and PLATON [35]. The summary of crystal data and relevant structure refinement parameters [36] are given in Table 1. CCDC 1945765 contains the supplementary crystallographic data for this paper.

2.4. Hirshfeld surface analysis

The Hirshfeld surface [37–40] of the title complex has been generated based on electron distribution of the molecule and are calculated as the sum of spherical atom electron densities [41,42]. Hirshfeld surface is distinctive for the investigating structure and a set of spherical atomic electron densities [43]. The normalized contact distance (d_{norm}) is based on d_e, d_i and the vd*W* radii of the atom. d_e and d_i are defined as the distance from the point to the nearest nucleus external and internal to the surface respectively. The 2D fingerprint plot provides summary of intermolecular contacts in the crystal [43–45]. The Hirshfeld surface analysis has been carried out using Crystal Explorer program [46].

2.5. Theoretical methods

We have performed the calculations for the wave function analysis by using Gaussian09 calculation package [47] at the B3LYP level with a large basis set 6–311++G(d,p). The crystallographic coordinates have been used for the theoretical analysis of the noncovalent interactions present in the solid state. The Bader's "Atoms in molecules" theory [48] has been used for analyzing the noncovalent interactions by means of the AIMall calculation package [49]. The topological properties of the charge density ($\rho(r)$) is characterized by their critical points (CPs) and it's Laplacian. The Laplacian is expressed in terms of $L(r) = -\nabla^2(\rho(r))$ that are calculated using the Atom In Molecule (AIM) theory [50]. The electron density is concentrated where $\nabla^2(\rho(r)) < 0$ and it is depleted where $\nabla^2(\rho(r)) > 0$. The NCI plot [51] is a visualization index based on the electron density and its derivatives. The NCI plot isosurfaces have been used to characterize the noncovalent interactions. Since the isosurfaces represent the noncovalent interactions instead of critical points, it permits proficient visualization and identification. The isosurfaces correspond to both favorable and unfavorable interactions, as differentiated by the sign of the second density Hessian eigenvalue and defined by the isosurface color. The color scheme is a red-yellow-green-blue scale with red for ρ^+cut (repulsive) and blue for ρ^-cut (attractive) [52]. Yellow and green surfaces correspond to weak repulsive and weak attractive interactions, respectively.

3. Results and discussion

3.1. Structural description

The molecular structure of the title complex is shown in Fig. 1 that comprised of one cationic moiety namely 5-ethyl-2-methylpyridinium and an anionic moiety namely *trans*-bis(iminodiacetato-k^3*N,O,O*')cobaltate(III). In the anionic moiety, the Co atom is coordinated by two different tridentate IDA ligands through their six donor (two nitrogen and four oxygen) atoms with a distorted octahedral geometry {CoN2O4}. The IDA ligands binds the metal ion in *fac*-chelating arrangement where two nitrogen atoms occupies *trans* positions. The Co–O bonding distances vary between 1.8777(14) and 1.9015(14) Å, while the Co–N bond lengths are 1.9283(16) and 1.9432(16)Å (Table 2). As expected, these bonding distances are in normal range and comparable to those in other Co(III) iminodiacetates reported earlier [53–56]. The rest bond distances are considered normal and correlate well with those reported complexes.

The deviation around Co^{3+} ion from octahedral geometry is noteworthy. The N–Co–O bond angles are the most distorted that varying between 86.53(6)° and 94.78(6)°, while the O–Co–O angles vary between 88.51(6)° and 92.09(6)°. The values of the trans bond angles O–Co–O and N–Co–N are 177.83(6)°, 178.41(6)° and 178.62(7)° (Table 2). In either five membered chelating rings Co1–O1–C1–C2–N1; Co1–O4–C4–C3–N1; Co1–O5–C5–C6–N2 and Co1–O8–C8–C7–N2, all atoms are almost coplanar with

Table 1
Crystal data and structure refinement parameters for the title complex.

Structure	(1)
Crystal data	
Empirical formula	$C_{16}H_{22}CoN_3O_8$
M_r	443.29
Crystal system, space group	Triclinic,
Temperature (K)	150(2)
a, b, c (Å)	8.574(5), 10.010(3), 11.351(5)
α, β, γ (°)	105.040(2), 101.856(5), 91.557(3)
V (Å^3)	917.4(7)
Z	2
Radiation type	Mo $K\alpha$
μ (mm^{-1})	0.987
Crystal size (mm)	0.16 × 0.11 × 0.08
Data collection	
Diffractometer	Bruker *SMART APEX* II CCD area-detector
Absorption correction	Multi-scan, *SADABS*
T_{min}, T_{max}	0.88, 0.92
No. of measured, independent and observed [$I > 2\sigma(I)$] reflections	8645, 3207, 3038
R_{int}	0.019
$(\sin \theta/\lambda)_{max}$ (Å^{-1})	0.595
Refinement	
$R[F^2 > 2\sigma(F^2)]$, $wR(F^2)$, S	0.028, 0.082, 1.06
No. of reflections	3207
No. of parameters	255
H-atom treatment	H-atom parameters constrained
$\Delta\rho_{max}$, $\Delta\rho_{min}$ (e Å^{-3})	0.42, −0.37

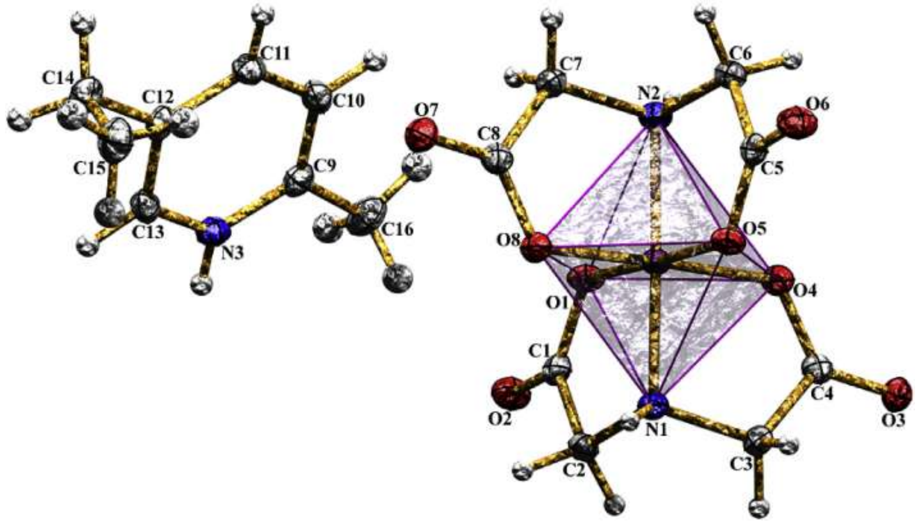

Fig. 1. View of the asymmetric unit with atom numbering of the title complex. Displacement ellipsoids (Granite stone) are drawn at 30% probability.

Table 2
Selected bond lengths (Å) and bond angles (°).

Co(1)–O(1)	1.878(2)	Co(1)–O(5)	1.902(2)
Co(1)–O(4)	1.896(2)	Co(1)–O(8)	1.881(2)
Co(1)–N(1)	1.928(2)	Co(1)–N(2)	1.943(2)
O(1)–Co(1)–O(8)	92.09(6)	O(4)–Co(1)–N(1)	86.53(6)
O(1)–Co(1)–O(4)	88.86(6)	O(5)–Co(1)–N(1)	93.50(6)
O(8)–Co(1)–O(4)	177.83(6)	O(1)–Co(1)–N(2)	91.64(6)
O(1)–Co(1)–O(5)	178.41(6)	O(8)–Co(1)–N(2)	87.14(6)
O(8)–Co(1)–O(5)	88.51(6)	O(4)–Co(1)–N(2)	94.78(6)
O(4)–Co(1)–O(5)	90.58(6)	O(5)–Co(1)–N(2)	86.92(6)
O(1)–Co(1)–N(1)	87.96(6)	N(1)–Co(1)–N(2)	178.62(7)
O(8)–Co(1)–N(1)	91.56(6)		

C2,N1; N1,C3; N2,C6 and C7,N2 have the largest deviations in opposite directions (Table 3) from the least-squares mean planes of the rings. The dihedral angles between the chelating rings (Co1–O1–C1–C2–N1; Co1–O4–C4–C3–N1) and (Co1–O5–C5–C6–N2; Co1–O8–C8–C7–N2) are 86.11(4) and 87.39(4), respectively.

In the solid state, complex (**1**) includes a combination of N–H···O, C–H···O hydrogen bonding, C–H···π and π–π stacking interactions (Tables 4 and 5). In (**1**), the amino N1 atom of one IDA molecule at (x, y, z) acts as donor to the carboxylate oxygen O(5) atom of another IDA unit of the partner molecule at (2-x, -y, 2-z), so generating a centrosymmetric $R^2_2(8)$ dimeric ring (M) centered at (1, 0, 1) (Fig. 2). Similarly, another amino N2 atom binds the carboxylate oxygen atom of the other IDA moiety in the molecule at (2-x, 1-y, 2-z) that generates another centrosymmetric $R^2_2(8)$ dimeric ring (N) centered at (1, ½, 1). The two types of $R^2_2(8)$ dimeric rings are alternately linked into infinite MNMNMN … chain that propagating along [010] direction (Fig. 2). In between two parallel MNMN … chains, the cationic moieties are juxtaposed through C–H···π

Table 3
Distances of atoms of the chelate rings from the ring planes (Å).

Plane	Co distance	N distance	O distance	C (carboxylate) distance	C (methylene) distance
Co1–O1–C1–C2–N1	0.006(4)	−0.093(2)	−0.047(2)	0.006(2)	0.111(2)
Co1–O4–C4–C3–N1	−0.009(4)	0.208(2)	0.106(2)	−0.032(2)	−0.241(2)
Co1–O5–C5–C6–N2	−0.007(4)	0.126(2)	0.048(2)	0.016(2)	−0.171(2)
Co1–O8–C8–C7–N2	0.007(4)	−0.165(2)	−0.072(2)	−0.005(2)	0.218(2)

Table 4
Hydrogen-bond geometry (Å, °).

D–H···A	D–H	H···A	D···A	D–H···A	Symmetry
N(1)–H(1)···O(5)	0.91	2.01	2.904(3)	168	2-x, -y, 2-z
N(2)–H(2)···O(1)	0.91	2.31	3.097(3)	144	2-x, 1-y, 2-z
N(2)–H(2)···O(4)	0.91	2.30	3.083(3)	144	2-x, 1-y, 2-z
N(3)–H(3)···O(6)	0.86	1.86	2.709(3)	167	x, y, −1+z
C(2)–H(2B)···O(7)	0.97	2.37	3.333(3)	172	1+x, y, z
C(3)–H(3B)···O(8)	0.97	2.51	3.399(3)	152	2-x, -y, 2-z
C(6)–H(6A)···O(3)	0.97	2.42	3.370(3)	167	−1+x, y, z
C(6)–H(6B)···O(2)	0.97	2.49	3.333(3)	145	2-x, 1-y, 2-z
C(10)–H(10)···O(3)	0.93	2.36	3.268(3)	165	2-x, 1-y, 2-z
C(11)–H(11)···O(2)	0.93	2.34	3.212(3)	156	−1+x, y, z
C(13)–H(13)···O(7)	0.93	2.46	3.275(3)	146	1-x, -y, 1-z
C(16)–H(16A)···O(2)	0.96	2.37	3.300(3)	162	–
C(15)–H(15A)···Cg(5)		2.91	3.563(3)	126	1-x, -y, 1-z

Cg(5) is the centroid of the pyridine ring.

and π–π stacking interactions. The methyl carbon C(15) of the cationic unit in the molecules at (x, y, z) acts as donor to the centroid of the pyridine ring at (1-x, -y, 1-z) with a separation distance of 2.91 Å, thus generating a centrosymmetric dimeric unit. In either side of the dimeric unit, the pyridine rings of the molecule at (x, y, z) and (1-x, 1-y, 1-z) are anti-parallel, with an interplanar spacing of 3.417(1)Å, and a ring centroid separation of 4.113(3)Å, corresponding to a ring offset of 2.289 Å. The combination of C–H···π and π–π stacking interactions leads the molecules to generate an infinite chain along [010] direction (Fig. 2). Finally, these anionic MNMN … chains and cationic chains are interconnected through N–H···O H-bond. The pyridine ring nitrogen N(3) atom from the cationic chain acts as donor to the carbonyl oxygen O(6) atom of the anionic chain at (x, y, −1+z), thus interconnects the two types of parallel chains by generating a two-

Table 5
Geometrical parameters (Å, °) for π-stacking interactions.

Rings i–j	Rc	R1v	R2v	α	β	γ	Slippage
Cg(5)–Cg(5)$^{(i)}$	4.112(3)	−3.4170(8)	−3.4169(8)	0.0	33.82	33.82	2.289

[Symmetry codes: (i) (1-x, 1-y, 1-z)]. Cg(5) is the centroids of the pyridine (N3/C9–C13) ring.

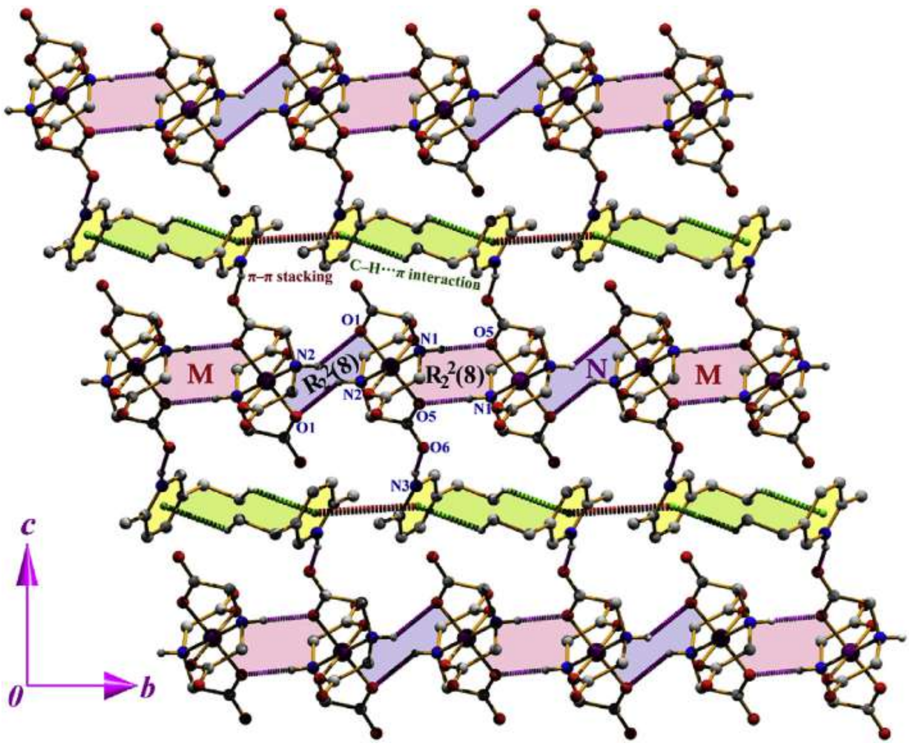

Fig. 2. Perspective view of the supramolecular network in (011) plane.

dimensional supramolecular network in (011) plane (Fig. 2) (see Table 4).

Again, the weak C—H···O H-bonds also played significant role in building supramolecular assemblies. The carbon atoms C(2) and C(6) of the IDA unit acts as donor to the carbonyl oxygen atoms O(7) and O(3) in the molecules at (1+x, y, z) and (−1+x, y, z) respectively, therefore generating a dimeric $R_2^2(12)$ ring. These hydrogen bonds leads the molecules of the anionic moiety to propagate an infinite chain along [100] direction (Fig. 3). The parallel infinite chains of the anionic moieties are further interacts with the cationic moieties. The pyridine ring carbon atom, substituted methyl carbon atom and ring nitrogen atom acts as donor to the carbonyl oxygen atoms of the anionic chain, thus generating a two-dimensional self-assembled network in (101) plane (Fig. 3).

3.2. NMR spectroscopic observations and Bond Valence Sum (BVS) calculation

NMR spectroscopic analysis reveals that the complex contains diamagnetic Cobalt in 3+ oxidation state (Fig. S2). Further, Bond Valence Sum (BVS) calculation was performed to establish the oxidation state of cobalt [57,58]. This calculation includes following equations:

$$s_{ij} = \exp[(r_o - r_{ij})/b] \tag{1}$$

where, i = donor centre, j = metal centre, $r_\circ$ = reported bond length between i and j, r_{ij} = the observed bond length, s_{ij} = the valence of a bond between two atoms i and j, and b is usually taken to be 0.37. The Pauling's valence sum rule (Pauling's second rule) is defined as

$$\mathrm{z_j} = \sum_i Sij \tag{2}$$

where, z_j is the valence of atom j connecting i–j bonds with all neighbouring i atoms.

From the BVS calculation, it is confirmed that complex **1** contain cobalt in 3+ oxidation state as the z_j value is around ~3 (Table 6). The slight deviation of the BVS from an integer value usually appears due to excessive thermal motion, possible steric constraints, and problems with the crystal structure report or some combination of all of these effects [59].

3.3. Hirshfeld surface

In this study, we have estimated the contribution of various available contacts that are contributed in the crystal packing. We have analyzed the Hirshfeld surface [37–39] of both anionic and cationic moieties separately and that are mapped with d_{norm}, shape-index, d_e and curvedness. The d_{norm} mapping (−0.6922 to 1.2777 Å) of the molecular aggregate is shown in Fig. 4. The protuberant hydrogen-bonding interactions are clearly identified from the circular depressions (red spots) on the d_{norm} surface that are dominated by the strong N—H···O (carboxylate) hydrogen bonds. Fingerprint plots are the key tool for the quantification of the available intermolecular contacts and can be decomposed to quantify individual contributions of the interactions [43,44]. The O···H/H···O interactions in the anionic moiety are clearly evident by two distinct spikes in the region of (d_i = 1.031 Å; d_e = 0.676 Å) and (d_e = 1.121 Å; d_i = 0.771 Å) respectively that comprises 67.8% of the total Hirshfeld surface area (Fig. S3). In contrast, there is no signature of the O···H interaction in the cationic moiety of the title complex. The only available spike in the region of (d_i = 0.681 Å; d_e = 1.031 Å) is for H···O contribution that comprises 30.7% to the total Hirshfeld surface area (Fig. S4). The N···H/H···N contributions are visible in the fingerprint plot of the cationic moiety that are represented by the wings in the region of (d_i = 2.069 Å; d_e = 1.232 Å) and (d_e = 2.049 Å; d_i = 1.227 Å). The N···H contacts contributed more (1.9%) compare to the H···N counterpart (1.7%); consequently, the N···H/H···N contacts contributed 3.6% to the total Hirshfeld surface of the molecule (Fig. S4). The C···H/H···C contacts are evident in the anionic moiety by the discrete spots as a spike that contributed 5.2% to the total Hirshfeld surface area (Fig. S3) whereas the C···H/H···C contacts are distinctly evident by the wings in the donor and acceptor region (Fig. S4) of the breakdown

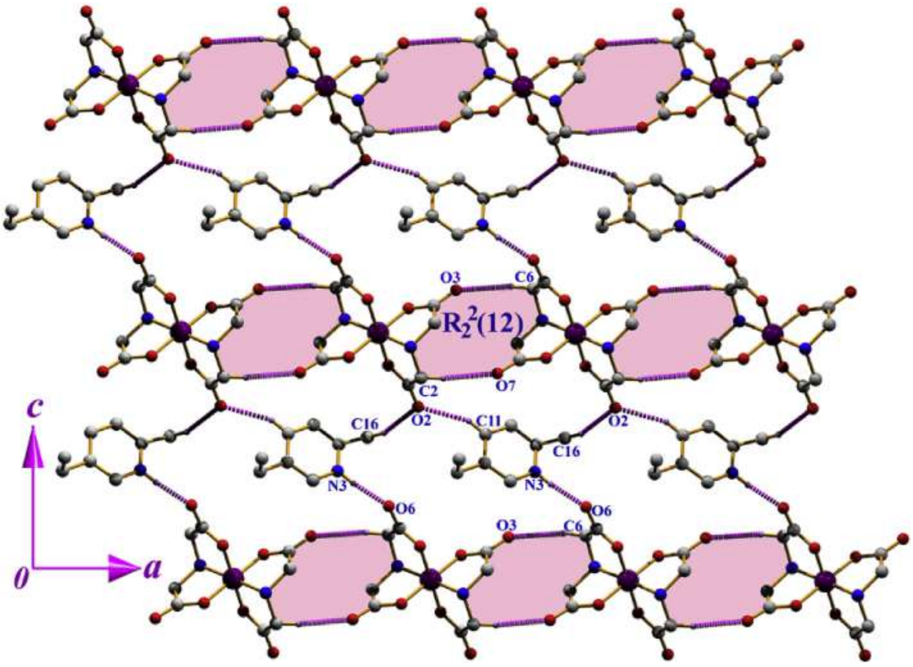

Fig. 3. View of the self-assembly in (101) plane.

Table 6
Bond valence sum calculation and related parameters for complex 1.

i–*j* (reported)	$r_◦$	*i*–*j* (complex 1)	r_{ij}	s_{ij}	z_j
O^{2-}–Co^{3+}	1.637	O(1)–Co(1)	1.878(2)	0.521	3.052
O^{2-}–Co^{3+}	1.637	O(4)–Co(1)	1.896(2)	0.496	
O^{2-}–Co^{3+}	1.637	O(5)–Co(1)	1.902(2)	0.488	
O^{2-}–Co^{3+}	1.637	O(8)–Co(1)	1.881(2)	0.517	
N^{3-}–Co^{3+}	1.690	N(1)–Co(1)	1.928(2)	0.525	
N^{3-}–Co^{3+}	1.690	N(2)–Co(1)	1.943(2)	0.505	

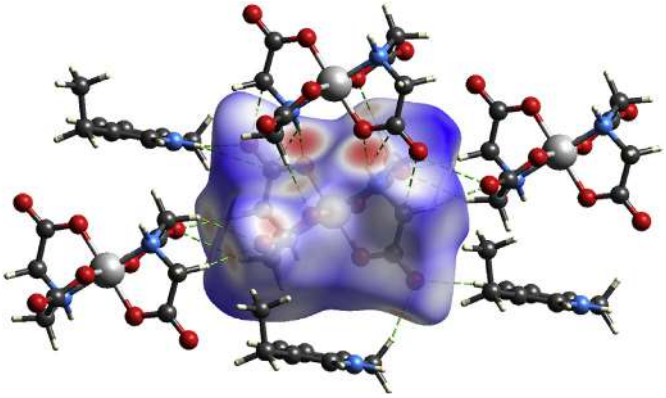

Fig. 4. Hirshfeld surface mapped with d_{norm} for the anionic moiety illustrating the interactions with partner molecules through hydrogen bonding interactions (green dotted lines).

fingerprint plot. The wings in the region of ($d_i = 2.063$; $d_e = 1.222$) comprised 7.1% and the counterpart part H···C contact ($d_i = 1.222$; $d_e = 2.068$) comprises 7.7% and as whole the C···H/H···C contact comprised of 14.8% to the total Hirshfeld surface area of the cationic moiety (Fig. S4).

As expected, the C–H•••π interactions are clearly visible on the d_e and shape-index surfaces of the cationic moiety (Fig. 5). The bright-orange depression above the π electron cloud of the pyridine ring and greenish-blue patch on the C–H donor site of the d_e surface are the indicator of C–H•••π interactions (Fig. 5a). The donors and acceptors of intermolecular C–H•••π interactions are further recognized by the red and blue regions around the participating atoms of the π-cloud and C–H donor respectively, on the shape-index surface (Fig. 5b). To examine the impact of π–π stacking interaction on the molecular packing, we have analyzed the Hirshfeld surface by mapping over shape-index and curvedness (Fig.5c and d). From the mapped Hirshfeld surfaces, it is clear that the protonated pyridine rings are related to one another through π–π stacking interaction. The π–π stacking between the rings is displayed by the red and blue triangles on the same region of the shape-index surface (Fig. 5c). The blue triangle denotes the convex regions resulting from the pyridine ring of the molecule inside the surface, while the red triangle signifies concave regions caused by pyridine ring atoms of the π-stacked molecule above it. The pattern of the red-blue triangle characterizes the anti-parallel π-stacking interaction of the cationic moiety (Fig. 5c). Moreover, the large flat region of the curvedness surface across the π-cloud of the pyridine ring of the cationic moiety further characterized the anti-parallel π-stacking interactions (Fig. 5d). The fingerprint plot corresponding to π–π stacking is shown as a blue region on the diagonal at around

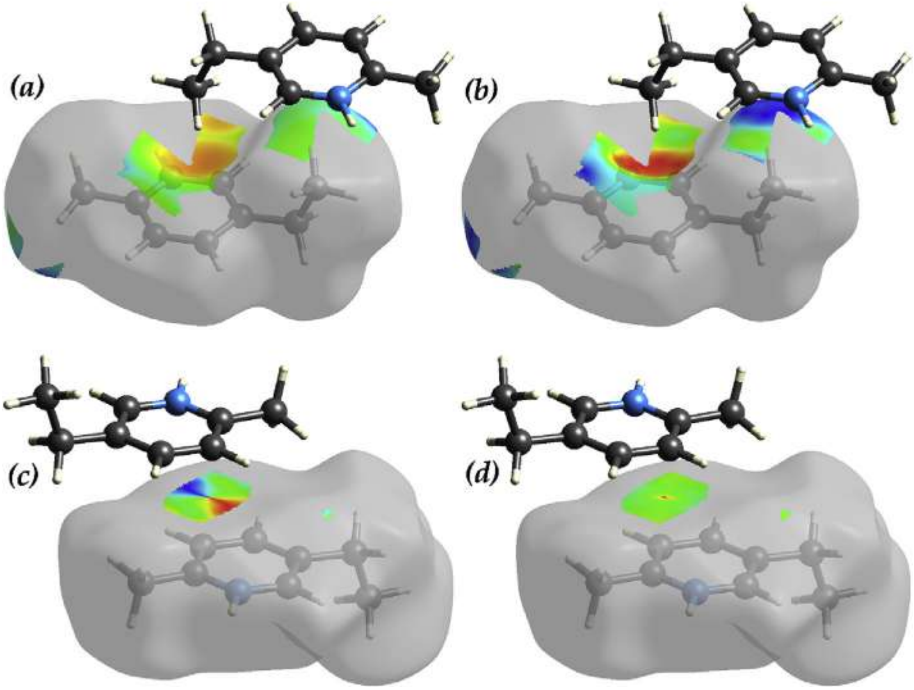

Fig. 5. Perspective view of the decomposed Hirshfeld surface mapped with d_e (a) and shape-index (b) property illustrating C–H•••π/π•••H–C contacts. The Hirshfeld surface mapped with shape-index (c) and curvedness (d) property illustrating π–π stacking contacts in the crystal of the title complex.

$d_i = d_e = 1.708$ Å (Fig. S4). All other available contacts are further quantified by the fingerprint plot and are depicted in Figs. S3 and S4 for anionic and cationic moiety, respectively. A significant difference between the molecular interactions in terms of H···H contacts (Figs. S3 and S4) are reflected in the distribution of scattered points in the region ($d_i = 1.116$ Å, $d_e = 1.176$ Å) in anionic moiety and ($d_i = 1.161$ Å, $d_e = 1.111$ Å) in cationic moiety.

3.4. *Theoretical analysis*

The Bader's theory of atoms in molecules (AIM) analysis [49] has been performed with the self-assembled dimeric units of the title complex. AIM analysis has been included for visualization and characterization of the noncovalent interactions that are involved within the structure through the distribution of bond critical points and the bond paths. The bond critical point (CP) and bond path that connects two atoms evidenced the existence of interaction between two atoms [48]. In Fig. 6, we represent the distribution of CPs and bond paths of the several self-assembled networks of the title complex. In the first model of Fig. 6, we used the molecular moiety of dimeric ring motif M (See Fig. 2). The bond paths connecting the H atom of two amine nitrogen and the carboxylate oxygen atoms designate the N—H···O bonding interaction. The ring CP that is presented by yellow sphere further characterize the dimeric ring M. Further, we analyzed the ρ(r) values of the bond CPs to verify the strength of the interaction [50] that are included in Fig. 6. The $\rho_{BCP} = 0.0094$ a.u. value characterize the N—H···O H-bonding (Fig. 6a). Moreover, two different carbon atom from the IDA unit interacts with the carboxylate and carbonyl oxygen atom and are characterized by the bond paths and ρ_{BCP} values (0.0080 a.u. and 0.0074 a.u.). In model 2 (Fig. 6b), the dimeric ring N (see Fig. 2) is characterized by the bond path connecting the hydrogen atom of the parent amine nitrogen and carboxylate oxygen atom having ρ_{BCP} (0.0118 a.u.). It is noteworthy that the ρ(r) values of the bond CPs for centrosymmetric ring M is larger (0.0094 a.u.) in comparison to the N ring (0.0118 a.u.). Therefore, it can be concluded that the N—H···O hydrogen bonds that generates ring M are stronger that the N—H···O bond of ring N that is in agreement with the geometrical parameters of X-ray structure (Table 4). In model 3, we have analyzed the C—H···π interaction. The bond critical point and the bond path connecting the hydrogen atom of the methyl carbon and the pyridine ring carbon atom characterizes the C—H···π interaction where the ρ_{BCP} is 0.0050 a.u. (Fig. 6c). The bond paths between two carbon atoms of the pyridine rings characterize the π–π interaction ($\rho_{BCPs} = 0.0063$ a.u.) (Fig. 6d).

Finally, we further characterized the noncovalent interactions using NCI plot index computational tool [51,52]. It permits an easy assessment of host-guest complementarity and the extent to which weak interactions stabilize the investigating structure. In Fig. 7, the NCI plot of the self-assembled structure (see Fig. 2) of the title complex has been presented. Various noncovalent interactions are clearly evident by the green, blue isosurfaces. The two types of ring motif M and N that are formed by the strong N—H···O bonding are clearly observed by the blue isosurfaces between amine nitrogen and carboxylate oxygen of the anionic moiety. The weak C—H···O H-bonds are observed as small green isosurface between two anionic moieties. In the same figure, the cooperativity of the C—H···π and π–π interaction between cationic moieties are represented. The presence of dual large green isosurface between methyl hydrogen atom and π-cloud of the pyridine ring clearly designate the C—H···π interaction. The isosurface that characterizes the π–π interaction embraces the pyridine ring and the ethyl groups. The large region and the greenish-blue color on the isosurface indicates that the π–π interaction is stronger than the C—H···π interaction in agreement with the ρ(r) values at the bond CPs mentioned above (see Fig. 6). It is worth mentioning the existence of strong blue isosurfaces between the cationic and anionic layers. These strong blue isosurfaces between the protonated pyridine ring nitrogen atom and the carbonyl oxygen atom of the IDA ligand clearly shows how the cationic and anionic layers are interconnected through the N—H···O bonds.

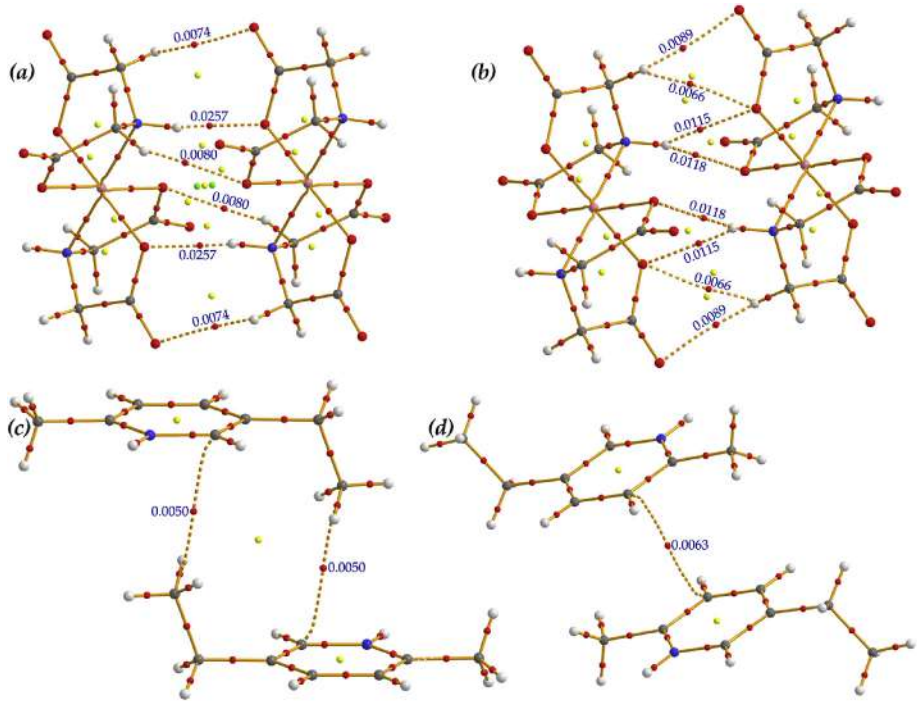

Fig. 6. Distribution of the critical points of various self-assembled networks of the title complex (*a*–*d*). Red, yellow and green spheres represent bond, ring and cage critical points, respectively.

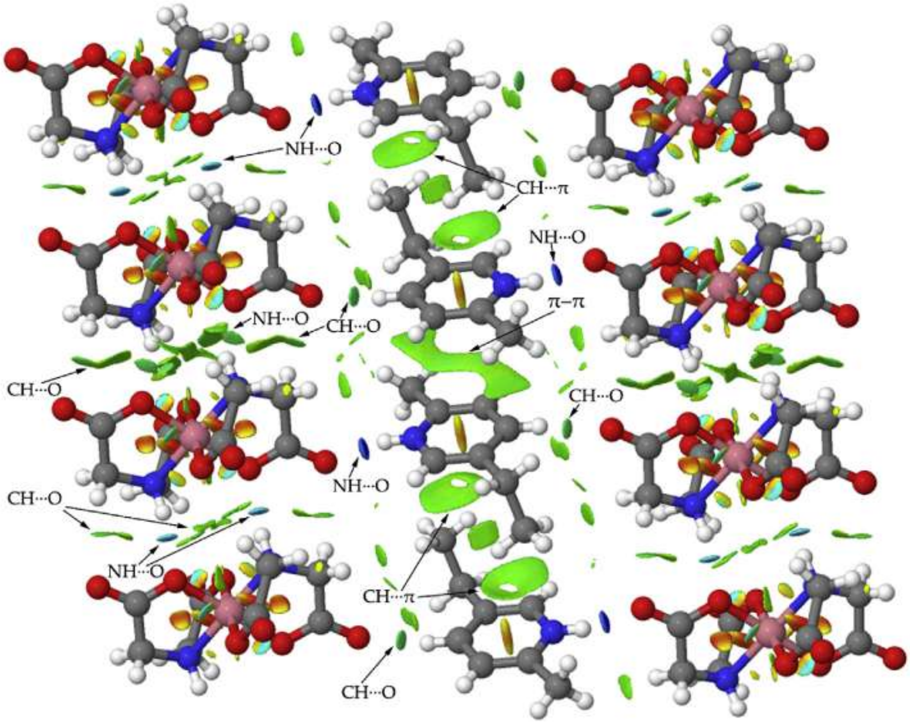

Fig. 7. NCI plot of the self-assembly in (**1**). The gradient cut-off is s = 0.35 au, and the color scale is $-0.04 < \rho < 0.04$ au.

4. Conclusions

In summary, a new octahedral mixed-ligand complex has been synthesized and structurally characterized. The cooperativity of weak noncovalent interactions in building supramolecular structures have been analyzed in detail and quantified by Hirshfeld surface analysis. Finally, these noncovalent interactions have been characterized theoretically by Bader's theory of “atoms-in-molecules” and also have been analyzed by NCI plot index. The theoretical investigations based on DFT functional, AIM and NCI analyses supports the experimental findings of the intricate combination of intermolecular interactions that characterized the studied complex. The results reported herein are expected to be useful for understanding of cooperativity effect of noncovalent interactions in the context of crystal engineering.

Author statement

Subrata Mukhopadhyay gave the planning of the synthesis of the complex, Suparna Tripathi and Anowar Hossain synthesized the complex, measured the structure and other physico-chemical experiments, Saikat Kumar Seth and Subrata Mukhopadhyay analyzed the data; Saikat Kumar Seth contributed performing some theoretical calculations; Saikat Kumar Seth and Subrata Mukhopadhyay wrote the paper.

Declaration of competing interest

The authors declare no competing financial interest.

Appendix A. Supplementary data

Supplementary data to this article can be found online at https://doi.org/10.1016/j.molstruc.2020.128207.

References

[1] G.R. Desiraju, J. Am. Chem. Soc. 135 (2013) 9952–9967.
[2] N.H. Evans, P.D. Beer, Angew. Chem. Int. Ed. 53 (2014) 11716–11754.
[3] J.W. Steed, J.L. Atwood, Supramolecular Chemistry, second ed., Wiley, Chichester, 2009.
[4] J.L. Atwood, G.W. Gokel, L.J. Barbour, Comprehensive Supramolecular Chemistry II, Elsevier, 2017.
[5] A. Bauza, S.K. Seth, A. Frontera, Coord. Chem. Rev. 384 (2019) 107–125.
[6] M.M. Watt, M.S. Collins, D.W. Johnson, Acc. Chem. Res. 46 (2012) 955–966.
[7] K.E. Riley, P. Hobza, Acc. Chem. Res. 46 (2012) 927–936.
[8] P. Seth, A. Bauzá, A. Frontera, C. Massera, P. Gamez, A. Ghosh, CrystEngComm 15 (2013) 3031–3039.
[9] S.K. Seth, J. Mol. Struct. 1070 (2014) 65–74.
[10] T. Maity, H. Mandal, A. Bauzá, B.C. Samanta, A. Frontera, S.K. Seth, New J. Chem. 42 (2018) 10202–10213.
[11] J.W.G. Bloom, S.E. Wheeler, Angew. Chem. Int. Ed. 50 (2011) 7847–7849.
[12] S.K. Seth, D. Sarkar, T. Kar, CrystEngComm 13 (2011) 4528–4535.
[13] S.K. Seth, P. Manna, N.J. Singh, M. Mitra, A.D. Jana, A. Das, S.R. Choudhury, T. Kar, S. Mukhopadhyay, K.S. Kim, CrystEngComm 15 (2013) 1285–1288.
[14] P. Manna, S.K. Seth, M. Mitra, A. Das, N.J. Singh, S.R. Choudhury, T. Kar, S. Mukhopadhyay, CrystEngComm 15 (2013) 7879–7886.
[15] A. Frontera, P. Gamez, M. Mascal, T.J. Mooibroek, J. Reedijk, Angew. Chem. Int. Ed. 50 (2011) 9564–9583.
[16] P. Manna, S.K. Seth, M. Mitra, S.R. Choudhury, A. Bauzá, A. Frontera, S. Mukhopadhyay, Cryst. Growth Des. 14 (2014) 5812–5821.
[17] P. Manna, S.K. Seth, A. Bauzá, M. Mitra, S.R. Choudhury, A. Frontera, S. Mukhopadhyay, Cryst. Growth Des. 14 (2014) 747–755.
[18] M. Mitra, P. Manna, A. Bauzá, P. Ballester, S.K. Seth, S.R. Choudhury, A. Frontera, S. Mukhopadhyay, J. Phys. Chem. B 118 (2014) 14713–14726.
[19] S.K. Seth, I. Saha, C. Estarellas, A. Frontera, T. Kar, S. Mukhopadhyay, Cryst. Growth Des. 11 (2011) 3250–3265.
[20] P. Manna, S.K. Seth, A. Das, J. Hemming, R. Prendergast, M. Helliwell, S.R. Choudhury, A. Frontera, S. Mukhopadhyay, Inorg. Chem. 51 (2012) 3557–3571.
[21] I. Geronimo, E.C. Lee, N.J. Singh, K.S. Kim, J. Chem. Theor. Comput. 6 (2010) 1931–1934.
[22] A. Das, A.D. Jana, S.K. Seth, B. Dey, S.R. Choudhury, T. Kar, S. Mukhopadhyay, N.J. Singh, I.C. Hwang, K.S. Kim, J. Phys. Chem. B 114 (2010) 4166–4170.
[23] M.B. Oliver, B.A. Baquero, A. Bauzá, A.G. Raso, A. Terrón, I. Mata, E. Molins, A. Frontera, CrystEngComm 14 (2012) 5777–5784.
[24] M.P. Brandi-Blanco, J.M. Gonzalez-Perez, D.C. Lazarte, R. Carballo, A. Castinereiras, J. Niclos-Gutierrez, Inorg. Chem. Commun. 6 (2003) 270–273.
[25] I. Yousuf, M. Zeeshan, F. Arjmand, M.A. Rizvi, S. Tabassum, Inorg. Chem. Commun. 106 (2019) 48–53.
[26] S.-J. Liu, X.-R. Xie, T.-F. Zheng, J. Bao, J.-S. Liao, J.-L. Chen, H.-R. Wen,

CrystEngComm 17 (2015) 7270−7275.
[27] S.K. Seth, B. Dey, T. Kar, S. Mukhopadhyay, J. Mol. Struct. 973 (2010) 81−88.
[28] S.K. Seth, A. Bauza, A. Frontera, CrystEngComm 20 (2018) 746−754.
[29] S.K. Seth, Crystals 8 (2018) 455.
[30] S.A.I.N.T. Bruker, Version 6.36a, Bruker AXS Inc., Madison, Wisconsin, USA, 2002.
[31] S.M.A.R.T. Bruker, Version 5.625 and *SADABS*, Version 2.03a, Bruker AXS Inc., Madison, Wisconsin, USA, 2001.
[32] G.M. Sheldrick, ActaCryst. A 64 (2008) 112−122.
[33] G.M. Sheldrick, ActaCryst. C 71 (2015) 3−8.
[34] L.J. Farrugia, J. Appl. Crystallogr. 45 (2012) 849−854.
[35] A.L. Spek, J. Appl. Crystallogr. 36 (2003) 7−13.
[36] M. Tahmasebi, M. Mirzaei, H. Eshtiagh-Hosseini, J.T. Mague, A. Bauzá, A. Frontera, Acta Crystallogr. C75 (2019) 469−477.
[37] M.A. Spackman, J.J. McKinnon, CrystEngComm 4 (2002) 378−392.
[38] J.J. McKinnon, D. Jayatilaka, M.A. Spackman, Chem. Commun. (2007) 3814−3816.
[39] F.P.A. Fabbiani, L.T. Byrne, J.J. McKinnon, M.A. Spackman, CrystEngComm 9 (2007) 728−731.
[40] S.K. Seth, CrystEngComm 15 (2013) 1772−1781.
[41] M.A. Spackman, P.G. Byrom, Chem. Phys. Lett. 267 (1997) 215−220.
[42] J.J. McKinnon, A.S. Mitchell, M.A. Spackman, Chem. Eur J. 4 (1998) 2136−2141.
[43] J.J. McKinnon, M.A. Spackman, A.S. Mitchell, Acta Crystallogr. B 60 (2004) 627−668.
[44] A.L. Rohl, M. Moret, W. Kaminsky, K. Claborn, J.J. Mckinnon, B. Kahr, Cryst. Growth Des. 8 (2008) 4517−4525.
[45] S.K. Seth, Acta Crystallogr. E74 (2018) 600–606.
[46] M.J. Turner, J.J. McKinnon, S.K. Wolff, D.J. Grimwood, P.R. Spackman, D. Jayatilaka, M.A. Spackman, CrystalExplorer17, University of Western Australia, 2017.
[47] M.J. Frisch, G.W. Trucks, H.B. Schlegel, G.E. Scuseria, M.A. Robb, J.R. Cheeseman, G. Scalmani, V. Barone, G.A. Petersson, H. Nakatsuji, et al., *Gaussian 09*, Revision *C.01*, Gaussian, Inc., Wallingford, CT, USA, 2009.
[48] R.F.W. Bader, Chem. Rev. 91 (1991) 893−928.
[49] T.A. Keith, AIMAll, Version 13.05.06, TK Gristmill Software, Overland Park, KS, USA, 2013.
[50] R.F.W. Bader, Atoms in Molecules, a Quantum Theory, Oxford University Press, New York, NY, USA, 1990.
[51] J. Contreras-García, E.R. Johnson, S. Keinan, R. Chaudret, J.P. Piquemal, D.N. Beratan, W. Yang, J. Chem. Theor. Comput. 7 (2011) 625−632.
[52] E.R. Johnson, S. Keinan, P. Mori-Sanchez, J. Contreras-Garcia, A.J. Cohen, W. Yang, J. Am. Chem. Soc. 132 (2010) 6498−6506.
[53] P.C. Junk, M.K. Smith, J. Coord. Chem. 55 (2002) 1091−1096.
[54] Q.-Z. Zhang, X. He, Y.-Q. Yu, S.-M. Chen, C.-Z. Lu, Z. Anorg. Allg. Chem. 631 (2005) 798−802.
[55] X.-L. Gao, L.-P. Lu, M.-L. Zhu, Acta Crystallogr. E65 (2009) m561.
[56] Q.-Z. Zhang, C.-Z. Lu, W.-B. Yang, J. Coord. Chem. 59 (2006) 837−844.
[57] I.D. Brown, D. Altermatt, Acta Crystallogr. B 41 (1985) 244−247.
[58] H.H. Thorp, Inorg. Chem. 31 (1992) 1585−1588.
[59] T. Basak, K. Ghosh, C.J. Gómez-García, S. Chattopadhyay, Polyhedron 146 (2018) 42−54.

Volume 22
Number 47
21 December 2020
Pages 8153–8276

CrystEngComm

rsc.li/crystengcomm

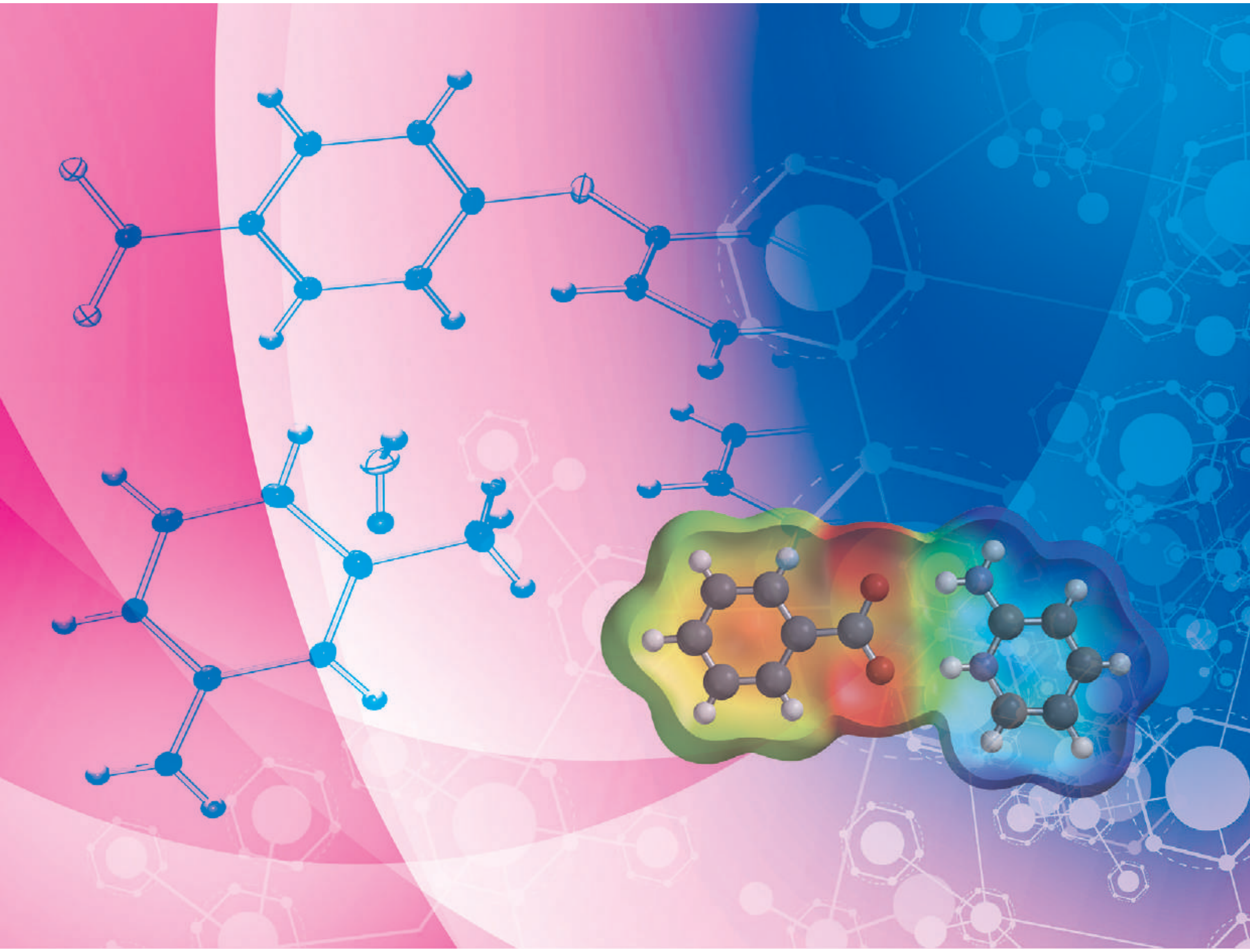

ISSN 1466-8033

ROYAL SOCIETY
OF **CHEMISTRY**

PAPER
Saikat Kumar Seth, Antonio Frontera *et al.*
Supramolecular assemblies involving salt bridges:
DFT and X-ray evidence of bipolarity

CrystEngComm

PAPER

Check for updates

Cite this: *CrystEngComm*, 2020, **22**, 8171

Supramolecular assemblies involving salt bridges: DFT and X-ray evidence of bipolarity†

Suparna Tripathi,[ab] Samiul Islam,[a] Saikat Kumar Seth, *[a] Antonio Bauzá, [c] Antonio Frontera *[c] and Subrata Mukhopadhyay[b]

Received 17th September 2020,
Accepted 15th October 2020

DOI: 10.1039/d0ce01356k

rsc.li/crystengcomm

A series of pyridinium-carboxylate salts (**1–3**) were designed, synthesized and structurally characterized to explore the importance of salt-bridge (SB) interactions in building self-assembled structures. We present a comprehensive analysis of the SB interaction in crystal structures of 4,4′-oxybis(benzoic acid) with substituted aminopyridines where the SBs display extremely well defined geometric preferences. In the solid-state, compound (**1**) exhibits lone-pair (l.p)···(SB)/(SB)···π^+ assemblies while compound (**2**) shows a C–H···(SB)/(SB)···π network. Interestingly, compound (**3**) exhibits two distinct networks π^+···(SB)/(SB)···(SB)/(SB)···π^+ and C–H···(SB)/(SB)···H–C. These extended supramolecular networks are studied and described in detail. The duality of the SBs in stabilizing the π-facial interactions with electron rich and/or electron poor moieties is also described. The energetic and geometric features of salt-bridge interaction are studied and its impact on the resultant supramolecular organization is analyzed using theoretical DFT-D3 calculations. The theoretical study combines the energetic features of the noncovalent forces that participate in the extended network and the characterization of the diverse interactions by means of Bader's theory of 'atoms in molecules'(AIM).

Introduction

The challenge of a systematic and thorough bulk analysis of factors directing the packing geometry of solid crystalline materials was raised by Desiraju over two decades ago.[1] The packing persuading features are described by strong and classical intermolecular interactions. To predict the actual crystal structure, precise understanding and complete control over the interplay of intermolecular interactions are required.[2] Therefore, an accurate relationship between crystal packing structures, in addition to molecular structures is essential for structural design. Weak noncovalent forces direct the formation of self-assembled supramolecular networks. The noncovalent forces like C–H···π,[3] π···stacking,[4] cation···π,[5] anion···π,[6] and lone pair···π[7] interactions, among others,[8] are prominent binding forces that have been used successfully to build solid-state networks.[8] Apart from these weak noncovalent interactions, hydrogen bonding plays a crucial role in crystal engineering due to specific, highly directive and relatively strong interactions.[9] The driving force that is predominant in the formation of synthons is hydrogen bonding and the supramolecular synthon serves as a backbone of the crystal structure by providing an articulate explanation of the entire structure.[10]

The salt bridge (SB) can be defined as an interaction between two groups of opposite charge where the protonated and deprotonated residues interact directly.[11] Therefore, salt bridges are hydrogen bonded ion pairs, which are important for the stabilization of molecular conformations. The hydrogen bonding of the SBs shows stronger binding compared to the normal hydrogen bonding interactions due to the zwitterionic charges (charge assisted hydrogen bond).[12] The formation of salt bridges is one of the significant noncovalent interactions that has been used to construct self-assembled structures in organic solvents.[13] In protein chemistry, SBs played a crucial role in substrate bonding, activity of catalytic triads, secondary-structure stabilization and stability of thermophilic proteins.[14] To generate new supramolecular systems,[15] intermolecular salt bridges are often used while biological systems such as proteins often comprise SBs that control their structure and function.[16] However, due to the geometric constraints placed by the electrostatic and H-bonding interactions, predicting SB interactions remains uniquely challenging.

---

[a] *Department of Physics, Jadavpur University, Kolkata-700032, India. E-mail: skseth@phys.jdvu.ac.in, saikatk.seth@jadavpuruniversity.in*
[b] *Department of Chemistry, Jadavpur University, Kolkata-700032, India*
[c] *Department of Chemistry, Universitat de les Illes Balears, Crta. De Valldemossa km 7.5, 07122 Palma de Mallorca, Baleares, Spain. E-mail: toni.frontera@uib.es*

† Electronic supplementary information (ESI) available: Three crystallographic files (CIF); Fig. S1–S9 represent various supramolecular networks of the title compounds and the theoretical models of compound (3). CCDC 1831105–1831107. For ESI and crystallographic data in CIF or other electronic format see DOI: 10.1039/d0ce01356k

We are particularly interested in exploring the associative network structures involving salt bridges. The influence of salt bridges on cation–π interaction had been investigated by computational analysis and synthetic studies.[17] However, a comprehensive study of the interaction between a planar salt bridge and aromatic rings and cooperativity of other noncovalent forces with SBs is not well explored. As depicted in Scheme 1, the SBs are very rich as binding motifs due to their dual character that makes it adequate for establishing a great deal of noncovalent interactions. As a matter of fact, we reported salt-bridge (SB)···π interaction by providing both experimental evidence and theoretical calculations.[18] Herein, we analyze the salt-bridge interaction of three salts and their self-assembled structures involving charged aromatic rings and other noncovalent interactions, by means of experimental and theoretical calculations. The structural analyses of these compounds revealed the formation of completely new and extended supramolecular networks by the formation of salt-bridge interactions. The combinations of weak forces in building the extended networks [lone-pair (l.p)···(SB)/(SB)···π^+ in (**1**), C–H···(SB)/(SB)···π in (**2**) and π^+···(SB)/(SB)···(SB)/(SB)···π^+ and C–H···(SB)/(SB)···H–C in (**3**)] are described in detail, including theoretical calculations. The binding energies of the networks have been calculated using theoretical DFT calculations and the noncovalent interactions have been analyzed by using Bader's quantum theory of "atoms in molecules" (QTAIM).

Experimental

Materials

The reagents [4,4′-oxybis(benzoic acid)], 2-amino-5-methylpyridine and 2-amino-4-methylpyridine)] and solvents [*N*,*N*-dimethylformamide (DMF) and dimethyl sulfoxide(DMSO)] were purchased from commercial sources (Sigma-Aldrich, India) and used without further purification.

Syntheses

Compounds **1–3** were prepared by reacting stoichiometric amounts of 4,4′-oxybis(benzoic acid) molecules with substituted aminopyridine ligands. 4,4′-Oxybis(benzoic acid) (0.258 g, 1.0 mmol) was dissolved in 20 ml of DMF for (**1–2**) and DMSO for (**3**) and heated at 50 °C resulting in a clear solution. Then, 2.0 mmol (0.216 g) of 2-amino-5-methylpyridine, 1 mmol (0.108 g) of 2-amino-4-methylpyridine and 2 mmol (0.216 g) of 2-amino-4-methylpyridine was added to 10 mL of water–methanol (1 : 1) for (**1–3**), respectively. These solutions were added drop wise to the acid solution with continuous stirring. The solution mixtures obtained were heated at 50 °C for 1 h with continuous stirring. The resulting solutions were kept undisturbed at ambient temperature and covered with paraffin film and a few small holes were made using a needle to allow the solvent to evaporate slowly. After 6–8 weeks, testable single crystals were grown. The utilization of DMSO instead of DMF in **3** is needed in order to obtain suitable crystals for X-ray measurements. Similarly, the utilization of 1 instead of 2 mmol of the aminopyridine derivate in compound **2** is needed to obtain crystals adequate for X-ray analysis.

X-ray crystal structure determination

Single crystal X-ray diffraction intensity data of the title compounds were collected at 150(2) K for (**1**) and 120(2) K for (**2–3**) using a Bruker APEX-II CCD diffractometer by using graphite monochromated MoKα radiation (λ = 0.71073 Å). Data reduction was performed by using the program Bruker SAINT[19] and empirical absorption correction was applied.[20] The structures were solved by direct methods and refined by the full-matrix least-squares technique on F^2 with anisotropic thermal parameters by describing the thermal motions of all non-hydrogen atoms using the programs (SHELXS-14)[21] and (SHELXL-18),[22] respectively. The hydrogen atoms were positioned from the difference Fourier map and consequently refined isotropically. The calculations were performed using the WinGX system V2014.1 (ref. 23) and PLATON.[24] The summary of crystal data and relevant structure refinement parameters for the title compounds are included in Table 1. CCDC 1831105–1831107 contain the ESI† crystallographic data for this paper.

Theoretical methods

We have used the BP86-D3/def2-TZVP level of theory to compute the energies of the H-bonding interactions by means of the program TURBOMOLE version 7.0.[25] The crystallographic coordinates have been used for the theoretical calculations. The binding energies were computed

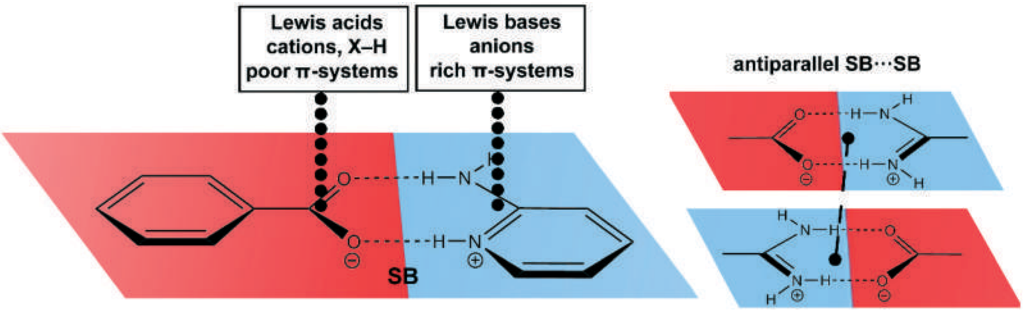

Scheme 1 Dual character of salt bridges (negative part in red and positive part in blue) and some of the interactions described herein.

Table 1 Crystal data and structure refinement parameters for (**1**–**3**)

Structure	(**1**)	(**2**)	(**3**)
Empirical formula	$C_{26}H_{28}N_4O_6$	$C_{20}H_{18}N_2O_5$	$C_{26}H_{28}N_4O_6$
Formula weight	492.52	366.36	492.52
Temperature (K)	150(2)	120(2)	120(2)
Wavelength (Å)	0.71073	0.71073	0.71073
Crystal system	Monoclinic	Monoclinic	Triclinic
Space group	$C2/c$	$P2_1/n$	$P\bar{1}$
a, b, c (Å)	13.864(11), 12.086(11), 14.994(12)	7.075(3), 19.857(2), 12.811(2)	6.855(4), 7.642(3), 24.281(4)
α, β, γ (°)	90, 111.62(2), 90	90, 94.991(2), 90	90.019(3), 92.555(2), 107.022(4)
Volume (Å^3)	2336(3)	1793.0(8)	1214.9(9)
Z/density (calc.) (mg m^{-3})	4/1.401	4/1.357	2/1.346
Absorption coefficient (mm^{-1})	0.101	0.099	0.097
F(000)	1040	768	520
Crystal size (mm^3)	0.18 × 0.11 × 0.06	0.19 × 0.11 × 0.05	0.19 × 0.15 × 0.09
Limiting indices	$-16 \le h \le 16$, $-14 \le k \le 14$, $-17 \le l \le 17$	$-8 \le h \le 8$, $-23 \le k \le 23$, $-15 \le l \le 15$	$-8 \le h \le 8$, $-9 \le k \le 9$, $-28 \le l \le 28$
Reflections collected/unique	9037/2021 [R(int) = 0.0741]	20 967/3155 [R(int) = 0.0363]	11 530/4260 [R(int) = 0.0238]
Completeness to θ (%)	98.7	100.0	99.8
Absorption correction	Semi-empirical from equivalents	Semi-empirical from equivalents	Semi-empirical from equivalents
Max. and min. transmission	0.99 and 0.98	0.99 and 0.98	0.99 and 0.98
Refinement method	Full-matrix least-squares on F^2	Full-matrix least-squares on F^2	Full-matrix least-squares on F^2
Data/parameters	2021/166	3155/245	4260/328
Goodness-of-fit on F^2	1.084	1.040	1.047
Final R indices [$I > 2\sigma(I)$]	R_1 = 0.0494, wR_2 = 0.1320	R_1 = 0.0355, wR_2 = 0.0927	R_1 = 0.0339, wR_2 = 0.0910
R indices (all data)	R_1 = 0.0540, wR_2 = 0.1371	R_1 = 0.0435, wR_2 = 0.0995	R_1 = 0.0388, wR_2 = 0.0947
Largest diff. peak and hole (e Å^{-3})	0.218 and −0.313	0.224 and −0.205	0.220 and −0.167
CCDC nos.	1831105	1831106	1831107

$R_1 = \sum||F_o| - |F_c||/\sum|F_o|$, w$R_2 = [\sum\{(F_o^2 - F_c^2)^2\}/\sum\{w(F_o^2)^2\}]^{1/2}$, $w = 1/\{\sigma^2(F_o^2) + (aP)^2 + bP\}$, where a = 0.0845 and b = 0.6212 for (**1**), a = 0.0506 and b = 0.5361 for (**2**) and a = 0.0461 and b = 0.3636 for (**3**). $P = (F_o^2 + 2F_c^2)/3$ for all structures.

applying the correction for the BSSE (basis set superposition error) by means of the counterpoise technique developed by Boys–Bernardi.[26] The AIMall calculation package[27] was employed to analyze the interactions studied using Bader's "atoms-in-molecules" (AIM) theory.[28] The molecular electrostatic potential (MEP) surfaces have been calculated using the SPARTAN10 program.[29] The calculations for the wavefunction analysis have been carried out at the BP86-D/def2TZVP level of theory using Gaussian-09 software.[30]

Results and discussion

Structural description

The ORTEP view of the title compounds (**1**–**3**) is shown in Fig. 1. In compounds (**1**) and (**3**), 4,4′-oxybis(benzoic acid) is fully deprotonated with two 2-amino-5-methylpyridinium and 2-amino-4-methylpyridinium cations, respectively, with one solvent water molecule. However, in (**2**), 4,4′-oxybis(benzoic acid) is partly deprotonated with one 2-amino-4-methylpyridinium cation. In (**1**), the oxygen atom O(3) lies on the inversion centre ($-x + 2$, y, $-z + 1/2$) and thus generates a symmetric counterpart (see Fig. 1a).

In (**1**), the pyridinium and amine nitrogen atoms N(1) and N(2) act as donors to the carboxylate oxygen atoms at ($1/2 - x$, $-1/2 + y$, $1/2 - z$), thus forming an $R_2^2(8)$ dimeric ring termed as salt bridge (SB) (Fig. S1†) (Table 2). Two nearby dimeric rings are interconnected by further interaction between amine nitrogen and carboxylate oxygen atoms. This hydrogen bond leads the molecules to form an $R_4^2(8)$ ring motif (Fig. S1†). Again the solvent water molecule acts as a double donor to the carboxylate oxygen atom O(1) at ($3/2 - x$, $1/2 + y$, $1/2 - z$), thus interconnecting the ring motifs and leading to the formation of a two-dimensional assembly in the (101) plane (Fig. S1†). In another substructure, the aryl ring carbon atom C(6) acts as a donor to the carboxylate oxygen atom O(2) in the molecule at ($3/2 - x$, $-1/2 + y$, $1/2 - z$) to form a two-dimensional anionic network in the (110) plane (Fig. S2†).

Interestingly, the lone-pair of the oxygen atom O(3) is oriented toward the salt-bridge unit with a separation distance of 3.312 Å. In the opposite side, the π-face of the pyridinium moiety is juxtaposed to the SB unit with a separation distance of 3.710 Å; thus, dual bridging of the SB⋯π^+ network is observed where the two pyridinium moieties are also optimized (Fig. 2). The pyridine rings at (x, y, z) and ($-x$, $-y$, $-z$) are anti-parallel, with an interplanar spacing of 3.272 Å, and a ring centroid separation of 3.720(3) Å, corresponding to a ring offset of 1.77 Å. Thus lone-pair (l.p)⋯SB/SB⋯π^+ is observed in (**1**) (Fig. 2). Again, the pyridinium ring and aryl ring of the acid moiety are optimized further in the molecule at ($1 - x$, y, $1/2 - z$) with a separation distance of 3.561(3) Å. Thus, the molecules of (**1**) generate an extended unique network lone-pair (l.p)⋯(SB)/(SB)⋯π^+ through the SB unit (Fig. 2).

In (**2**), the pyridinium and amine nitrogen atoms N(1) and N(2) act as donors to the carboxylate oxygen atoms O(1) and O(2), respectively (see Table 2) in the molecule at ($-x$, $1 - y$, 2

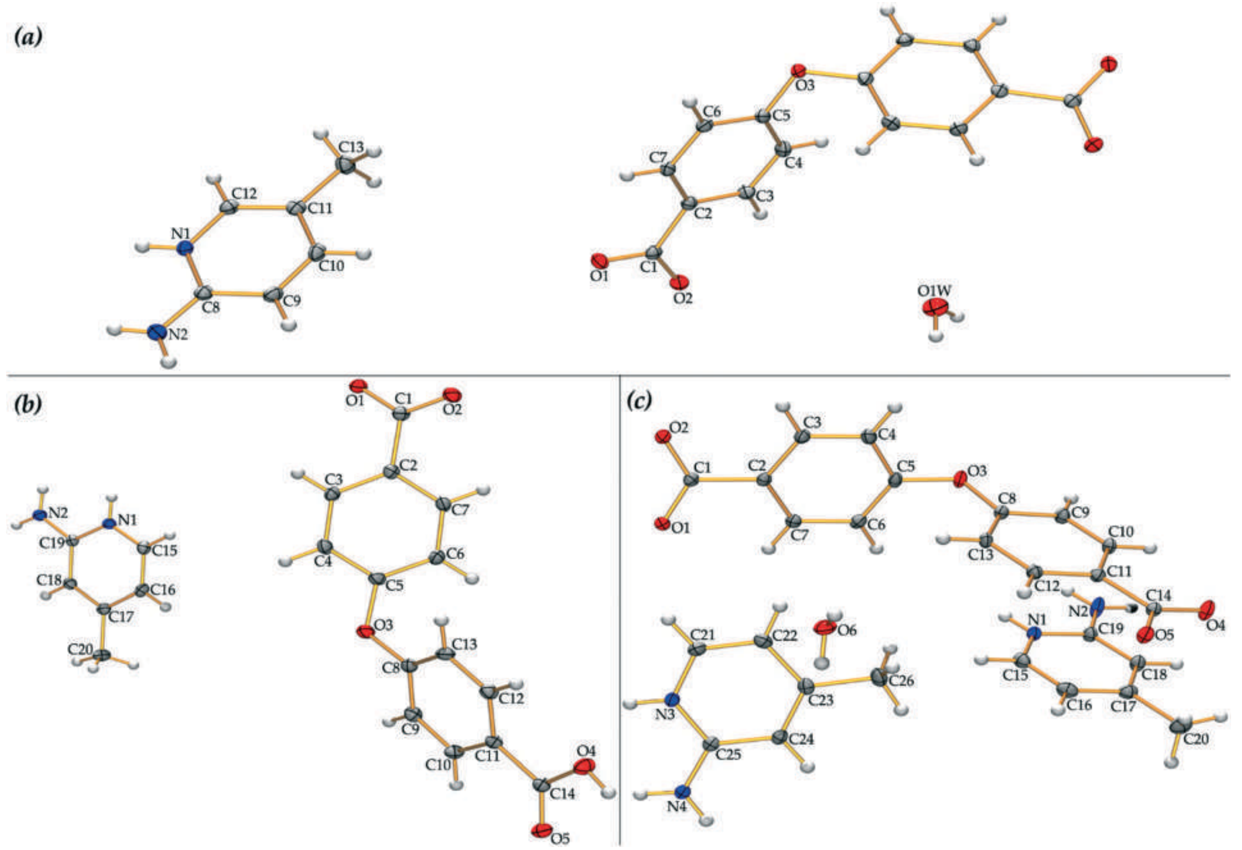

Fig. 1 Molecular view (ORTEP) of the asymmetric unit of the title compounds (**1**–**3**) (a–c) with the atom numbering scheme. In compound (**1**), the unlabelled counterpart has been generated through the symmetry operation (−x + 2, y, −z + 1/2). The thermal ellipsoids are drawn at the 30% probability level.

Table 2 Relevant hydrogen bonding parameters in (**1**–**3**)

D–H···A	D–H	H···A	D···A	D–H···A	Symmetry
Compound (**1**)					
N(1)–H(1)···O(1)	0.86	1.86	2.712(3)	173	$1/2 - x, -1/2 + y, 1/2 - z$
N(2)–H(2A)···O(2)	0.86	1.90	2.762(3)	179	$1/2 - x, -1/2 + y, 1/2 - z$
N(2)–H(2B)···O(2)	0.86	2.06	2.839(3)	150	$-1 + x, 1 - y, -1/2 + z$
O(1w)–H(1w)···O(1)	0.82	2.00	2.813(3)	170	$3/2 - x, 1/2 + y, 1/2 - z$
C(6)–H(6)···O(2)	0.93	2.49	3.404(3)	168	$3/2 - x, -1/2 + y, 1/2 - z$
C(13)–H(13C)···Cg(1)	0.93	2.70	3.565(4)	150	$-1/2 + x, -1/2 + y, z$
Compound (**2**)					
N(1)–H(1)···O(3)	0.86	1.92	2.774(2)	172	$-x, 1 - y, 2 - z$
N(2)–H(2A)···O(4)	0.86	1.93	2.790(2)	174	$-x, 1 - y, 2 - z$
N(2)–H(2B)···O(3)	0.86	2.25	2.865(2)	129	$1 + x, 1 + y, z$
O(2)–H(2)···O(1)	0.82	1.78	2.585(2)	169	$1/2 - x, -1/2 + y, 3/2 - z$
C(5)–H(5)···O(4)	0.93	2.44	3.298(2)	154	$-1/2 + x, 1/2 - y, 1/2 + z$
Compound (**3**)					
N(1)–H(1)···O(5)	0.86	1.84	2.698(2)	172	$x, -1 + y, z$
N(2)–H(2A)···O(4)	0.86	1.88	2.737(2)	172	$x, -1 + y, z$
N(2)–H(2B)···O(4)	0.86	2.08	2.848(2)	148	$1 - x, 1 - y, -z$
N(3)–H(3)···O(1)	0.86	1.81	2.654(2)	165	$1 - x, -y, 1 - z$
N(4)–H(4A)···O(2)	0.86	2.04	2.899(2)	173	$1 - x, -y, 1 - z$
N(4)–H(4B)···O(6)	0.86	2.11	2.899(2)	153	$1 + x, y, z$
O(6)–H(6A)···O(1)	0.83	1.98	2.794(2)	169	$x, 1 + y, z$
O(6)–H(6B)···O(2)	0.83	1.95	2.775(2)	174	$1 + x, 1 + y, z$
C(6)–H(6)···O(5)	0.93	2.54	3.400(3)	154	$x, -1 + y, z$
C(21)–H(21)···O(1)	0.93	2.57	3.313(3)	137	—

In (**1**), Cg(1) is the centroid of the (C2–C7) ring.

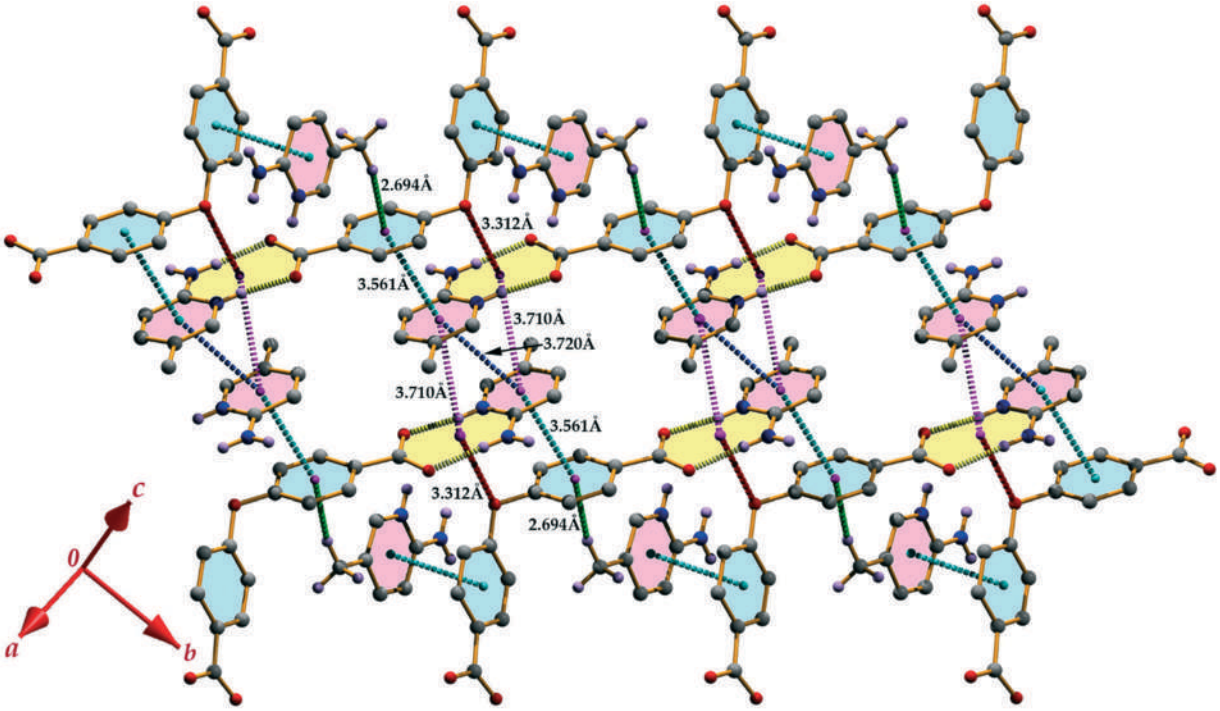

Fig. 2 Perspective view of the extended lone-pair (l.p)⋯SB/SB⋯π^+ network in (**1**). The SB unit is highlighted by yellow colour whereas the π^+ and π moieties are shown by pink and turquoise colour, respectively.

− z) to form the SB unit $R_2^2(8)$ (Fig. S3†). Again the amine hydrogen atom acts as a secondary donor to the carboxylate oxygen atom at (1 + x, 1 + y, z), thus forming an $R_4^2(8)$ ring. Due to self-complementarity, the non-protonated carboxy oxygen atom O4 acts as a donor to protonate the carboxylate oxygen atom O1 and interconnect the ring motifs to build a two-dimensional framework in the (110) plane (Fig. S3†). In another substructure, the methyl carbon atom of the pyridinium moiety is in contact with the SB unit with a separation distance of 2.912 Å. On the other side of the SB unit, the π-cloud of the aryl ring is oriented towards the SB unit with a separation distance of 2.060 Å. Thus, a unique C–H⋯SB/SB⋯π network is observed in (**2**) (Fig. 3).

In (**3**), two SB units [$R_2^2(8)$ ring motifs] are generated through the N–H⋯O hydrogen bonding interactions (Table 2). These two SB units are interconnected by CH⋯O hydrogen bonds thus propagating into a one-dimensional chain along the [010] direction (Fig. S4†). The parallel chains are further interconnected by hydrogen bonds between the amine nitrogen and carboxylate oxygen atoms. This combination of interactions leads the molecules to generate a two-dimensional framework in the (011) plane (Fig. S4†). In another substructure, one SB unit is in contact with the solvent water molecule where the amine nitrogen atom acts as a donor to the water oxygen atom and the water oxygen atom acts as a donor to the carboxylate oxygen atom. Thus, the mutual interaction of N–H⋯O and O–H⋯O hydrogen bonds generates an $R_6^4(12)$ ring motif that leads the molecules to propagate along the [100] direction (Fig. S5†). In the other side of the carboxylate anion, the SB is interconnected with another SB of the partner

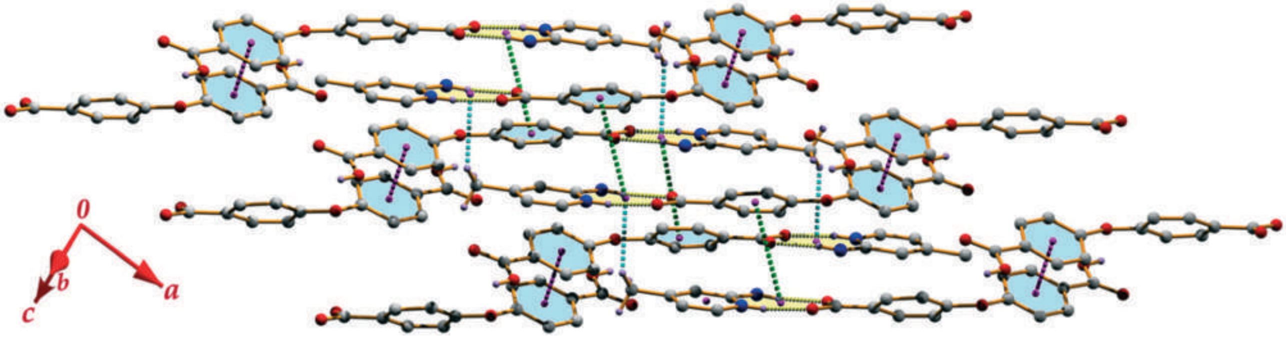

Fig. 3 Extended C–H⋯SB/SB⋯π network in (**2**). The SB, C–H⋯SB, SB⋯π and π–π stacking interactions are represented by the yellow, turquoise, green and pink dotted lines, respectively.

molecule through the N–H⋯O hydrogen bond and generates a supramolecular layered assembly in the (110) plane (Fig. S5†). In another substructure, the aryl ring of the acid moiety is oriented towards the π-cloud of the pyridine ring with an interplanar spacing of 3.426 Å with an intercentroid separation of 3.805 Å. Again the pyridine ring is juxtaposed to the aryl ring of the acid moiety through π-stacking interaction with a separation distance of 3.667 Å. Repetition of the π–π^+/π^+–π network leads the molecules to propagate into a one-dimensional ribbon along the [100] direction (Fig. S6†). These parallel ribbons are interconnected through the SB unit and generate a supramolecular layered assembly in the (110) plane (Fig. S6†). Compound (**3**) exhibits two distinctly different supramolecular networks involving the SB unit. In one substructure, the SB unit lies just above the π-cloud of the pyridine ring with a separation distance of 3.754 Å. Thus a face-to-face dual SB⋯π^+ unit is generated (Fig. 4a). Two adjacent dual SB⋯π^+ units are juxtaposed through SB⋯SB interaction with a separation distance of 3.616 Å. Thus, an extended π^+⋯SB/SB⋯SB/SB⋯π^+ network is generated in (**3**) (Fig. 4a). In another substructure, the second SB unit that is generated through the second carboxylate unit also takes part in building the extended network. The methyl carbon atom of the pyridine moiety is oriented towards the SB unit with a separation distance of 3.237 Å (Fig. 4b). Another methyl carbon from the aminopyridine moiety is in contact with the SB unit with a separation distance of 2.840 Å. Thus a CH⋯SB/SB⋯HC network is generated in (**3**) (Fig. 4b). These unique and extended two distinct networks are also observed in a supramolecular-layered assembly (Fig. S7†).

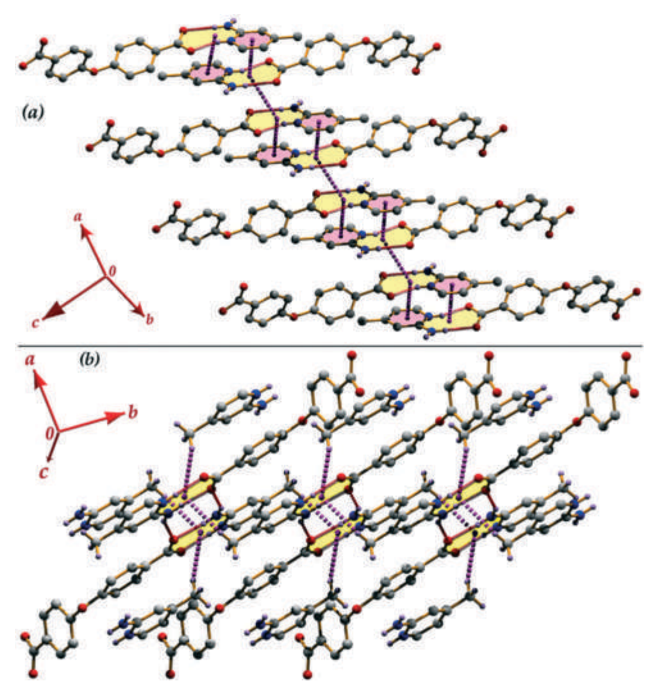

Fig. 4 Perspective view of the π^+⋯SB/SB⋯SB/SB⋯π^+ network (a) and the CH⋯SB/SB⋯HC network (b) in (**3**). The SB units are highlighted by yellow colour whereas the π^+ moieties are shown in pink colour.

Theoretical calculations

We have executed the computational study using density functional theory with dispersion correction (DFT-D3) calculations to analyze the noncovalent interactions involved in the interesting architectures of compounds (**1**–**3**).

We are particularly interested in performing the calculations of the extended networks involving the salt bridge unit. We have focused our efforts on two main issues. First, we have studied the energetic features of the noncovalent interactions and second we have analyzed the interplay between them and characterized the interactions using Bader's theory of "atoms-in-molecules" (AIM). The crystallographic coordinates have been used in theoretical models/calculations and in some cases, we have modified the small fragments to evaluate the contributions for the formation of the self-assembly.

First of all, we have computed the MEP surface of the 2-aminopyridinium-benzoate salt bridge as a model of compounds (**1**–**3**) in order to illustrate the dual donor–acceptor ability of the salt bridge. Fig. 5 depicts the MEP surface where the most positive MEP value is located at the H-atom of the amino group (+57 kcal mol^{-1}) and the most negative at the O-atom of the carboxylate group (−52 kcal mol^{-1}). Interestingly, the surface clearly confirms the existence of two different halves of the salt bridge, one electron poor and the other electron rich, as illustrated by the opposite values over the center of the aromatic ring. Consequently, the large dipole moment (11.7 D) and the planarity of the system also facilitate the formation of antiparallel stacking interactions, either with itself or any other planar system with large dipole moments like charged aromatic rings.

For compound (**1**), we have prepared some models (following Fig. 2) to evaluate the formation energies (see Fig. 6). In Fig. 6a, the acid moiety is simplified (see the red arrow) in which the formation energy of the salt bridge (SB) is ΔE_1 = −110.6 kcal mol^{-1}. Due to the ion-pair nature of the interaction, the formation energy ΔE_1 is very large. In the model shown in Fig. 6b, the carboxylate units are modified

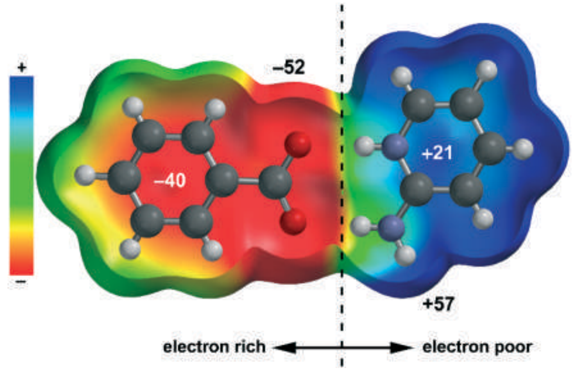

Fig. 5 MEP surface of the aminopyridinium-benzoate salt bridge using the 0.001 a.u. isosurface. The values are the selected points of the surface indicated in kcal mol^{-1}.

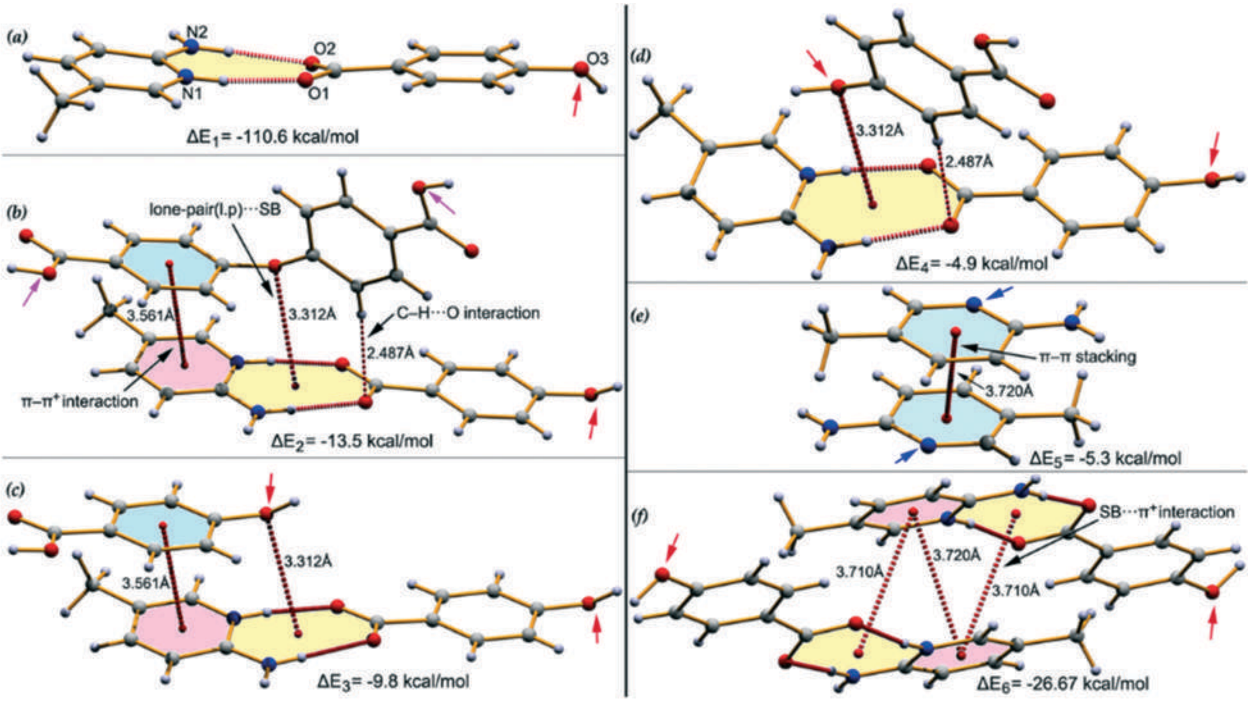

Fig. 6 Various theoretical models (a–f) used to analyse the noncovalent interactions observed in the supramolecular assembly observed in the solid state structure of compound (**1**).

(see the pink arrows) to make the model neutral. The formation energy of the cooperative interactions [lone-pair (l.p)···SB, π–π^+ and CH···O H-bonding] is moderately strong $\Delta E_2 = -13.5$ kcal mol^{-1}. We have used several theoretical models to evaluate the contribution of each interaction separately. In this context, we prepared two models where the benzoic acid moiety is simplified: (i) to avoid the C–H···O interaction in Fig. 6c and (ii) to avoid the π–π^+ interaction in Fig. 6d. The first model where lone-pair (l.p) ···SB and π–π^+ are evaluated exhibits a formation energy of $\Delta E_3 = -9.8$ kcal mol^{-1}. So, the binding energy of the CH···O interaction can be evaluated as a difference, *i.e.* $\Delta E_2 - \Delta E_3 = -3.7$ kcal mol^{-1}. The formation energy of the second model where lone-pair (l.p)···SB and CH···O interactions are estimated is $\Delta E_4 = -4.9$ kcal mol^{-1} (see Fig. 6d). So, the formation energy of the π–π^+ interaction can also be deduced by difference, which is $\Delta E_2 - \Delta E_4 = -8.6$ kcal mol^{-1}. The energy of the lone-pair (l.p)···SB interaction is $(-4.9 + 3.7 = -1.2)$ kcal mol^{-1}. Moreover, we have used the neutral aminopyridine moiety (see the blue arrows in Fig. 6e) to estimate the energy of the π-stacking interaction in the absence of the strong electrostatic repulsion between the cationic arenes.

Finally, the model dimer shown in Fig. 6f is crucial to understand the π^+···SB/SB···SB/SB···π^+ network discussed above in Fig. 4a. The formation energy of the model shown in Fig. 6f, where two SB···π^+ and one π^+–π^+ interactions are acting mutually, is very large $\Delta E_6 = -26.67$ kcal mol^{-1}, thus confirming that it is a strong binding motif. In order to estimate the contribution of both SB···π^+ interactions, we have subtracted the energy of the π–π interaction evaluated in Fig. 6e to the formation energy of the assembly, which is $(\Delta E_6 - \Delta E_5) = -21.36$ kcal mol^{-1}, thus evidencing that each SB···π^+ interaction is moderately strong (-10.68 kcal mol^{-1}).

For compound (2), the models used to compute the formation energies are shown in Fig. 7. We have used

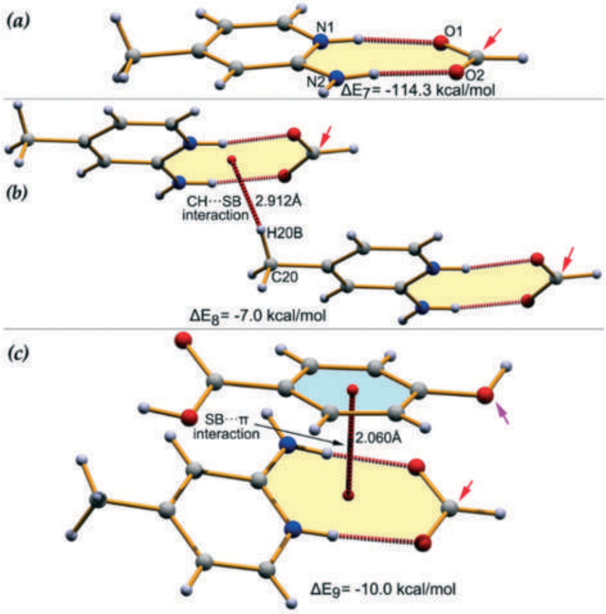

Fig. 7 The different interactions observed in the self-assembly of compound (**2**) are shown by the models (a–c) which are used for theoretical computation.

formate ions (see the red arrow) as a model of 4,4′-oxybis(benzoic acid) in building the SB unit. This model allows us to study the stacking interaction between the neutral moieties (formate and protonated aminopyridine ion-pairs). The formation energy of the SB is higher ($\Delta E_7 = -114.3$ kcal mol^{-1}) compared to compound (**1**). We have used the neutral models to evaluate the formation energy of the CH⋯SB interaction ($\Delta E_8 = -7.0$ kcal mol^{-1}) (Fig. 7b).

Following Fig. 3, we have calculated the formation energy of the SB⋯π interaction using the model where the acid moiety is simplified (see the pink arrow in Fig. 7c). The formation energy of the SB⋯π interaction in (**2**) is $\Delta E_9 = -10.0$ kcal mol^{-1} which is comparable to the energy value of the SB⋯π^+ interaction of compound (**1**) (−10.68 kcal mol^{-1}).

In compound (**3**), two SB units are generated by the two-protonated carboxylate groups of 4,4′-oxybis(benzoic acid). Therefore, two distinctly different networks are generated involving the SB units. We have simplified the model (see red arrow in Fig. 8a) to calculate the formation energy of the SB, which is $\Delta E_{10} = -108.8$ kcal mol^{-1}. It is slightly weaker than those of compounds (**1**) and (**2**). In another model (Fig. 8b), we have used 2-aminopyridine instead of 2-amino-4-methylpyridine to avoid the CH contacts with partner molecules (see the blue arrows). The binding energy of the dual SB⋯π^+ interaction is strong ($\Delta E_{11} = -24.4$ kcal mol^{-1}). Finally, we have computed the binding energy of the SB⋯SB interaction, which is also strong ($\Delta E_{12} = -21.8$ kcal mol^{-1}). Therefore, the antiparallel SB⋯SB interaction is much more favorable in comparison to the SB⋯π^+ interaction (−12.2 kcal mol^{-1}) due to the dual ion-pair interaction. These large interaction energies confirm the importance of both interactions in building the π^+⋯SB/SB⋯SB/SB⋯π^+ network shown in Fig. 4a. The energies associated with the other SB network are given in the ESI† (see Fig. S8).

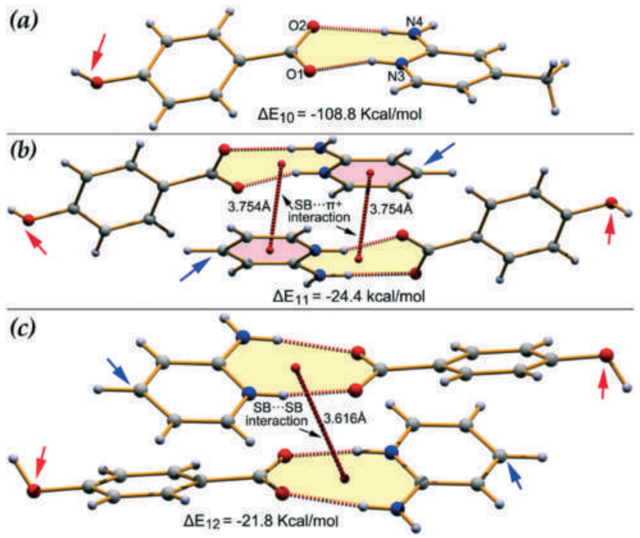

Fig. 8 Theoretical models (a–c) of compound (**3**) and their interaction energies.

Previous reports have also evaluated different types of salt-bridge assemblies, showing comparable interaction energies. For instance, lp⋯SB and SB⋯π interactions have been described[31] in the solid state of Cu(ii)-malonate-2-amino-5-chloropyridine-perchlorate ternary salts and evaluated theoretically with energies ranging from −5 to −10 kcal mol^{-1}. Similarly, the structure guiding ability of SB⋯π interactions in Cu(ii)-malonate-2-aminopyridine-hexafluoridophosphate ternary systems has been demonstrated both theoretically and experimentally.[32] Furthermore, it has been demonstrated that SB⋯π interactions favor the cell penetration of arginine/tryptophan-rich cell-penetrating peptides.[33]

We have performed the Bader's theory of atoms in molecules (AIM)[28] analysis of the self-assembled network structures of compounds (**1–3**) by using the models described above. The AIM is used to visualize and characterize the noncovalent interactions involved within the structures by paying attention to the distribution of the critical points and bond paths. The existence of a bond critical point (CP) and bond path connecting two atoms is clear evidence of interaction, since it indicates that electron density is accumulated between the nuclei that are linked by the associated atomic interaction line.[27] AIM analysis has been recently used to rationalize similar noncovalent interactions.[34] In Fig. 9, we represent the distribution of CPs and bond paths of the extended networks of compounds (**1–3**). The CH⋯SB/SB⋯HC network of compound (**3**) is shown in Fig. S9.† In all cases, the SB is characterized by the presence of the two bond CPs (represented as purple spheres in Fig. 9) and bond paths connecting the H atoms of the aminopyridine and the carboxylate oxygen atoms (Fig. 9 and S9†). A ring CP (yellow sphere) further characterizes the SBs due to the formation of a supramolecular ring. The $\rho(r)$ values at the bond CPs are indicated in Fig. 9. For the SBs of all compounds, the $\rho(r)$ values at the bond CPs that characterize the pyridine N$^+$H⋯O bond are larger than those of the amine NH⋯O bonds which is in agreement with their shorter distances. Therefore, it can be concluded that the protonated pyridine N$^+$H⋯O hydrogen bond is stronger than the exocyclic NH⋯O bond.

For compound (**1**), the interactions shown in Fig. 6b are clearly evident by the distribution of bond CPs and bond paths (Fig. 9a). The lone-pair (l.p)⋯SB interaction is characterized by a bond CP (purple sphere) and bond path connecting the O and pyridine N atom of the SB unit ($\rho_{\mathrm{BCP}} = 0.0054$ a.u.). The CH⋯O H bond is also characterized by the corresponding BCP ($\rho_{\mathrm{BCP}} = 0.0094$ a.u.) and bond path. The π–π^+ interaction (ρ_{BCPs} = 0.0064 and 0.0052 a.u.) is characterized by the presence of two BCPs and bond paths interconnecting two carbon atoms of the aryl and pyridine rings (Fig. 9a). The SB⋯π^+ interaction (see Fig. 6f) is characterized by two BCPs where one bond path connects one carbon atom of the pyridine ring and nitrogen atom of the pyridine ring ($\rho_{\mathrm{BCP}} = 0.0063$ a.u.) and another bond path connects the pyridine ring carbon atom and carboxylate oxygen atom ($\rho_{\mathrm{BCP}} = 0.0063$ a.u.). In compound (**2**), the $\rho(r)$

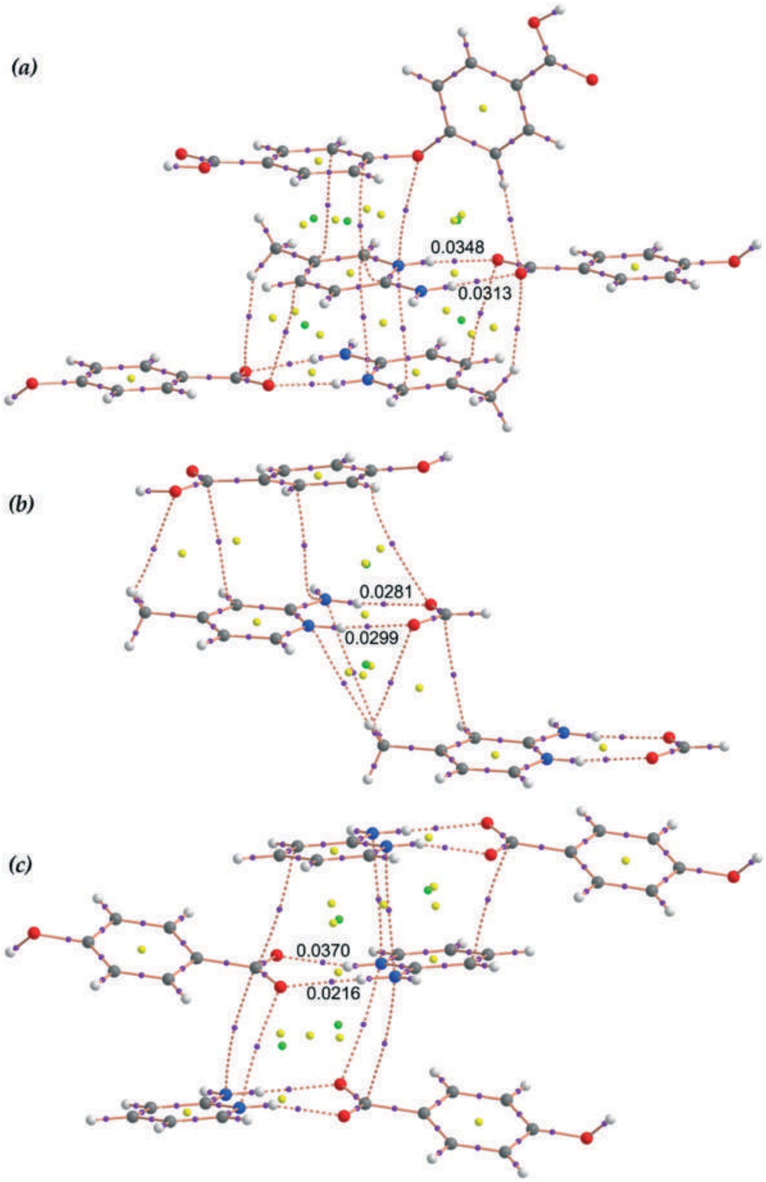

Fig. 9 Distribution of the critical points of the self-assembled extended networks of compounds (**1**–**3**) (a–c). Red, yellow and green spheres represent the bond, ring and cage critical points, respectively.

values of the SB and bond paths are shown in Fig. 9b. The BCP and bond path connecting the amine nitrogen and carbon atom of the aryl ring characterizes the extended SB⋯π interaction where the ρ_{BCP} value is 0.0058 a.u. The CH⋯SB interaction in (**2**) is characterized by two BCPs and bond paths connecting one hydrogen atom of the methyl group with one carboxylate oxygen and pyridine ring nitrogen atom (ρ_{BCPs} = 0.0039 and 0.0033 a.u. respectively) (see Fig. 9b). An additional bond path connects another hydrogen atom of the methyl group and amine nitrogen atom that further characterizes the CH⋯SB interaction (ρ_{BCP} = 0.0013 a.u.). In compound (**3**), two SBs are evidenced and the associated networks are depicted in Fig. 9c and S9.†

The SB⋯π^+ interaction is characterized by two BCPs where one bond path connects the carbon atoms of the pyridine ring and carboxylate moiety (ρ_{BCP} = 0.0046 a.u.) and another bond path connects the pyridine ring nitrogen and amine nitrogen atom (ρ_{BCP} = 0.0052 a.u.). Four BCPs and bond paths characterize the SB⋯SB interaction (Fig. 9c). The CH⋯SB/SB⋯HC network is characterized by two BCPs and two bond paths connecting methyl hydrogen atoms with the carboxylate oxygen atom where the $\rho(r)$ values are 0.0073 and 0.0062 (see Fig. S9†).

Conclusions

Three new aminopyridinium/4,4′-oxydibenzoate salts have been synthesized and their structures have been determined by single-crystal X-ray diffraction. A common feature of these compounds in the formation of salt bridges between aminopyridinium cations and 4,4′-oxydibenzoate succinate anions is observed. They participate in a great variety of interactions due to the dual nature of the salt bridge. These interactions determine the crystal packing architecture of all the salts and have been evaluated using theoretical calculations and AIM analysis that confirm the existence of the interactions. The evaluation of the contributions of several interactions to the total formation energy of the assemblies evidences that the SB$\cdots\pi$ and antiparallel SB$\cdots$SB interactions are very strong. Since salt-bridge formation between the side chain of aspartate or glutamate and arginine is very common in protein and enzymes, π-facial interactions with the side chain or aromatic amino acids or substrates can be very common, thus suggesting that more research in this direction is needed.

Conflicts of interest

There are no conflicts to declare.

Acknowledgements

S. K. Seth gratefully acknowledges the financial support from SERB (New Delhi) India for research project (EEQ/2019/000384). We thank the MICIU/AEI from Spain for financial support (project number CTQ2017-85821-R, FEDER funds). We also thank the CTI (UIB) for computational facilities.

Notes and references

1 G. R. Desiraju, *Chem. Commun.*, 1997, 1475–1482.

2 (*a*) J. Y. Lee, B. H. Hong, W. Y. Kim, S. K. Min, Y. Kim, M. V. Jouravlev, R. Bose, K. S. Kim, I.-C. Hwang, L. J. Kaufman, C. W. Wong, P. Kim and K. S. Kim, *Nature*, 2009, **460**, 498–501; (*b*) T. S. Thakur and G. R. Desiraju, *Cryst. Growth Des.*, 2008, **8**, 4031; (*c*) S. L. Price, *Acc. Chem. Res.*, 2009, **42**, 117–126.

3 P. Seth, A. Bauzá, A. Frontera, C. Massera, P. Gamez and A. Ghosh, *CrystEngComm*, 2013, **15**, 3031–3039.

4 (*a*) J. W. G. Bloom and S. E. Wheeler, *Angew. Chem., Int. Ed.*, 2011, **50**, 7847–7849; (*b*) S. K. Seth, D. Sarkar and T. Kar, *CrystEngComm*, 2011, **13**, 4528–4535; (*c*) S. K. Seth, D. Sarkar, A. D. Jana and T. Kar, *Cryst. Growth Des.*, 2011, **11**, 4837–4849; (*d*) S. K. Seth, P. Manna, N. J. Singh, M. Mitra, A. D. Jana, A. Das, S. R. Choudhury, T. Kar, S. Mukhopadhyaya and K. S. Kim, *CrystEngComm*, 2013, **15**, 1285–1288.

5 (*a*) A. Frontera, P. Gamez, M. Mascal, T. J. Mooibroek and J. Reedijk, *Angew. Chem., Int. Ed.*, 2011, **50**, 9564–9583; (*b*) P. Manna, S. K. Seth, M. Mitra, S. R. Choudhury, A. Bauzá, A. Frontera and S. Mukhopadhyay, *Cryst. Growth Des.*, 2014, **14**, 5812–5821; (*c*) P. Manna, S. K. Seth, A. Bauzá, M. Mitra, S. R. Choudhury, A. Frontera and S. Mukhopadhyay, *Cryst. Growth Des.*, 2014, **14**, 747–755; (*d*) M. Mitra, P. Manna, A. Bauzá, P. Ballester, S. K. Seth, S. R. Choudhury, A. Frontera and S. Mukhopadhyay, *J. Phys. Chem. B*, 2014, **118**, 14713–14726; (*e*) J. C. Ma and D. A. Dougherty, *Chem. Rev.*, 1997, **97**, 1303–1324.

6 (*a*) A. Bauzá, I. Alkorta, J. Elguero, T. J. Mooibroek and A. Frontera, *Angew. Chem., Int. Ed.*, 2020, **59**, 17482–17487; (*b*) M. Karmakar, A. Frontera, S. Chattopadhyay, T. J. Mooibroek and A. Bauzá, *Int. J. Mol. Sci.*, 2020, **21**, 7091; (*c*) I. Alkorta, J. Elguero and A. Frontera, *Crystals*, 2020, **10**, 180.

7 (*a*) B. Notash, N. Safari and H. R. Khavasi, *CrystEngComm*, 2012, **14**, 6788–6796; (*b*) S. K. Seth, I. Saha, C. Estarellas, A. Frontera, T. Kar and S. Mukhopadhyay, *Cryst. Growth Des.*, 2011, **11**, 3250–3265; (*c*) P. Manna, S. K. Seth, A. Das, J. Hemming, R. Prendergast, M. Helliwell, S. R. Choudhury, A. Frontera and S. Mukhopadhyay, *Inorg. Chem.*, 2012, **51**, 3557–3571; (*d*) I. Alkorta, F. Blanco, P. M. Deya, J. Elguero, C. Estarellas, A. Frontera and D. Quinonero, *Theor. Chem. Acc.*, 2010, **126**, 1–14.

8 J. W. Steed, D. R. Turner and K. J. Wallace, *Core Concepts in Supramolecular Chemistry and Nanochemistry*, John Wiley & Sons, Ltd., Chichester, UK, 2007, pp. 194–228.

9 M. R. Shimpi, S. P. Velaga, F. U. Shah and O. N. Antzutkin, *Cryst. Growth Des.*, 2017, **17**, 1729–1734.

10 G. R. Desiraju, *Angew. Chem., Int. Ed.*, 2007, **46**, 8342–8356.

11 (*a*) F. O. Tzul, K. L. Schweiker and G. I. Makhatadze, *Proc. Natl. Acad. Sci. U. S. A.*, 2015, **112**, E259–E266; (*b*) M. P. Williamson, A. M. Hounslow, J. Ford, K. Fowler, M. Hebditch and P. E. Hansen, *Chem. Commun.*, 2013, **49**, 9824–9826; (*c*) I. Gitlin, J. D. Carbeck and G. M. Whitesides, *Angew. Chem., Int. Ed.*, 2006, **45**, 3022–3060.

12 V. Ferretti, V. Bertolasi and L. Pretto, *New J. Chem.*, 2004, **28**, 646–651.

13 (*a*) E. Yashima, K. Maeda and Y. Furusho, *Acc. Chem. Res.*, 2008, **41**, 1166–1180; (*b*) H. Katagiri, Y. Tanaka, Y. Furusho and E. Yashima, *Angew. Chem., Int. Ed.*, 2007, **46**, 2435–2439.

14 (*a*) A. Warshel, P. K. Sharma, M. Kato and W. W. Parson, *Biochim. Biophys. Acta, Proteins Proteomics*, 2006, **1764**, 1647–1676; (*b*) Q. Xu, H. Guo, A. Wlodawer and H. Guo, *J. Am. Chem. Soc.*, 2006, **128**, 5994–5995.

15 (*a*) B. Kuberski and A. Szumna, *Chem. Commun.*, 2009, 1959–1961; (*b*) L. E. R. O'Leary, J. A. Fallas, E. L. Bakota, M. K. Kang and J. D. Hartgerink, *Nat. Chem.*, 2011, **3**, 821–828.

16 J. M. Christie, A. S. Arvai, K. J. Baxter, M. Heilmann, A. J. Pratt, A. O'Hara, S. M. Kelly, M. Hothorn, B. O. Smith, K. Hitomi, G. I. Jenkins and E. D. Getzoff, *Science*, 2012, **335**, 1492–1496.

17 (*a*) V. Dvornikovs and D. B. Smithrud, *J. Org. Chem.*, 2002, **67**, 2160–2167; (*b*) P.-O. Norrby and T. Liljefors, *J. Am. Chem. Soc.*, 1999, **121**, 2303–2306.

18 M. Mitra, P. Manna, S. K. Seth, A. Das, J. Meredith, M. Helliwell, A. Bauzá, S. R. Choudhury, A. Frontera and S. Mukhopadhyay, *CrystEngComm*, 2013, **15**, 686–696.

19 Bruker, *SAINT, Version 6.36a*, Bruker AXS Inc., Madison, Wisconsin, USA, 2002.

20 Bruker, *SMART, Version 5.625 and SADABS, Version 2.03a*, Bruker AXS Inc., Madison, Wisconsin, USA, 2001.

21 G. M. Sheldrick, *Acta Crystallogr., Sect. A: Found. Crystallogr.*, 2008, **64**, 112–122.

22 G. M. Sheldrick, *Acta Crystallogr., Sect. C: Struct. Chem.*, 2015, **71**, 3–8.

23 L. J. Farrugia, *J. Appl. Crystallogr.*, 2012, **45**, 849–854.

24 A. L. Spek, *J. Appl. Crystallogr.*, 2003, **36**, 7–13.

25 R. Ahlrichs, M. Bär, M. Hacer, H. Horn and C. Kömel, *Chem. Phys. Lett.*, 1989, **162**, 165–169.

26 S. B. Boys and F. Bernardi, *Mol. Phys.*, 1970, **19**, 553–566.

27 R. F. W. Bader, *Chem. Rev.*, 1991, **91**, 893–928.

28 T. A. Keith, *AIMAll (Version 13.05.06)*, TK Gristmill Software, Overland Park KS, USA, 2013.

29 Y. Shao, L. F. Molnar, Y. Jung, J. Kussmann, C. Ochsenfeld, S. T. Brown, A. T. B. Gilbert, L. V. Slipchenko, S. V. Levchenko, D. P. O'Neill, R. A. DiStasio Jr., R. C. Lochan, T. Wang, G. J. O. Beran, N. A. Besley, J. M. Herbert, C. Y. Lin, T. Van Voorhis, S. H. Chien, A. Sodt, R. P. Steele, V. A. Rassolov, P. E. Maslen, P. P. Korambath, R. D. Adamson, B. Austin, J. Baker, E. F. C. Byrd, H. Dachsel, R. J. Doerksen, A. Dreuw, B. D. Dunietz, A. D. Dutoi, T. R. Furlani, S. R. Gwaltney, A. Heyden, S. Hirata, C.-P. Hsu, G. Kedziora, R. Z. Khalliulin, P. Klunzinger, A. M. Lee, M. S. Lee, W. Z. Liang, I. Lotan, N. Nair, B. Peters, E. I. Proynov, P. A. Pieniazek, Y. M. Rhee, J. Ritchie, E. Rosta, C. D. Sherrill, A. C. Simmonett, J. E. Subotnik, H. L. Woodcock III, W. Zhang, A. T. Bell, A. K. Chakraborty, D. M. Chipman, F. J. Keil, A. Warshel, W. J. Hehre, H. F. Schaefer, J. Kong, A. I. Krylov, P. M. W. Gill and M. Head-Gordon, *Phys. Chem. Chem. Phys.*, 2006, **8**, 3172.

30 M. J. Frisch, G. W. Trucks, H. B. Schlegel, G. E. Scuseria, M. A. Robb, J. R. Cheeseman, G. Scalmani, V. Barone, G. A. Petersson, H. Nakatsuji, X. Li, M. Caricato, A. Marenich, J. Bloino, B. G. Janesko, R. Gomperts, B. Mennucci, H. P. Hratchian, J. V. Ortiz, A. F. Izmaylov, J. L. Sonnenberg, D. Williams-Young, F. Ding, F. Lipparini, F. Egidi, J. Goings, B. Peng, A. Petrone, T. Henderson, D. Ranasinghe, V. G. Zakrzewski, J. Gao, N. Rega, G. Zheng, W. Liang, M. Hada, M. Ehara, K. Toyota, R. Fukuda, J. Hasegawa, M. Ishida, T. Nakajima, Y. Honda, O. Kitao, H. Nakai, T. Vreven, K. Throssell, J. A. Montgomery Jr. , J. E. Peralta, F. Ogliaro, M. Bearpark, J. J. Heyd, E. Brothers, K. N. Kudin, V. N. Staroverov, T. Keith, R. Kobayashi, J. Normand, K. Raghavachari, A. Rendell, J. C. Burant, S. S. Iyengar, J. Tomasi, M. Cossi, J. M. Millam, M. Klene, C. Adamo, R. Cammi, J. W. Ochterski, R. L. Martin, K. Morokuma, O. Farkas, J. B. Foresman and D. J. Fox, *Gaussian 09, Revision C.02*, Gaussian, Inc., Wallingford CT, 2009.

31 M. Mitra, P. Manna, A. Das, S. K. Seth, M. Helliwell, A. Bauza, S. R. Choudhury, A. Frontera and S. Mukhopadhyay, *J. Phys. Chem. A*, 2013, **117**, 5802–5811.

32 M. Mitra, P. Manna, S. K. Seth, A. Das, J. Meredith, M. Helliwell, A. Bauza, S. R. Choudhury, A. Frontera and S. Mukhopadhyay, *CrystEngComm*, 2013, **15**, 686–696.

33 A. Walranta, A. Bauzá, C. Girardet, I. D. Alves, S. Lecomte, F. Illiena, S. Cardona, N. Chaianantakula, M. Pallerla, F. Burlina, A. Frontera and S. Sagan, *Biochim. Biophys. Acta, Biomembr.*, 2020, **1862**, 183098.

34 (*a*) A. Hossain, S. K. Seth, A. Bauzá and S. Mukhopadhyay, *Polymer*, 2018, **10**, 182; (*b*) S. K. Seth, A. Bauzá and A. Frontera, *CrystEngComm*, 2018, **20**, 746–754; (*c*) T. Maity, H. Mandal, A. Bauzá, B. C. Samanta, A. Frontera and S. K. Seth, *New J. Chem.*, 2018, **42**, 10202–10213; (*d*) G. Mahmoudi, S. K. Seth, A. Bauzá, F. I. Zubkov, A. V. Gurbanov, J. White, V. Stilinović, T. Doert and A. Frontera, *CrystEngComm*, 2018, **20**, 2812–2821.

Journal of Molecular Structure 1226 (2021) 129254

Contents lists available at ScienceDirect

Journal of Molecular Structure

journal homepage: www.elsevier.com/locate/molstr

Supramolecular association and quantification of intermolecular interactions of 4′-functionalized 2,2′:6′,2″-terpyridines: Experimental observation and theoretical studies

Suparna Tripathi[a,b], Anowar Hossain[b], Saikat Kumar Seth[a,*], Subrata Mukhopadhyay[b,**]

[a] *Department of Physics, Jadavpur University, Kolkata 700032, India*
[b] *Department of Chemistry, Jadavpur University, Kolkata 700032, India*

ARTICLE INFO

Article history:
Received 26 May 2020
Revised 10 September 2020
Accepted 10 September 2020
Available online 18 September 2020

Keywords:
4′-functionalized 2,2′:6′,2″-terpyridine compounds
Supramolecular self-assembly
Hirshfeld surface
Bader's theory of 'atoms-in-molecules' (AIM)
Theoretical 'Noncovalent interaction' (NCI) plot index

ABSTRACT

Three versatile 4′-substituted 2,2′:6′,2″-terpyridine compounds (**1**–**3**) having different substitutions (4-ethoxyphenyl, 4-methoxyphenyl and pyridyl) at 4′-position of the central pyridine ring have been synthesized and structurally characterized. Three representative crystal structures have been determined through single crystal X-ray diffraction analysis. X-ray crystallography revels that the structures are stabilized through C–H···π and π–π stacking interactions. In the solid-state, the supramolecular assemblies of the title compounds have been explored in detail. Compounds (**1**) and (**3**) exhibits both C–H···π and π–π interactions in building supramolecular assemblies whereas compound (**2**) exhibit π–π interaction only. All the intermolecular interactions that are involved within the structures are quantified through Hirshfeld surface analyses. The weak noncovalent interactions that played significant role in building supramolecular assemblies are further characterized by Bader's theory of 'atoms-in-molecules' (AIM). Finally, the supramolecular networks are characterized by theoretical 'Noncovalent Interaction' (NCI) plot index.

The supramolecular solid-state frameworks of three 4′-functionalized 2,2′:6′,2″-terpyridine derivatives have been quantified which are further characterized theoretically by the Bader's theory of 'atoms-in-molecules'(AIM) and 'noncovalent interaction' (NCI) plot index.

1. Introduction

Terpyridine compounds are treated as most significant ligand in the fields ranging from chemical synthesis [1-3] to supramolecular design [4-10]. Morgan and Burstall published first synthesis of terpyridine around 80 years back [11]. Since that time, the chemistry of terpyridine corresponds to the maturity of supramolecular chemistry [12-15]. Terpyridine compounds containing N-donor heterocyclic rings is a tridentate NNN-type Pincer ligand that have attracted widespread significant attention as building blocks in coordination chemistry and for preparation of functional materials [16,17]. Terpyridine ligands have been extensively investigated, modified and utilized in the area of supramolecular chemistry [18-20] due to ease of synthesizing [19,21] and various properties. Substitution of terpyridine moiety with various groups induces altered physical properties [22] and exhibit good nonlinear optical property [23-25]. Among terpyridine compounds, the 2,2′:6′,2″-terpyridine is one enthralling ligand that has caught substantial attentions over the past decades for various applications [20, 26-29]. These compounds are used as photosensitizers in Dye-Sensitized Solar Cells (DSSCs) [30] in materials science, as an antitumor [31] and chemotherapy agent [32,33] in medicinal chemistry. Moreover, the 2,2′:6′,2″-terpyridines with the substituent at 4′ position have also been investigated extensively [6-10,34-37]. The 4′-position offers a broad range of substituents that permits us to modify inductive influence largely [38,39]. Moreover, substitution of aromatic ring at the 4′-position of terpyridine leads the molecules to form a conjugated system with moderate planar structure through π–π stacking interactions. Therefore, Structural design of molecular architectures is extremely important that offers an opportunity to control properties of the desired products at the molecular level.

Supramolecular architectures involving organic ligands have become an important research topic in the field of crystal engineering due to its wide applications [40,41]. Crystal engineering is the

---

[*] Corresponding author.
[**] Corresponding author.
E-mail addresses: saikatk.seth@jadavpuruniversity.in (S.K. Seth), ju_subrata@yahoo.co.in (S. Mukhopadhyay).

https://doi.org/10.1016/j.molstruc.2020.129254
0022-2860/

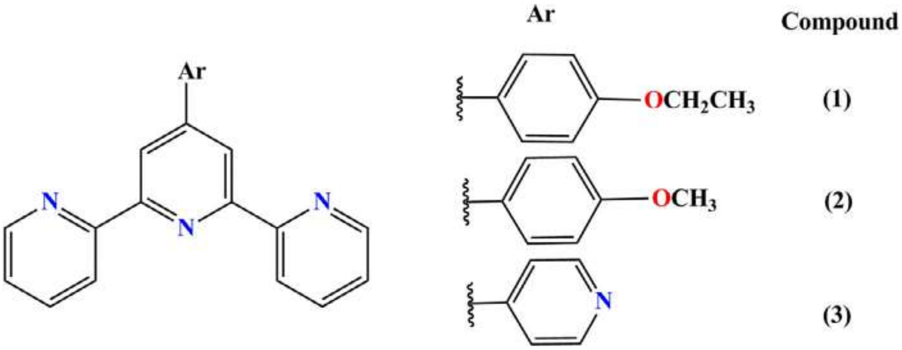

Scheme 1. Schematic representation of the chemical structure of the title compounds.

purposeful design of new crystalline solids with emphasis on finding plans to regulate their properties by exploring crystal structure prediction [42-44]. The noncovalent interactions have attracted widespread interest to explore the influence of the interactions in determining the structures and properties of molecular assemblies in the field of supramolecular chemistry and materials science [45-49]. In crystal engineering, proper understanding and utilization of noncovalent interactions is extremely important to control the supramolecular association since they are composed of a combination of interactions [50,51]. Noncovalent interactions including hydrogen bonding and other dispersive π-interactions like C-H···π [52-54], π-π [6-8,55,56], anion···π [9,10,57,58], lp···π [59-61] etc. are ubiquitous interactions that played pivotal role in crystal engineering. The dispersive π-π stacking interactions play crucial role in crystal engineering and molecular recognition [57,62,63]. Moreover, the molecular entities of π-systems having π^+/π^- moieties is an intriguing subject in the study of π-π interactions [6-10,64]. Since the cooperativity of intermolecular interactions significantly pretentious the final solid-state structures, it is desirable to explore the quantitative contribution of cooperative effect of noncovalent interactions in the design of supramolecular frameworks [65,66].

Keeping in mind the above facts, in continuation of our effort to further advanced the supramolecular behavior of 2,2′:6′,2″-terpyridines [6-10], herein we have structurally characterized three terpyridine compounds. Apart from reporting the crystal structures, we have analyzed the weak noncovalent interactions that govern the stability of the structures. The intermolecular interactions have been inspected critically and quantified by Hirshfeld surface analysis. The characteristics of the noncovalent interactions are studied theoretically using Bader's theory of “atoms-in-molecules” (AIM). Moreover, we have also performed theoretical noncovalent interaction (NCI) plot index analyses to confirm and to characterize the noncovalent interactions in a novel visual manner.

2. Experimental sections

2.1. Materials

All reactions were carried out in ethanol medium and in aerobic condition. All chemicals used were of reagent grade quality, purchased from Sigma Aldrich Chemical Co.

2.2. Syntheses

2.2.1. 4′-(4-ethoxyphenyl)- 2,2′:6′,2″-terpyridine (1)

The terpyridine ligand was prepared following the literature method [67]. In order to synthesize the title compound, 2-acetylpyridine (1 mmol, 0.12 gm) was first taken in a round-bottom flask in 200 ml ethanol and then 4-ethoxybenzaldehyde (2 mmol, 0.30 gm) was added. To this reaction mixture excess of KOH bead (8 mmol, 0.448 gm) was then added and stirred at room temperature for 15 minute. Finally, 25 ml of ammonia was added and stirred at room temperature for another four hours. Pale yellow powdered product obtained was filtered, washed with distilled water and dried in air. Single crystal suitable for X-ray analysis was obtained by dissolving the synthesized compound (0.176 gm, 0.5 mmol) in ethanol (150 ml) and slow evaporation of the solvent at room temperature for about 25 days. The chemical structure of the compound has shown in Scheme 1.

2.2.2. 4′-(4-methoxyphenyl)- 2,2′:6′,2″-terpyridine (2)

Title compound (**2**) was synthesized previously by two different ways [67-69,6]. Here, we prepared the compound using the reported Hanan's method [67,6]. Single crystal suitable for X-ray analysis was obtained by dissolving the synthesized compound (0.170 gm, 0.5 mmol) in ethanol (150 ml) and slow evaporation of the solvent at room temperature for 25 days. The chemical structure of compound (**2**) has shown in Scheme 1.

2.2.3. 4′-(pyridyl)- 2,2′:6′,2″-terpyridine (3)

Compound (**3**) was also prepared by the reported one step Hanan's method [67,70,7]. Single crystal suitable for X-ray analysis was obtained by dissolving the synthesized compound (0.155 gm, 0.5 mmol) in ethanol (150 ml) and slow evaporation of the solvent at room temperature for about 25 days. Scheme 1 shows the chemical structure of the title compound.

2.3. X-ray crystal structure determination

Single crystal X-ray diffraction data was collected by using Bruker APEX-II CCD diffractometer with graphite monochromated MoKα radiation (λ = 0.71073 Å) at 150(2)K, 293(2)K and 150(2)K of compounds (**1**–**3**) respectively. The program Bruker SAINT [71] was used for data reduction process. Then, an empirical absorption correction was used based on multi-scan method [72]. The structure of the title compounds were solved by direct method and refined by the full-matrix least-square technique on F^2 using the programs (SHELXS-14) [73] and (SHELXL-18) [74], respectively. The hydrogen atoms were placed at their geometrically idealized positions and refined isotropically. The structure solution of the title compounds were carried out by using WinGX program V2014.1 [75] and geometrically analyzed by PLATON [76]. The details of crystal data and structure refinement parameters are included in Table 1. CCDC 2003133–2003135 contain the supplementary crystallographic data for this paper.

Table 1
Crystal data and structure refinement parameters for the title compounds (**1**–**3**).

Structure	**(1)**	**(2)**	**(3)**
Empirical formula	$C_{23}H_{19}N_3O_1$	$C_{22}H_{17}N_3O_1$	C_{20} H_{14} N_4
Formula Weight	353.41	339.38	310.35
Temperature (K)	150(2)	293(2)	150(2)
Wavelength (Å)	0.71073	0.71073	0.71073
Crystal system	Monoclinic	Monoclinic	Orthorhombic
space group	$P2_1/c$	$P2_1/c$	Pbcn
a (Å)	9.3390(18)	19.0733(13)	11.0196(6)
b (Å)	37.293(7)	5.2262(3)	11.3966(6)
c (Å)	11.227(2)	17.3887(11)	12.0792(7)
α (°)	90	90	90
β (°)	113.566(4)	91.695(2)	90
γ (°)	90	90	90
Volume (Å^3)	3583.9(12)	1732.56(19)	1516.98(14)
Z / Density (calc.) (Mg/m^3)	8/1.310	4/ 1.301	4/1.359
Absorption coefficient (mm^{-1})	0.082	0.082	0.084
F(000)	1488	712	648
Crystal size (mm^3)	0.15 × 0.11 × 0.07	0.12 × 0.08 × 0.05	0.18 × 0.13 × 0.09
θ range for data collection (°)	1.092–24.999	2.136–24.996	2.571–24.990
Limiting indices	$-11 \leq h \leq 10$ $-44 \leq k \leq 44$ $-13 \leq l \leq 13$	$-22 \leq h \leq 22$ $-6 \leq k \leq 6$ $-19 \leq l \leq 18$	$-13 \leq h \leq 13$ $-13 \leq k \leq 13$ $-14 \leq l \leq 14$
Reflections collected / unique	33796 / 6318 [R(int) = 0.0603]	15103 / 2885 [R(int) = 0.0437]	16321 / 1341 [R(int) = 0.0246]
Completeness to θ (%)	100.0	94.4	100.0
Absorption correction	Semi-empirical from equivalents	Semi-empirical from equivalents	Semi-empirical from equivalents
Max. and min. transmission	0.99 and 0.98	0.996 and 0.990	0.99 and 0.98
Refinement method	full-matrix least-squares on F^2	full-matrix least-squares on F^2	full-matrix least-squares on F^2
Data/ restraints/ parameters	6318/0/490	2885/0/ 236	1341/0/112
Goodness-of - fit on F^2	1.054	1.048	1.074
Final R indices [I > 2σ(I)]	R_1 = 0.0433 wR_2 = 0.1061	R_1 = 0.0494 wR_2 = 0.1375	R_1 = 0.0308 wR_2 = 0.0822
R indices (all data)	R_1 = 0.0646 wR_2 = 0.1170	R_1 = 0.0735 wR_2 = 0.1588	R_1 = 0.0335 wR_2 = 0.0851
Largest diff. peak and hole (e.Å^{-3})	0.214 and -0.194	0.175 and -0.207	0.186 and -0.171

$R_1 = \Sigma||F_o|-|F_c||/\Sigma|F_o|$, $wR_2 = [\Sigma\{(F_o{}^2-F_c{}^2)^2\}/\Sigma\{w(F_o{}^2)^2\}]^{1/2}$, $w = 1/\{\sigma^2(F_o{}^2) + (aP)^2 + bP\}$, where, a = 0.0556 and b = 0.2925 for (**1**); a = 0.0877 and b = 0.1428 for (**2**); a = 0.0425 and b = 0.4574 for (**3**).

2.4. Hirshfeld surface analysis

The Hirshfeld surface [77-80] of compounds (**1**–**3**) have been carried out based on electron distribution of the molecules and are calculated as the sum of spherical atom electron densities [81,82]. Hirshfeld surface is unique for the investigating molecule and a set of spherical atomic electron densities [83]. The normalized contact distance (d_{norm}) is generated based on d_e, d_i and the vd*W* radii of the atom where d_e and d_i are defined as the distance from the point to the nearest nucleus external and internal to the surface respectively. The 2D fingerprint plot [83-86] is generated by using the d_e and d_i parameters that provides summary of intermolecular contacts in the crystal structures. The Hirshfeld surface analyses have been carried out using the program *Crystal Explorer17* [87].

2.5. Theoretical methods

The wave function analyses have been performed by using Gaussian09 calculation package [88] at the B3LYP level with a large basis set 6-311++G(d,p). We have used the crystallographic coordinates for the theoretical calculations by using the models that are generated from the supramolecular networks. We have used Bader's "Atoms in molecules" theory [89] to analyze the weak noncovalent interactions by AIMall calculation package [90]. The charge density (ρ(r)) is characterized by their critical points (CPs) and it's Laplacian that is expressed in terms of $L(r) = -\nabla^2(\rho(r))$ and are calculated using the Atom In Molecule (AIM) theory [91]. According to the topological properties, electron density is concentrated over $\nabla^2(\rho(r)) < 0$ and is depleted for $\nabla^2(\rho(r)) > 0$. The theoretical NCI plot [92] is a visualization index that has been used for the characterization of noncovalent interactions. The noncovalent interactions are represented by isosurfaces instead of critical points. These isosurfaces represent both favorable and unfavorable interactions and are differentiated by the isosurface colour scheme with red-yellow-green-blue scale. The red and blue surfaces represent ρ^+cut (repulsive) and ρ^-cut (attractive) interactions [93] respectively. However, weak repulsive and weak attractive interactions are represented by the yellow and green colour respectively.

3. Results and discussion

3.1. Molecular structure

The molecular view of the title compounds (**1**–**3**) are included in Fig. 1. In (**1**), the asymmetric unit consists of two molecular moieties whereas there are one moiety in compounds (**2**) and (**3**). The terpyridine unit has an 4-ethoxyphenyl, 4-methoxyphenyl and pyridyl substituent in (**1**–**3**) respectively at the 4′-position of the central pyridyl ring. The structure of compound (**2**) was determined at low temperature (100 K) by Anthonysamy et al. [68] with an R value of 0.056 and later the structure was re-determined by Emmerling et al. [69] with an R value of 0.058 at room temperature (293 K). The structure of compounds (**2**) and (**3**) were reported earlier [68-70] and we are reporting the re-determination of the structures with highest precision with an *R*-value of 0.0494 and 0.0308 respectively. In (**1**–**3**), the terminal pyridine rings of the terpyridine unit adopt *trans-trans* conformation with respect to the interannular C–C bonds. Various terpyridine ligands have *trans-*

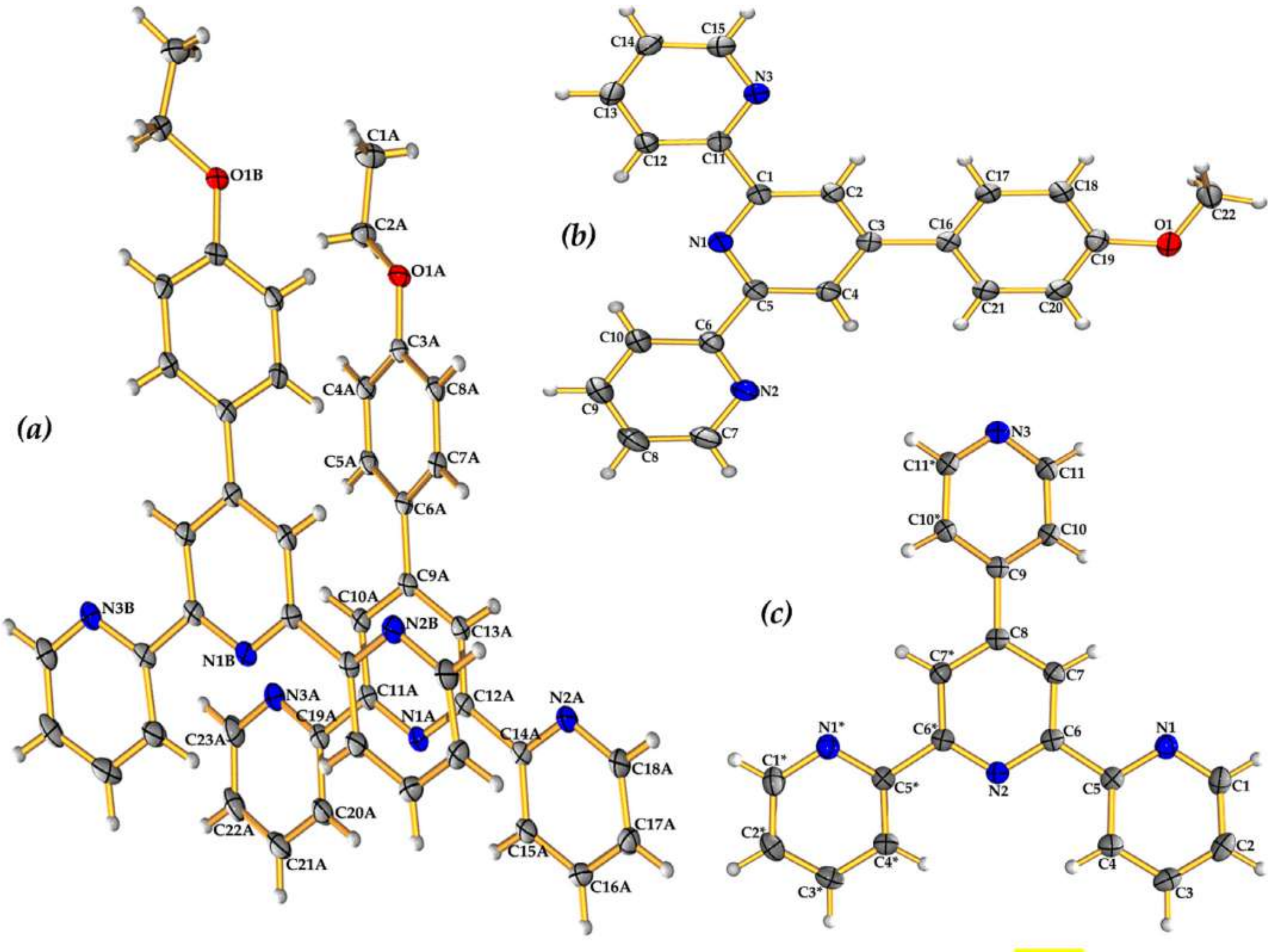

Fig. 1. ORTEP view and atom-numbering scheme of the title compounds (**1–3**)(*a–c*). The thermal ellipsoids are drawn at 50% probability level. Symmetry transformations used to generate equivalent atoms in compound (**3**) (* = -x+1, y, -z+1/2).

Table 2
Selected bond distances and angles (Å, °) of compounds (**1–3**).

Compound (**1**) (Moiety A)		Compound (**1**) (Moiety B)		Compound (**2**)		Compound (**3**)	
C(11A)–C(19A)	1.492(2)	C(11B)–C(19B)	1.490(2)	C(1)–C(11)	1.489(3)	C(5)–C(6)	1.492(2)
C(12A)–C(14A)	1.493(2)	C(12B)–C(14B)	1.492(2)	C(5)–C(6)	1.490(3)	C(5)*–C(6)*	1.492(2)
C(6A)–C(9A)	1.482(2)	C(6B)–C(9B)	1.483(2)	C(3)–C(16)	1.493(3)	C(8)–C(9)	1.491(2)
N(3A)–C(19A)–C(11A)	116.51(15)	N(3B)–C(19B)–C(11B)	116.87(15)	N(3)–C(11)–C(1)	117.59(16)	N(1)–C(5)–C(6)	116.36(10)
C(11A)–N(1A)–C(12A)	117.55(14)	C(11B)–N(1B)–C(12B)	117.66(14)	C(1)–N(1)–C(5)	117.58(15)	C(6)–N(2)–C(6)*	117.97(13)
C(12A)–C(14A)–N(2A)	116.61(14)	C(12B)–C(14B)–N(2B)	117.48(14)	C(5)–C(6)–N(2)	117.24(17)	C(6)*–C(5)*–N(1)*	116.36(10)

Table 3
Geometrical Parameters for C–H···π Interaction.

X–H···Cg	**H···Cg**	**X···Cg**	**H···Perp**	**X-H···Cg**	**Symmetry**
Compound (1)					
C(4A)–(H4A)···Cg(8)	2.91	3.689(2)	2.88	143	1-x, -y, -z
C(4B)–(H4B)···Cg(4)	2.84	3.540(2)	2.83	133	-1+x, y, z
C(7B)–(H7B)···Cg(4)	2.71	3.417(2)	2.69	133	x, y, z
Compound (3)					
C(10)–(H10)···Cg(1)	2.68	3.4726(12)	2.670	144	1/2+x, -1/2+y, 1/2-z

Cg(4), Cg(8) and Cg(1) are the centroids of the [C(3A)–C(8A)], [C(3B)–C(8B)] and [N(1)/C(1)–C(5)] rings respectively.

Table 4
Geometrical Parameters for π-Stacking Interactions.

Rings *i*–*j*[a]	Rc[b]	R1v[c]	R2v[d]	α[e]	β[f]	γ[g]	symmetry
Compound (1)							
Cg(1)–Cg(6)	3.6849(12)	3.450	3.447	8.87	20.71	20.58	x, y, z
Cg(2)–Cg(5)	3.6665(12)	3.470	3.518	5.18	16.39	18.83	1+x, y, z
Cg(2)–Cg(2)	3.6666(12)	3.518	3.470	5.18	18.83	16.39	-1+x, y, z
Cg(6)–Cg(1)	3.6848(12)	3.447	3.450	8.87	20.58	20.71	x, y, z
Compound (2)							
Cg(1)–Cg(2)	3.9994(12)	3.423	3.447	1.45	30.5	31.2	x, -1+y, z
Cg(1)–Cg(3)	4.2043(12)	3.437	3.446	1.60	34.9	35.2	x, 1+y, z
Cg(2)–Cg(1)	3.9993(12)	3.447	3.423	1.45	31.2	30.5	x, 1+y, z
Compound (3)							
Cg(1)–Cg(2)	4.0416(6)	3.276	3.669	11.23	24.79	35.85	1-x, -y, 1-z
Cg(1)–Cg(2)	4.0416(6)	3.276	3.669	11.23	24.79	35.85	x, -y, 1/2+z
Cg(2)–Cg(1)	4.0416(6)	3.669	3.276	11.23	35.85	24.79	1-x, -y, 1-z
Cg(2)–Cg(1)	4.0416(6)	3.669	3.276	11.23	35.85	24.79	x, -y, -1/2+z

For compound **1**: Cg(1), Cg(2), Cg(5), and Cg(6) are the centroids of the [N(1A)/C(9A)–C(13A)], [N(2A)/C(14A)–C(18A)], [N(1B)/C(9B)–C(13B)] and [N(2B)/C(14B)–C(18B)] rings, respectively. For compound **2**: Cg(1), Cg(2) and Cg(3) are the centroids of the [N(1)/C(1)–C(5)], [N(2)/C(6)–C(10)] and [N(3)/C(11)–C(15)] rings respectively. For compound **3**: Cg(1) and Cg(2) are the centroids of the [N(1)/C(1)–C(5)] and [N(2)/C(6)/C(7)/C(8)/C(7*)/C(6*)] rings respectively.

[b] Centroid distance between ring *i* and ring *j*. [c]Vertical distance from ring centroid *i* to ring *j*. [d]Vertical distance from ring centroid *j* to ring *i*. [e]Dihedral angle between the first ring mean plane and the second ring mean plane of the partner molecule. [f]Angle between centroids of first ring and second ring mean planes. [g]Angle between the centroid of the first ring and the normal to the second ring mean plane of the partner molecule.

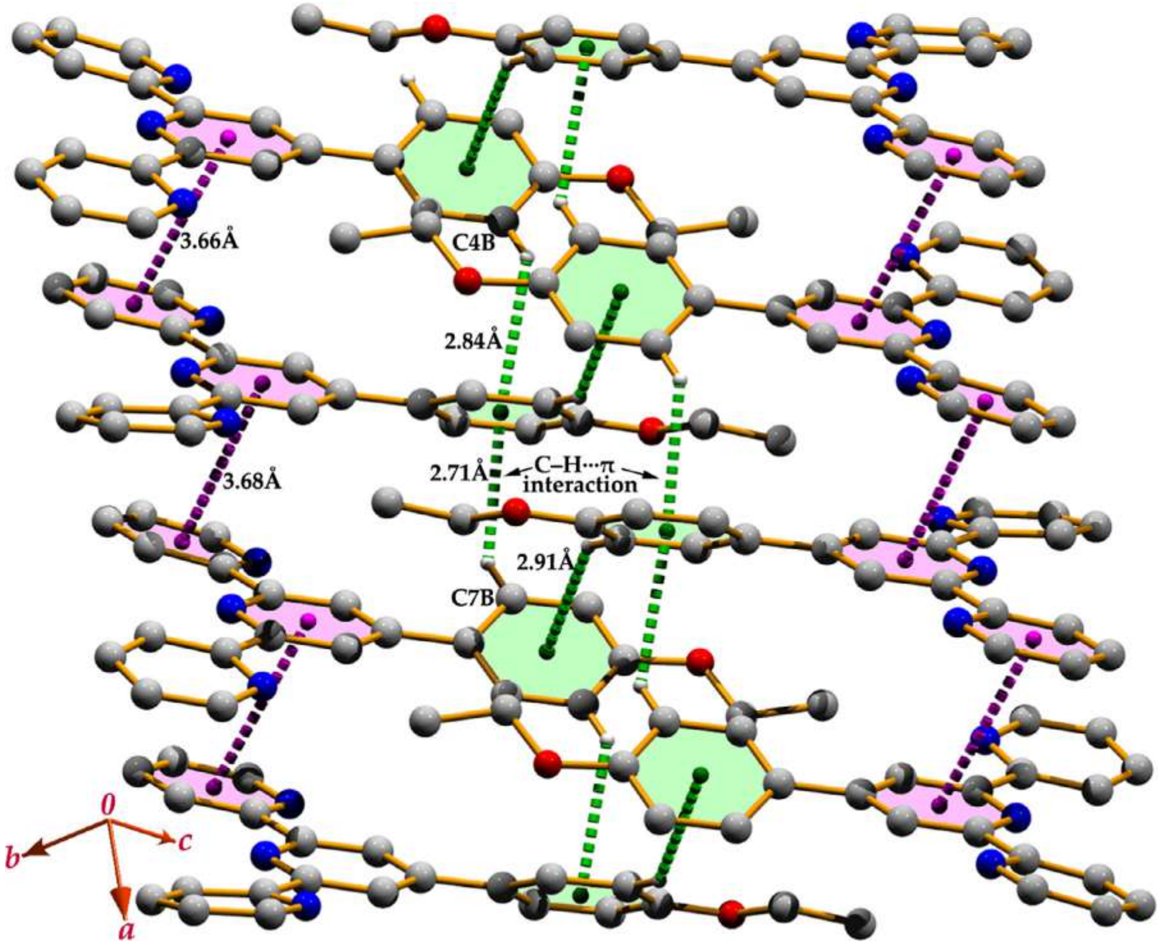

Fig. 2. Supramolecular network generated through dual C–H···π and π–π stacking interactions in (**1**). The C–H···π and π–π contacts are shown as green and pink dotted lines respectively.

trans geometry [94-96] in the X-ray structure that are energetically more favorable in comparison to other conformations [97]. The interannular bond distances varies from 1.489(3)Å to 1.493(2)Å (Table 2) which are in the normal range and comparable with the averaged values of 1.49(1)Å [94,98]. The molecular conformation of the title compounds are determined by the dihedral angles between the plane of central pyridine ring with terminal pyridine rings and the ring of the substituent group. The terpyridine unit of both moieties in (**1**) and in (**2**–**3**) are almost planar with small dihedral angles between the planes of central pyridine ring and terminal pyridine rings. The aryl ring of the ethoxyphenyl and methoxyphenyl substituent in (**1**–**2**) and pyridyl ring substituent

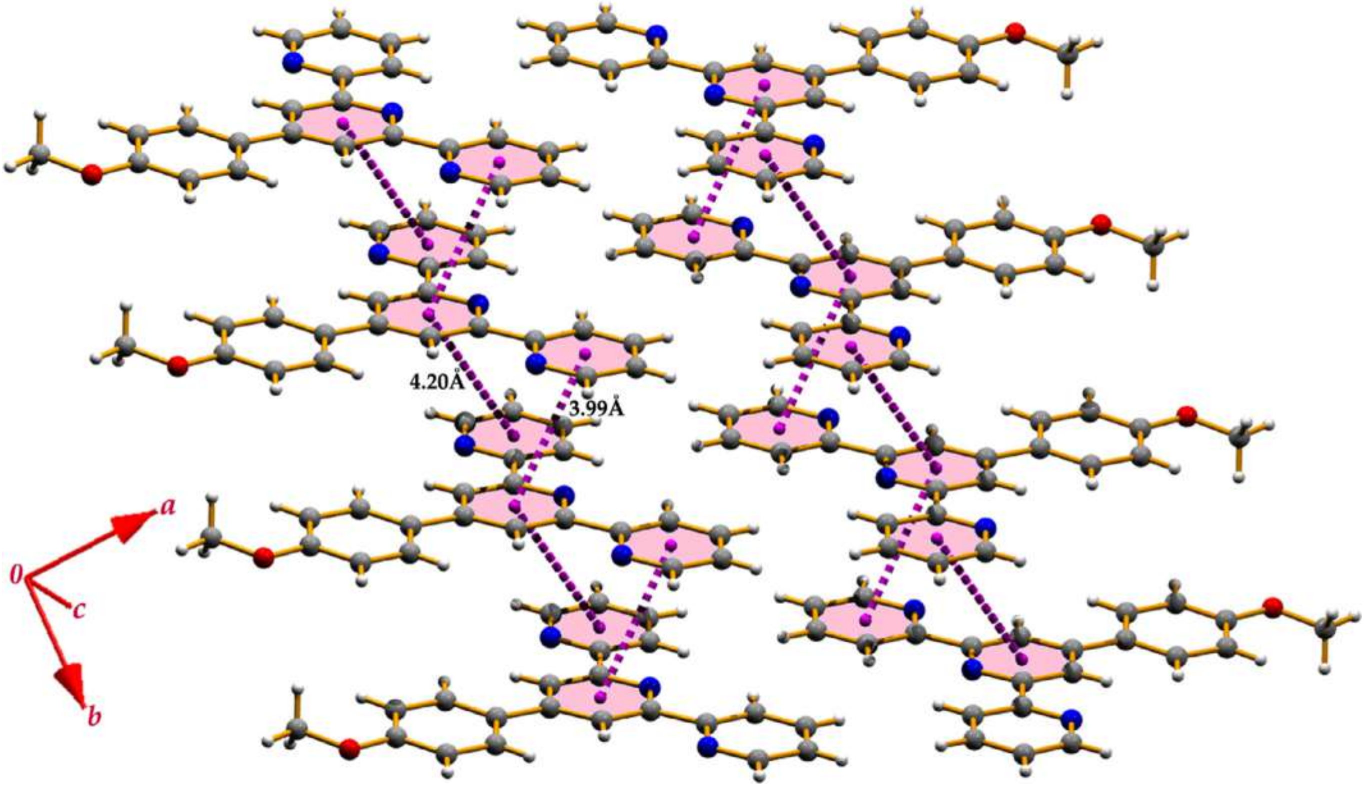

Fig. 3. Perspective view of the molecular assembly of (**2**) that is generated through $\pi-\pi$ stacking interactions. Pink dotted lines show the $\pi-\pi$ contacts.

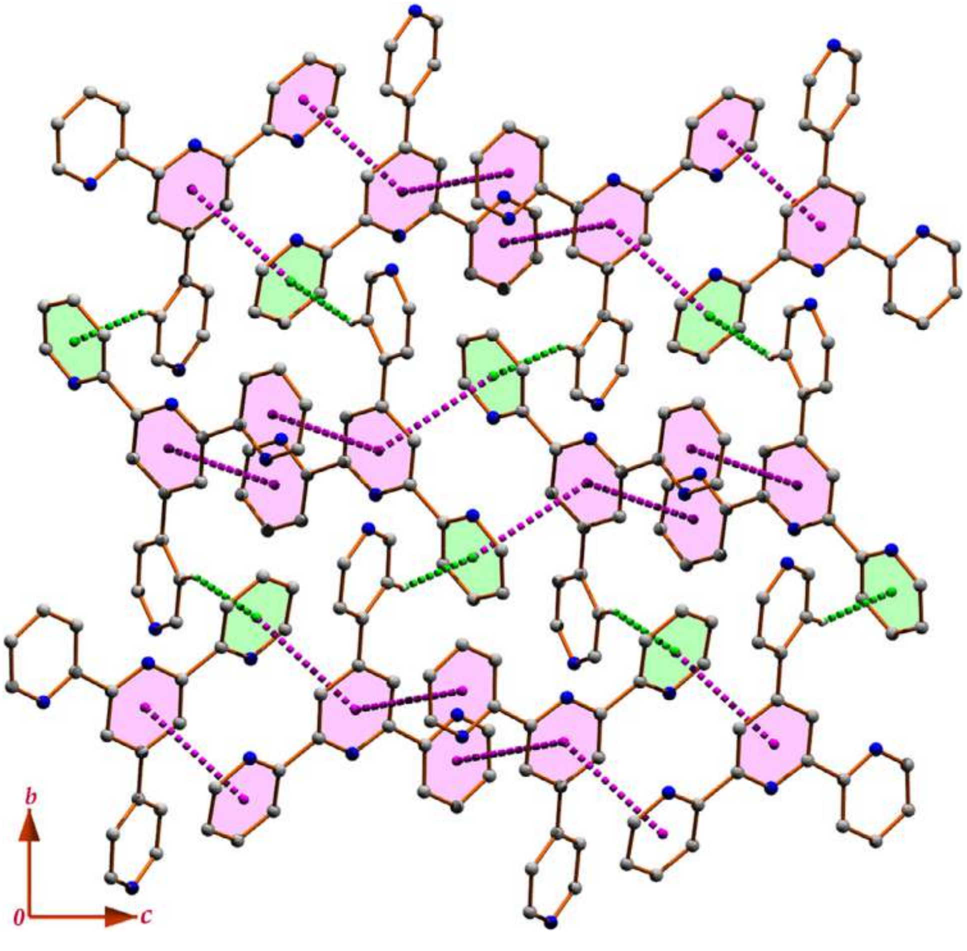

Fig. 4. Supramolecular framework generated through C–H···π and $\pi-\pi$ stacking interactions in (**3**). The C–H···π and $\pi-\pi$ contacts are shown as green and pink dotted lines respectively.

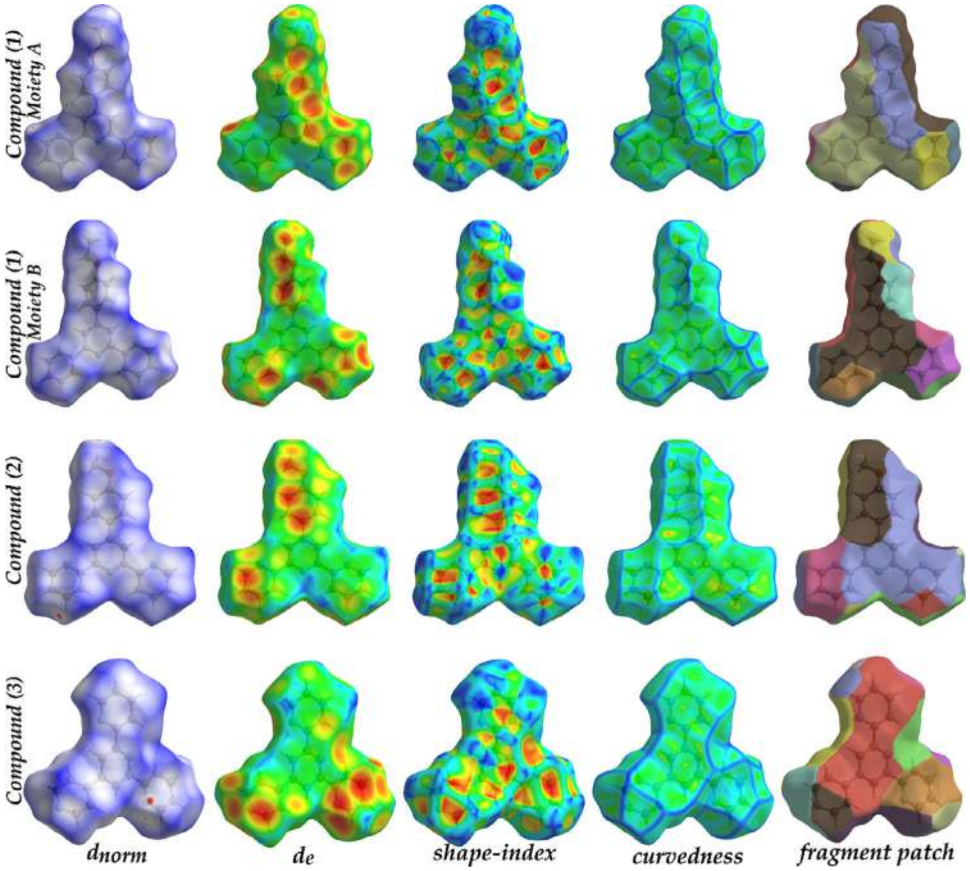

Fig. 5. Hirshfeld surfaces mapped with d_{norm}, d_e, shape-index, curvedness and fragment patches for compounds (**1**–**3**).

in (**3**) is slightly twisted. The dihedral angle between the central pyridine ring and the aryl ring in (**1**) is 29.34(6)° and 27.93(5)° in moieties A and B respectively, whereas the angles are 5.72(4)° and 18.62(3)° in (**2**) and (**3**) respectively. These dihedral angles are in normal range and comparable with the related structures reported earlier [94,96,99,100]. In (**1**), the C(20A) and C(23A) atoms of moiety-A, C(18B) and C(15B) atoms of moiety-B have the largest deviations in opposite direction from the mean plane generated through the atoms of the terpyridine unit. The atoms C(3A) and C(1A) of moiety-A, C(2B) and C(1B) from moiety-B have the largest deviations from the least square mean planes generated through the atoms of the ethoxyphenyl group. In (**2**), C(14) and C(12) atoms of the terpyridine unit and C(22) and O(1) atoms of the substituent group have the largest deviations in opposite directions. In (**3**), C(1) and C(4) atoms of the terpyridine unit and C(10) and C(11) atoms of the substituent pyridyl ring have the largest deviations in opposite directions from the least-square mean plane generated through the atoms of the terpyridine unit and substituent unit respectively.

3.2. Supramolecular assembly

Compound (**1**) is stabilized through intermolecular C–H···π and π–π stacking interactions (Tables 3, 4). Due to the self-complementarity nature, the centroid of the aryl ring of moiety A is juxtaposed from both sides by two B moieties through C–H···π interactions. The carbon atoms C(4B) and C(7B) of the aryl ring of 4-ethoxyphenyl group from moiety B in the molecules at (-1+x, y, z) and (x, y, z) binds the centroid of the aryl ring of the same group of moiety A with separation distances of 3.540(2)Å and 3.417(2)Å respectively (Table 3). The aryl ring carbon atom C(4A) is again juxtaposed the centroid of the aryl ring of moiety B in the molecule at (1-x, -y, -z) through C–H···π interaction (Fig. 2). The packing in compound (**1**) is such that the π–π stacking interactions between the terminal pyridine rings of one moiety with the central pyridine ring of another moiety of adjacent layers are optimized. The terminal pyridine ring of moiety A and the central ring of moiety B at (x, y, z) and (1+x, y, z) are juxtaposed through π–π stacking, with an interplanar spacing of 3.470Å, and a ring centroid separation of 3.666(2)Å (Table 4). In another layer, the central ring of moiety A and terminal ring of moiety B are in contact through π stacking with a ring centroid separation of 3.685(2)Å. The combination of C–H···π and π–π stacking interactions results in a two-dimensional layered assembly in (**1**) (Fig. 2).

Compound (**2**) is stabilized through intermolecular π–π interactions (Table 4). The hydrogen bonding interactions that were explored by Anthonysamy et al [68] in the previously reported structure of the compound are not found in the investigating structure. In the solid-state, the title structure is optimized through dual π-interactions that are exhibited in between the central pyridine ring and two terminal pyridine rings. The central ring and terminal ring at (x, y, z) and (x, -1+y, z) are juxtaposed through a intercentroid separation distance of 3.999Å. The molecular assembly that is generated through the π–π interactions is depicted in Fig. 3.

Despite the similarity between compounds (**1**) and (**2**) in terms of their general composition and detailed molecular geometries, compound (**3**) have some substantial alterations in the nature of the supramolecular aggregation. The molecules of (**3**) are linked into different molecular framework by a combination of C–H···π and π–π stacking interactions. In the first sub-structure, both the carbon atom C(10) and C(10)* of the substituted pyridine ring (see

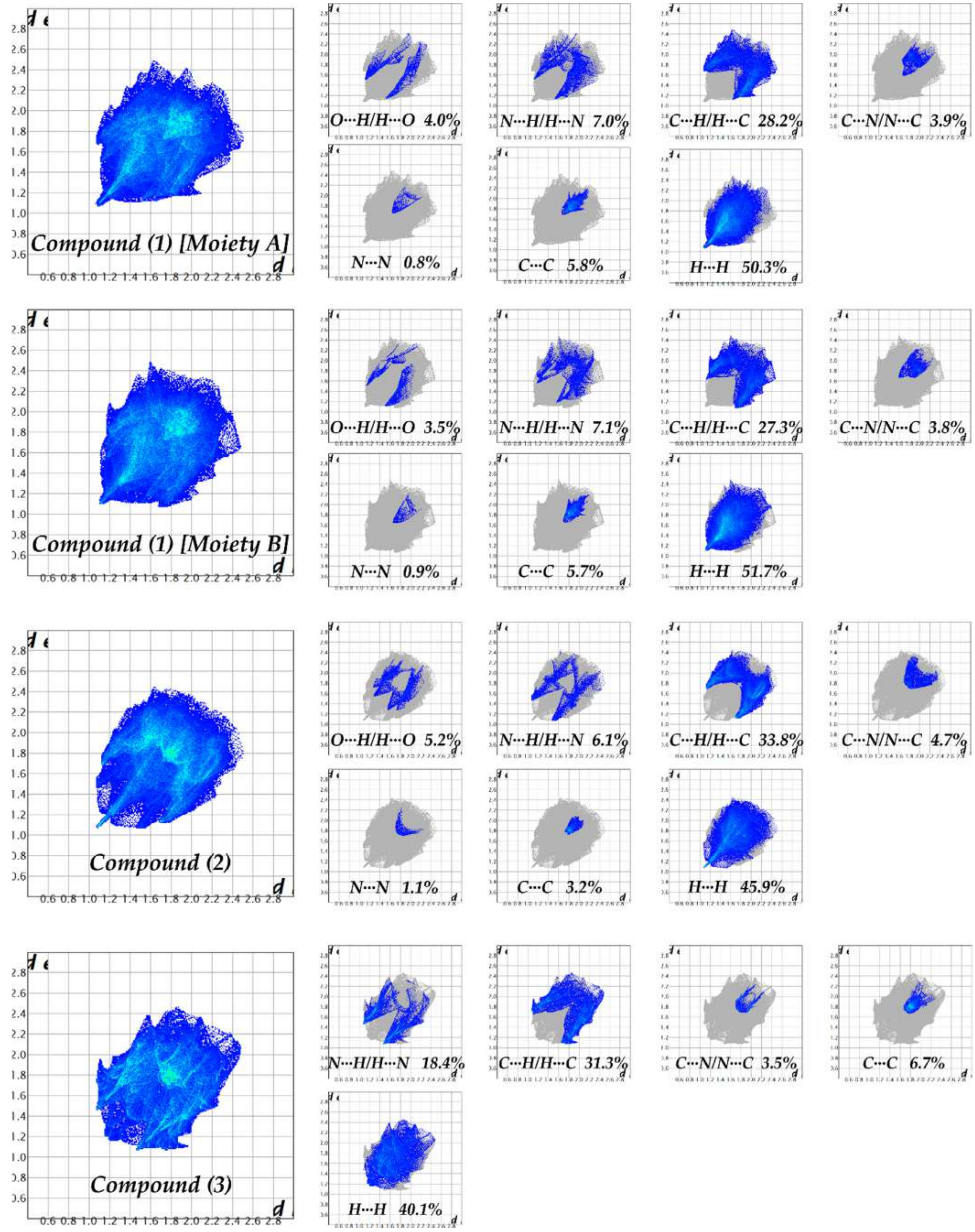

Fig. 6. Fingerprint plots (Full) and decomposed plots for each individual interactions in (**1**–**3**).

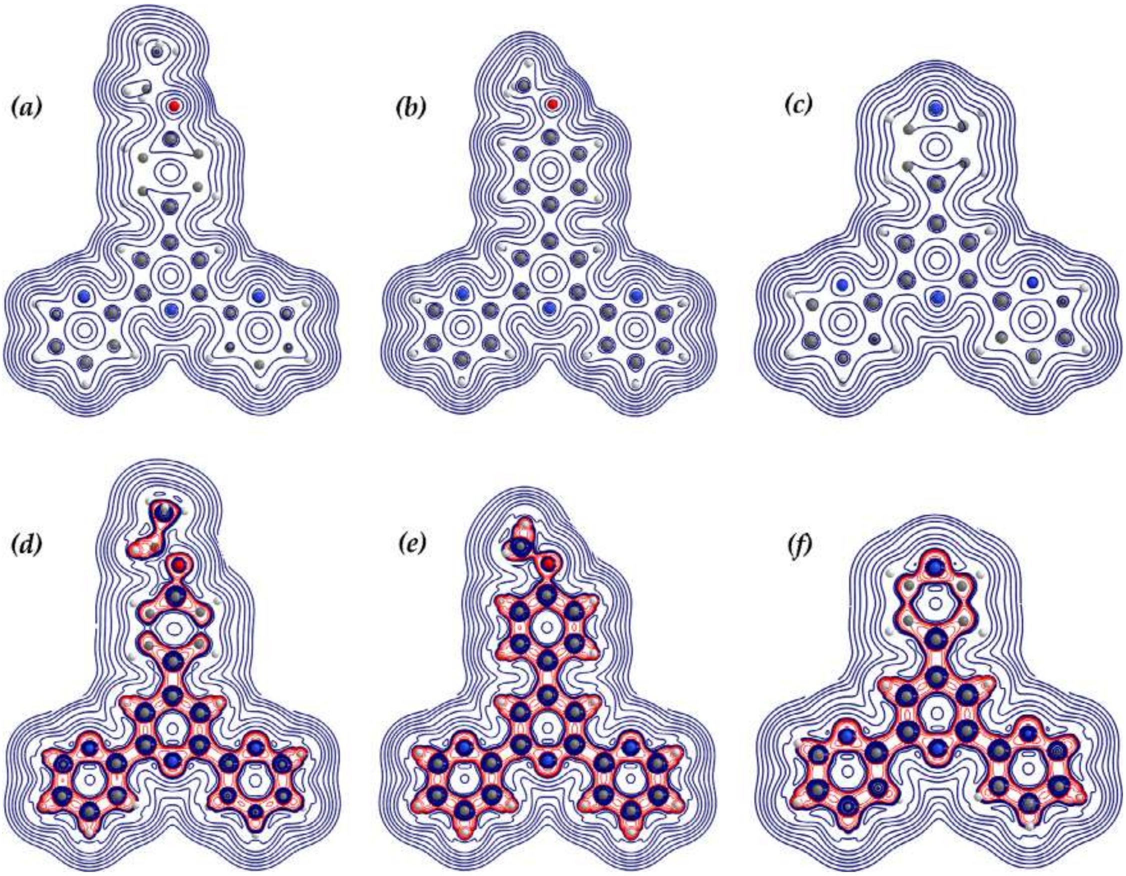

Fig. 7. contour maps of the electron density (*a–c*) and Laplacian of the electron density (*d–f*) for compounds (**1**–**3**) respectively.

Fig. 1c) are in contact with the centroids of the terminal pyridine rings of the terpyridine moiety in the molecule at (1/2+x, -1/2+y, 1/2-z) with a separation distance of 2.68Å. Due to the inversion symmetry, the substituted pyridine ring carbon atoms of the parent molecule binds two-partner molecules in both side of the ring through C–H···π interaction. Accordingly, a two-dimensional supramolecular layered assembly is generated in the (110) plane (Fig. S1). In the final structure, the central and terminal pyridine rings are optimized through π–π stacking interaction. In one side, the central ring and terminal ring at (x, y, z) and (1-x, -y, 1-z) are juxtaposed with an intercentroid separation of 3.99Å. In the other side of the central ring at (x, y, z), symmetrically generated terminal ring at (x, -y, 1/2+z) of another partner molecule is in contact through π–π stacking interaction. Consequently, the central pyridine ring is sandwiched through the dual π–π stacking interaction (Fig. 4). Finally, the substituted pyridine ring carbon atom is in contact with the terminal pyridine through C–H···π interaction. Therefore, a unique C–H···π/π–π/π–π network is self-generated to build the supramolecular assembly in (011) plane (Fig. 4).

3.3. Hirshfeld Surface

The similarities of the title structures (**1**–**3**) in terms of their molecular geometries and the pattern of the noncovalent interactions encouraged us to quantify the contribution of the interactions. In this context, we have calculated Hirshfeld surface [77-80] of the title compounds that are illustrated in Fig. 5. In compound (**1**), two molecular moieties (A and B) have been calculated separately. We have analyzed various surfaces for the title compounds that have been mapped over d_{norm}, d_e, shape-index, curvedness and fragment patches (see Fig. 5). No large circular depressions are evident on the d_{norm} surfaces due to absence of strong hydrogen bonding contacts. The weak interactions like C–H···π and π–π contacts that are involved within the structures are examined and evidenced by different surfaces. Moreover, the 2D fingerprint plot [83-86] represent all intermolecular interactions that are involved within the structures (Fig. 6). To quantify each individual contacts, we have decomposed the full-fingerprint plots in unique visual mode. The O···H/H···O contacts are evidenced by the spoon like tips in the region ($d_i + d_e \approx$ 2.653Å) of both moieties of compound (**1**), whereas in (**2**) the tips are located in the region ($d_i + d_e \approx$ 2.828Å) (Fig. 6). The O···H/H···O contacts contributed 4.0% and 3.5% in moiety A and B respectively of (**1**) whereas the contribution is 5.2% to the total Hirshfeld surface area of (**2**). The N···H/H···N contacts varies from 6.1% in (**2**) to 18.4% in (**3**). The sharp tips in the (d_i, d_e) region of (1.462Å, 1.076Å) and (1.457Å, 1.066Å) designate the N···H/H···N interaction in compounds (**2**) and (**3**) respectively (Fig. 6).

The C–H···π contacts are evidenced by the bright-orange spots on the d_e surface which is also viewed as distinct 'wings' in the fingerprint plots [101]. As evidenced and discussed in the X-ray structural discussion section, the bright-orange spots are evidenced on the substituted aryl ring of both moieties of compound (**1**) and symmetrically generated terminal pyridine rings in (**3**) that are the characteristics feature of C–H···π interaction. The 'wings' are other characteristics of C–H···π interaction which are evidenced in the bottom right [(d_i, d_e) = (2.088Å, 1.197Å)], top left [(d_i, d_e) = (1.192Å, 2.088Å)] and both sides [(d_i, d_e) = (1.943Å, 1.111Å)] of the fingerprint plots of moiety A, Moiety B (compound **1**) and compound (**3**) respectively (Fig. 6). The C···N/N···C contacts varies from 3.5% in (**3**) to 4.7% in (**2**). The contribution of N···N close contacts are 0.0 % in (**3**) whereas compound (**2**) contributed the maximum contribution (1.1%). The decomposed d_{norm} plots (Figs. S2–S4) also evidence all these available contacts in (**1**–**3**). To explore the π–π contacts, we have critically inspected the shape-index and curvedness surfaces. An adjacent red-blue triangle on the π-cloud of a ring and a flat region on both sides of a ring on the shape-index and curvedness surface respectively characterize the π–π stacking interactions [56]. The red-blue triangles and consequently the flat regions are evidenced on the central and terminal pyridine rings of (**1**–**3**) (Fig. 5). In the decomposed fingerprint plot, the π–π stacking interactions are evidenced by the region of blue/green colour on the diagonal at around $d_i = d_e = 1.071$Å, $d_i = d_e = 1.677$Å, $d_i = d_e = 1.753$Å and $d_i = d_e = 1.713$Å of compounds (**1**–**3**) respectively. The contribution of C···C contacts varies from 3.2% in (**2**) to 6.7% in (**3**). The visual representation of the fragment patches represents the identification of their closeness to adjacent molecules. (Fig. 5). A substantial variance is observed for H···H contacts (40.1% in (**3**) to 51.7% in moiety B of (**1**)) that is reflected in the scattered points of the fingerprint plots at $d_i = d_e = 1.692$Å in moiety A of (**1**), $d_i = d_e = 1.091$Å in moiety B of (**1**), $d_i = d_e = 1.071$Å in (**2**) and $d_i = d_e = 1.176$Å in (**3**) (Fig. 6). The variety of contacts that are involved within the structures of (**1**–**3**) are quantified and compared in a novel visual manner.

3.4. Theoretical analysis

We have carried out the Bader's theory of "atoms in molecules"(AIM) of compounds (**1**–**3**). In this calculation, the molecular graph consists of various colored spheres that are shown in Fig. S1. For compound (**1**), we have used moiety A in this calculation. The white, gray, red and yellow spheres are corresponds to hydrogen nuclei, carbon nuclei, bond critical point (BCP) and ring critical point (RCP) respectively. Black paths are bond paths that originate at BCPs and terminate at nuclei. In Fig. S1, the RCP to BCP paths are shown as green colored paths whereas RCP attractor paths are shown as yellow dotted paths. We have analyzed the interatomic surface eigen vector (IAS EV) paths for the title compounds (**1**–**3**). The IAS EV paths are shown by the pink colored paths (see Fig. S2) that are locally parallel or antiparallel with two negative-eigenvalued eigenvectors of the Hessian of Rho (HessRho). To get an idea of the shape of the interatomic surface, we have used all bond paths to generate the IAS EV paths where there are four IAS EV paths for each BCP (Fig. S2). We have analyzed the contour maps of the electron density (ρ) and Laplacian of the electron density ($\nabla^2\rho$) (Fig. 7). The Laplacian of electron density provides the measure of the local charge concentration or depletion for compounds (**1**–**3**) (see Figs. 7d-f). The Laplacian of the electron density is extremely important due to two facts: (i) it recov-

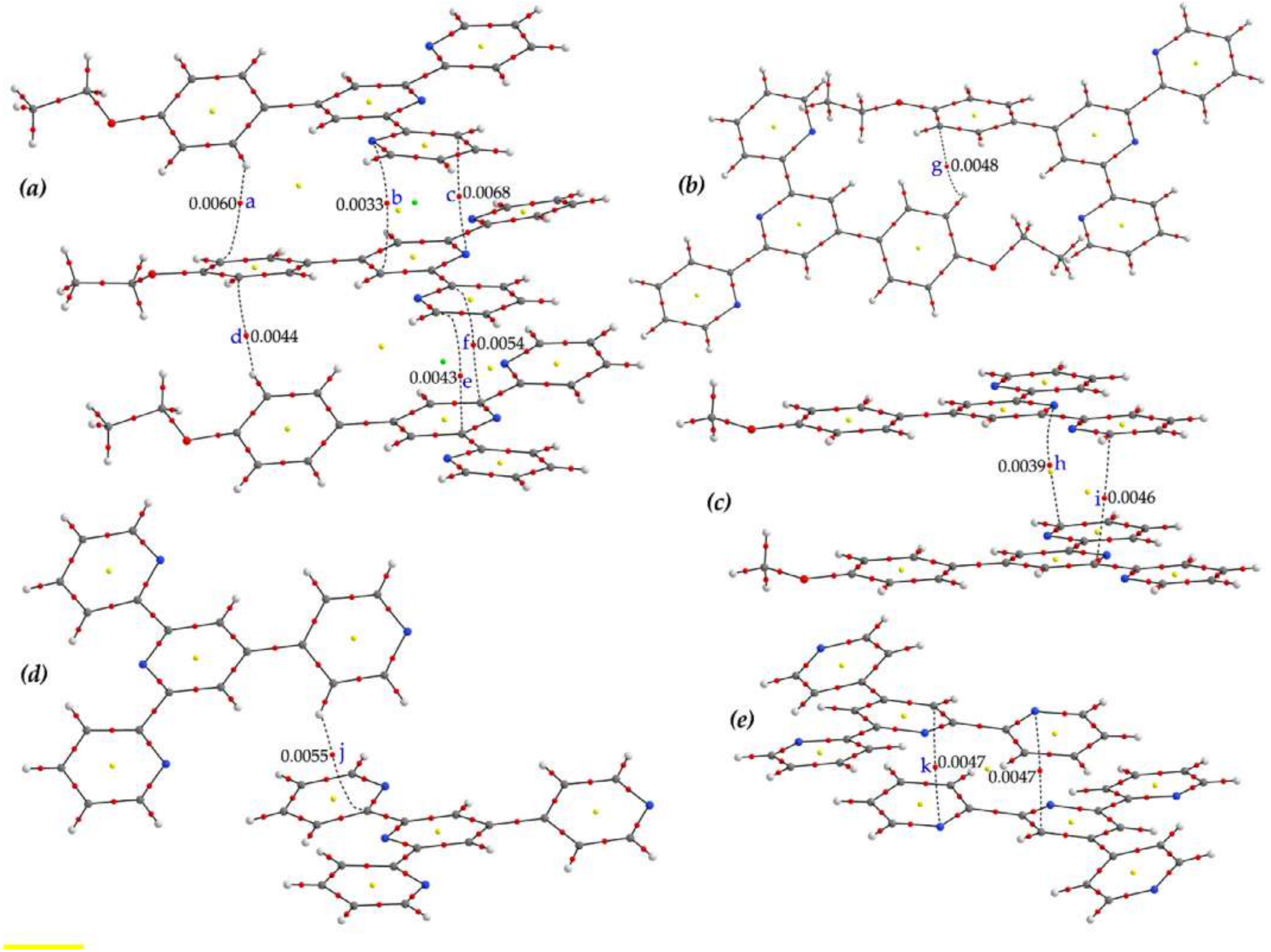

Fig. 8. AIM analyses of compounds **1**(*a,b*), **2**(*c*), **3**(*d,e*). Red and yellow spheres represent bond and ring critical points, respectively. The ρ(r) values at the bond critical points are included in atomic units (a.u.).

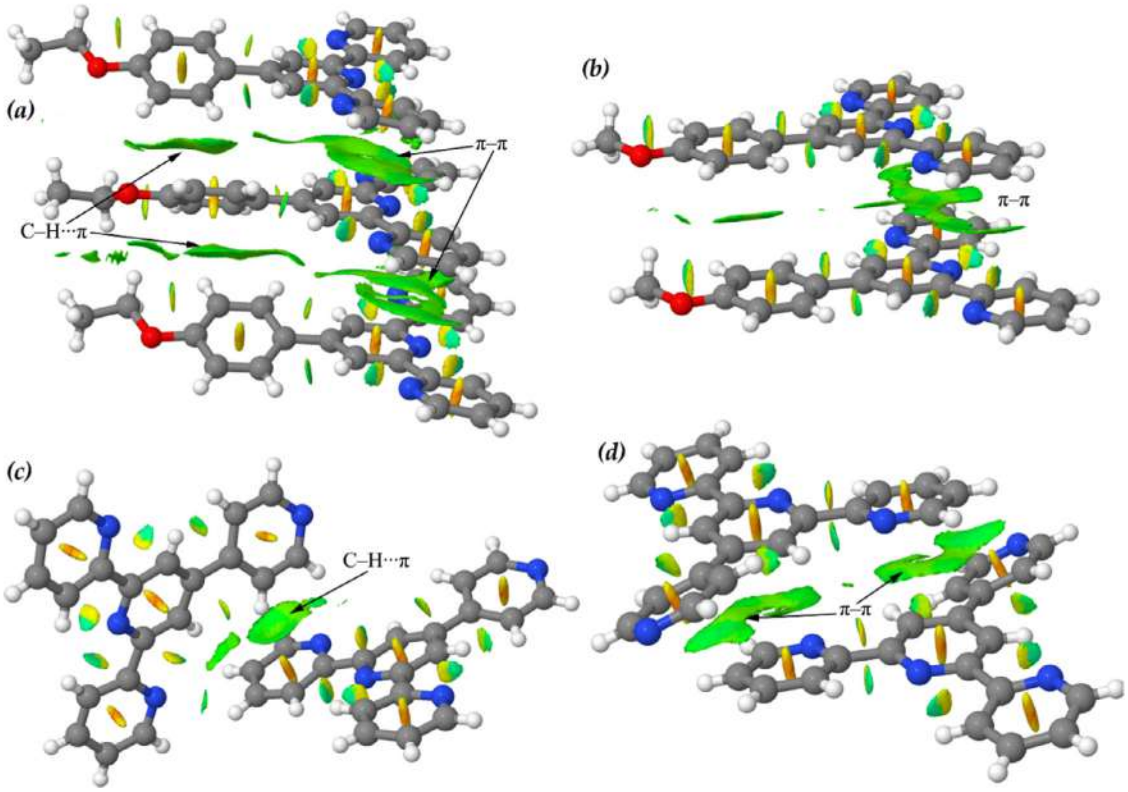

Fig. 9. NCI plot of the self-assembled structure of compounds (**1**)(*a*), (**2**)(b) and (**3**)(*c,d*).

Table 5
Detailed AIM parameters (ρ, $\nabla^2\rho$, ε, V, G and K, a.u.) at the BCPs (See Fig. 8).

Bond CP	ρ	$\nabla^2\rho$	ε	V	G	K
a (CH···π)	0.0060	0.0234	2.2826	-0.0036	0.0047	-0.0011
b (π···π)	0.0033	0.0155	0.9624	-0.0022	0.0030	-0.0009
c (π···π)	0.0068	0.0244	0.7393	-0.0046	0.0053	-0.0008
d (CH···π)	0.0044	0.0175	2.3895	-0.0024	0.0034	-0.0010
e (π···π)	0.0043	0.0148	6.9146	-0.0027	0.0032	-0.0005
f (π···π)	0.0054	0.0174	4.1648	-0.0033	0.0038	-0.0005
g (CH···π)	0.0048	0.0174	1.0454	-0.0028	0.0036	-0.0008
h (π···π)	0.0039	0.0169	1.5800	-0.0024	0.0033	-0.0009
i (π···π)	0.0046	0.0164	1.7373	-0.0027	0.0034	-0.0007
j (CH···π)	0.0055	0.0218	2.3462	-0.0032	0.0043	-0.0011
k (π···π)	0.0047	0.0193	1.0733	-0.0032	0.0040	-0.0008

ers the shell structure of atoms; (ii) it allows to trace the effects of the chemical bonding in the total charge density. In these contour maps blue and red colour denotes the positive values of the mean local charge depletion and negative values of the mean local charge concentration.

Again, we have carried out the AIM calculations by using various models that are depicted in Fig. 8. These models are generated from the X-ray structure of the title compounds. In this theoretical calculation, the interactions are confirmed through the bond path and a bond critical point that interconnects two atoms [102]. The distribution of critical points displays that the C–H···π interaction (models 1, 2, 4) that is characterized by the presence of a bond CP and bond path connecting the aryl/pyridine H-atom to one of the carbon atoms of the aryl/pyridine ring (Fig. 8a,b,d). In Table 5, we summarize the charge electron density, Laplacian, ellipticity, virial field density, Lagrangian kinetic energy density and Hamiltonian kinetic energy density [ρ, $\nabla^2\rho$, ε, V, G and K, respectively] at the BCPs of (**1–3**). The π–π stacking interaction (models 1, 3, 5) is characterized by the presence of CP and bond path interconnecting central to terminal and/or terminal to central pyridine rings (Fig. 8a,c,e). Following Fig. 2, two models (Fig. 8a,b) are used for compound (**1**) to characterize the interactions. In Fig. 8a, one aryl ring of the substituted ethoxyphenyl group is sandwitched through C–H···π interaction where the bond paths are connected between two carbon atoms of the aryl ring and the aromatic H-atom of two rings. Similarly, in Fig. 8b, the bond path interconnecting the aryl ring carbon and ring hydrogen atom characterized the C–H···π interaction; the charge density ρ(r) at the bond CPs is included in the Fig. 8a,b. In compound (**3**), the bond CP (ρ_{BCP} = 0.0055 a.u.) and bond path connecting substituted pyridine ring H-atom and carbon atom of the terminal pyridine ring characterized the C–H···π interaction (see Fig. 8d). The BCP and bond paths between pyridine nitrogen and carbon atoms of the pyridine rings characterizes the π–π stacking interactions in compounds (**1–3**) (Fig. 8a,c,e). The inspection of the results indicates that the values of ρ(r) at the bond CP (ρ_{BCP} = 0.0068/0.0054 a.u.) in (**1**) are larger in comparison to the other two compounds, in good agreement with the intercentroid separation distances observed from X-ray structures.

The noncovalent interactions are further characterized by using ‘noncovalent interaction’ (NCI) plot computational tool that permits to assess the self-assembled structure. The cooperativity of C–H···π and π–π interactions in (**1–3**) have been characterized by using the same model that were used in AIM calculations (Fig. 8acde). The absence of the strong blue isosurface clearly indicates that the title structures do not exhibit strong hydrogen bonds. The large green dual isosurfaces (See Fig. 9a) in between the phenyl rings of the substituted ethoxyphenyl groups of the model undoubtedly designate the cooperative C–H···π/π···H–C interactions in (**1**). Similarly, a large green isosurface above the π-cloud of a terminyl pyridine ring (Fig. 9c) designate C–H···π interaction in (**3**). The presence of the larger isosurfaces in between terminal to central pyridine ring (Fig. 9a,b) and terminal to terminal pyridine ring (Fig. 9d) designates the π–π stacking interactions in compounds (**1–2**) and (**3**) respectively.

4. Conclusions

In summary, three 4′-functionalized 2,2′:6′,2″-terpyridine compounds (**1**–**3**) have been synthesized and structurally characterized. Compounds (**1**) and (**3**) exhibits both C–H···π and π–π stacking interactions however, compound (**2**) exhibits π–π stacking only. Compounds (**1**) and (**3**) shows cooperative C–H···π/π···H–C and C–H···π/π–π extended networks respectively. Nevertheless, compound (**2**) shows π–π/π–π cooperative network in the solid-state. The entire supramolecular self-assembly and consequent cooperativity of weak noncovalent interactions have been analyzed in detail and further quantified by theoretical Hirshfeld surface analysis. All the interactions are quantified through the infographic fingerprint plots. Additionally, the noncovalent interactions have been characterized by Bader's theory of 'atoms-in-molecules'(AIM). Furthermore, the interplay of the interactions that played significant role in building the final structures have been analyzed by theoretical 'Noncovalent Interaction' (NCI) plot index. The theoretical investigations based on the AIM and NCI analyses verifies the experimental findings by characterizing the intricate combination of intermolecular interactions of the title compounds. Therefore, the results described herein are expected to be beneficial for understanding the cooperativity effect and quantification of noncovalent interactions.

Credit Author Statement

S. Tripathi and A. Hossain synthesized, characterized and solve the structures; S. K. Seth and S. Mukhopadhyay analyzed the data; S. K. Seth contributed in the theoretical calculations; all authors contributed in writing and original draft preparation; S. K. Seth and S. Mukhopadhyay contributed in final review and editing. All authors have read and agreed to the published version of the manuscript.

Supplementary information

CCDC 2003133–2003135 contains the supplementary crystallographic data for compounds (**1–3**). These data can be obtained free of charge via http://www.ccdc.cam.ac.uk/conts/retrieving.html, or from the Cambridge Crystallographic Data Centre, 12Union Road, Cambridge CB21EZ, UK; fax: (+44)1223-336-033; oremail:deposit@ccdc.cam.ac.uk. The full and breakdown fingerprint plots are included as supplementary data.

Declaration of Competing Interest

The authors declare no competing financial interest.

Acknowledgements

S. K. Seth gratefully acknowledges the financial support from SERB (New Delhi) India, for Research Project (EEQ/2019/000384). The research project from RUSA 2.0 programme of Jadavpur University is also gratefully acknowledged by S. K. Seth.

Supplementary materials

Supplementary material associated with this article can be found, in the online version, at doi:10.1016/j.molstruc.2020.129254.

References

[1] K. Yamamoto, J. Li, J.A.O. Garber, J.D. Rolfes, G.B. Boursalian, J.C. Borghs, C. Genicot, J. Jacq, M.V. Gastel, F. Neese, T. Ritter, Palladium-catalysed electrophilic aromatic C-H fluorination, Nature 554 (2018) 511–514.

[2] L. An, C. Xu, X. Zhang, Highly selective nickel-catalyzed gem-difluoropropargylation of unactivated alkylzinc reagents, Nature Commun 8 (2017) 1460.

[3] S. Krautwald, M.J. Bezdek, P.J. Chirik, Cobalt-Catalyzed 1,1-Diboration of Terminal Alkynes: Scope, Mechanism, and Synthetic Applications, J. Am. Chem. Soc. 139 (2017) 3868–3875.

[4] Y.-J. He, T.-H. Tu, M.-K. Su, C.-W. Yang, K.V. Kong, Y.-T. Chan, Facile Construction of Metallo-supramolecular Poly(3-hexylthiophene)-block-Poly(ethylene oxide) Diblock Copolymers via Complementary Coordination and Their Self--Assembled Nanostructures, J. Am. Chem. Soc. 139 (2017) 4218–4224.

[5] D. Samanta, I. Paul, M. Schmittel, Supramolecular five-component nano-oscillator, Chem. Commun. 53 (2017) 9709–9712.

[6] A. Das, A.D. Jana, S.K. Seth, B. Dey, S.R. Choudhury, T. Kar, S. Mukhopadhyay, N.J. Singh, I.-C. Hwang, K.S. Kim, Intriguing $\pi+$–π Interaction in Crystal Packing, J. Phys. Chem. B 114 (2010) 4166–4170.

[7] S.K. Seth, P. Manna, N.J. Singh, M. Mitra, A.D. Jana, A. Das, S.R. Choudhury, T. Kar, S. Mukhopadhyay, K.S. Kim, Molecular architecture using novel types of noncovalent π-interactions involving aromatic neutrals, aromatic cations and π-anions, CrystEngComm 15 (2013) 1285–1288.

[8] P. Manna, S.K. Seth, M. Mitra, A. Das, N.J. Singh, S.R. Choudhury, T. Kar, S. Mukhopadhyay, A successive layer-by-layer assembly of supramolecular frameworks driven by a novel type of face-to-face $\pi+$–$\pi+$ interactions, CrystEngComm 15 (2013) 7879–7886.

[9] P. Manna, S.K. Seth, Antonio Bauzá, M. Mitra, S.R. Choudhury, A. Frontera, S. Mukhopadhyay, pH Dependent Formation of Unprecedented Water−Bromide Cluster in the Bromide Salts of PTP Assisted by Anion−π Interactions: Synthesis, Structure, and DFT Study, Cryst. Growth Des. 14 (2014) 747–755.

[10] P. Manna, S.K. Seth, M. Mitra, S.R. Choudhury, Antonio Bauzá, A. Frontera, S. Mukhopadhyay, Experimental and Computational Study of Counterintuitive ClO4−···ClO4− Interactions and the Interplay between $\pi+$–π and Anion···$\pi+$ Interactions, Cryst. Growth Des. 14 (2014) 5812–5821.

[11] G.T. Morgan, F.H. Burstall, Dehydrogenation of pyridine by anhydrous ferric chloride, J. Chem. Soc. (1932) 20–30.

[12] J.M. Lehn, Supramolecular chemistry, Science 260 (1993) 1762–1763.

[13] M.D. Ward, P.R. Raithby, Functional behaviour from controlled self-assembly: challenges and prospects, Chem. Soc. Rev. 42 (2013) 1619–1636.

[14] A.K. Pal, G.S. Hanan, Design, synthesis and excited-state properties of mononuclear Ru(II) complexes of tridentate heterocyclic ligands, Chem. Soc. Rev 43 (2014) 6184–6197.

[15] A. Sil, D. Giri, S.K. Patra, Arylene–vinylene terpyridine conjugates: highly sensitive, reusable and simple fluorescent probes for the detection of nitroaromatics, J. Mater. Chem. C 5 (2017) 11100–11110.

[16] Y. Chi, P.T. Chou, Transition-metal phosphors with cyclometalating ligands: fundamentals and applications, Chem. Soc. Rev. 39 (2010) 638–655.

[17] S. Chakraborty, G.R. Newkome, Terpyridine-based metallosupramolecular constructs: tailored monomers to precise 2D-motifs and 3D-metallocages, Chem. Soc. Rev. 47 (2018) 3991–4016.

[18] R. Sakamoto, K.-H. Wu, R. Matsuoka, H. Maeda, H. Nishihara, π-Conjugated bis(terpyridine)metal complex molecular wires, Chem. Soc. Rev. 44 (2015) 7698–7714.

[19] J. Husson, M. Knorr, Syntheses and applications of furanyl-functionalised 2,2':6',2''-terpyridines, Beilstein J. Org. Chem. 8 (2012) 379–389.

[20] A. Wild, A. Winter, F. Schlütter, U.S. Schubert, Advances in the field of π-conjugated 2,2′:6′,2″-terpyridines, Chem. Soc. Rev. 40 (2011) 1459–1511.

[21] I. Eryazici, C.N. Moorefield, S. Durmus, G.R. Newkome, Synthesis and Single-Crystal X-ray Characterization of 4,4″-Functionalized 4′-(4-Bromophenyl)-2,2′:6′,2″-terpyridines, J. Org. Chem. 71 (2006) 1009–1014.

[22] S. Romain, C. Baffert, C. Duboc, J.C. Lepretre, A. Deronzier, M.N. Collomb, Mononuclear MnIII and MnIV Bis-terpyridine Complexes: Electrochemical Formation and Spectroscopic Characterizations, Inorg. Chem. 48 (2009) 3125–3131.

[23] Q. Zhang, X.H. Tian, H.P. Zhou, J.Y. Wu, Y.P. Tian, Lighting the Way to See Inside Two-Photon Absorption Materials: Structure–Property Relationship and Biological Imaging, Materials 10 (2017) 223.

[24] B.B. Cui, Y.W. Zhong, J. Yao, Three-State Near-Infrared Electrochromism at the Molecular Scale, J. Am. Chem. Soc. 137 (2015) 4058–4061.

[25] R. Sakamoto, S. Katagiri, H. Maeda, H. Nishihara, Bis(terpyridine) metal complex wires: Excellent long-range electron transfer ability and controllable intrawire redox conduction on silicon electrode, Coord. Chem. Rev. 257 (2013) 1493–1506.

[26] G. Chelucci, R.P. Thummel, Chiral 2, 2‘-Bipyridines, 1, 10-Phenanthrolines, and 2,2′:6′,2″-Terpyridines: Syntheses and Applications in Asymmetric Homogeneous Catalysis, Chem. Rev. 102 (2002) 3129–3170.

[27] G. Zhang, J. Tan, T. Phoenix, D.R. Manke, J.A. Golen, A.L. Rheingold, Amalgamating 4′-substituted 4,2′:6′,4″-terpyridine ligands with double-helical chains or ladder-like networks, RSC Adv 6 (2016) 9270–9277.

[28] D. Zych, A. Slodek, M. Matussek, M. Filapek, G. S-Gorol, S. Maślanka, S. Krompiec, S. Kotowicz, E. S-Balcerzak, K. Smolarek, S. Maćkowski, M. Olejnik, W. Danikiewicz, 4′-Phenyl-2,2′:6′,2″-terpyridine derivatives-synthesis, potential application and the influence of acetylene linker on their properties, Dyes Pigments 146 (2017) 331–343.

[29] E.C. Constable, 2,2′:6′,2″-Terpyridines: From chemical obscurity to common supramolecular motifs, Chem. Soc. Rev. 36 (2007) 246–253.

[30] A.O. Adeloye, P.A. Ajibade, Towards the Development of Functionalized PolypyridineLigands for Ru(II) Complexes as Photosensitizers in Dye-Sensitized Solar Cells (DSSCs), Molecules 19 (2014) 12421–12460.

[31] A.M. Burger, F. Dai, C.M. Schultes, A.P. Reszka, M.J. Moore, J.A. Double, S. Neidle, The G-Quadruplex-Interactive Molecule BRACO-19 Inhibits Tumor Growth, Consistent with Telomere Targeting and Interference with Telomerase Function, Cancer Res 65 (2005) 1489–1496.

[32] D. Mahendiran, R.S. Kumar, V. Viswanathan, D. Velmurugan, A.K. Rahiman, Targeting of DNA molecules, BSA/c-Met tyrosine kinase receptors and anti-proliferative activity of bis(terpyridine)copper(II) complexes, Dalton Trans 45 (2016) 7794–7814.

[33] D. Mahendiran, R.S. Kumar, A.K. Rahiman, Heteroleptic silver(I) complexes with 2,2′:6′,2′′-terpyridines and naproxen: DNA interaction, EGFR/VEGFR2 kinase, growth inhibition and cell cycle arrest studies, Mater. Sci. Eng. C 76 (2017) 601–615.

[34] C. Wei, Y. He, X. Shi, Z. Song, Terpyridine-metal complexes, Applications in catalysis and supramolecular chemistry, Coord. Chem. Rev. 385 (2019) 1–19.

[35] D. Zych, A. Slodek, S. Krompiec, K. Malarz, A. Mrozek-Wilczkiewicz, R. Musiol, 4′-Phenyl208;2,2′:6′,2′′-terpyridine Derivatives Containing 1-Substituted-2,3-Triazole Ring: Synthesis, Characterization and Anticancer Activity, ChemistrySelect 3 (2018) 7009–7017.

[36] D. Zych, A. Slodek, M. Matussek, M. Filapek, G. Szafraniec-Gorol, S. Krompiec, S. Kotowicz, M. Siwy, E. Schab-Balcerzak, K. Bednarczyk, M. Libera, K. Smolarek, S. Maćkowski, W. Danikiewicz, Highly Luminescent 4′-(4-ethynylphenyl)208;2,2′:6′,2′′-Terpyridine Derivatives as Materials for Potential Applications in Organic Light Emitting Diodes, ChemistrySelect 2 (2017) 8221–8233.

[37] D. Zych, A. Slodek, M. Matussek, M. Filapek, G. Szafraniec-Gorol, S. Maślanka, S. Krompiec, S. Kotowicz, E. Schab-Balcerzak, K. Smolarek, S. Maćkowski, M. Olejnik, W. Danikiewicz, 4′-Phenyl-2,2′:6′,2′′-terpyridine derivatives-synthesis, potential application and the influence of acetylene linker on their properties, Dyes and Pigments 146 (2017) 331–343.

[38] L. Saghatforoush, K. Adil, M. Hasanzadeh, A. Aminkhani, S. Safarinezhad, Synthesis, Crystal Structure and Electrochemical Behavior of Two New Ni-based Complexes: [Ni2(ttpy)2(SCN)4] and [Ni(ttpy)2](CH3OH)2 (2I), Acta Chim. Slov. 59 (2012) 322–330.

[39] J. Schönle, E.C. Constable, C.E. Housecroft, M. Neuburger, Tuning peripheral π-stacking motifs in {Cr(tpy)2}3+ domains (tpy = 2,2′:6′,2′′-terpyridine), Inorg. Chem. Commun. 53 (2015) 80–83.

[40] D. Maspoch, D. Ruiz-Molina, J. Veciana, Old materials with new tricks: multifunctional open-framework materials, Chem. Soc. Rev. 36 (2007) 770–818.

[41] A.Y. Robin, K.M. Fromm, Coordination polymer networks with O- and N–donors: What they are, why and how they are made, Coord. Chem. Rev. 250 (2006) 2127–2157.

[42] D. Braga, F. Grepioni, L. Maini, S. D'Agostino, Making crystals with a purpose; a journey in crystal engineering at the University of Bologna, IUCrJ 4 (2017) 369–379.

[43] D. Braga, F. Grepioni, L. Maini, S. D'Agostino, From Solid-State Structure and Dynamics to Crystal Engineering, Eur. J. Inorg. Chem. 2018 (2018) 3597–3605.

[44] T.S. Thakur, R. Dubey, G.R. Desiraju, Crystal Structure and Prediction, Annu. Rev. Phys. Chem 66 (2015) 21–42.

[45] K.E. Riley, P. Hobza, On the Importance and Origin of Aromatic Interactions in Chemistry and Biodisciplines, Acc. Chem. Res. 46 (2013) 927–936.

[46] S. Goyal, A. Chattopadhyay, K. Kasavajhala, U.D. Priyakumar, Role of Urea–Aromatic Stacking Interactions in Stabilizing the Aromatic Residues of the Protein in Urea-Induced Denatured State, J. Am. Chem. Soc. 139 (2017) 14931–14946.

[47] C. Sutton, C. Risko, J.-L. Brédas, Noncovalent Intermolecular Interactions in Organic Electronic Materials: Implications for the Molecular Packing vs Electronic Properties of Acenes, Chem. Mater. 28 (2016) 3–16.

[48] S.K. Seth, A. Bauzá, A. Frontera, Bipolar behaviour of salt-bridges: a combined theoretical and crystallographic study, New J. Chem 42 (2018) 12134–12142.

[49] A. Bauzá, S.K. Seth, A. Frontera, Tetrel bonding interactions at work: Impact on tin and lead coordination Compounds, Coord. Chem. Rev. 384 (2019) 107–125.

[50] H.-J. Schneider, Binding Mechanisms in Supramolecular Complexes, Angew. Chem. Int. Ed. 48 (2009) 3924–3977.

[51] H. Eshtiagh-Hosseini, M. Mirzaei, M. Biabani, V. Lippolis, M. Chahkandi, C. Bazzicalupi, Insight into the connecting roles of interaction synthons and water clusters within different transition metal coordination compounds of pyridine-2,5-dicarboxylic acid: experimental and theoretical studies, CrystEngComm 15 (2013) 6752–6768.

[52] P. Seth, A. Bauzá, A. Frontera, C. Massera, P. Gamez, A. Ghosh, Analysis of the contribution of the π-acidity of the s-tetrazine ring in the crystal packing of coordination polymers, CrystEngComm 15 (2013) 3031–3039.

[53] T. Maity, H. Mandal, A. Bauzá, B.C. Samanta, A. Frontera, S.K. Seth, Quantifying conventional C–H···π(aryl) and unconventional C–H···π(chelate) interactions in dinuclear Cu(II) complexes: experimental observations, Hirshfeld surface and theoretical DFT study, New J. Chem. 42 (2018) 10202–10213.

[54] S, K Seth, The Importance of CH···X (X = O, π) Interaction of a New Mixed Ligand Cu(II) Coordination Polymer: Structure, Hirshfeld Surface and Theoretical Studies, Crystals 8 (2018) 455.

[55] J.W.G. Bloom, S.E. Wheeler, Taking the Aromaticity out of Aromatic Interactions, Angew. Chem. Int. Ed. 50 (2011) 7847–7849.

[56] S.K. Seth, D. Sarkar, T. Kar, Use of π–π forces to steer the assembly of chromone derivatives into hydrogen bonded supramolecular layers: crystal structures and Hirshfeld surface analyses, CrystEngComm 13 (2011) 4528–4535.

[57] A. Frontera, P. Gamez, M. Mascal, T.J. Mooibroek, J. Reedijk, Putting Anion–π Interactions Into Perspective, Angew. Chem. Int. Ed. 50 (2011) 9564–9583.

[58] M. Mitra, P. Manna, A. Bauzá, P. Ballester, S.K. Seth, S.R. Choudhury, A. Frontera, S. Mukhopadhyay, 3-Picoline Mediated Self-Assembly of M(II)−Malonate Complexes (M = Ni/Co/Mn/Mg/Zn/Cu) Assisted by Various Weak Forces Involving Lone Pair−π, π−π, and Anion···π−Hole Interactions, J. Phys. Chem. B 118 (2014) 14713–14726.

[59] S.K. Seth, I. Saha, C. Estarellas, A. Frontera, T. Kar, S. Mukhopadhyay, Supramolecular Self-Assembly of M-IDA Complexes Involving Lone-Pair···π Interactions: Crystal Structures, Hirshfeld Surface Analysis, and DFT Calculations [H2IDA = iminodiacetic acid, M = Cu(II), Ni(II)], Cryst. Growth Des. 11 (2011) 3250–3265.

[60] P. Manna, S.K. Seth, A. Das, J. Hemming, R. Prendergast, M. Helliwell, S.R. Choudhury, A. Frontera, S. Mukhopadhyay, Anion Induced Formation of Supramolecular Associations Involving Lone pair−π and Anion−π Interactions in Co(II) Malonate Complexes: Experimental Observations, Hirshfeld Surface Analyses and DFT Studies, Inorg. Chem. 51 (2012) 3557–3571.

[61] A. Bauza, S.K. Seth, A. Frontera, Molecular Electrostatic Potential and “Atoms-in-Molecules” Analyses of the Interplay between π-Hole and Lone Pair···π/X–H···π/Metal···π Interactions, J. Comput. Chem. 39 (2018) 458–463.

[62] Y. Cotelle, S. Benz, A.-J. Avestro, T.R. Ward, N. Sakai, S. Matile, Anion-π Catalysis of Enolate Chemistry: Rigidified Leonard Turns as a General Motif to Run Reactions on Aromatic Surfaces, Angew. Chem. Int. Ed. 55 (2016) 4275–4279.

[63] A.-B. Bornhof, A. Bauzá, A. Aster, M. Pupier, A. Frontera, E. Vauthey, N. Sakai, S. Matile, Synergistic Anion–(π)n–π Catalysis on π-Stacked Foldamers, J. Am. Chem. Soc. 140 (2018) 4884–4892.

[64] S.E. Wheeler, K.N. Houk, Substituent Effects in the Benzene Dimer are Due to Direct Interactions of the Substituents with the Unsubstituted Benzene, J. Am. Chem. Soc. 130 (2008) 10854–10855.

[65] E.R.T. Tiekink, Supramolecular assembly based on “emerging” intermolecular interactions of particular interest to coordination chemists, Coord. Chem. Rev. 345 (2017) 209–228.

[66] F. Biedermann, H.J. Schneider, Experimental Binding Energies in Supramolecular Complexes, Chem. Rev. 116 (2016) 5216–5300.

[67] J. Wang, G.S. Hanan, A Facile Route to Sterically Hindered and Non-Hindered 4′-Aryl-2,2′:6′,2′′-Terpyridines, Synlett 8 (2005) 1251–1254.

[68] A. Anthonysamy, S. Balasubramanian, K. Chinnakali, H.-K. Fun, 4′-(4-Methoxy phenyl)-2,2′:6′,2′′-terpyridine, Acta Cryst. E 63 (2007) o1148–o1150.

[69] F. Emmerling, J.L. Bricks, U. Resch-Genger, W. Kraus, B. Schulz, Y.Q. Li, G. Reck, Influence of the donor substituent and acceptor alkylation on the structure—analytical properties of mono- and bifunctional biphenyl-type fluorescent reporters, J. Mol. Struct. 874 (2008) 14–27.

[70] E.C. Constable, C.E. Housecroft, M. Neuburger, D. Phillips, P.R. Raithby, E. Schofield, Emma Sparr, D.A. Tocher, M. Zehnder, Y. Zimmermann, Development of supramolecular structure through alkylation of pendant pyridyl functionality, J. Chem. Soc., Dalton Trans. (2000) 2219–2228.

[71] BrukerSAINT, Version 6.36a, Bruker AXS Inc., Madison, Wisconsin, USA, 2002.

[72] BrukerSMART, Version 5.625 and SADABS, Version 2.03a, Bruker AXS Inc., Madison, Wisconsin, USA, 2001.

[73] G.M. Sheldrick, A short history of SHELX, Acta Cryst. A 64 (2008) 112–122.

[74] G.M. Sheldrick, Crystal structure refinement with SHELXL, Acta Cryst. C 71 (2015) 3–8.

[75] L.J. Farrugia, WinGX and ORTEP for Windows: an update, J. Appl. Cryst. 45 (2012) 849–854.

[76] A.L. Spek, Single-crystal structure validation with the program PLATON, J. Appl. Crystallogr. 36 (2003) 7–13.

[77] M.A. Spackman, J.J. McKinnon, Fingerprinting intermolecular interactions in molecular crystals, CrystEngComm 4 (2002) 378–392.

[78] J.J. McKinnon, D. Jayatilaka, M.A. Spackman, Towards quantitative analysis of intermolecular interactions with Hirshfeld surfaces, Chem. Commun. (2007) 3814–3816.

[79] S.K. Seth, A. Bauzá, A. Frontera, Screening polymorphism in a NiIJII) metal–organic framework: experimental observations, Hirshfeld surface analyses and DFT studies, CrystEngComm 20 (2018) 746–754.

[80] S.K. Seth, Tuning the formation of MOFs by pH influence: X-ray structural variations and Hirshfeld surface analyses of 2-amino-5-nitropyridine with cadmium chloride, CrystEngComm 15 (2013) 1772–1781.

[81] M.A. Spackman, P.G. Byrom, A novel definition of a molecule in a crystal, Chem. Phys. Lett. 267 (1997) 215–220.

[82] J.J. McKinnon, A.S. Mitchell, M.A. Spackman, Hirshfeld Surfaces: A New Tool for Visualising and Exploring Molecular Crystals, Chem.–Eur. J. 4 (1998) 2136–2141.

[83] J.J. McKinnon, M.A. Spackman, A.S. Mitchell, Novel tools for visualizing and exploring intermolecular interactions in molecular crystals, Acta Crystallogr. Sect. B 60 (2004) 627–668.

[84] A.L. Rohl, M. Moret, W. Kaminsky, K. Claborn, J.J. Mckinnon, B. Kahr, Hirshfeld Surfaces Identify Inadequacies in Computations of Intermolecular Interactions in Crystals: Pentamorphic 1,8-Dihydroxyanthraquinone, Cryst. Growth Des. 8 (2008) 4517–4525.

[85] S.K. Seth, Structural characterization and Hirshfeld surface analysis of a CoII complex with imidazo[1,2-a]-pyridine, Acta Cryst. E 74 (2018) 600–606.

[86] S. Tripathi, A. Hossain, S.K. Seth, S. Mukhopadhyay, Quantitative insights into the crystal structure of a mixed-ligand Co(III) complex: Experimental and theoretical studies, J. Mol. Struct. 1216 (2020) 128207.

[87] M.J. Turner, J.J. McKinnon, S.K. Wolff, D.J. Grimwood, P.R. Spackman, D. Jayatilaka, M.A. Spackman, CrystalExplorer17; University of Western Australia, 2017.

[88] M.J. Frisch, G.W. Trucks, H.B. Schlegel, G.E. Scuseria, M.A. Robb, J.R. Cheese-

man, G. Scalmani, V. Barone, G.A. Petersson, H. Nakatsuji, et al., Gaussian 09, Revision C.01, Gaussian, Inc., Wallingford, CT, USA, 2009.
[89] R.F.W. Bader, A quantum theory of molecular structure and its applications, Chem. Rev. 91 (1991) 893–928.
[90] T.A. Keith, AIMAll, Version 13.05.06, TK Gristmill Software: Overland Park, KS, USA, 2013.
[91] R.F.W. Bader, Atoms in Molecules, a Quantum Theory, Oxford University Press, New York, NY, USA, 1990.
[92] J. Contreras-García, E.R. Johnson, S. Keinan, R. Chaudret, J.P. Piquemal, D.N. Beratan, W. Yang, NCIPLOT: A Program for Plotting Noncovalent Interaction Regions, J. Chem. Theory Comput. 7 (2011) 625–632.
[93] E.R. Johnson, S. Keinan, P. Mori-Sanchez, J. Contreras-Garcia, A.J. Cohen, W. Yang, Revealing Noncovalent Interactions, J. Am. Chem. Soc. 132 (2010) 6498–6506.
[94] E.C. Constable, J. Lewis, M.C. Liptrot, P.R. Raithby, The coordination chemistry of 4′-phenyl-2,2′:6′, 2″-terpyridine; the synthesis, crystal and molecular structures of 4′-phenyl-2,2′:6′,2″-terpyridine and bis(4′-phenyl-2,2′;:6′,2″-terpyridine)nickel(II) chloride decahydrate, Inorg. Chim. Acta 178 (1990) 47–54.
[95] P. Ledwaba, O.Q. Munro, K. Stewart, 4′-[2-(Trifluoromethyl)phenyl]-2,2′:6′,2″-Terpyridine, Acta Cryst. E 65 (2009) o376–o377.
[96] T. Takase, Y. Soga, D. Oyama, 4′-(3,4-Dimethoxyphenyl)-2,2′:6′,2′′-terpyridine, IUCrData 1 (2016) x160950.
[97] R.P. Thummel, Y. Jahng, Polyaza cavity shaped molecules. 4. Annelated derivatives of 2,2′:6′,2"-terpyridine, J. Org. Chem. 50 (1985) 2013–2407.
[98] C.A. Bessel, R.F. See, D.L. Jameson, M.R. Churchill, K.J. Takeuchi, Structural considerations of terdentate ligands: crystal structures of 2,2′;:6′,2″-terpyridine and 2,6-bis(pyrazol-1-yl)pyridine, J. Chem. Soc., Dalton Trans. (1992) 3223–3228.
[99] E.C. Constable, F.K. Khan, V.E. Marquez, P.R. Raithby, 6, 6′’-Dibromo-4′-phenyl-2, 2′:6′,2′’-terpyridine, Acta Cryst. C 48 (1992) 932–934.
[100] G.D. Storrier, S.B. Colbran, D.C. Craig, Bis[4′-(4-anilino)-2,2′:6′;,2″-terpyridine] transition-metal complexes: electrochemically active monomers with a range of magnetic and optical properties for assembly of metallo oligomers and macromolecules, J. Chem. Soc. Dalton Trans. (1997) 3011–3028.
[101] S.K. Seth, Exploration of supramolecular layer and bi-layer architecture in M(II)–PPP complexes: Structural elucidation and Hirshfeld surface analysis [PPP = 4-(3-Phenylpropyl)pyridine, M = Cu(II), Ni(II)], J. Mol. Struct. 1070 (2014) 65–74.
[102] R.F.W. Bader, A Bond Path: A Universal Indicator of Bonded Interactions, J. Phys. Chem. A 102 (1998) 7314–7323.